

FINAL REPORT

Estimating Mobile-Immobile Mass Transfer Parameters Using Direct Push Tools

SERDP Project ER-2529

OCTOBER 2020

Robert Borden
Draper Aden Associates

Ron Falta
Clemson University

Gaisheng Liu
James J. Buter, Jr.
University of Kansas

Distribution Statement A

This document has been cleared for public release



Page Intentionally Left Blank

REPORT DOCUMENTATION PAGE				Form Approved OMB No. 0704-0188	
Public reporting burden for this collection of information is estimated to average 1 hour per response, including the time for reviewing instructions, searching existing data sources, gathering and maintaining the data needed, and completing and reviewing this collection of information. Send comments regarding this burden estimate or any other aspect of this collection of information, including suggestions for reducing this burden to Department of Defense, Washington Headquarters Services, Directorate for Information Operations and Reports (0704-0188), 1215 Jefferson Davis Highway, Suite 1204, Arlington, VA 22202-4302. Respondents should be aware that notwithstanding any other provision of law, no person shall be subject to any penalty for failing to comply with a collection of information if it does not display a currently valid OMB control number. PLEASE DO NOT RETURN YOUR FORM TO THE ABOVE ADDRESS.					
1. REPORT DATE (DD-MM-YYYY) 10-15-2020		2. REPORT TYPE SERDP Final Report		3. DATES COVERED (From - To) 7/13/2015 - 3/30/2021	
4. TITLE AND SUBTITLE Estimating Mobile-Immobile Mass Transfer Parameters Using Direct Push Tools				5a. CONTRACT NUMBER W912HQ-15-C-0013	
				5b. GRANT NUMBER	
				5c. PROGRAM ELEMENT NUMBER	
6. AUTHOR(S) Robert C. Borden, Ki Young Cha, Ron Falta, Gaisheng Liu and James J. Buter, Jr.				5d. PROJECT NUMBER ER-2529	
				5e. TASK NUMBER	
				5f. WORK UNIT NUMBER	
7. PERFORMING ORGANIZATION NAME(S) AND ADDRESS(ES) Draper Aden Associates, 114 Edinburgh South Drive, Suite 200, Cary, NC 27511 Clemson University, Brackett Hall, Room 340C, Clemson SC 29634-0919 Kansas Geological Survey, University of Kansas 1930 Constant Ave., Lawrence, KS 66047				8. PERFORMING ORGANIZATION REPORT NUMBER ER-2529	
9. SPONSORING / MONITORING AGENCY NAME(S) AND ADDRESS(ES) Strategic Environmental Research and Development Program 4800 Mark Center Drive, Suite 17D08, Alexandria, VA 22350				10. SPONSOR/MONITOR'S ACRONYM(S) SERDP	
				11. SPONSOR/MONITOR'S REPORT NUMBER(S) ER-2529	
12. DISTRIBUTION / AVAILABILITY STATEMENT Unlimited Distribution					
13. SUPPLEMENTARY NOTES					
14. ABSTRACT Back diffusion of contaminants stored in zones with lower hydraulic conductivity (K) can slow aquifer recovery, greatly extending the time to reach remediation goals. In this project, a suite of field and modeling approaches are developed allowing users to better characterize low-K zones in the field, more accurately simulate mass transfer between low-K and high-K zones, and evaluate the impact of these processes on the time to reach groundwater cleanup goals following source removal. Work included: 1) development of low-cost direct push (DP) methods for high-resolution characterization of K; 2) high-resolution characterization and solute transport modeling to evaluate ability to simulate back-diffusion processes; 3) development of methods to calibrate existing and new mobile-immobile zone models; and 4) development of simplified methods for estimating the impact of matrix diffusion on cleanup time.					
15. SUBJECT TERMS hydraulic profiling tool, HPT, hydraulic conductivity, matrix diffusion, modeling					
16. SECURITY CLASSIFICATION OF:			17. LIMITATION OF ABSTRACT UU	18. NUMBER OF PAGES 213	19a. NAME OF RESPONSIBLE PERSON Robert C. Borden
a. REPORT unclassified	b. ABSTRACT unclassified	c. THIS PAGE unclassified			19b. TELEPHONE NUMBER (include area code) 919-349-8472

Page Intentionally Left Blank

This report was prepared under contract to the Department of Defense Strategic Environmental Research and Development Program (SERDP). The publication of this report does not indicate endorsement by the Department of Defense, nor should the contents be construed as reflecting the official policy or position of the Department of Defense. Reference herein to any specific commercial product, process, or service by trade name, trademark, manufacturer, or otherwise, does not necessarily constitute or imply its endorsement, recommendation, or favoring by the Department of Defense.

Page Intentionally Left Blank

TABLE OF CONTENTS

TABLE OF CONTENTS	I
LIST OF FIGURES.....	III
LIST OF TABLES	X
ACRONYMS AND ABBREVIATIONS.....	XI
ACKNOWLEDGEMENTS.....	XII
ABSTRACT	XIII
EXECUTIVE SUMMARY	XVI
INTRODUCTION	XVI
ES-1 DIRECT PUSH (DP) METHODS DEVELOPMENT	XVII
ES-2 SITE CHARACTERIZATION AND NUMERICAL MODEL DEVELOPMENT	XIX
ES-3 MOBILE-IMMOBILE ZONE MODEL PARAMETER ESTIMATION	XXI
ES-4 ESTIMATING THE IMPACT OF MATRIX DIFFUSION ON CLEANUP TIME	XXIV
1.0 INTRODUCTION	1
1.1 OBJECTIVES	1
1.2 REPORT ORGANIZATION	2
2.0 DIRECT PUSH (DP) METHODS DEVELOPMENT.....	3
2.1 INTRODUCTION.....	3
2.2 SIMULATION OF DIRECT PUSH INJECTION LOGGING	3
2.2.1 Background.....	3
2.2.2 Direct push injection logging (DPIL)	5
2.2.3 Numerical simulation overview	6
2.2.4 Results	8
2.2.5 Summary and Conclusions	21
2.3 LOW K HPT TOOL CONSTRUCTION AND LABORATORY EXPERIMENTS	23
2.3.1. Construction of the low-K HPT tool.....	23
2.3.2 Laboratory experiments	26
2.4 LOW-K HPT TESTS AT GEMS.....	29
2.5 A PHYSICALLY BASED EQUATION FOR ESTIMATING K	34
2.5.1 Developing New Relationship for Estimating K	36
2.5.2 Field Evaluation of K Estimation Relationships.....	39
2.5.3 Dependence of P_c on Q and V	42
2.5.4 Summary.....	43
3.0 SITE CHARACTERIZATION AND NUMERICAL MODEL DEVELOPMENT	45
3.1 AIR FORCE PLANT 3	45
3.1.1 AFP3 EVO Pilot Test	46
3.1.2 AFP3 Site Characterization	50
3.1.3 Flow and Transport Modeling with DP Technologies.....	67
3.2 NTC ORLANDO OU2 OVERVIEW	84
3.2.1 OU2 EVO Barrier	85
3.2.2 OU2 Site Characterization	87
3.3 FLOW AND SOLUTE TRANSPORT SIMULATION	94
3.4 LESSONS LEARNED	95
4.0 MOBILE-IMMOBILE ZONE MODEL PARAMETER ESTIMATION.....	97
4.1 INTRODUCTION.....	97
4.2 SEMI-ANALYTICAL MATRIX DIFFUSION METHOD.....	98
4.3 MATRIX DIFFUSION MASS FLOW	101
4.4 NUMERICAL FORMULATION	102
4.5 SEMI-ANALYTICAL METHOD PARAMETERS	103
4.6 SEMI-ANALYTICAL MODEL SIMULATION OF MATRIX DIFFUSION IN A HETEROGENEOUS SAND TANK EXPERIMENT.....	104

4.7	USING SEMI-ANALYTICAL METHOD TO REPRODUCE FINE-GRID HETEROGENEOUS NUMERICAL SIMULATIONS.....	109
4.8	COMPARISON OF SEMI-ANALYTICAL AND DUAL-DOMAIN METHODS FOR SIMULATING MATRIX DIFFUSION IN PARALLEL FRACTURES	118
5.0	ESTIMATING THE IMPACT OF MATRIX DIFFUSION ON CLEANUP TIME	133
5.1	INTRODUCTION.....	133
5.2	APPROACH	134
5.3	REGRESSION ANALYSIS FOR NON-REACTIVE TRACER	136
5.3.1	Heterogeneous Aquifer without Low K Boundaries.....	138
5.3.2	Homogeneous Aquifer with Low K Boundaries.....	139
5.4	CONTAMINANT LOADING PERIOD	140
5.5	CONTAMINANT SORPTION.....	141
5.6	IMPLICATIONS FOR REMEDIATION SYSTEM DESIGN	143
5.7	SUMMARY	144
6.0	REFERENCES	146
	APPENDIX A FIELD OPERATING PROCEDURE OF LOW-K HYDRAULIC PROFILING TOOL (HPT).....	151
A.1	BACKGROUND.....	151
A.2	Low-K HPT.....	152
A.3	FIELD EQUIPMENT SETUP.....	152
A.4	PRE-LOGGING PREPARATION	153
A.5	RUNNING THE LOW-K HPT LOG	154
A.6	Low-K HPT LOG ANALYSIS.....	155
A.7	K ESTIMATION FROM LOW-K HPT DEPTH LOG	155
	APPENDIX B HYDRAULIC CONDUCTIVITY CHARACTERIZATION METHODS	159
B.1	INTRODUCTION.....	159
B.2	HYDRAULIC TESTING APPROACHES	161
B.2.1	Pumping Tests	161
B.2.2	Slug Tests	161
B.2.3	Borehole Flowmeter Profiling	166
B.2.4	DP Injection Logging.....	167
B.2.5	DP Permeameter.....	170
B.2.6	Laboratory Permeameter Tests on Core Samples	172
B.3	INDIRECT APPROACHES.....	172
B.3.1	Geophysical Methods	172
B.3.2	Cone Penetrometer profiling.....	174
B.3.3	Laboratory Grain Size Analyses on Core Samples	174
B.4	CHOOSING THE RIGHT APPROACHES	175
B.5	SUMMARY	176
B.6	REFERENCES	176
B.7	SEE ALSO	179
	APPENDIX C PUBLICATIONS AND PRESENTATIONS.....	180
C.1	JOURNAL ARTICLES.....	180
C.2	ENVIRO.WIKI ARTICLES	180
C.3	PRESENTATIONS AND POSTERS.....	180

LIST OF FIGURES

- Figure 2-1.** (A) Schematic of the DPIL with a water injection screen attached to the probe rod, (B) Artistic rendering of the HPT (continuous DPIL coupled with an EC Wenner array)..... 4
- Figure 2-2.** Model setup for DPIL simulations. (A) The simulation domain is 4 m long, 4 m wide, and 1.8 m thick, with the DPIL probe (diameter 4.445 cm) at the center, (B) Discontinuous DPIL injection at a single depth where water is injected through the screen (green circle), and (C) Continuous DPIL where the screen moves with the advancement of the probe and water injection is divided into a sequence of vertical 1.5-cm intervals (blue rectangles). 7
- Figure 2-3.** Injection pressure head distributions from discontinuous DPIL simulations: (A) pressure on the surface of the probe for a homogenous and isotropic K field; expanded view of the pressure near the injection screen for (B) a homogenous and isotropic K field, (C) a homogenous and anisotropic K field (vertical K component is $1/10^{\text{th}}$ of the horizontal), (D) a low-K skin (the skin is 1 cm thick with a K value $1/10^{\text{th}}$ that of the aquifer), (E) a low-K layer intersecting the screen, (F) a low-K layer immediately above the screen, (G) a high-K layer intersecting the screen, (H) a high-K layer immediately above the screen. The pressure head is shown after three seconds of injection (470 mL/min) in all plots. Figures B to H are plotted along a vertical plane perpendicular to the center of the injection screen. In (E) and (F), the low-K layer is 1.5 cm thick with a K value $1/100^{\text{th}}$ that of the aquifer. In (G) and (H), the high-K layer is 1.5 cm thick with a K value 100 times that of the aquifer. Due to the very high- and low-pressure heads, respectively, the legends for (E) and (G) are different from the other plots..... 9
- Figure 2-4.** Injection pressure head versus time for different diffusivities from discontinuous DPIL simulations in a uniform aquifer. 10
- Figure 2-5.** (A) Simulated injection rate/pressure head versus hydraulic conductivity, and (B) injection rate/pressure head/specific storage versus hydraulic diffusivity for discontinuous DPIL. The injection pressure is averaged over the entire screen after 3 seconds of injection. Figure (A) shows that for the considered specific storage range (1.7×10^{-6} to 0.08 m^{-1}), the ratio of injection rate to pressure head is linear with K in a log-log plotting format when K is essentially greater than 10^{-6} m/s . Figure (B) shows that by dividing the ratio of injection rate to pressure head by the specific storage, $Q/P/S_s$ is uniquely determined by the hydraulic diffusivity over the entire K range. 11
- Figure 2-6.** The DPIL Q/P ratio for (A) K anisotropy (the ratio of vertical to horizontal K, $K_v:K_h$, varies from 1:1 to 1:1024; the horizontal K is fixed at 10^{-4} m/s), (B) low-K skin with fixed thickness (the skin thickness is fixed at 1 cm; the skin K (K_s) varies from 1 to $1/1024^{\text{th}}$ of the aquifer K, 10^{-4} m/s), and (C) low-K skin with fixed K (K_s is fixed at $1/10^{\text{th}}$ of the aquifer K; skin thickness varies from 0.5 to 3.5 cm. The specific storage is the same in all plots ($7 \times 10^{-5} \text{ m}^{-1}$). The dashed lines in (A) and (B) are the simulation results for the isotropic and uniform K field for comparison. In (A), assuming no anisotropy, the Q/P value at the diamond ($K_v=4 \times 10^{-6} \text{ m/s}$, $K_h=10^{-4} \text{ m/s}$) would lead to an estimated $K^*=5 \times 10^{-5} \text{ m/s}$ (see the dotted lines with arrows). In (B), assuming no skin, the Q/P value at the diamond ($K_s=4 \times 10^{-6} \text{ m/s}$, aquifer $K=10^{-4} \text{ m/s}$) would lead to an estimated $K^*=1.3 \times 10^{-5} \text{ m/s}$ (see the dotted lines with arrows). 12
- Figure 2-7.** Pressure head increase during continuous DPIL: (A) Spatial distribution at 140 seconds since the start of probe advancement, (B) Pressure head versus time at depth 1.25 m below top of the model. In (A), half of the model domain is cut out to facilitate visualization.

In the expanded inset in (B), the different components of the total pressure head measured at the screen are labelled.	16
Figure 2-8. (A) Q/P versus K and (B) Q/P/Ss versus D during continuous DPIL at an advancement speed of 1 cm/s. Neither the impact of water injection at previous depths nor probe advancement is considered here. The plotted Q and P are calculated as the average over each rectangular measurement interval (1.5 cm vertical by 1 cm horizontal) during injection. ...	17
Figure 2-9. (A) Pressure head increase measured at the injection screen due to probe advancement (P_{rod}) at 1 cm/s as a function of K and S_s , (B) Contours of Q/P measured at the injection screen (P includes the pressure head due to both probe advancement and water injection) as a function of K and S_s , and (C) Q/P versus K for all simulated S_s . In (A), the values on the S_s and K axes are reversed so that pressure heads are better displayed visually. In (B), the gray area indicates the conditions where the pressure head produced by probe advancement exceeds the measurement limit, the yellow zone indicates the transition conditions where the impact of probe advancement is likely high, and the dashed box represents the typical range of S_s for unconsolidated sediments. In (C), the results are subdivided into those for $S_s < 10^{-3} \text{ m}^{-1}$ and those for $S_s > 10^{-3} \text{ m}^{-1}$	19
Figure 2-10. Simulated Q/P versus K during continuous DPIL at different advancement speeds for (A) $S_s = 7 \times 10^{-5} \text{ m}^{-1}$, and (B) $S_s = 9 \times 10^{-3} \text{ m}^{-1}$. Based on (A), for $S_s = 7 \times 10^{-5} \text{ m}^{-1}$ and $K = 5 \times 10^{-7} \text{ m/s}$, the simulated Q/P is 2.9×10^{-8} and $2.4 \times 10^{-8} \text{ m}^3/\text{s/m}$, at advancement speeds of 0.5 and 2 cm/s, respectively; this represents a 16% reduction in Q/P. Based on (B), where S_s is increased to $9 \times 10^{-3} \text{ m}^{-1}$, this change in advancement speeds results in the 16% reduction in Q/P when K is $3 \times 10^{-7} \text{ m/s}$ (the simulated Q/P at $K = 3 \times 10^{-7} \text{ m/s}$ is 2.7×10^{-8} and $2.2 \times 10^{-8} \text{ m}^3/\text{s/m}$, respectively).	21
Figure 2-11. The flowmeter/controller used in the low-flow HPT system (https://www.omega.com/pptst/FLR1600.html).	24
Figure 2-12. The design of low-K HPT system. The low-K HPT extension is achieved by adding a low-flow control box to the standard HPT system. A) through G) mark the key components of the HPT system. The typical flow rate for the standard HPT ranges from 200 to 600 mL/min, the low-flow HPT injection rate can be reduced to 5 mL/min.	25
Figure 2-13. The prototype low-K HPT system.	26
Figure 2-14. (A) schematic of the flow box for testing the low-K HPT, and (B) picture of the flow box constructed in the lab.	27
Figure 2-15. (A) injection rate and pressure versus time prior to de-airing the source water, and (B) injection rate and pressure versus time after de-airing the source water.	28
Figure 2-16. Three HPT profiles in the lab flow box obtained with the new low-K HPT system. The HPT injection rate used in the silt layer, from the left to right profile, are 4 mL/min, 0.4 mL/min, and 0.1 mL/min, respectively. The transition of the top sand layer to the middle silt layer is indicated by the increase in both EC and HPT pressure (marked by the shaded intervals).	29
Figure 2-17. Location of GEMS and a profile of the shallow stratigraphy at the site (after Butler, 2005). The EC variation in the upper 12 m is a function of clay content. The water table is shown by the inverted triangle. Testing of the low-K HPT system was performed in the upper silt and clay layer.	30
Figure 2-18. (A) Picture of low-K HPT field operation, (B) Distribution of the HPT test profiles at GEMS (different symbols indicate two separate time periods during which the profiles are performed).	30

Figure 2-19. Comparison of low-K HPT profiles at three different flow rates. The red, green and blue profiles are for injection rates 260, 20, and 5 mL/min, respectively. The probe advancement speed is fixed at 2 cm/s for all three profiles.	31
Figure 2-20. Comparison of low-K HPT profiles at two different probe advancement rates. The red and green profiles are for advancement speeds 2 and 0.5 cm/s, respectively. The water injection rate is fixed at 20 mL/min for both profiles.	32
Figure 2-21. An example K profile estimated from the injection pressure and flow rate by the low-K HPT tool at GEMS. The injection rate for this profile is 5 mL/min. “Rod” represents the probe advancement pressure, estimated based on the numerical simulation results presented in Section 2.2.3 . The injection pressure is computed as the difference between HPT pressure and probe advancement pressure.	33
Figure 2-22. Comparison of slug test K estimates with HPT K profiles. The slug test K estimates are plotted as solid squares. Three HPT K profiles are plotted, which show a consistent overall pattern with some local variations.	34
Figure 2-23. Schematic of Hydraulic Profiling Tool (HPT). During HPT profiling, water is injected through the flow tube and out of the screened port, and pressure is measured inside the connection rod right above the injection port. Formation bulk electrical conductivity is measured near the bottom of probe to provide additional information on subsurface conditions (Schulmeister et al., 2003; McCall et al., 2017).	35
Figure 2-24. Numerical simulation results from Liu et al. (2019) relating hydraulic diffusivity (K/S_s) to pressure generated by HPT probe advance (P_p) and fluid injection through the HPT probe (P_i). Note that the summation of P_p and P_i is the pressure change at the injection port that is measured during field HPT profiling.	37
Figure 2-25. K as a function of corrected pressure (P_c) for varying specific storage (S_s), probe speed (V) and injection rate (Q). In all three plots, the base case parameter values are $S_s=0.001/m$, $V=2$ cm/s, and $Q=200$ mL/min. In the left plot, S_s is varied between 0.0003 and 0.001 /m; in the right plot, Q is varied between 50 and 600 mL/min. In the middle plot, the probe velocity is varied between 0.5 and 2 cm/s at two different flow rates (200 and 50 mL/min).	38
Figure 2-26. Comparison of reference K with estimates generated by Eq 2-9.	39
Figure 2-27. Comparison of K estimates from slug tests and HPT profiling using Eq 2-10. The HPT K is vertically averaged over the saturated screened interval of the adjoining slug test well.	42
Figure 2-28. Pressure generated for varying Q and K at $V=2$ and 0.5 cm/s.	43
Figure 3-1. Location of pilot test area (dashed box) in relation to CVOCs and 1,4-D plumes. .	45
Figure 3-2. Location of monitor and injection wells in the vicinity of EVO pilot test.	46
Figure 3-3. Water table elevation during seven monitoring events in line extending from MW-1 to 8-20.	47
Figure 3-4. Bromide concentration versus time in injection and monitoring wells.	48
Figure 3-5. TCE, cDCE, VC and ethene concentration versus time in injection and monitoring wells.	49
Figure 3-6. Chlorine number (Cl#) and total ethenes versus time in injection and monitoring wells.	49
Figure 3-7. Normalized CPT SBT chart. OCR stands for over consolidation ratio. (Robertson, 1990; Robertson and Cabal 2010).	50
Figure 3-8. CPT Boring Log from CPT-04 location.	51

Figure 3-9.	Location of the CPT cross-sections and includes the lithologic legend.....	52
Figure 3-10.	CPT Cross-section from CPT A to A' approximately parallel to flow.....	53
Figure 3-11.	CPT Cross-section from B to B' approximately perpendicular to flow.....	53
Figure 3-12.	Example dissipation test to determine t_{50}	54
Figure 3-13.	HPT and CPT Boring locations.....	56
Figure 3-14.	HPT Boring Logs from HPT-13. The EC, HPT Pressure, HPT Flow rate, and Estimated K (Geoprobe equation) presented from left to right with elevation.....	58
Figure 3-15.	Profiles of estimated K from HPT parallel to flow (HPT A- HPT A').....	59
Figure 3-16.	Profiles of estimated K from HPT perpendicular to flow (HPT B- HPT B')	60
Figure 3-17.	Typical boring log showing TCE concentrations and visual classification of soil.....	63
Figure 3-18.	Profiles of TCE and DCE concentration and Cl# in soil samples. DPT-3 is 20 ft upgradient of the PRB, DPT-2 is 20 ft downgradient, and DPT-1 is 50 ft downgradient....	64
Figure 3-19.	Cumulative frequency distribution (CFD) of hydraulic conductivity (K) in HPT borings at AFP3.	68
Figure 3-20.	Distribution of low K and high K material for different high/low cutoff values. Low K material is shown in orange and high K material in white. Material distribution is overlain by soil profiles generated from HPT borings.....	69
Figure 3-21.	Transitional probability plots in vertical direction from T-PROGS. Filled circles is the transitional probability generated from borehole data. Solid line is fitted Markov Chain Model.	70
Figure 3-22.	Plan view and longitudinal cross-section view of realizations 1 to 5. Plan-view at Layer 12 (620.7 ft. msl). Longitudinal cross section is at the center line of model domain passing through MW-2 and 3.....	72
Figure 3-23.	Simulated bromide concentration in layer 12 (620.7 ft msl) for realization #1 at 0, 1, 2, 3, 6, and 12 months after Injection.	75
Figure 3-24.	Comparison of observed Br concentrations at injection wells (left) and monitoring wells (right) with simulation results for realizations 1 to 5.	76
Figure 3-25.	Contaminant distribution after 50 years of source loading and 5 years after source removal.	78
Figure 3-26.	Relative concentrations (C/C_0) versus time in downgradient monitor wells following PRB installation.	79
Figure 3-27.	Projected long-term trends in Q-weighted TCE concentrations in monitor wells following PRB installation.....	80
Figure 3-28.	TCE concentrations versus time from REMChlor-MD with complete source removal after 50-year loading period.....	83
Figure 3-29.	The graphs of C/C_0 vs. time at four monitoring well locations.....	84
Figure 3-30.	CPT and HPT boring locations in the northern characterization area.....	86
Figure 3-31.	HPT Locations (HPT-7 through HPT-21) for January 2018 Fieldwork.	86
Figure 3-32.	Variation in TCE, cDCE, VC and Cl# versus time in OU2-43B and OU2-47B. ..	87
Figure 3-33.	CPT borings and interpolated soil units in cross section extending from CPT 1 to 13.....	88
Figure 3-34.	HPT borings and interpolated soil units in cross section extending through OU2-17A.....	89
Figure 3-35.	Electrical conductivity (EC), hydraulic conductivity (K) and solute transport velocity versus elevation plus and minus one standard deviation.	90

Figure 3-36. TCE, cDCE, VC, and ethene at varying depths upgradient, within, and downgradient of the EVO injection zone. Area in pie chart is proportional to concentration.....	91
Figure 3-37. Profiles of soil composition, K, and TCE, cDCE and VC concentrations in soil samples collected from a boring adjoining OU2-43B.	92
Figure 3-38. Comparison of measured concentrations versus simulated TCE profile generated with Dandy-Sale Model (Sale et al., 2008).	93
Figure 3-39. Predicted mass discharge and average TCE concentrations in a monitoring well (10-ft screen) installed immediately above the confining layer and adjoining the GOAA canal.	93
Figure 3-40. Simulated vertical distribution of TCE in aquifer prior to PRB installation (T=0 yr) and 40 years after PRB installation.	94
Figure 3-41. Comparison of simulated and observed TCE concentrations in monitor wells OU2-43B and OU2-47B following following PRB installation.	95
Figure 3-42. Projected long-term TCE concentrations in monitor wells OU2-43B and OU2-47B following PRB installation.	95
Figure 4-1. Sandbox experiment setup. Adapted from Doner (2008).	104
Figure 4-2. Approximate dimensions of clay lenses estimated from Doner (2008).	105
Figure 4-3. Effluent concentration vs time profile comparing the semi-analytical model using 50 gridblocks with experimental data for Doner (2008) for a) bromide and b) fluorescein.	107
Figure 4-4. Effect of diffusion length on effluent concentration profile for the case of matrix diffusion from suspended low k zones for a) bromide and b) fluorescein.	108
Figure 4-5. Boreholes used for T-PROGS simulation (z magnification = 2).	109
Figure 4-6. Material distribution from T-PROGS for lens case (z magnification=2).	110
Figure 4-7. Specified head conditions for the flow field in lens case.	110
Figure 4-8. Head contours for lens case.	111
Figure 4-9. Location of TCE source for MT3DMS simulation.	111
Figure 4-10. MT3DMS simulated TCE concentration distribution after 30 years.	112
Figure 4-11. MT3DMS simulated TCE concentration distribution after 230 years (200 years of flushing).	113
Figure 4-12. Illustration of weighted average L calculation.	114
Figure 4-13. TCE mass discharge rate vs time profile comparing the MT3DMS model with REMChlor-MD for lens case with $L = 1.85$ m.	115
Figure 4-14. TCE mass discharge rate vs time profile comparing the MT3DMS model with REMChlor-MD for lens case with $L = 1.5$ m.	116
Figure 4-15. Comparison of MT3DMS ($k=200$) and REMChlor-MD (layer #18) models in xy plane at $t=10$ yrs for lens case. Above: REMChlor-MD contours over MT3DMS contours. Below: MT3DMS contours (left) and REMChlor-MD contours (right).	117
Figure 4-16. Comparison of MT3DMS ($k=200$) and REMChlor-MD (layer #18) models in xy plane at $t=30$ yrs for lens case. Above: REMChlor-MD contours over MT3DMS contours. Below: MT3DMS contours (left) and REMChlor-MD contours (right).	117
Figure 4-17. Comparison of MT3DMS ($k=200$) and REMChlor-MD (layer #18) models in xy plane at $t=130$ yrs for lens case. Above: REMChlor-MD contours over MT3DMS contours. Below: MT3DMS contours (left) and REMChlor-MD contours (right).	118
Figure 4-18. Characteristic diffusion time in systems of varying fracture spacing (m).	121
Figure 4-19. Mobile porosity and immobile porosity as fracture spacing increases.	122
Figure 4-20. Darcy velocity and hydraulic conductivity as fracture spacing increases.	123
Figure 4-21. Concentration profiles for fracture spacing of 10m, 2m, 0.5m, and 0.1m.	126

Figure 4-22. Concentration profile without diffusion for fracture spacing $a = 0.1$ m	127
Figure 4-23. Comparison of analytical, semi-analytical, and dual domain concentration profiles for a fracture spacing of 10 m at 1, 49, 51, and 100 years.	129
Figure 4-24. Comparison of analytical, semi-analytical, and dual domain concentration profiles with a fracture spacing of 2 m at 1, 49, 51, and 100 years.....	130
Figure 4-25. Comparison of analytical, semi-analytical, and dual domain concentration profiles with a fracture spacing of 0.1m at 1, 49, 51, and 100 years.....	131
Figure 4-26. Average marginal NRMSEs comparison between semi-analytical and uncalibrated dual-domain models over fracture spacing range between 0.1 <i>m</i> and 10 <i>m</i>	132
Figure 5-1. Example contaminant breakthrough and flush out curves for homogeneous aquifer with zero (0 BD) and one (1 BD) low K boundaries and aquifer transport velocity (V) = 105 and 10.5 m/yr.	134
Figure 5-2. Aquifer conditions evaluated: a) heterogeneous aquifer with no low K boundaries; and a) homogeneous aquifer with semi-infinite low K boundaries.	135
Figure 5-3. Comparison of cleanup times calculated with RemChlor-MD and simplified regression equations for heterogeneous aquifer without low K boundaries and homogeneous aquifer with low K boundaries.....	138
Figure 5-4. Cleanup time (T) and normalized cleanup time (T/T_{PV}) in a heterogeneous aquifer without low K boundaries for 1 OoM (90%), 2 OoM (99%) and 3 OoM (99.9%) reductions in contaminant concentrations for complete source removal after a 50-year loading period.	139
Figure 5-5. Effect of travel time (T_t) and aquifer thickness divided by number of low K boundaries (B/BD) on cleanup time (T) and normalized cleanup time (T/T_t) in a homogeneous aquifer with low K boundaries for 1 OoM (90%), 2 OoM (99%) and 3 OoM (99.9%) with a 50 year loading period.	140
Figure 5-6. Cleanup time ratio (CTR) for 10, 25 and 100 yr loading periods in homogeneous and heterogeneous aquifers.....	141
Figure 5-7. Effect of varying R_H and R_L on the Cleanup Time Ratio for Retardation (CTR_R) for homogeneous aquifers with low K boundaries and heterogeneous aquifers without low K boundaries.	143
Figure 5-8. Impact of installing multiple PRBs on overall cleanup time.	144
Figure A1. Standard HPT components (from HPT Standard Operating Procedure by Geoprobe).	151
Figure A2. Low-flow control box.	152
Figure A3. Low-K HPT equipment setup during field profiling.	153
Figure A4. Simulated relations for hydraulic diffusivity versus rod advancement-induced pressure measured at the HPT screen (red curve), and for diffusivity versus the ratio of water injection rate over injection-induced pressure (blue curve). The simulated probe speed is 5 mm/s. Rod Q is the equivalent water injection rate from rod advancement, calculated as the product of the cross-section area of the HPT probe and advancement speed.	156
Figure A5. The first few example of an example Excel file “getinputfromfielddata”.....	157
Figure A6. Example profiles of estimated K (left) and pressures (right) from HPT logging at the GEMS. The HPT pressure is calculated as the field pressure measurement minus the estimated hydrostatic background pressure. The rod pressure is the estimated pressure from rod advancement at a speed of 5 mm/s. The sum of rod pressure and injection pressure is equal to the HPT pressure.....	158

Figure B1. Schematic of Darcy’s Law flow experiment.	160
Figure B2. (A) Schematic of a falling-head slug test (water flows from well into aquifer) performed in a multi-level slug-test system. Head change is introduced in standpipe, which is directly connected to the interval isolated by the straddle packers (not to scale). (B) Example data plot from a multilevel slug test at GEMS. Test is initiated by sudden depressurization of a pressurized air column ^[19]	163
Figure B3. K estimates from different field methods at GEMS ^[5] . Well DW is located 2 m east of GEMS4S.	164
Figure B4. Schematic illustrating hydrostratigraphic profiling, the combination of electrical conductivity (EC) and multilevel slug test profiling ^[23]	165
Figure B5. Schematic diagram showing the borehole flowmeter profiling procedure ^[24]	166
Figure B6. (A) Schematic of the DPIL with a screen attached to the probe rod at its lower end ^[6] , (B) Artistic rendering of the HPT ^[33] (continuous DPIL probe combined with an EC Wenner array), and (C) Six example DPIL (red curve) K profiles calibrated by collocated DPP tests (blue bars) at the MacroDispersion Experiment (MADE) site, Columbus, MS ^[35] . In (C), the dashed curves represent the upper K limit for continuous DPIL under the given tool operating procedure.....	169
Figure B7. (A) Schematic of the DPP (not to scale), and (B) example DPP test sequence at GEMS ^[6]	171
Figure B8. Comparison of DPP and DP multilevel slug test K profiles at GEMS ^[5] . The slug test profile is located 2 m northwest of DPP profile 1 and 2 m southeast of DPP profile 2.	171
Figure B9. (A) Measurement domain around a NMR borehole probe, (B) NMR responses as a function of pore size ^[48] , and (C) Comparison of NMR and DPP K estimates at two GEMS locations ^[49] . In (B), A is the initial magnetization, T ₂ is NMR relaxation time. In (C), the dash lines show the range of the NMR K estimates due to the uncertainty in the empirical parameters used in the pore size - K relationship.	173

LIST OF TABLES

Table 2-1.	Summary of Slug Test and HPT Results.	41
Table 3-1.	Estimated K from CPT Dissipation tests	55
Table 3-2.	Geotechnical Properties of Undisturbed Samples	61
Table 3-3.	Soil Organic Carbon and Particle Size Fraction	61
Table 3-4.	Slug Tests Results.....	65
Table 3-5.	Bromide Tracer Test Modeling Parameters.....	73
Table 3-6.	Injection setup at the wells.....	73
Table 3-7.	Root Mean Squared Error (RMSE) of realizations.....	77
Table 3-8.	Model Parameters for REMChlor-MD Simulation	82
Table 4-1.	Parameters used in fractured media experiments	124
Table 5-1.	Parameter Values Evaluated in Sensitivity Analysis.	136
Table 5-2.	Regression Coefficients for Estimating Non-Reactive Solute Cleanup Time.	137
Table 5-3.	Regression Coefficients for Estimating Clean Time Ratio for Retardation (CTR _R).	142

ACRONYMS AND ABBREVIATIONS

1-D	One-dimensional
2-D	Two-dimensional
AFB	Air Force Base
AFCEC	Air Force Civil Engineering Center
ASTM	American Society for Testing and Materials
BGS	Below Ground Surface
CA	Chloroethane
CH ₄	Methane
Cl ⁻	Chloride Ion
CO ₂	Carbon Dioxide
CVOCs	Chlorinated Volatile Organic Compounds
<i>cis</i> -DCE	<i>cis</i> -1,2-Dichloroethene
DNAPL	Dense Non-aqueous Phase Liquid
DO	Dissolved Oxygen
DoD	Department of Defense
DP	Direct Push
ESTCP	Environmental Security Technology Certification Program
ERD	Enhanced Reductive Dechlorination
GMS	Groundwater Modeling Software
HRT	Hydraulic Retention Time
K	Hydraulic Conductivity
KGS	Kansas Geological Survey
LPF	Layer-Property Flow (a MODFLOW package)
MCL	Maximum Contamination Limit
MODFLOW	U.S. Geological Survey Modular Ground-Water Model
MT3DMS	Modular 3-D Multi-Species Transport Model
NAPL	Non-Aqueous Phase Liquid
NFESC	Naval Facilities Engineering Service Center
O&M	Operation and Maintenance
ORP	Oxidation-Reduction Potential
PCE	Tetrachloroethene
ppb	Parts Per Billion
PRB	Permeable Reactive Barrier
PV	Pore Volume
PVC	Polyvinyl Chloride
REMChlor	Remediation Evaluation Model for Chlorinated Solvents
SERDP	Strategic Environmental Research and Development Program
T	Transmissivity
TCE	Trichloroethene
TOC	Total Organic Carbon
USEPA	U.S. Environmental Protection Agency
VC	Vinyl Chloride
VOCs	Volatile Organic Compounds

ACKNOWLEDGEMENTS

The research described in this report was conducted by a team of Robert C. Borden and Ki Young Cha with Draper Aden Associates, Ron Falta with Clemson University, and Gaisheng Liu and James Butler with the Kansas Geological Survey. The research described in this interim project report was supported by the U.S. Department of Defense, through the Strategic Environmental Research and Development Program (SERDP). Dr. Andrea Leeson and other SERDP staff are gratefully acknowledged for their assistance and support.

ABSTRACT

INTRODUCTION AND OBJECTIVES

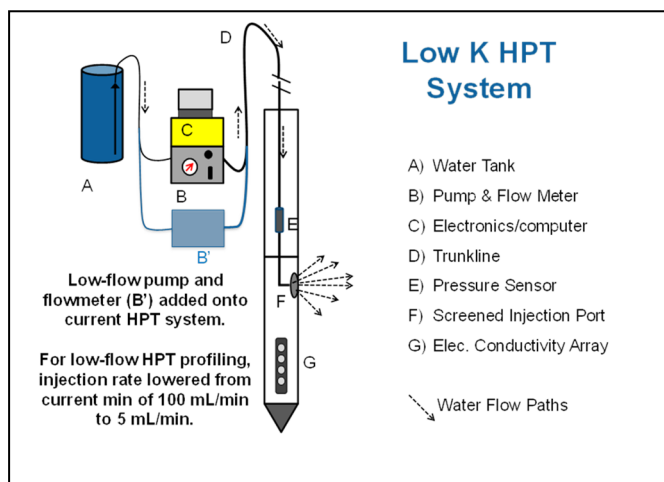
Extensive research has shown that back diffusion of contaminants stored in zones with lower hydraulic conductivity (K) can slow aquifer recovery, greatly extending the time to reach remediation goals. We address this research gap by developing a suite of field and modeling approaches that will allow users to better characterize low-K zones in the field, more accurately simulate mass transfer between low-K and high-K zones, and evaluate the impact of these processes on the time to reach groundwater cleanup goals following source removal. Specific technical objectives include:

- 1) Develop low-cost direct push (DP) methods for high-resolution characterization of hydraulic conductivity.
- 2) Determine if high-resolution solute transport models, primarily calibrated using DP tools, can provide satisfactory predictions of contaminant mass transfer between high and low K zones.
- 3) Develop methods to calibrate existing and new mobile-immobile zone models using high-resolution K distributions obtained with DP equipment.
- 4) Develop simplified methods for estimating the impact of matrix diffusion on cleanup time.

TECHNICAL APPROACH

A complementary set of field and modeling methods is developed for quantifying mobile-immobile mass transfer in shallow, unconsolidated settings.

The hydraulic profiling tool (HPT) is commonly used for high-resolution (1.5 cm) characterization of K in moderate to high permeability formations. The HPT system consists of a water injection port with a transducer positioned behind it and an electrical conductivity (EC) sensor array. The original system is modified to allow water injection at lower flowrates, reducing pressure buildup, and allowing K measurement in lower permeability formations. To evaluate the value of this approach, high resolution site characterizations are completed at two contaminated sites where back diffusion of chlorinated solvents from low permeability zones is expected to extend cleanup times. These results are used to calibrate high-resolution flow and solute transport models and simulate the long-term impacts of back diffusion on site cleanup time. This information is also used to evaluate the use of a new semi-analytical modeling approach developed for simulating back-diffusion. Sensitivity analyses are conducted to identify the parameters that have the greatest impact on cleanup times.



RESULTS

The current HPT system was modified for use in low-K settings. A combination of numerical simulations, lab experiments and field tests were performed to facilitate the low-K HPT tool development. The existing HPT system was modified by altering the water pump and flow meter, and then evaluated in a low permeability aquifer test cell and in the field. Simulation results were used to develop a simplified relationship for estimating K from the injection flow rate, pressure, probe advancement speed, and specific storage. This simplified relationship was evaluated by comparing HPT K estimates with slug test results in adjoining monitor wells.

Detailed field characterizations were completed at two contaminated sites – Air Force Plant 3 (AFP3) in Tulsa and Former Naval Training Center Orlando, Operable Unit 2 (OU2) in Orlando. Work included HPT profiling, Cone Penetrometer Test (CPT) profiling, and traditional site characterization approaches. Numerical simulations showed that at both AFP3 and OU2, large spatial variations in K had a major influence on the groundwater cleanup rate in downgradient monitor wells. TCE was rapidly flushed from higher K zones, but declined much more slowly in lower K zones. In long-screened monitor wells, this gave the appearance of a slow gradual decline in TCE concentrations.

A new modeling approach (semi-analytic method) was developed and tested, that allows for simple, efficient simulation of diffusive mass transfer between high and low K zones. This semi-analytic method accurately reproduces analytical and high-resolution numerical model results for a variety of geometries. The new method has three geometrical parameters, but these can be reduced to two parameters by assuming a logical relationship between the low permeability zone volume, the interfacial area, and the characteristic diffusion length. The key matrix diffusion parameters needed for this model, the volume fraction of high permeability material and the characteristic diffusion length, can be estimated from well logs.

Sensitivity analyses were conducted with REMChlor-MD to identify the physical parameters that have the greatest influence on the time to reach one, two and three order-of-magnitude reductions in contaminant concentrations following source removal. These results were then used to develop simplified relationships for estimating cleanup time.

BENEFITS

This project has substantially improved our understanding of mobile-immobile mass transfer and its impacts on the fate and transport of contaminants in shallow groundwater systems. Project results include a set of tools to better characterize sites with significant low-K zones; estimate the rate, timing and duration of contaminant release from those zones; and evaluate the impact of contaminant mass stored in low K zones on long-term plume behavior. This will provide site managers with more accurate estimates of the time to reach groundwater cleanup goals following source removal.

PUBLICATIONS

- Falta, R.W. and Wang, W., 2017. A semi-analytical method for simulating matrix diffusion in numerical transport models. *Journal of contaminant hydrology*, 197, pp.39-49.
- Muskus, N. and Falt, R.W., 2018. Semi-analytical method for matrix diffusion in heterogeneous and fractured systems with parent-daughter reactions. *Journal of contaminant hydrology*, 218, p. 94-109.
- Liu, G., R. Borden, and J.J. Butler, Jr., 2019, Simulation assessment of direct push injection logging for high resolution aquifer characterization. *Groundwater*, doi: 10.1111/gwat.12826.
- Borden, R.C., Cha, K.Y. and Liu, G., 2020, A Physically Based Approach for Estimating Hydraulic Conductivity from HPT Pressure and Flowrate, *Groundwater*, <https://doi.org/10.1111/gwat.13039>.

EXECUTIVE SUMMARY

INTRODUCTION

Extensive research has shown that back diffusion of contaminants stored in lower K zones can slow aquifer recovery, greatly extending the time to reach remediation goals. These processes can be simulated with high resolution numerical models and newly developed semi-analytical approaches. However, there is very little information on how to efficiently measure the spatial variation in hydraulic conductivity (K) and geometry of low K zones or how to effectively incorporate this information into models. As a result, low-K zones are often poorly defined and inadequately represented in most models. We address this research gap by developing a suite of field and modeling approaches that will allow users to better characterize low-K zones in the field, and more accurately simulate mass transfer between low-K and high-K zones.

This project addressed two objectives listed in the Statement of Need (SON):

- Develop and validate field-scale methods for estimating important parameters such as back diffusion, sorption, and degradation of contaminants.
- Develop mathematical and simulation estimation methodologies for these important natural processes that can be incorporated into commonly used models to predict contaminant behavior in groundwater.

OBJECTIVES

In this project, we develop and validate direct push (DP)-based field methods for quantifying the spatial distribution of important parameters controlling mass transfer between immobile and mobile zones and resulting impacts on back diffusion of chlorinated volatile organic compounds (CVOCs) and other groundwater contaminants. Data generated with these methods can be combined with currently available and emerging modeling procedures to provide improved predictions of contaminant release from low-permeability zones over time. This information is critical for site managers to evaluate the effect of natural attenuation on contaminant migration.

The overarching goal of this project is to develop methods to better characterize and model mass transfer of contaminants between higher and lower mobility zones and its impact on the long-term release of contaminants in groundwater. Specific technical objectives include:

1. Develop low-cost direct push (DP) methods for high-resolution characterization of hydraulic conductivity (K).
2. Determine if high-resolution solute transport models, primarily calibrated using DP tools, can provide satisfactory predictions of contaminant mass transfer between high and low K zones.
3. Develop methods to calibrate existing and new mobile-immobile zone models using high-resolution K distributions obtained with DP equipment.
4. Develop simplified methods for estimating the impact of matrix diffusion on cleanup time.

TECHNICAL APPROACH

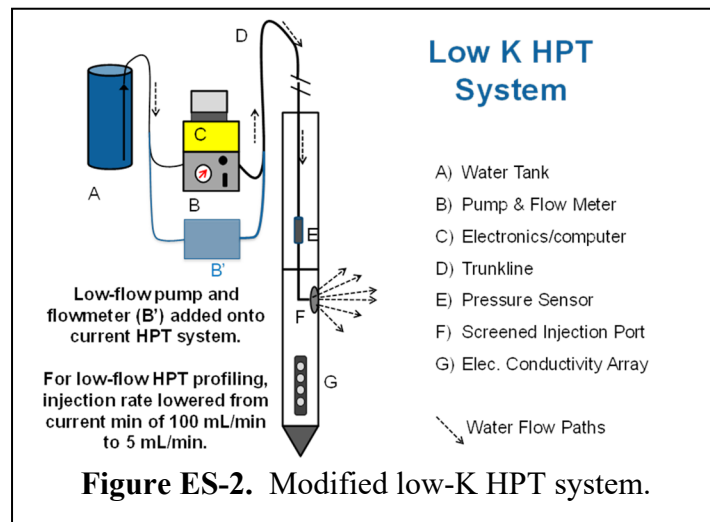
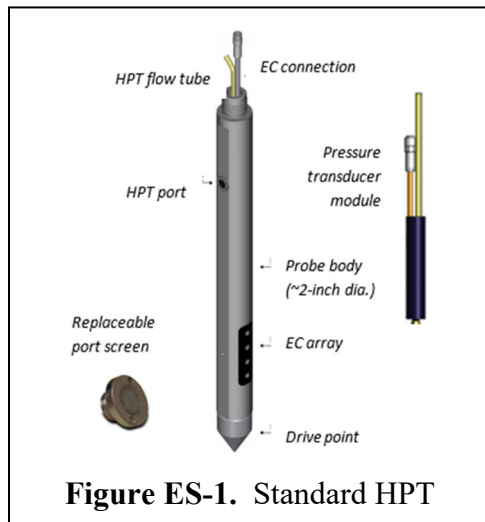
A complementary set of field and modeling methods is developed for quantifying mobile-immobile mass transfer in shallow, unconsolidated settings. The existing hydraulic profiling tool (HPT) is modified to allow water injection at lower flowrates, reducing pressure buildup, and allowing K measurement in lower permeability formations. To evaluate the value of this approach, high resolution site characterizations are completed at two contaminated sites where back diffusion of chlorinated solvents from low permeability zones is expected to extend cleanup times. These results are used to calibrate high-resolution flow and solute transport models and simulate the long-term impacts of back diffusion on site cleanup time. This information is also used to evaluate the use of a new semi-analytical modeling approach developed for simulating back-diffusion. Sensitivity analyses are conducted to identify the parameters that have the greatest impact on cleanup times. This work is organized in the following tasks.

1. Direct Push (DP) Methods Development
2. Site Characterization and Numerical Model Development
3. Mobile-Immobile Zone Model Parameter Estimation
4. Estimating the Impact of Matrix Diffusion on Cleanup Time

RESULTS AND DISCUSSION

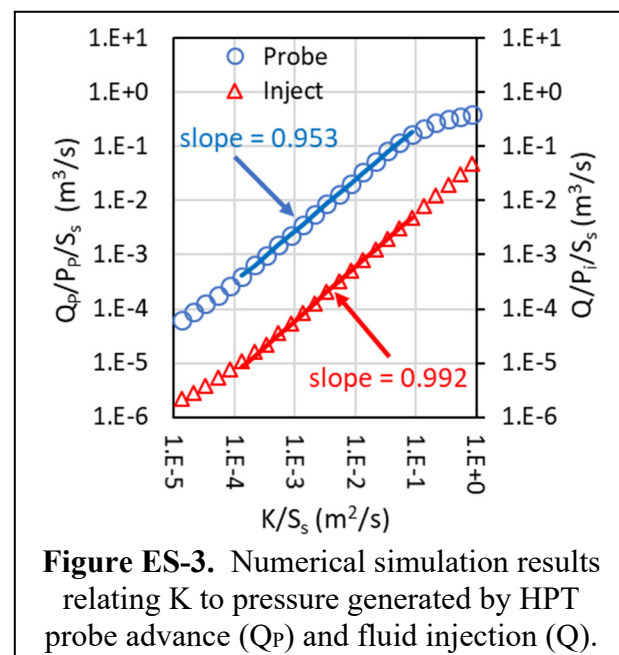
Direct Push (DP) Methods Development

The main goal of DP methods development is to modify the current Hydraulic Profiling Tool (HPT) manufactured by Geoprobe Systems (**Figure ES-1**) for use in lower K formations. As the HPT probe is advanced through saturated aquifer material, water is injected through a port on the side of the probe while continuously monitoring injection rate (Q) at the surface and pressure (P) directly behind the injection screen. The measured pressure is the sum of hydrostatic pressure, atmospheric pressure, pressure generated by water injection, and pressure generated by displacement of aquifer material as the probe is advanced through the aquifer.



To facilitate the low-K HPT tool development, a combination of lab experiments, field tests and numerical simulations were performed. Two key components of the current HPT system, the water pump and flow meter, were modified to allow injection at much lower flow rates. **Figure ES-2** shows the design of low-K HPT system, constructed by adding a low-flow control box (B') to standard HPT. The new low-flow control box allows injection rates to be reduced from the current minimum of ~100 mL/min to 5 mL/min. The new low-flow control box is as an add-on, so the standard HPT system can still be used in higher K formations. The new low-K HPT system was first tested in a lab flow box and then in the field.

A series of high-resolution numerical simulations were conducted to gain a better understanding of the underlying physical processes controlling pore pressure during HPT profiling. Pressure change observed at the water injection port is the sum of injection-induced pressure (P_i) and the pressure change generated by probe advancement (P_p). The impacts of water injection rate (Q), speed of probe advance through the aquifer material (V) and formation properties (K and specific storage, S_s) on pressure (P) at injection port are illustrated in curves relating K/S_s to $Q_p/P_p/S_s$ and $Q/P_i/S_s$ (**Figure ES-3**). Q_p is equivalent to the volume per unit time of groundwater displaced as the HPT probe is advanced through the aquifer material ($V \cdot A$) where A is the cross-sectional area of the HPT probe. Q is the flow rate of fluid injected through the HPT port.



The following simplified equations were then developed to calculate K from Q and P data collected during HPT profiling for equipment in common use in the United States (K in ft/d, P in psi) and for SI units (K in m/s, P in m of hydraulic head). An empirically derived efficiency factor (E) is included to account for permeability loss in the disturbed zone surrounding the HPT probe.

$$K(\text{ft/d}) = (0.1235 V[\text{cm/s}] D^2[\text{cm}] + 0.119 Q[\text{mL/min}]) P[\text{psi}]^{-1.017}$$

$$K(\text{m/s}) = (4.061\text{E-}07 V[\text{cm/s}] D^2[\text{cm}] + 4.262\text{E-}07 Q[\text{mL/min}]) P[\text{m}]^{-1.017}$$

The accuracy of the HPT measurement approach was evaluated by comparing K values measured in monitor wells to adjoining HPT profiles at 23 locations (**Figure ES-4**). Using the best fit efficiency factor ($E=2.02$), the vertically averaged K calculated from the HPT results provided an excellent match to the slug test measurements. The NRMSE of 67% is considered excellent, given the natural variability in slug test results and that the slug test and HPT profiles were located about 3 ft apart.

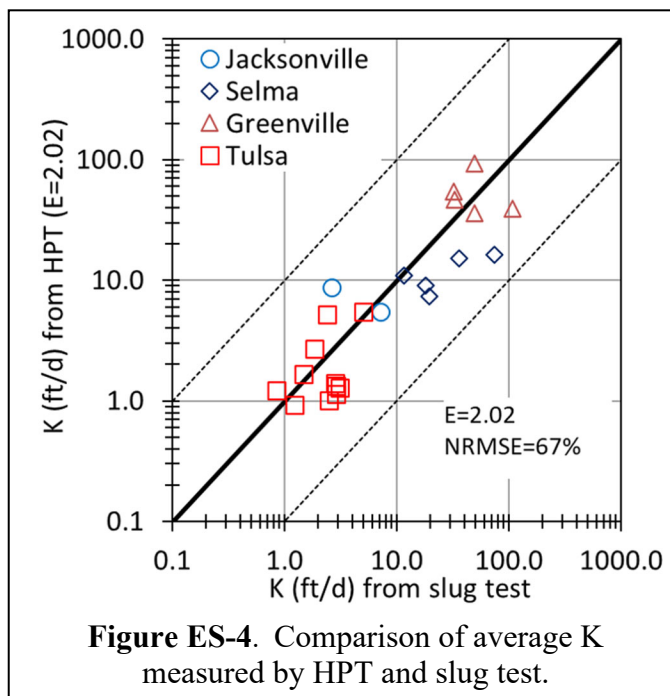
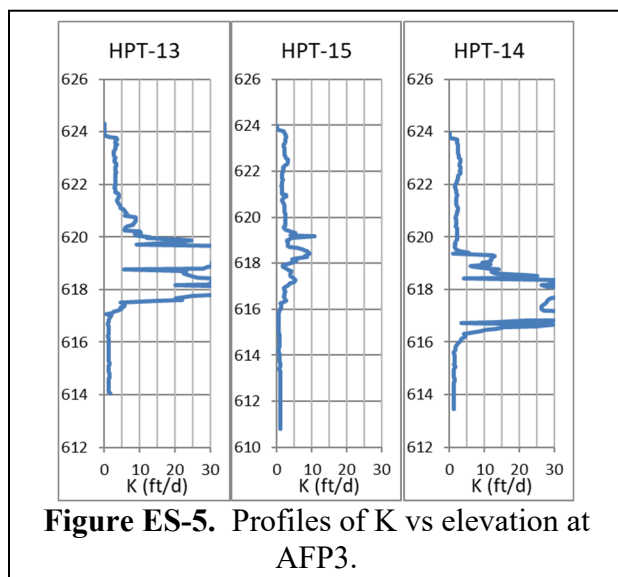


Figure ES-4. Comparison of average K measured by HPT and slug test.

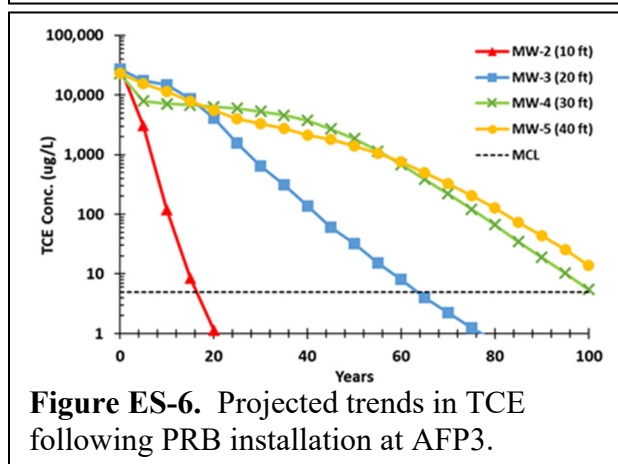
Site Characterization and Numerical Model Development

Two sites were selected for detailed characterization and modeling – Air Force Plant 3 (AFP3) in Tulsa, OK and Former Naval Training Center Orlando, Operable Unit 2 (OU2) in Orlando, FL. Permeable reactive barriers (PRBs) had been previously installed at both AFP3 and OU2 by injecting emulsified vegetable oil (EVO) to stimulate biodegradation of trichloroethylene (TCE). At both sites, TCE was effectively treated within the PRB, with concentrations declining to near zero. However, downgradient TCE concentrations declined more slowly than expected.

Detailed site characterizations were conducted at both sites, to understand the physical and chemical processes controlling groundwater cleanup, including installation of multiple cone penetrometer test (CPT) and HPT borings. Characterization results were used to develop analytical and numerical models and evaluate the effect of mass transfer between high and low K zones on the rate of groundwater cleanup downgradient of the PRBs.

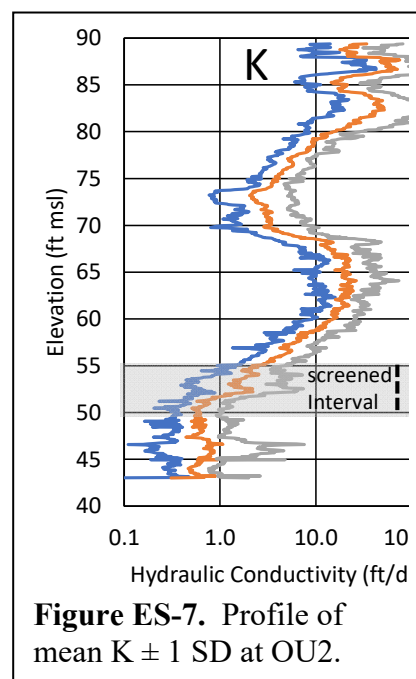


At the AFP3 site, the aquifer consists of clayey silt to very fine sandy silt with embedded zones of sandy gravel. High K sand zones were observed in some, but not all, HPT profiles (**Figure ES-5**). These sands may act as conduits allowing rapid downgradient migration of dissolved TCE. Prior to PRB installation, TCE migrated through these sands and diffused into the surrounding low K zones. Once the PRB was installed, TCE levels in the sands declined, and TCE began to diffuse out of the low K zones.

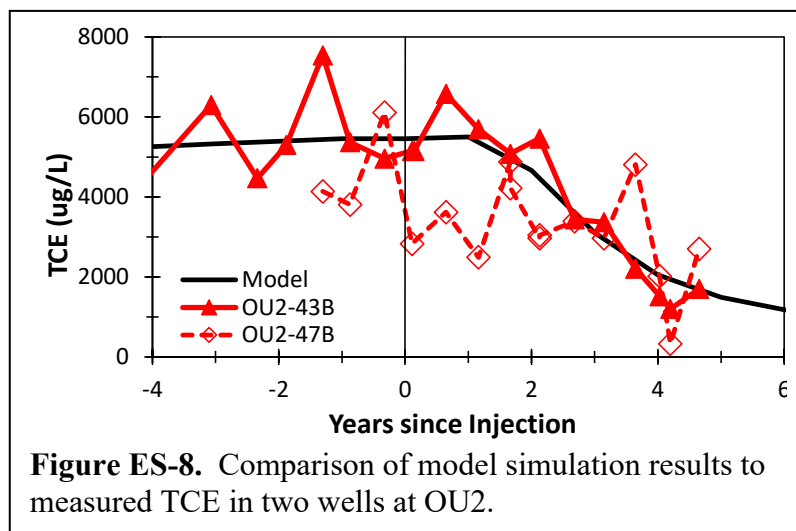


The geostatistical analysis program T-PROGS was used to calculate the spatial statistics of the high and low K zones, and to generate random 3-D realizations of the K distribution. These realizations were used to calibrate a high-resolution numerical model and a semi-analytical model to simulate matrix diffusion. Both the numerical and semi-analytical modeling approaches provided reasonably good matches to the available monitoring data. Long-term simulations (**Figure ES-6**) indicate that slow mass transfer from low K to high K zones will significantly extend groundwater cleanup times.

At the OU2 site, the aquifer consists of interbedded sand and silty sand layers, overlying a clay-silt confining unit. HPT profiles showed the presence of three layers with varying permeability: A Zone (75-90 ft) consisting of high K sands and gravel; B Zone (70-75 ft) consisting of moderate K silty sand; and C Zone (55-70 ft) consisting of moderate to high K sand. Beneath C Zone is a low K confining layer. There were large variations in K with depth (**Figure ES-7**). The standard deviation (SD) in K at each elevation was relatively low, consistent with spatially extensive, relatively homogeneous aquifer layers. Residual contaminant concentrations are highest at 50 to 55 ft elevation where the high K C zone transitions into the underlying clay confining layer. HPT profiles showed a gradual transition in K through this interval, without a well-defined boundary between high and low K layers.



A numerical flow and solute transport model was used to simulate transport of TCE in the aquifer at OU2 and remediation following EVO injection. K for each model layer was equal to the mean K measured by HPT. Model simulation results closely matched measured TCE concentrations in two wells (OU2-43B and OU2-47B) located a short distance downgradient of the PRB (**Figure ES-8**). Long-term simulations indicate that substantial levels of TCE will persist at these monitoring points for many years.



The site characterization and numerical simulations showed that at both AFP3 and OU2, large spatial variations in K had a major influence on the groundwater cleanup rate in downgradient monitor wells. TCE was rapidly flushed from higher K zones, but declined much more slowly in lower K zones. In long-screened monitor wells, this gave the appearance of a slow gradual decline in TCE concentrations.

Using methods developed in this project, the HPT provided valuable information on spatial variations in K. When this information was used to calibrate high resolution flow and transport models, these models provided reasonably accurate simulations of cleanup rates in monitor wells.

Mobile-Immobile Zone Model Parameter Estimation

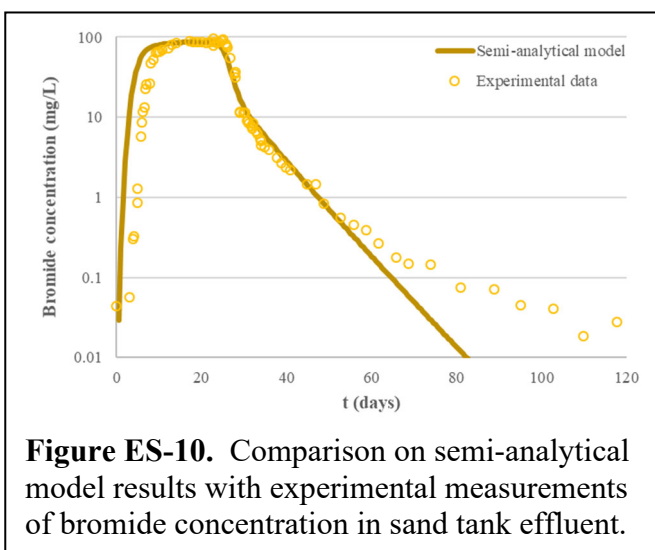
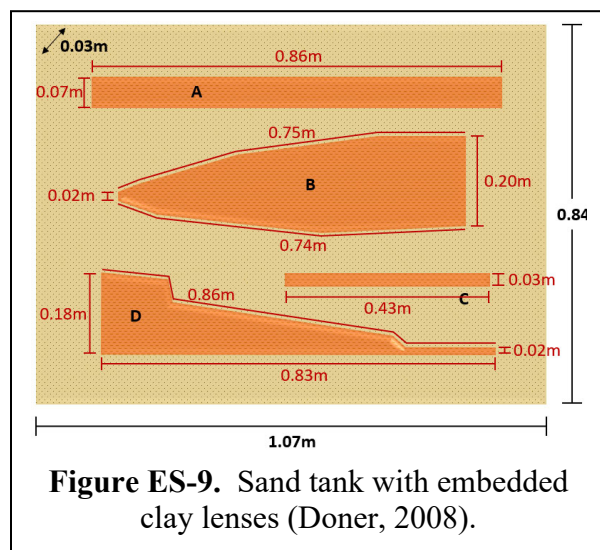
In this task, a semi-analytical approximation for transient matrix diffusion is developed for use in numerical contaminant transport simulators. The method uses a fitting function to approximate the transient concentration profile in the low permeability part of each gridblock so that the matrix diffusion flux into the high permeability part of the gridblock can be computed as a concentration dependent source-sink term. Since only the high permeability zones need to be discretized, the numerical formulation is extremely efficient compared to traditional approaches that require discretization of both the high and low permeability zones.

A variety of different geometries can be simulated with the semi-analytical approach including a homogeneous aquifer bounded above and/or below by semi-infinite low K confining layers and fractured rock or clay. The effect of low K lenses in a high K aquifer can be represented as low K matrix embedded within a numerical gridblock, having finite average thickness, a specified volume fraction and a specified interfacial area within the high K domain. The new formulation also allows for coupled parent-daughter decay reactions with multiple species that each have

independent retardation factors, decay rates, and yield coefficients in both the high and low permeability parts of the system.

The accuracy of this new approach was evaluated by comparing results from the semi-analytical method with prior experimental studies, analytical solutions for transient one-dimensional diffusion with first order decay, with a two-layer aquifer/aquitard solution, an analytical solution for matrix diffusion in fractured media with parallel fractures, with an analytical solution for matrix diffusion with parent-daughter decay reactions, with fine grid numerical simulations of transport in highly heterogeneous systems, and with a fully numerical solution for transport in a thin sand zone bounded by clay with variable decay rates.

In one set of simulations, the semi-analytical approach was compared to experimental results from a $1.07 \times 0.03 \times 0.84$ m laboratory tank experiment (Doner, 2008). **Figure ES-9** shows the location of four clay lenses suspended in the sand tank. A tracer solution was introduced into the sand tank along the left boundary, transported through the sand tank, and was discharged out the right side. As shown in **Figure ES-10**, simulation results generated with the semi-analytical model compare favorably with experimental measurements of bromide concentration in the sand tank effluent.



We conducted fine-grid 3D numerical simulations using highly heterogeneous grids in MODFLOW/MT3DMS to generate realistic contaminant transport plumes that are strongly affected by matrix diffusion. These simulations use several million gridblocks, and take 60-80 hours to run on a fast computer. We are then using the REMChlor-MD model to reproduce these results with a few tens of thousands of gridblocks. The REMChlor-MD simulations take about a minute to run on the same computer. These comparisons have allowed us to develop relatively simple methods for estimating the key matrix diffusion parameters needed for the semi-analytical method (Muskus and Falta, 2018).

The semi-analytic method requires 3 geometrical parameters: the volume fraction of high permeability material (V_f), the interfacial area between the high permeability and low permeability materials (A_{md}), and the characteristic maximum average diffusion length, L . This

diffusion length is infinite for the case of diffusion into an infinite thickness aquitard, and for systems of parallel fractures, L is equal to one-half of the fracture spacing. A key finding in this project was that the 3 geometrical parameters can be combined with a volume balance on the low permeability material to reduce the number of parameters needed to 2. For a total volume of V , the volume of low permeability material is $(1-V_f)V$. For consistency, that volume should be equal to the product of L and A_{md} . Then

$$(1 - V_f) = \frac{A_{md}}{V} L$$

Given estimates for V_f and L , the interfacial area per unit volume (A_{md}/V) can be calculated. This relationship is built in to REMChlor-MD, and was demonstrated in the fine grid 3-D transport simulations shown in Muskus and Falta (2018).

The semi-analytic method has been tested against the dual porosity method for fractured systems. A key feature of the semi-analytic method is that the parameters (V_f , A_{md} , and L) have a direct physical meaning, and can be estimated from direct push and other field data. The dual porosity model also requires the volume fraction (V_f), but it uses a first order mass transfer coefficient, β . In almost all cases, β is treated as a calibration parameter, where its value is adjusted to get a best fit with field data.

The semi-analytic and dual porosity methods were compared to an analytical solution for matrix diffusion in a system of parallel fractures. It was found that the dual-domain method was unable to match the analytical solution at large fracture spacing. In particular, β values that produced a reasonable match of the contaminant loading period were not capable of matching the analytical solution during the unloading (back diffusion) period. In contrast, the semi-analytical method produced good matches with the analytical solutions at all times, and without calibration. With close fracture spacing ($\sim 0.2\text{m}$ or less), the dual porosity model was able to match the analytical solution using a calibrated mass transfer coefficient. The semi-analytical method also matched the analytical solution under these conditions but did not require calibration.

Figure ES-11 shows a comparison of results generated by the semi-analytical and analytical methods for two different fracture spacings (0.5 and 2 m). These results highlight the impact of fracture spacing on the shape of the concentration profiles in the fractures.

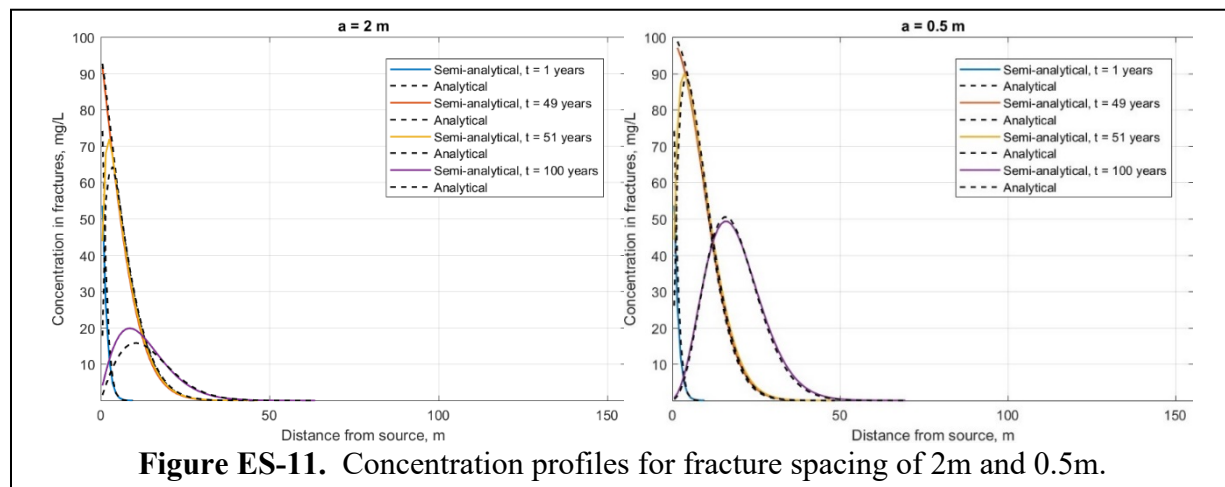


Figure ES-11. Concentration profiles for fracture spacing of 2m and 0.5m.

Estimating the Impact of Matrix Diffusion on Cleanup Time

The semi-analytical modeling approach described above are applied to identify the aquifer characteristics that have the greatest impact the time (T) to reach 1 OoM (90%), 2 OoM (99%) and 3 OoM (99.9%) reductions in contaminant concentration. Regression analysis is then used to develop simplified methods that can provide preliminary estimates of the time after complete source removal to reach different cleanup levels. Two general conditions are evaluated: (a) a heterogeneous aquifer containing one or more embedded low K zones with a defined thickness, interfacial area, and volume fraction; and (b) homogeneous aquifer of thickness B bounded below and/or above by semi-infinite low K boundaries. The semi-infinite low K boundaries are thick low K zones where the solute diffusing into this zone does not reach the end of the layer within the simulation period. In contrast, low K zones embedded within the heterogeneous aquifer are sufficiently thin that contaminants diffusing into these zones may encounter boundaries or contaminants diffusing from the other side within the simulation period. In all cases, advection through low K zones was assumed to be zero.

Parameters examined in the sensitivity analysis included high K zone hydraulic conductivity, distance to the monitoring point (X), high K zone non-reactive solute transport velocity (V), high-K travel time ($T_t = X/V$), aquifer thickness (B), number of semi-infinite low K boundaries (BD), maximum distance in aquifer to low K boundary (B/BD), aquifer high K volume fraction (V_F), time to flush one pore volume through aquifer ($T_{PV} = T_t/V_F$), number of interfaces between high and low K zones in heterogeneous aquifer (# interface), low K diffusion length (D_L), contaminant loading period prior to source removal, high K retardation factors (R_H), and low K retardation factor (R_L). A total of ~28,000 simulations are run generating values of T for 1, 2 and 3 OoM reductions for a range of parameter values. JMP Pro (Sall et al., 2017) was used to conduct standard least squares regressions to identify the parameters that had the greatest influence on cleanup time.

The statistically significant parameters ($p < 0.001$) that have the greatest impact on cleanup time in heterogeneous aquifers without low K boundaries are T_{PV} and D_L . T_t and V_F are not significant when T_{PV} was included. Number of interfaces and V_F are not significant when D_L was included. The parameters with the greatest impact on cleanup time in homogeneous aquifers with low K boundaries are T_t and B/BD. High K velocity and distance to monitoring point are not statistically significant when T_t is included. Similarly, B and BD are not significant when the parameter B/BD is included.

Figure ES-12 shows a series of curves developed to provide preliminary estimates of the time to reach 1, 2 and 3 OoM reduction in contaminant concentration. Overall, cleanup times are longer for homogeneous aquifers bounded by thick low K zones compared to heterogeneous aquifers without low K boundaries.

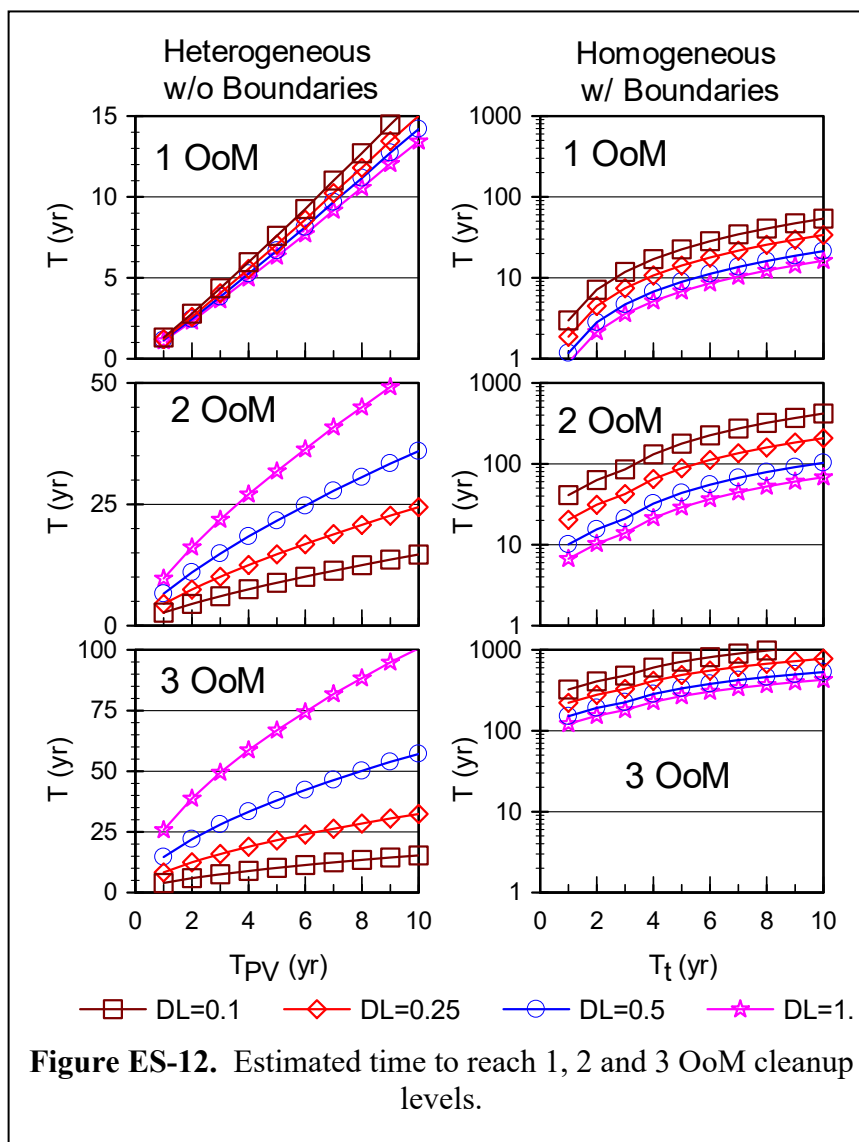
In heterogeneous aquifers without low K boundaries, the parameters with the greatest impact on cleanup time are time to flush one pore volume through the aquifer ($T_{PV} = T_t/V_F$) and diffusion length (D_L). For $T_{PV} > 5$ yr, the time to reach 1, 2 and 3 OoM reductions are 1.2-1.6 T_{PV} , 1.5-6 T_{PV} , and 2-15 T_{PV} , respectively. Greater values of D_L reduce the time to reach 1 OoM cleanup,

but increase the time to reach 2 and 3 OoM cleanup. For 2 and 3 OoM cleanup, T/T_{PV} increases rapidly for $T_{PV} < 2$ yr indicating cleanup time is mass transfer limited.

In homogeneous aquifers bounded by thick low K zones, the parameters with the greatest impact on cleanup time are travel time (T_t) and aquifer thickness divided by the number of low K boundaries (B/BD). For $T_t > 5$ yr, the time to reach 1, 2 and 3 OoM reductions are 1-6 T_t , 5-50 T_t , and 40-150 T_t , respectively. Cleanup time is greater for smaller B/BD for all cleanup levels since, since diffusive flux is greater relative to advective flux for thinner aquifers.

Contaminant loading period had a relatively modest impact on cleanup time. In both heterogeneous aquifers and homogeneous aquifers with low K boundaries, shorter loading periods reduced cleanup times, but the impact was modest with different loading periods changing cleanup time by less than a factor of 2.

Sorption of contaminants to high and low K aquifer material had a moderate impact on cleanup time. For all conditions evaluated, cleanup time increased with R_H and R_L . However, the increase in cleanup time was generally less than the values of R_H and R_L . For example, increasing both R_H and R_L to 10, increased CTR_R by roughly a factor of 8 for 1 and 2 OoM cleanup in a heterogeneous aquifer. Generally, cleanup times in heterogeneous aquifers are more sensitive to R_H and R_L than for homogeneous aquifers with low K boundaries.



Overall, these results demonstrate that matrix diffusion can dramatically extend the time to reach remediation goals after complete source removal. The overall cleanup time can be somewhat reduced by installing one or more Permeable Reactive Barriers (PRBs), subdividing a long contaminant plume into a series of shorter sections. In one example, installing one PRB separating a 500 ft long plume into two 250 ft long sections reduced the time to reach a 3 OoM

reduction by about one-third. Installation of additional PRBs further reduces cleanup time, but the incremental benefits of each additional barrier progressively decline.

IMPLICATIONS FOR FUTURE RESEARCH AND BENEFITS

This project has substantially improved our understanding of mobile-immobile mass transfer and its impacts on the fate and transport of contaminants in shallow groundwater systems. Project results include a set of tools to better characterize sites with significant low-K zones; estimate the rate, timing and duration of contaminant release from those zones; and evaluate the impact of contaminant mass stored in low K zones on long-term plume behavior. This will provide site managers with more accurate estimates of the time to reach groundwater cleanup goals following source removal.

In this project, we show that mobile-immobile zone models can be used to simulate the transport of dissolved solutes in heterogeneous aquifers with large spatial variations in K. However, at many sites, there is a continuous transition in K from low to high, and no obvious boundary between high K and low K zones. Additional research is needed to identify when the mobile-immobile modeling approach is appropriate and develop procedures to identify what zones should be classified as ‘mobile’ and what zones should be classified as ‘immobile’.

1.0 INTRODUCTION

One of the grand challenges facing the site remediation community is the slow, yet persistent, release of contaminants from low-hydraulic conductivity (K) zones, which can continue for decades after the contaminant source is controlled. Extensive research has shown that back diffusion and slow advection of contaminants stored in lower K zones can slow aquifer recovery, greatly extending the time to reach remediation goals (Liu and Ball, 1999; Chapman and Parker, 2005). With support from SERDP and others, a variety of different modeling approaches have been developed to estimate changes in contaminant concentration versus time following source control (Farhat et al., 2012; Chapman et al., 2012). However, there is very little information on how to efficiently measure the spatial variation in K and geometry of low-K zones or how to effectively incorporate this information into models. As a result, low-K zones are often poorly defined and inadequately represented in most models. Given the very limited field testing, there is no way to know if these models accurately simulate back diffusion at contaminated sites. We address this research gap by developing a suite of field and modeling approaches that will allow users to better characterize low-K zones in the field, and more accurately simulate mass transfer process between low-K (immobile) and high-K (mobile) zones.

1.1 OBJECTIVES

This project is particularly relevant to two specific objectives listed in the Statement of Need (SON):

- Develop and validate field-scale methods for estimating important parameters such as back diffusion, sorption, and degradation (both biotic and abiotic) of contaminants.
- Develop mathematical and simulation estimation methodologies for these important natural processes that can be incorporated into commonly used models to predict contaminant behavior in groundwater.

In this project, we develop and validate direct push (DP)-based field methods for quantifying the spatial distribution of important parameters controlling mass transfer between immobile and mobile zones and resulting impacts on back diffusion of chlorinated volatile organic compounds (CVOCs) and other groundwater contaminants. Data generated with these methods can be combined with currently available and emerging modeling procedures to provide improved predictions of contaminant release from low-permeability zones over time. This information is critical for site managers to evaluate the effect of natural attenuation on contaminant migration.

The overarching goal of this project is to develop methods to better characterize and model mass transfer of contaminants between higher and lower mobility zones and its impact on the long-term release of contaminants in groundwater. Specific technical objectives are:

- 1) Develop low-cost DP methods for high-resolution characterization of spatial variations in K.
- 2) Determine if high-resolution solute transport models, primarily calibrated using DP tools, can provide satisfactory predictions of contaminant mass transfer between high- and low-K zones.

- 3) Develop methods to calibrate or parameterize existing and new mobile-immobile zone models using high-resolution K distributions obtained with DP tools.
- 4) Develop simplified methods for estimating the impact of matrix diffusion on cleanup time.

1.2 REPORT ORGANIZATION

This final technical report describes the results of this project. **Section 2** describes development of DP methods for K measurement. **Section 3** describes site characterization and modeling work at two sites where mass transfer between low-K zones and the mobile aquifer is expected to be important. **Section 4** describes development of methods to estimate analytical and semi-analytical model parameters using results from DP tools. **Section 5** presents results from a series of sensitivity analyses conducted to identify the parameters that have the greatest impact on matrix diffusion in different settings. These results were then used to develop simplified relationships for estimating cleanup time.

2.0 DIRECT PUSH (DP) METHODS DEVELOPMENT

Objective: Develop low-cost DP methods for high-resolution characterization of hydraulic conductivity (K).

2.1 INTRODUCTION

The main goal of DP methods development is to modify the current HPT (manufactured by Geoprobe Systems, Inc.) so that it can be used for characterizing high-resolution K in low-K settings. The current HPT has been widely used for investigating contaminated sites. Profiling variations of permeability with the HPT has been recently established as an international standard practice by American Society for Testing and Materials (ASTM) under ASTM designation D8037 (ASTM, D8037). However, the current HPT is only applicable to moderately permeable units with a K range of 0.03 to 25 m/d. For low permeability units, such as clays and silts, where K is typically lower than 0.03 m/d and the slow release of contaminants remains a difficult challenge at many sites, the current HPT has been of limited utility.

In order to facilitate the low-K HPT tool development, a combination of numerical simulations, lab experiments and field tests have been performed. **Section 2.2** describes the results of the numerical simulations on injection logging (a central part of HPT). **Section 2.3** describes the construction of the low-K HPT tool and the results of lab experiments. **Section 2.4** describes the results of the low-K HPT tests under field conditions. **Section 2.5** describes the development and field testing of an equation for estimating K from HPT data.

2.2 SIMULATION OF DIRECT PUSH INJECTION LOGGING

2.2.1 Background

Spatial variations in K over short distances are a key control on groundwater flow and contaminant transport in heterogeneous media (Boggs et al., 1992; Dagan and Neuman, 1997; Liu et al., 2004; Berkowitz et al., 2006; Zheng et al., 2011; Haslauer et al., 2017). However, traditional aquifer characterization methods, such as pumping tests, have proven to be of limited use for acquiring the information on K variations needed for transport studies (Butler, 2005, 2009). In order to characterize K variations at a resolution and accuracy that are suitable for investigations at sites of groundwater contamination, a series of DP-based field approaches have been developed over the last two decades (Dietrich and Leven, 2009; Liu et al., 2012; Maliva, 2016).

DP technology uses hydraulic rams supplemented with vehicle weight and high-frequency percussion hammers to rapidly advance small-diameter tools into the subsurface (McCall et al., 2005). It is primarily used for investigations in relatively shallow (within 30-40 m of land surface) unconsolidated sediments. The most significant advantage of DP-based approaches, as compared to other characterization methods, is their flexibility for rapidly acquiring information at a scale of relevance for contaminant investigations; this information can be acquired virtually wherever it is needed with minimal site disturbance.

Among the various DP approaches that have been developed for subsurface characterization, two are particularly noteworthy for their simplicity and effectiveness: electric conductivity (EC) profiling and direct push injection logging (DPIL). EC profiling measures the bulk EC of the subsurface (using a dipole or Wenner sensor array on the DP probe); this approach can provide valuable information about vertical lithological variations when the EC of the fluid in the formation does not vary with depth (Schulmeister et al., 2003). Although EC profiles can potentially be used for estimating K , either through Archie's law (relating EC to porosity) and the Carmen – Kozeny equation (relating porosity to permeability) or through a site-specific calibration, this is typically not recommended due to the large uncertainty in the resulting K estimates (Liu et al., 2012). The DPIL, on the other hand, measures the pressure response to water injection through a screened port on the probe (**Figure 2-1**); the ratio of the injection rate to the injection-induced pressure can be used as a K index (Cho et al., 2004) or transformed into K estimates using empirical relationships that often need site-specific calibration (Dietrich et al., 2008; Liu et al., 2009; Lessoff et al., 2010).

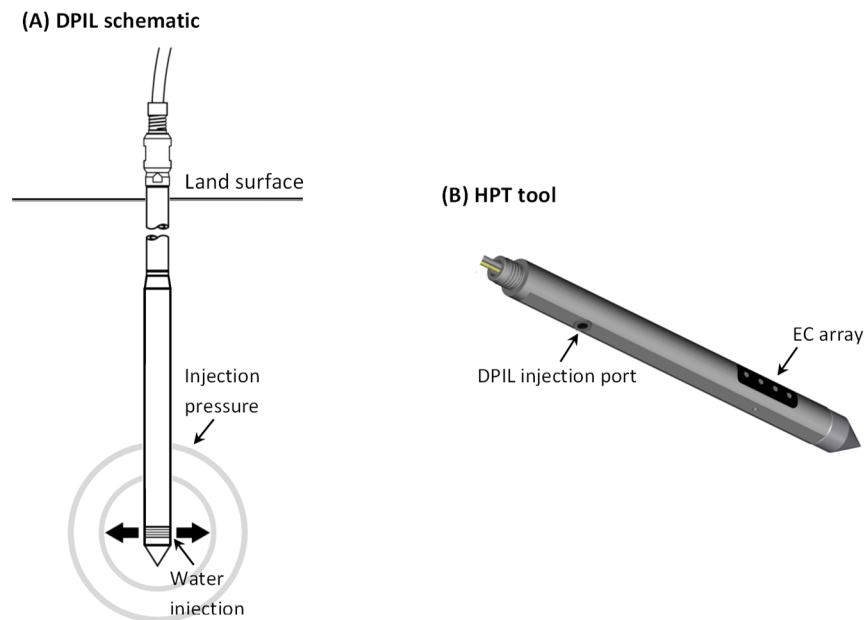


Figure 2-1. (A) Schematic of the DPIL with a water injection screen attached to the probe rod, (B) Artistic rendering of the HPT (continuous DPIL coupled with an EC Wenner array).

In this work, we focus on the DPIL, since it is one of the most powerful approaches for K characterization (in terms of resolution and speed of acquisition) and is also one of the most widely used techniques in environmental site investigations (Liu et al., 2012; Maliva, 2016). The DPIL, supplemented with an EC sensor, forms a commercially available HPT probe (**Figure 2-1**), that is used for continuous DPIL profiling. Recently, profiling K variations with the HPT has been established as a standard practice by the ASTM (D8037). Despite its widespread use, however, there has been no rigorous analysis of the underlying physical processes that take place during DPIL profiling or how the approach performs under commonly met conditions. Those are the issues we address here through a series of numerical simulations.

2.2.2 Direct push injection logging (DPIL)

There are currently two variants of DPIL: discontinuous (Dietrich et al., 2008; Lessoff et al., 2010) and continuous (McCall et al., 2005; Liu et al., 2009). In both cases, water is injected as the probe is advanced. In the discontinuous mode, after the desired measurement depth is reached, probe advancement ceases, and water injection is stopped. While the probe is positioned at the measurement depth, the pore water pressure change produced by probe advancement and previous water injection is allowed to dissipate. Once the pressure stabilizes (this may take a considerable amount of time in low-K formations), one or more step injection tests are performed, after which the measured injection rate and pressure are used to estimate K. In the case of multiple injection tests, the injection rates are typically varied in a step-wise fashion; use of multiple rates allows for a better assessment of near-probe conditions during the tests (e.g., the change of K estimates between tests might indicate formation alteration at higher flow rates). During discontinuous DPIL, there are essentially no limits on the range of injection rates that can be used.

The main advantage of discontinuous DPIL is that the impacts of probe advancement and previous water injection can be minimized, so that the quality of K estimates is relatively high. However, due to frequent suspension of probe advancement, the time required to complete a profile can be great, especially when a large number of measurement intervals are involved. In addition, no information about formation conditions between test intervals can be obtained.

In the continuous DPIL mode (e.g., HPT), both the injection rate and pressure are monitored during advancement, providing a continuous vertical profile of the transmissive characteristics of the subsurface. In the HPT (**Figure 2-1**), injection rate is measured at the surface, while the injection pressure is measured behind the injection screen (inside the probe). The measured pressure represents the total pressure (i.e. the sum of injection pressure, advancement pressure, atmospheric pressure, and hydrostatic pressure). To convert that into the net HPT pressure, both the atmospheric and hydrostatic background pressures must be removed (Liu et al., 2012). Although not essential, a stable injection rate is preferred during continuous DPIL. The advantage of maintaining a stable injection rate is that line and screen head losses can be assumed to be relatively constant with depth and, as a result, can be neglected during data analysis. If the injection rate varies significantly, these losses should be quantified and accounted for, requiring additional measurements in the field (Liu et al., 2012). Compared to discontinuous DPIL, continuous DPIL is more time efficient and provides continuous information about the vertical variations in K.

For the injection screen used in the current HPT tool, there is a practical limit on the range of flow rates that can be used. Based on our experience, that range is about 1 to 800 mL/min. When the injection rate is smaller than 1 mL/min, screen clogging by fine-grained materials is likely, as it becomes difficult for the injected water to prevent the smearing of fine materials over screen openings. When the injection rate is larger than 800 mL/min, line and screen head losses can be so large that they dwarf injection pressure signals; there is also a much greater chance of formation alteration due to water jetting out of the screen.

In both discontinuous and continuous modes, the ratio of injection rate over pressure is used to estimate K based on empirical relationships (Dietrich et al., 2008; Liu et al., 2009; Lessoff et al., 2010). Although a general relationship has been presented by McCall and Christy (2010), site-specific calibrations are typically used to improve the reliability of K estimates. The site-specific calibrations can be performed by comparing the DPIL profiles to nearby K estimates obtained via other means (Dietrich et al., 2008; Lessoff et al., 2010) or by a modeling approach that directly combines the DPIL data with collocated hydraulic tests (Liu et al., 2009). A common assumption in all these studies is that there is a unique relationship between K and the ratio of DPIL injection rate over pressure. As shown here, the validity of this assumption depends on both subsurface conditions and profiling procedures. In the following sections, we describe the numerical modeling approach used in this work, and then apply that approach to examine the impact of subsurface conditions and profiling procedures on DPIL K estimates.

2.2.3 Numerical simulation overview

2.2.3.1 Governing equation

The governing equation for the movement of water during DPIL under saturated conditions is,

$$\frac{\partial}{\partial x} \left(K_{xx} \frac{\partial h}{\partial x} \right) + \frac{\partial}{\partial y} \left(K_{yy} \frac{\partial h}{\partial y} \right) + \frac{\partial}{\partial z} \left(K_{zz} \frac{\partial h}{\partial z} \right) + q_w = S_s \frac{\partial h}{\partial t}, \quad (2-1)$$

where the head h is a function of spatial coordinate (x, y, z) and time t ; K_{xx} , K_{yy} , and K_{zz} are the hydraulic conductivity values along the x , y , and z axes, respectively; q_w is the DPIL injection rate per unit aquifer volume; and S_s is the specific storage. Numerical solutions of equation (Eq 2-1) with associated initial and boundary conditions are obtained using COMSOL (www.comsol.com); we chose COMSOL because of its ability to accurately represent the probe geometry with finite elements.

2.2.3.2 Model setup

Figure 2-2 shows the model setup for the DPIL simulations. The simulated aquifer is 4 m long, 4 m wide, and 1.8 m thick, with the DPIL probe at the center. The aquifer is treated as confined, a reasonable approximation of field conditions except very close to the water table. The top and bottom of the aquifer are specified as no flow, while the four sides are specified as constant heads at 5 m. For the probe, the injection screen (about 1 cm in diameter) is defined as a specified flux boundary with the flux rate set proportional to the aquifer K to produce similar pressure responses among simulations with different K , while the rest of the probe surface is specified as a no flow boundary. The initial head is set to 5 m throughout the aquifer, so that there is no water movement prior to the start of DPIL injection.

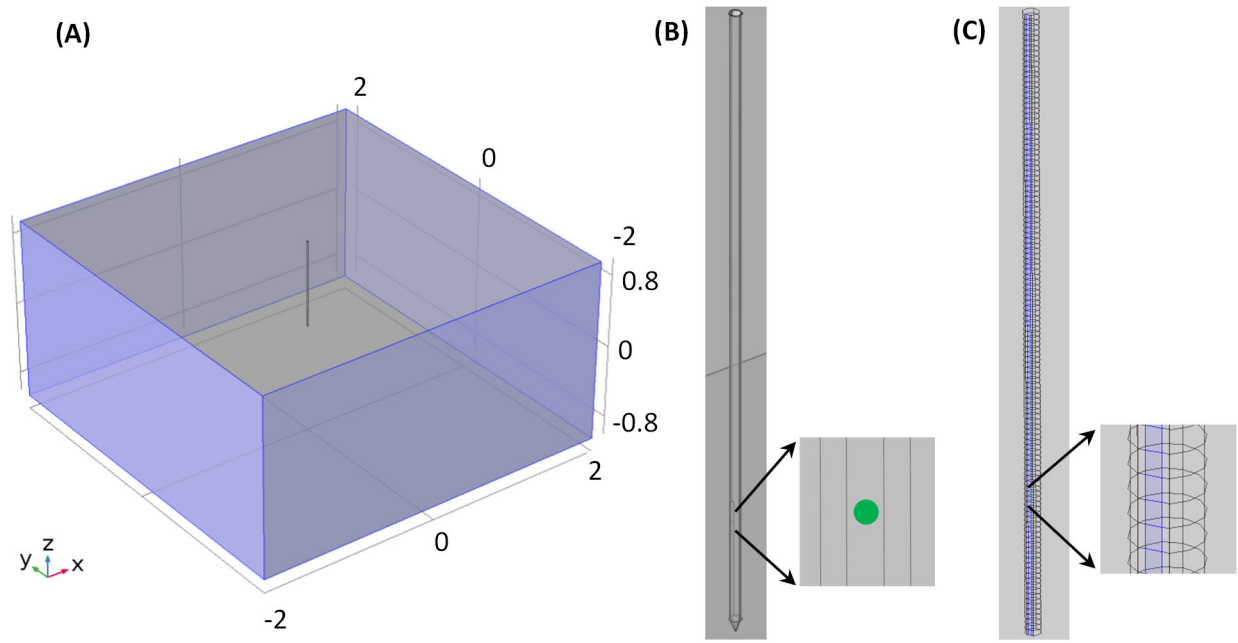


Figure 2-2. Model setup for DPIL simulations. (A) The simulation domain is 4 m long, 4 m wide, and 1.8 m thick, with the DPIL probe (diameter 4.445 cm) at the center, (B) Discontinuous DPIL injection at a single depth where water is injected through the screen (green circle), and (C) Continuous DPIL where the screen moves with the advancement of the probe and water injection is divided into a sequence of vertical 1.5-cm intervals (blue rectangles).

The two current variants of DPIL are simulated, discontinuous mode (Dietrich et al., 2008) and continuous mode (McCall et al., 2005). In the discontinuous DPIL simulations, only the aquifer responses to DPIL injection at a single location are considered; the impacts of probe advancement and water injection at other locations are assumed negligible (**Figure 2-2**). By contrast, in the continuous mode, aquifer responses to water injection are measured as the probe is advanced, so the impacts of both probe advancement and injection need to be considered. For continuous DPIL, water injection is simulated as a sequence of vertical 1.5-cm intervals (**Figure 2-2**); this interval is consistent with the vertical resolution provided by the HPT (McCall et al., 2005).

In order to explore the performance of DPIL under a range of conditions, a series of simulations were conducted during which K and S_s were varied systematically. The simulation domain was discretized using a very fine mesh (element size 0.2 cm) near the injection screen that gradually transitioned to a coarser mesh (element size 0.5 m) away from the probe. The total number of finite elements ranged from 859,894 to 1,118,372; the mesh changes when the aquifer structure changes (e.g., inclusion of thin layers or low- K skins around the probe).

2.2.4 Results

2.2.4.1 Discontinuous Mode

In the discontinuous DPIL simulations, the injection screen is set 0.5 m above the bottom of aquifer. The injection rate, Q , is proportional to aquifer K ,

$$Q = 0.0785 \text{ [m}^2\text{]}\times K, \quad (2-2)$$

where the coefficient 0.0785 is used so that the injection rate will be 400 mL/min (a common DPIL injection rate) for $K = 9.2$ m/d. For discontinuous DPIL, we assume there are no limits on the injection rate, which is typically the case in the field. The proportionality of Q with K ensures that the injection-induced pressures are comparable among the simulations. The total injection time is three seconds in most simulations (the injection time is increased in some additional simulations as discussed below; three seconds is the time HPT spends in each 1.5-cm measurement interval at an probe advancement speed of 0.5 cm/s).

Four sets of simulations are performed. In the first set (baseline), the aquifer is uniform with respect to both K and S_s . Between simulations, K is varied from 10^{-8} to 10^{-3} m/s and S_s from 1.7×10^{-6} to 0.08 m⁻¹. In the second set, the impact of anisotropy in K is explored. In the third set, the impact of a low- K skin, a thin zone immediately adjacent to the probe that can be potentially created by compaction of near-probe materials during advancement, is assessed. In the fourth set, a single thin layer (1.5 cm thick, K either 100 times smaller or larger than the rest of the aquifer) is placed at different positions relative to the injection screen.

2.2.4.1.1 Uniform Aquifer

Figure 2-3 and **Figure 2-3** show an example of the spatial distribution of injection pressure heads (P) when the aquifer is uniform with respect to K and S_s . Clearly, due to the short injection time (3 seconds), pressure responses are restricted to a very small area around the screen during injection. The small area of influence allows aquifer properties to be characterized by DPIL at a much finer resolution than with other field methods.

Figure 2-4 shows the injection pressure head versus time for different hydraulic diffusivities (D , ratio of K over S_s). The larger the D , the greater the injection-induced pressure, and the faster it approaches the asymptotic value controlled by the boundary conditions; the ratio of Q to K does not change, so the asymptotic pressure head is the same across the simulations (4 m in **Figure 2-4**). These results indicate that in fine-grained unconsolidated materials such as silts and clays, where generally K is small and S_s is large (small D), the DPIL injection pressure takes a longer time to stabilize. As a result, the measured injection pressure may be subjected to greater variability in fine-grained settings, particularly when the injection time is limited by practical constraints.

Figure 2-5A shows the ratio of injection rate over pressure head versus K from discontinuous DPIL simulations in uniform aquifers. In field applications, this ratio is used to estimate K (Dietrich et al., 2008; Liu et al., 2009; Lessoff et al., 2010). Our simulation results show that this practice is only strictly valid for K larger than 10^{-6} m/s, where the ratio is linear with K in a log-log plotting format (**Figure 2-5A**). When K is smaller than 10^{-6} m/s, S_s begins to exert an

influence on the injection pressure, causing an increasing spread of Q/P as K decreases. Therefore, in low-K materials, information on Ss may be needed for accurately determining K from the DPIL ratio.

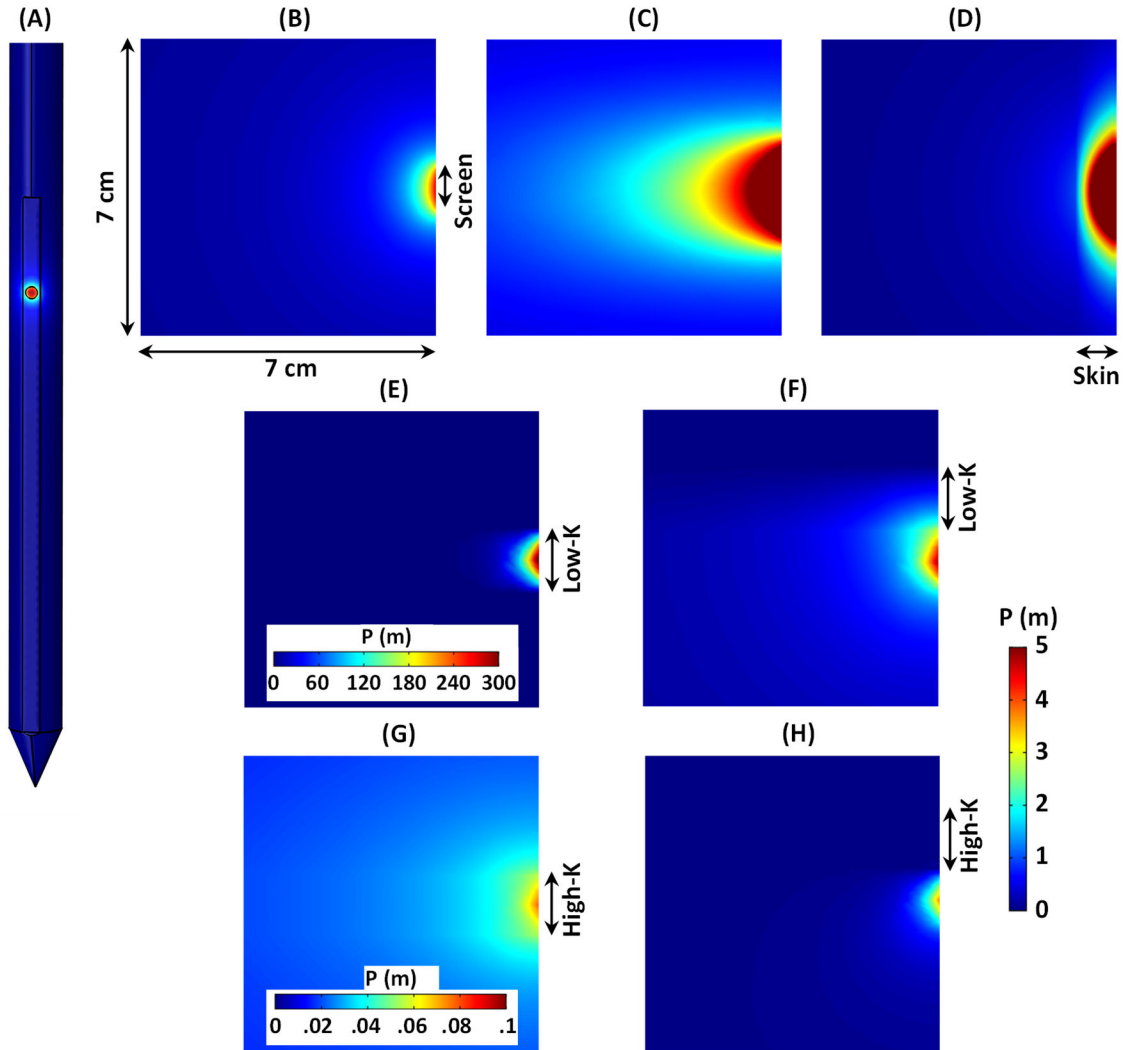


Figure 2-3. Injection pressure head distributions from discontinuous DPIL simulations: (A) pressure on the surface of the probe for a homogenous and isotropic K field; expanded view of the pressure near the injection screen for (B) a homogenous and isotropic K field, (C) a homogenous and anisotropic K field (vertical K component is 1/10th of the horizontal), (D) a low-K skin (the skin is 1 cm thick with a K value 1/10th that of the aquifer), (E) a low-K layer intersecting the screen, (F) a low-K layer immediately above the screen, (G) a high-K layer intersecting the screen, (H) a high-K layer immediately above the screen. The pressure head is shown after three seconds of injection (470 mL/min) in all plots. Figures B to H are plotted along a vertical plane perpendicular to the center of the injection screen. In (E) and (F), the low-K layer is 1.5 cm thick with a K value 1/100th that of the aquifer. In (G) and (H), the high-K layer is 1.5 cm thick with a K value 100 times that of the aquifer. Due to the very high- and low-pressure heads, respectively, the legends for (E) and (G) are different from the other plots.

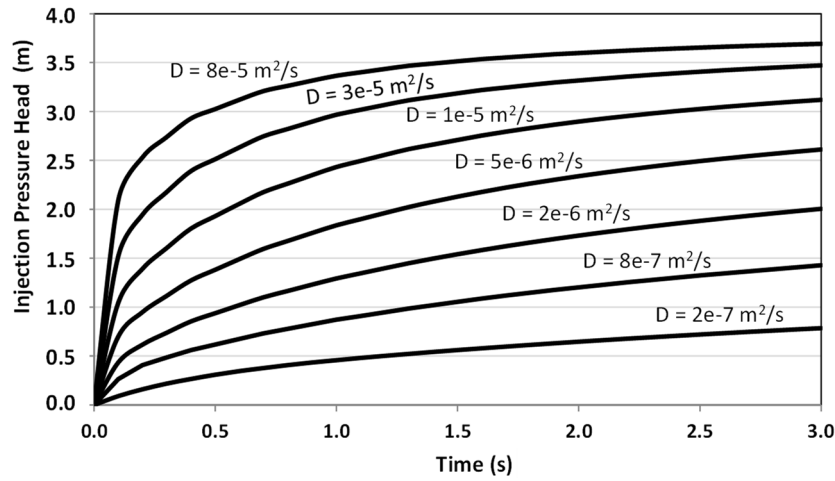


Figure 2-4. Injection pressure head versus time for different diffusivities from discontinuous DPIL simulations in a uniform aquifer.

The threshold K below which S_s begins to exert an influence on Q/P is a function of the injection time. As shown in **Figure 2-4**, a longer injection time will allow the injection pressure to more closely approach a stable value, thereby decreasing the impact of S_s . Additional simulations (not presented here) show that when the injection time is increased to 30 seconds, the threshold K reduces to 10^{-7} m/s. Clearly, for discontinuous DPIL in low- K materials, a longer injection time is highly recommended (fewer tests with longer injection times are preferred over more tests with shorter injection times).

The spread of Q/P at lower K in **Figure 2-5** can be compressed into a single curve after dividing both Q/P and K by S_s (**Figure 2-5**). After dividing Q/P by the S_s , the relationship between Q/P/ S_s and aquifer D becomes uniquely defined. Therefore, in low- K formations where S_s exerts an impact on Q/P, **Figure 2-5** can be used to directly estimate D and K from discontinuous DPIL Q/P measurements if information on S_s can be obtained via other means.

2.2.4.1.2 Anisotropic K

The impact of anisotropy is explored with ten additional simulations in which the vertical component of K (K_v) is varied while the horizontal component is fixed at 1×10^{-4} m/s; the ratio of vertical to horizontal K ranges from 1:1024 to 1:1 and the S_s is fixed at 7×10^{-5} m⁻¹. **Figure 2-3** shows the injection pressure head when the vertical K is $1/10^{\text{th}}$ of the horizontal. As a result of the suppression of flow in the vertical direction, pressure propagates further horizontally than in the isotropic simulation. In addition, due to the decrease in the vertical K , the injection-induced pressure increase is more pronounced, resulting in a noticeably larger area of significant injection pressure in the vertical direction than in the isotropic case.

Figure 2-6 shows the discontinuous DPIL Q/P ratio as a function of K_v (different anisotropic factors). When the vertical component of K is smaller than the horizontal, the Q/P ratio is smaller than that in the isotropic K case; this is indicated by simulated Q/P values for anisotropic conditions that are lower than the corresponding Q/P value for the isotropic case (intersection of

anisotropic and isotropic lines). The rate of decline in the Q/P ratio decreases as the vertical K decreases and the injection-induced flow field increasingly resembles a radial flow field (no vertical flow). Furthermore, as shown in **Figure 2-6**, the use of the DPIL Q/P ratio in anisotropic conditions while assuming isotropic conditions will result in a K estimate between the horizontal and vertical K but much closer to the horizontal K (value given by the intersection of the horizontal dotted line with the isotropic line).

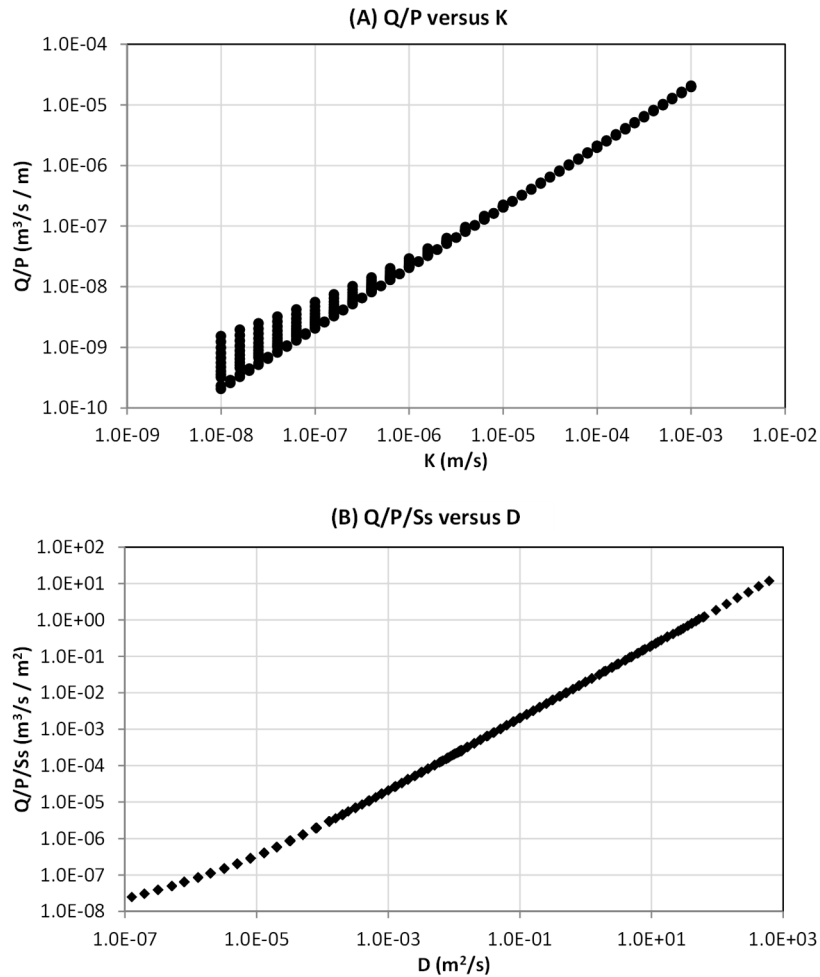


Figure 2-5. (A) Simulated injection rate/pressure head versus hydraulic conductivity, and (B) injection rate/pressure head/specific storage versus hydraulic diffusivity for discontinuous DPIL. The injection pressure is averaged over the entire screen after 3 seconds of injection. Figure (A) shows that for the considered specific storage range (1.7×10^{-6} to 0.08 m^{-1}), the ratio of injection rate to pressure head is linear with K in a log-log plotting format when K is essentially greater than 10^{-6} m/s . Figure (B) shows that by dividing the ratio of injection rate to pressure head by the specific storage, $Q/P/Ss$ is uniquely determined by the hydraulic diffusivity over the entire K range.

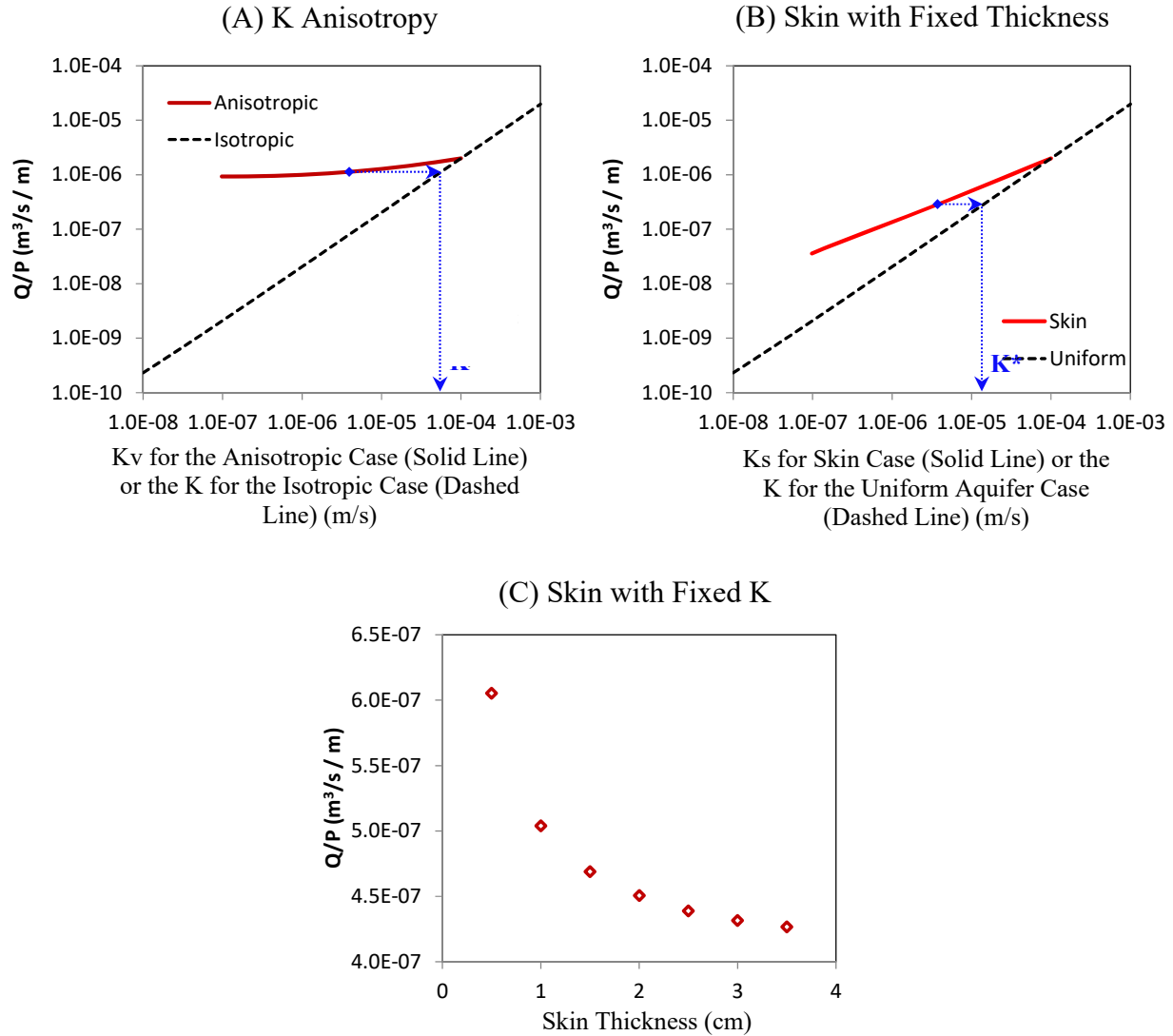


Figure 2-6. The DPIL Q/P ratio for (A) K anisotropy (the ratio of vertical to horizontal K, $K_v:K_h$, varies from 1:1 to 1:1024; the horizontal K is fixed at 10^{-4} m/s), (B) low-K skin with fixed thickness (the skin thickness is fixed at 1 cm; the skin K (K_s) varies from 1 to $1/1024^{\text{th}}$ of the aquifer K, 10^{-4} m/s), and (C) low-K skin with fixed K (K_s is fixed at $1/10^{\text{th}}$ of the aquifer K; skin thickness varies from 0.5 to 3.5 cm). The specific storage is the same in all plots (7×10^{-5} m⁻¹). The dashed lines in (A) and (B) are the simulation results for the isotropic and uniform K field for comparison. In (A), assuming no anisotropy, the Q/P value at the diamond ($K_v=4 \times 10^{-6}$ m/s, $K_h=10^{-4}$ m/s) would lead to an estimated $K^*=5 \times 10^{-5}$ m/s (see the dotted lines with arrows). In (B), assuming no skin, the Q/P value at the diamond ($K_s=4 \times 10^{-6}$ m/s, aquifer $K=10^{-4}$ m/s) would lead to an estimated $K^*=1.3 \times 10^{-5}$ m/s (see the dotted lines with arrows).

2.2.4.1.3 Low-K skin

The impact of a low-K skin is explored with two sets of simulations: 1) a set of ten simulations in which the skin thickness is fixed at 1 cm while the skin K (K_s) value varies from $1/2$ to $1/1024^{\text{th}}$ of the aquifer K, and 2) a set of seven simulations in which the skin K is fixed at $1/10^{\text{th}}$ that of the aquifer while the thickness varies from 0.5 to 3.5 cm. **Figure 2-3** shows the DPIL injection pressure head with a 1-cm thick low-K skin (K_s $1/10^{\text{th}}$ of the aquifer K [10^{-4} m/s]). Clearly, the low-K skin causes a significant increase in the injection pressure around the screen within the skin.

Figure 2-6 shows the Q/P ratio as a function of K_s for the skin thickness fixed at 1 cm. As K_s decreases, the injection pressure at the screen increases and the simulated Q/P decreases. The simulated Q/P, however, remains larger than that for the uniform aquifer case with a K value equal to that of the skin. Based on **Figure 2-6**, if a low-K skin is present but not taken into account during the analysis, the Q/P ratio would produce a K estimate between K_s and the aquifer K. The impact of a low-K skin on DPIL is also dependent on the skin thickness. **Figure 2-6** shows the simulated Q/P at different skin thicknesses with K_s fixed at $1/10^{\text{th}}$ of the aquifer K. As expected, the Q/P ratio decreases when the skin thickness increases. However, the decline rate decreases significantly when the skin thickness is greater than 2 cm because the DPIL is only sensitive to a small area around the injection screen (**Figure 2-3**). Thus, when the skin is thicker than 2 cm, the injection pressure will be primarily determined by the skin and will be nearly insensitive to aquifer conditions.

2.2.4.1.4 Thin K layer

One of the major advantages of DPIL is its high measurement resolution, so it is necessary to assess the impact of a thin layer near the injection screen. The impact of a thin K layer extending the full width of the model area is explored with two sets of simulations, 1) four simulations in which the thin layer has a K value 100 times greater than the aquifer and is placed at different distances from the screen, and 2) four simulations in which the layer has a K value 100 times smaller than the aquifer and is placed at different distances from the screen. The thickness of the layer is 1.5 cm in all simulations.

Figure 2-3 to **Figure 2-3** show the injection pressure heads for different layer K values and locations. When the low-K layer intersects the screen, the injection pressure is significantly increased within that layer relative to the uniform-aquifer case (**Figure 2-3**); similarly, when the high-K layer intersects the screen, the pressure is significantly reduced (**Figure 2-3**). By contrast, when the layer does not directly intersect the screen, its impact on the injection pressure is much less (**Figure 2-3** and **Figure 2-3**). If the layer above the screen has a lower K (**Figure 2-3**), that layer becomes a barrier to the movement of injected water, and the injection pressure around the screen is increased compared to that in the uniform case. On the other hand, if the layer above the screen has a higher K (**Figure 2-3**), that layer becomes a preferential flow path for the injected water, and the injection pressure around the screen is reduced. Consistent with those visual observations, the calculated Q/P ratios for different layer K values and locations (not shown) also indicate that 1) when the layer intersects the screen, Q/P is significantly different from that in the uniform-aquifer case, and 2) when the layer does not intersect the screen, Q/P

quickly approaches that for the uniform K case at a small distance between the layer and screen. These results indicate that DPIL can provide a high-resolution characterization of K because the measurement at a given interval is not significantly affected by nearby conditions.

2.2.4.2 Continuous mode

Continuous DPIL profiling has three major differences with profiling in the discontinuous mode: 1) the injection screen is moving as water is injected into the formation, 2) injection at previous depths can impact the pressure measured at the current injection depth, and 3) probe advancement produces pore water pressure changes at the probe tip that may have a large impact on the pressure measured at the injection screen. As a result, during continuous DPIL profiling, the pressure change measured at the screen consists of three components: the injection-induced pressure, the pressure produced by injection at previous depths, and the pressure change generated by probe advancement. Clearly, if the pressure changes by previous injection and probe advancement are significant, they have to be considered when using the Q/P ratio to estimate K.

Water injection during continuous DPIL is simulated using a series of 1.5-cm vertical intervals (**Figure 2-2**), which is the measurement resolution of the HPT (McCall et al., 2005). For each vertical interval, water injection begins at a time that is dependent on probe depth and advancement speed and continues for a duration that is dependent on the advancement speed,

$$t_{\text{start}} = \text{starting depth}/v_{\text{probe}}, \quad (2-3a)$$

$$\Delta t = 1.5 \text{ [cm]}/v_{\text{probe}}, \quad (2-3b)$$

where t_{start} is the injection start time at the starting depth of a measurement interval; v_{probe} is the speed of probe advancement; and Δt is the injection duration. In this way, the impact of water injection at all previous depths is simulated as the probe is continuously advanced.

Because no material is removed during DPIL advancement, the pressure generated by probe advancement can be approximated by water injection around the tip at a rate that is equivalent to the volumetric rate of material displacement by the probe (Elsworth, 1993; Elsworth and Lee, 2005). The rate of material displacement is computed based on probe geometry and the speed of advancement,

$$Q_{\text{tip}} = A \times v_{\text{probe}}, \quad (2-4)$$

where A is the cross-sectional area of the probe. In this work, the standard-sized HPT probe (4.445 cm in diameter) is used as the basis for computing A (0.0015 m²). Probe advancement can potentially cause compaction (or dilation) of solids and change formation properties around the probe. That impact, however, is difficult to evaluate and is thus not considered in this initial assessment.

Due to the practical constraints on the range of injection rates that can be used in the field, we assume the minimum and maximum injection rates are 1 and 800 mL/min, respectively, in the following simulations. The simulated aquifer is uniform, with K varying from 10⁻⁸ to 2.5x10⁻⁴ m/s and S_s from 1.7x10⁻⁶ to 0.08 m⁻¹ between simulations.

2.2.4.2.1 A simulation example

Figure 2-7 shows the pressure head increase caused by water injection and probe advancement in a uniform aquifer with $K = 10^{-4}$ m/s and $S_s = 7.5 \times 10^{-5}$ m⁻¹ for an injection rate of 470 mL/min and an advancement speed of 1 cm/s. **Figure 2-7** shows that there are two distinct areas of significant pressure increase during continuous DPIL, one at the tip produced by probe advancement and the other at the injection screen produced by water injection. For the probe speed of 1 cm/s, the material displacement produced by probe advancement is equivalent to a water injection rate of 900 mL/min. However, unlike the injection at the screen where water is injected through a small circular screen (1 cm in diameter) on the side of probe, the equivalent injection at the tip is through the entire cylindrical surface of the probe. As a result, the spatial area of significant pressure increase is larger at the tip, but the magnitude of the pressure increase is smaller than that at the injection screen.

Figure 2-7 shows the impacts of probe advancement and water injection at previous depths on the pressure head measured at the injection screen. At the plotted depth (1.25 m below top of aquifer), the impact of probe advancement is initially very small, indicated by the slow increase of pressure head during the first 75 seconds. After 75 seconds, as the probe moves closer to the plotted depth, the increase by probe advancement becomes progressively larger. At 125 seconds when the tip arrives at the plotted depth, the pressure head increase by probe advancement reaches a maximum (about 0.9 m). After the probe passes by, the pressure head quickly decreases; the decline in the short period following the passage of the probe tip (125 to 150 seconds) is very similar to the increase prior to the arrival of tip. After 150 seconds, as the injection screen approaches the plotted depth, the impact of water injection at previous depths becomes more significant. As a result, instead of continuing to drop, the pressure head increases until the screen arrives at the plotted depth (166 seconds).

During continuous DPIL profiling, the pressure head at a given depth can only be measured when the injection screen arrives at that depth and the measured pressure is assumed to be produced primarily by injection at that depth (after removing the hydrostatic and barometric background pressures) (McCall et al., 2005; Dietrich et al., 2008; Liu et al., 2012). That assumption, however, may not be valid under certain conditions that depend on the advancement speed, injection rate, and formation properties. For the example in **Figure 2-7** (see expanded plot on the right of **Figure 2-7**), the total pressure head increase measured at the screen is 1.376 m, the pressure head increase produced by injection at previous depths is approximately 0.149 m, and the pressure head increase produced by probe advancement is approximately 0.023 m. The actual injection-induced pressure head change is about 1.204 m ($1.376 - 0.149 - 0.023$ m), 87.5% of the total measured value at the screen. Clearly, the impacts of probe advancement and water injection at previous depths will vary depending on probe speed, injection rate, and formation properties.

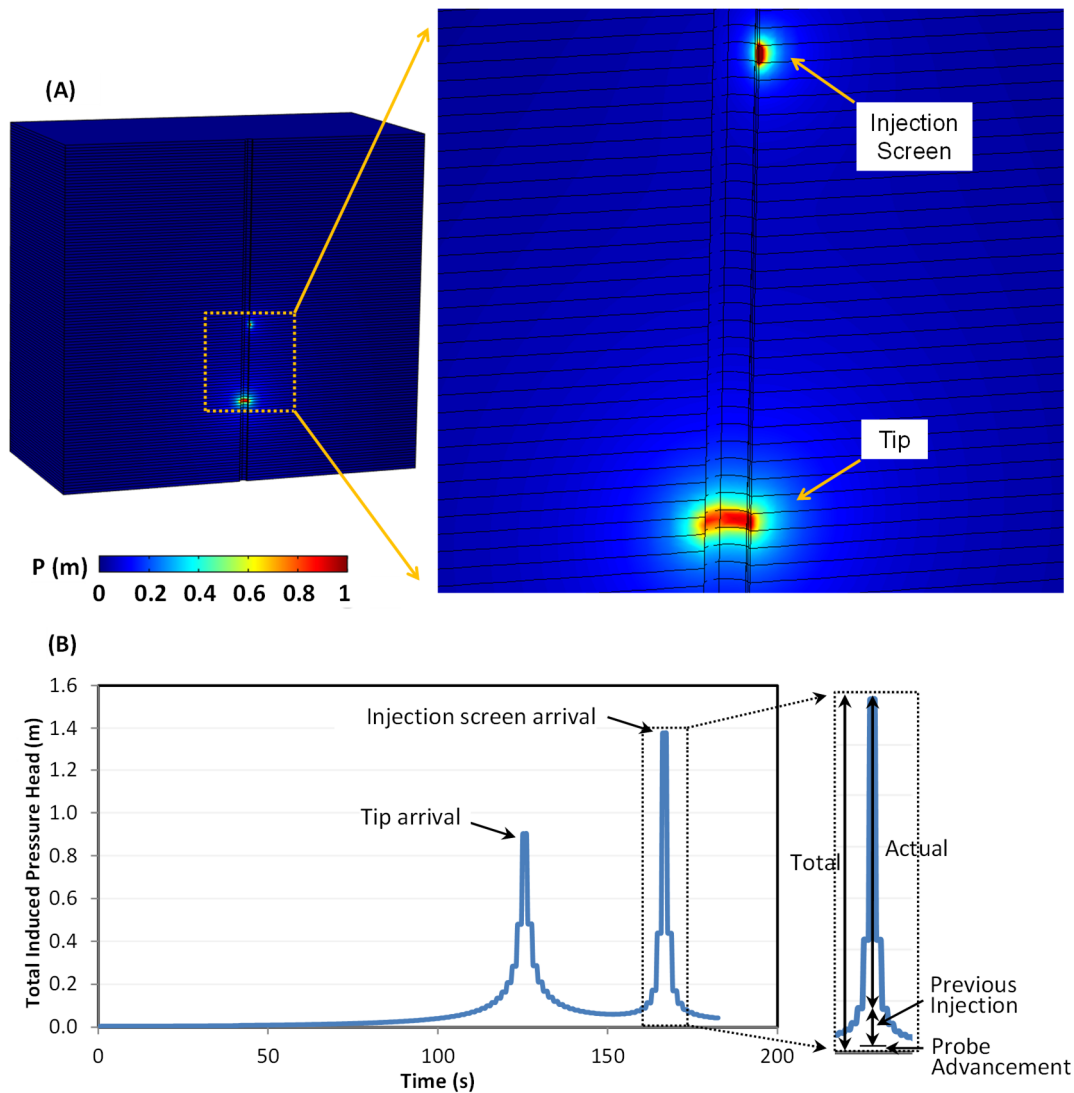


Figure 2-7. Pressure head increase during continuous DPIL: (A) Spatial distribution at 140 seconds since the start of probe advancement, (B) Pressure head versus time at depth 1.25 m below top of the model. In (A), half of the model domain is cut out to facilitate visualization. In the expanded inset in (B), the different components of the total pressure head measured at the screen are labelled.

2.2.4.2.2 Impacts of probe advancement and water injection at previous depths

The impacts of probe advancement and water injection at previous depths are assessed using three sets of additional simulations that consider the following conditions: 1) water injection at the given screen depth (neglect injection at previous depths and the impact of probe advancement), 2) conditions of the first set of simulations with water injection at previous depths, 3) the impact of probe advancement alone (neglect water injection). These additional simulations, along with the base simulations where the impacts of water injection at all depths

and probe advancement are considered, provide information about the performance of continuous DPIL and how it is affected by different field procedures and formation properties.

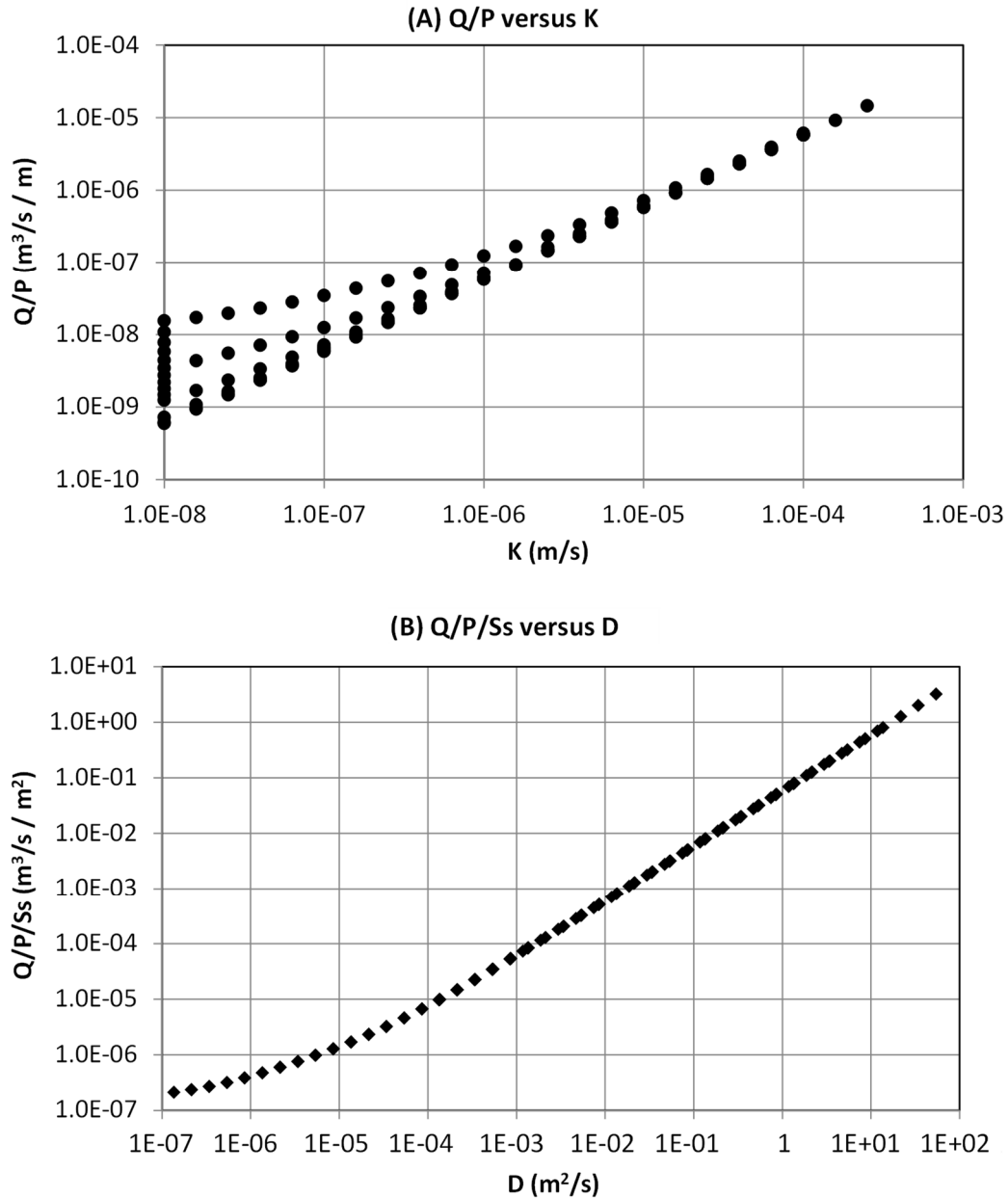


Figure 2-8. (A) Q/P versus K and (B) $Q/P/Ss$ versus D during continuous DPIL at an advancement speed of 1 cm/s. Neither the impact of water injection at previous depths nor probe advancement is considered here. The plotted Q and P are calculated as the average over each rectangular measurement interval (1.5 cm vertical by 1 cm horizontal) during injection.

The first set of simulations only considers water injection at the current depth; these simulations are essentially equivalent to the discontinuous DPIL simulations discussed in **Section 2.2.4.1**, except for the different injection area and duration. **Figure 2-8** shows the results for the

advancement speed of 1 cm/s with K and S_s varying between simulations. As expected, the plots of Q/P versus K and $Q/P/S_s$ versus D show a similar pattern to those in the discontinuous DPIL simulations (**Figure 2-5**). The threshold K below which S_s begins to have a significant impact on the DPIL response is between 10^{-6} and 10^{-5} m/s.

The second set of simulations assesses the impact of water injection at previous depths. The plots for this set of simulations (not shown) are very similar to those in **Figure 2-8**, indicating that the impact of water injection at previous depths is small across the range of simulated conditions. The injection rate remains constant at different depths during these simulations, which is consistent with common field practices (Liu et al., 2012).

Figure 2-9 presents the results from the third set of simulations in which only the impact of probe advancement (1 cm/s) is simulated. The plotted pressure head is the pressure due to probe advancement measured at the injection screen, which is lower than the pressure generated at the tip because of the time needed for the screen to travel to the tip position. For a given S_s , the pressure at the screen generated by probe advancement becomes more significant as hydraulic conductivity decreases.

In field applications, there is always a limit on the range of measurable pressure, which is imposed by the pressure sensor used in the probe. The upper limit of pressure head measurement with the typical HPT sensor is about 77 m. Given atmospheric and hydrostatic background pressures, we assume the maximum DPIL pressure head increase that can be measured practically is about 56 m. In other words, if the pressure head generated by probe advancement is greater than 56 m at the screen, the pressure sensor will be maxed out and the DPIL results will be invalid. In **Figure 2-9**, we use the pressure head threshold of 56 m to subdivide the pressure increase generated by probe advancement. The yellow-red colors represent the settings that cannot be characterized by continuous DPIL at an advancement speed of 1 cm/s. Specifically, injection pressure cannot be measured when K is smaller than 7×10^{-8} m/s and S_s smaller than 10^{-3} m^{-1} . In order to use DPIL in these settings, the advancement speed has to be reduced or the distance between the tip and the injection screen must be increased to allow the advancement-induced pressure to drop below the upper limit of the sensor.

Figure 2-9 and **Figure 2-9** present the results of the continuous DPIL simulations where probe advancement and water injection at both current and previous depths are considered. The speed of probe advancement is 1 cm/s, while K and S_s are varied between simulations. Given the practical constraints on injection rates under field conditions, the minimum and maximum Q values used in the simulations are 1 and 800 mL/min, respectively.

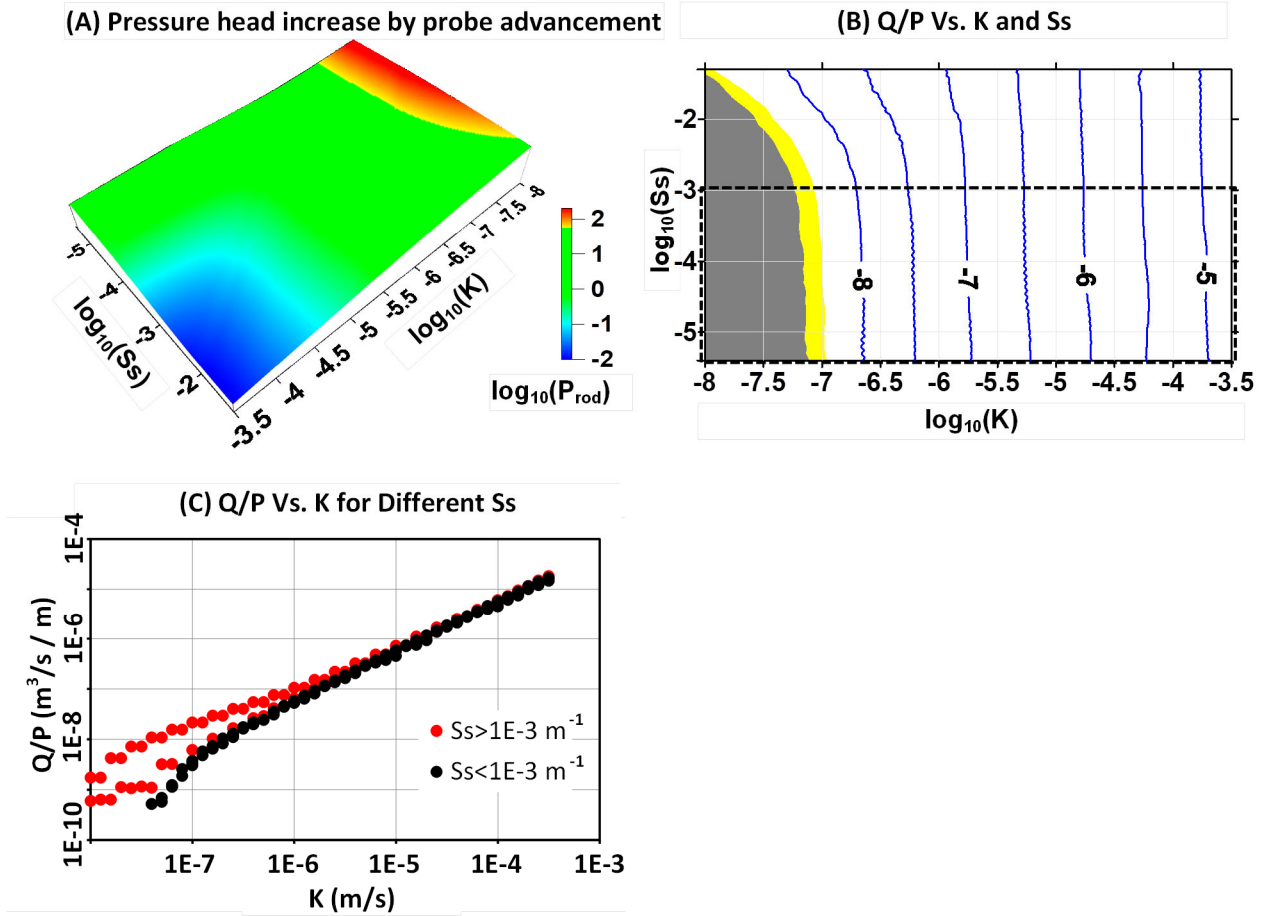


Figure 2-9. (A) Pressure head increase measured at the injection screen due to probe advancement (P_{rod}) at 1 cm/s as a function of K and S_s , (B) Contours of Q/P measured at the injection screen (P includes the pressure head due to both probe advancement and water injection) as a function of K and S_s , and (C) Q/P versus K for all simulated S_s . In (A), the values on the S_s and K axes are reversed so that pressure heads are better displayed visually. In (B), the gray area indicates the conditions where the pressure head produced by probe advancement exceeds the measurement limit, the yellow zone indicates the transition conditions where the impact of probe advancement is likely high, and the dashed box represents the typical range of S_s for unconsolidated sediments. In (C), the results are subdivided into those for $S_s < 10^{-3} \text{ m}^{-1}$ and those for $S_s > 10^{-3} \text{ m}^{-1}$.

Figure 2-9 shows the contours of Q/P as a function of K and S_s . The gray area indicates the conditions where the pressure head produced by advancement exceeds the measurement limit (i.e., the yellow-red contours in **Figure 2-9**). The yellow zone near the edge of the gray area indicates transition conditions where the ratio of injection rate over pressure is measurable but will likely be significantly affected by the advancement-generated pressure. Similar to discontinuous DPIL, when K is larger than 10^{-6} m/s , Q/P is primarily a function of K and can thus provide an accurate estimate for K during continuous DPIL (the Q/P contours relatively straight). When K is smaller than 10^{-6} m/s , however, Q/P becomes more sensitive to S_s for $S_s > 10^{-3} \text{ m}^{-1}$ (as indicated by the increasing curvature of the contours). For unconsolidated

formations of moderate K or higher, S_s is typically less than 10^{-3} m^{-1} (dashed box on **Figure 2-9**). Thus, the ratio of injection rate over pressure should provide a good estimate of K in those situations.

The impact of S_s on the simulated Q/P can be further illustrated in **Figure 2-9**, where the scatter plot of simulated Q/P versus K is subdivided based on whether S_s is greater than or smaller than 10^{-3} m^{-1} . Similar to discontinuous DPIL (**Figure 2-5**), when K is larger than 10^{-6} m/s , Q/P in continuous DPIL is primarily a function of K and there is little sensitivity to S_s . When K is smaller than 10^{-6} m/s , the simulated Q/P values still show little sensitivity for $S_s < 10^{-3} \text{ m}^{-1}$; however, the Q/P values show considerable sensitivity for $S_s > 10^{-3} \text{ m}^{-1}$ (indicated by the increasing spread of red points in **Figure 2-9**).

2.2.4.2.3 Impact of probe advancement speed

During continuous DPIL, the speed of probe advancement has a major impact on the measured pressure responses. First, the speed determines the magnitude of pore water pressure generated at the tip, as the equivalent water injection rate is proportional to the speed (Eq 2-4). A slower speed results in less pressure generated at the tip. Second, the speed determines the time to travel between the tip and screen. A slower speed translates into a longer time for the screen to reach the tip location, allowing for more dissipation of the advancement-generated pressure. Third, a low speed means increased time spent at each measurement interval (Eq 2-3b), which will result in a larger amount of water injected per interval (assuming constant injection rate). Based on **Figure 2-4**, in coarse-grained materials, the increased time at each measurement interval is not expected to have a significant impact on the measured pressure because much of the response to injection occurs early in the injection time; in fine-grained materials, however, D is relatively small and the increased time at each measurement interval will lead to an increase in the measured pressure.

To further evaluate the impacts of probe advancement, four additional sets of simulations are performed using advancement speeds of 2 cm/s, 1.5 cm/s, 0.7 cm/s, and 0.5 cm/s. **Figure 2-10** shows the simulated Q/P versus K relationships for these speeds. For $S_s = 7 \times 10^{-5} \text{ m}^{-1}$, the impact of advancement speed becomes noticeable when K is lower than $5 \times 10^{-7} \text{ m/s}$, as indicated by the increasing separation among the curves; at $K = 5 \times 10^{-7} \text{ m/s}$, Q/P decreases by 16% as the speed increases from 0.5 to 2 cm/s. A significantly larger S_s (**Figure 2-10**) produces some reduction of the impact of advancement speed in low- K materials; at $K = 5 \times 10^{-7} \text{ m/s}$, Q/P decreases by 11% as the speed increases from 0.5 to 2 cm/s. Using the 16% Q/P reduction between the speeds of 0.5 and 2 cm/s as the threshold, the K value under which the impact of advancement speed needs to be considered decreases from $5 \times 10^{-7} \text{ m/s}$ to $3 \times 10^{-7} \text{ m/s}$ when S_s increases from $7 \times 10^{-5} \text{ m}^{-1}$ to $9 \times 10^{-3} \text{ m}^{-1}$. As the S_s for most unconsolidated formations is expected to be lower than 10^{-3} m^{-1} , the impact of advancement speed should always be considered when K is smaller than $5 \times 10^{-7} \text{ m/s}$.

The findings from this set of simulations result in two recommendations for field practices. First, if the K is expected to be larger than $5 \times 10^{-7} \text{ m/s}$, which is the case for most sandy materials, DPIL profiling can be performed using the standard HPT speed (2 cm/s), since Q/P shows little dependence on advancement speed. On the other hand, if K is expected to be less than $5 \times 10^{-7} \text{ m/s}$, which is the case for most silts and clays, the advancement speed should be kept as low as possible (e.g., 0.5 cm/s).

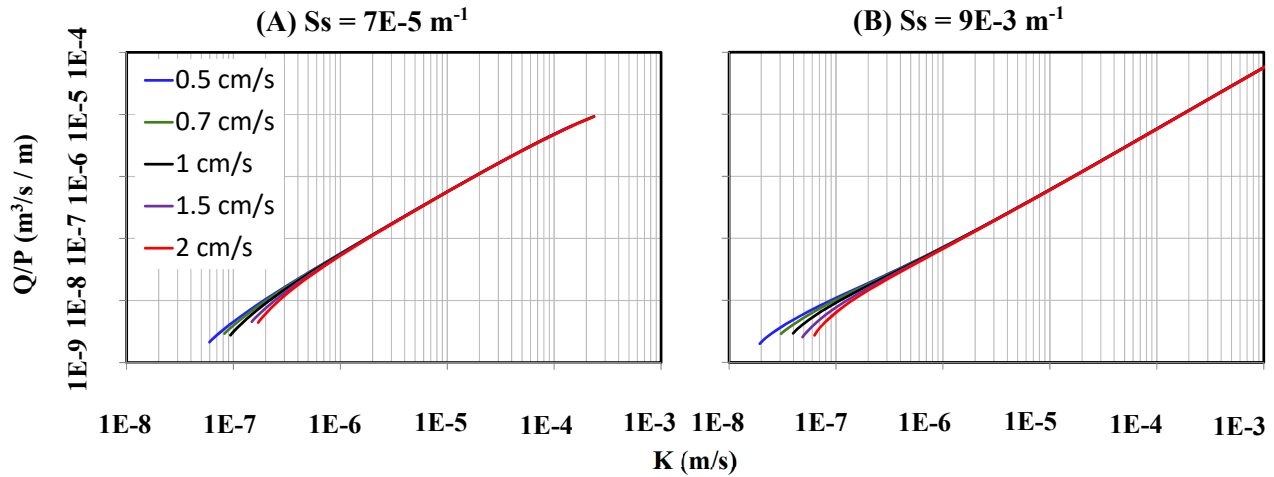


Figure 2-10. Simulated Q/P versus K during continuous DPIL at different advancement speeds for (A) $S_s = 7 \times 10^{-5} \text{ m}^{-1}$, and (B) $S_s = 9 \times 10^{-3} \text{ m}^{-1}$. Based on (A), for $S_s = 7 \times 10^{-5} \text{ m}^{-1}$ and $K = 5 \times 10^{-7} \text{ m/s}$, the simulated Q/P is 2.9×10^{-8} and $2.4 \times 10^{-8} \text{ m}^3/\text{s/m}$, at advancement speeds of 0.5 and 2 cm/s, respectively; this represents a 16% reduction in Q/P. Based on (B), where S_s is increased to $9 \times 10^{-3} \text{ m}^{-1}$, this change in advancement speeds results in the 16% reduction in Q/P when K is $3 \times 10^{-7} \text{ m/s}$ (the simulated Q/P at $K = 3 \times 10^{-7} \text{ m/s}$ is 2.7×10^{-8} and $2.2 \times 10^{-8} \text{ m}^3/\text{s/m}$, respectively).

2.2.5 Summary and Conclusions

DP injection logging has become a widely accepted approach for investigating near-surface, unconsolidated formations (Liu et al., 2012; Maliva, 2016). Despite its widespread use, however, there has been no rigorous analysis of the underlying physical processes that take place during DPIL profiling or how the approach performs under various hydrogeological and operating conditions. Addressing that knowledge gap was the purpose of this simulation study.

There are currently two variants of DPIL: discontinuous mode (Dietrich et al., 2008; Lessoff et al., 2010) and continuous mode (McCall et al., 2005; Liu et al., 2009, 2012). In the discontinuous mode, the probe remains at the measurement depth while the injection tests are performed. Due to the suspension of advancement, the impacts of probe advancement and water injection at previous depths should be very small and are thus not considered in the discontinuous DPIL simulations. The five major findings from the discontinuous DPIL simulations are: 1) during DPIL injection, significant pressure responses are restricted to a small area around the injection screen, which allows aquifer properties to be characterized at a fine resolution; 2) the ratio of injection rate over injection pressure head (Q/P), which is commonly used to estimate K, should be applicable for that purpose for K greater than 10^{-6} m/s . When K is lower than 10^{-6} m/s , Q/P may be affected by S_s ; 3) when the vertical K component is smaller than the horizontal, the injection pressure propagates more horizontally and the pressure measured at the screen is larger than that in the isotropic K case. As a result, if anisotropy is present but not considered in the analysis, the measured Q/P will produce a K estimate between the horizontal and vertical K, but much closer to the horizontal component; 4) when there is a low-K skin around the probe, the Q/P ratio is mostly determined by the skin if the skin thickness is greater than 2 cm. If the skin is

thinner than 2 cm, the measured Q/P will produce an estimate between the skin K and aquifer K when skin effects are not considered in the analysis; 5) when there are thin K layers near the injection screen, their impacts on the measured Q/P are only significant when the screen directly intersects these layers. If the layers do not intersect the screen, the simulated Q/P values quickly approach those for the uniform K case at a small distance from the screen.

In the continuous DPIL mode, water is injected continuously as the probe is advanced. As a result, in the continuous DPIL simulations, the impacts of probe advancement and water injection at previous depths must be considered in addition to water injection at the current depth. Simulation results indicate that water injection at previous depths has generally a small impact on the measured pressure at the current depth (about 10 to 15% of the total pressure). The impacts of probe advancement, however, can be much more significant. This is especially true in formations with small K and Ss where probe advancement generates a large pressure increase at the tip and the residual pressure can dwarf the pressure produced by injection. Based on the typical upper limit of the sensor used to measure injection pressure head in the field (56 m), we have identified the range of conditions for which continuous DPIL is not viable due to the exceedingly large pressure produced by probe advancement (for an advancement speed of 1 cm/s, DPIL is not viable when K is less than 7×10^{-8} m/s and Ss less than 10^{-3} m⁻¹).

Similar to discontinuous DPIL, the Q/P ratio during continuous DPIL can be used to estimate K when K is larger than 10^{-6} m/s, regardless of Ss. When K is less than 10^{-6} m/s, Q/P still provides a good estimate of K when $S_s < 10^{-3}$ m⁻¹, but becomes increasingly affected by Ss when $S_s > 10^{-3}$ m⁻¹. Fortunately, Ss is typically less than 10^{-3} m⁻¹ in formations of moderate K or higher, so the Q/P ratio should provide a good estimate of K in many cases.

During continuous DPIL, the speed of probe advancement is a critical factor, especially when K is smaller than 5×10^{-7} m/s. When a relatively low advancement rate is used, the pressure generated by probe advancement at the tip is relatively small and there is more time for that pressure to dissipate before the screen arrives at the tip location. As a result, the advancement-generated pressure has a relatively small impact on the pressure measured at the screen. It is therefore recommended that the probe advancement speed be reduced when continuous DPIL is applied to fine-grained materials. In our experience, the lowest rate we can consistently maintain is 0.5 cm/s.

In this work, we simulated the impact of probe advancement using an equivalent rate of water injection (Elsworth, 1993; Elsworth and Lee, 2005). An important limitation of this approach is that formation alteration, which may likely occur in the field due to the materials being pushed aside by the probe, is not explicitly considered. Although the low-K skin simulations in the discontinuous mode have provided some insights into potential K reduction during DPIL, the actual impacts of formation alteration on DPIL measurements will be difficult to quantify in the field. This is especially true in fine-grained materials where the altered K can be smaller (compression) or larger (dilatancy) than the original K. In future work, we will assess the impact of formation alteration during probe advancement using poroelastic simulations and other relevant approaches.

Finally, this simulation study provides a theoretical basis for analyzing DPIL data collected in the field. Currently, the DPIL data are typically transformed into K estimates using empirical relationships that often require site-specific calibration (Dietrich et al., 2008; Liu et al., 2009, 2012). Here we have shown that estimates of K can be directly determined from the Q/P ratio and probe advancement speed for most unconsolidated formations. Further field tests are needed to fully assess the utility of these simulation results for K estimation under the range of conditions faced in field settings.

2.3 LOW K HPT TOOL CONSTRUCTION AND LABORATORY EXPERIMENTS

2.3.1. Construction of the low-K HPT tool

The goal of this task is to develop a low-K HPT system that can be used for high-resolution characterization of K in low-permeability settings ($K < 0.01$ m/d). In order to accomplish this, the injection rate has to be much lower than the typical range of HPT tool (200 - 600 mL/min) to avoid over pressuring and potential formation alteration. This requires modification of two key components of the current HPT system, the water pump and flow meter. Originally, we had proposed the use of a continuous push/pull syringe pump (Cole-Parmer S-74905-56) that could inject water at the flow rate range of 5 mL/min to 220 mL/min. However, after some preliminary lab tests, it was found that there was a significant pause in flow injection when the piston in the syringe pump reversed directions. This was caused by entrapped air in the tubing in the manufacturer-provided continuous high-pressure pinch valve box. Further equipment modifications (e.g., replacing the pinch valve box with four check valves that were installed much more closely to the two ends of the steel syringes) largely reduced the duration of pause, but still could not completely eliminate the issue (that is, the flow rate still showed a notable reduction whenever the piston reversed directions). As a result, we changed the design of the low-flow injection system.

The new low-flow injection system is based on the flow meter/controller produced by Omega (**Figure 2-11**). This flow meter/controller allows a target flow rate to be entered, then the output flow will be adjusted to the target rate using a linear relationship between the flow and pressure under laminar conditions (the pressure losses over a unit length of the flow path are a linear function of flow rates under laminar flow conditions, so that the flow rates can be accurately determined by measuring the differential pressure across the laminar element after correcting for temperature effects). Deionized water is used as the source water for HPT injection to avoid chemical buildup and ensure the accuracy of flowmeter measurements over time. A vane pump is used to generate the inflow at the desirable pressure range (0 to 100 psi) for the Omega flow meter/controller. The real-time flow rate of the flow meter/controller can be output into a computer at 1 Hz via a digital connector cable.



Figure 2-11. The flowmeter/controller used in the low-flow HPT system (<https://www.omega.com/pptst/FLR1600.html>).

Figure 2-12 shows the design of low-K HPT system. The low-K HPT system is constructed by adding a low-flow control box (B') to standard HPT. There are 7 components in HPT, source water tank, a flow control box with pump and flow meter, an electronic box with a computer, trunkline, pressure sensor, injection port covered with a screen, and an EC (electronic conductivity) sensor array. During HPT operation, a pump in the flow control box withdraws water from the source tank and sends it down the injection tube inside the trunkline, and the flow rate is continuously monitored by a flow meter. The electronic box sends electric current to various sensors on the probe and converts the resulting signals into digital formats that can be stored on a computer and visually displayed in real time. The flow rate measurements, as well as some supplemental data from the flow control box (e.g., the pressure in the injection lines inside the flow box), are also transmitted to the electronic box for storage and display. On the HPT probe, there is an EC sensor array located closely above the bottom tip. The bulk EC of subsurface formation can be measured in a Wenner array (when all 4 sensor pins are functioning), or in a dipole configuration using any of the two neighboring pins (if one or two of the pins are not working). The injection port is located about 16 inches above the bottom tip; this distance allows a reasonable amount of time for advancement-induced pore water pressure to dissipate before the injection port reaches the tip location. The injection port is protected by a steel mesh screen so that sediments do not get pushed into the injection tube to cause clogging. Prior to the HPT probe being driven into the subsurface, a series of steel connection rods need to be pre-strung with the trunkline so that flow and EC profiling can be continuously performed once logging starts. As the probe is driven into the subsurface, water is continuously injected into the formation, and the ratio of injection rate over pressure is used to estimate K. To prevent the screen from clogging, water injection should always be turned on before probe advancement is initiated. During active probe advancement and flow profiling, trunkline and connection rod movement should be avoided to reduce noise in HPT pressure measurements.

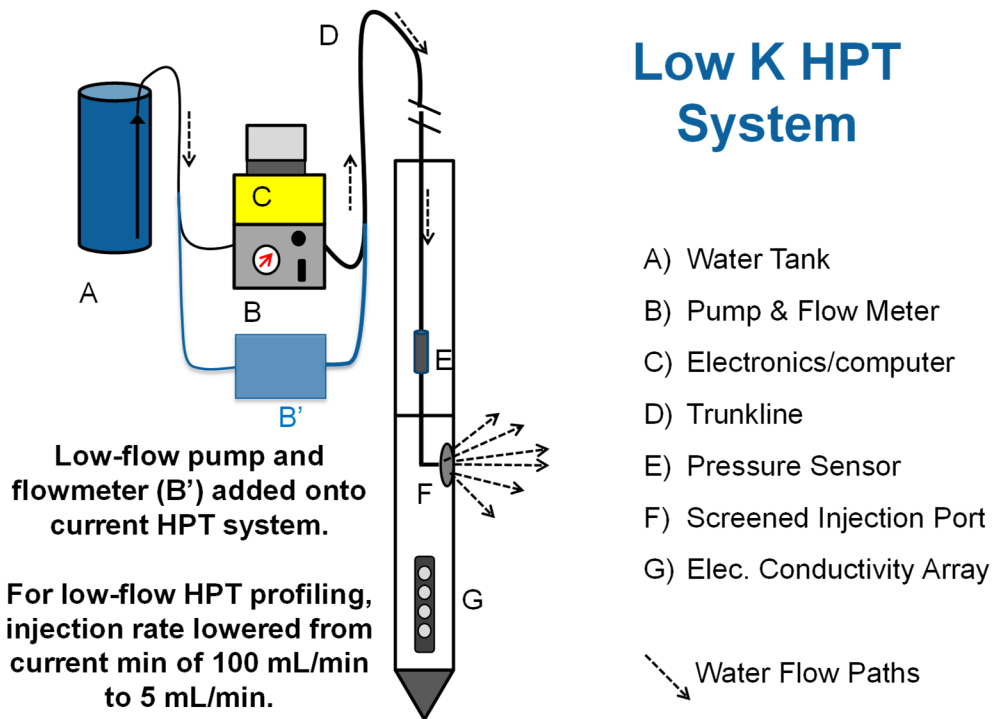


Figure 2-12. The design of low-K HPT system. The low-K HPT extension is achieved by adding a low-flow control box to the standard HPT system. A) through G) mark the key components of the HPT system. The typical flow rate for the standard HPT ranges from 200 to 600 mL/min, the low-flow HPT injection rate can be reduced to 5 mL/min.

The flow control box in the standard HPT system does not provide stable flow injection when the rate is less than 100 mL/min. With the new low-flow control box, the injection rate can be reduced to 5 mL/min. An even lower injection rate is possible; however, screen clogging becomes much more likely when the rate is smaller than 5 mL/min. Because the low-flow control box is built as an add-on, the standard HPT system can still be used in formations that require an injection rate higher than 100 mL/min to improve the pressure signal. There is a manifold switch between the trunkline and the two flow control boxes that allows field personnel to choose in real time which flow box to use during profiling.

Figure 2-13 shows the picture of the prototype low-K HPT system built in this project. In the low-flow control box (black boxes in the picture), a de-air system is also included to remove the air entrapped in the source injection water. As discussed, low-flow profiling is particularly sensitive to entrapped air so that the injection water needs to be de-aired to improve data quality.

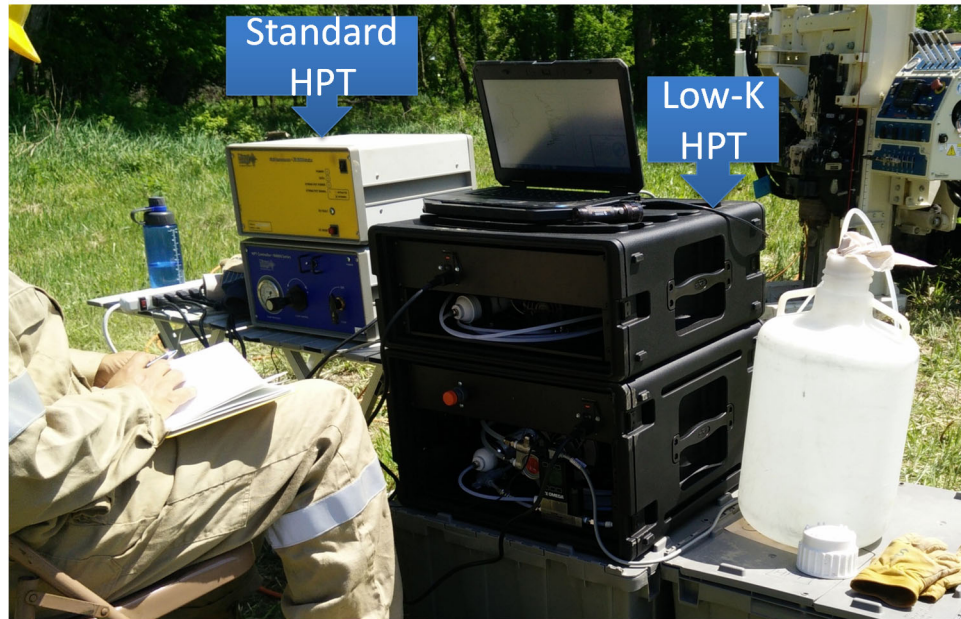


Figure 2-13. The prototype low-K HPT system.

2.3.2 Laboratory experiments

The developed low-K HPT system was first tested in a lab flow box. **Figure 2-14** and **Figure 2-14** show the schematic of the flow box and a picture of the box constructed in the lab. The sand layers are made of commercial medium grade sands (Quikrete, Medium No. 1962, #20 - #50, grain size 0.3-0.8 mm), and the silt layer is composed of the loess deposits from a quarry in the upland of Missouri River valley in Kansas City. Both the sands and silts are wet packed to avoid air trapping. Several months of natural compaction were allowed before tests were performed. Hydraulic tests in the sand layers produced a K of roughly 600 ft/d, while the cross-layer tests indicated that the K of the silt layer was about 0.1 ft/d.

Figure 2-15 shows an example injection flow rate and pressure versus time as the probe was pushed into the box during the early stage of testing. Probing depth was not plotted here as our focus was to check if the flow injection rate and pressure could be accurately measured and controlled over time. The early injection rates and pressure responses were obtained during the continuous advancement of probe to the bottom of the box (the first pressure increase indicated by the red curve). After the probe reached the bottom (injection screen 0.4 m above the bottom), the advancement ceased and flow injection was stopped, while the injection rate and pressure were continuously monitored. As expected, the pressure increase from the probe advancement and water injection gradually reduces with time. At 45 minutes after the stopping of probe advancement, with the probe still at the bottom of the flow box, water injection was turned back on to assess how the formation would respond to injection without probe advancement. As the amount of pressure increase due to flow injection only was similar to that due to both probe advancement and flow injection, our intention was that for the box we constructed in the lab, the impact of probe advancement on HPT measurement was not significant.

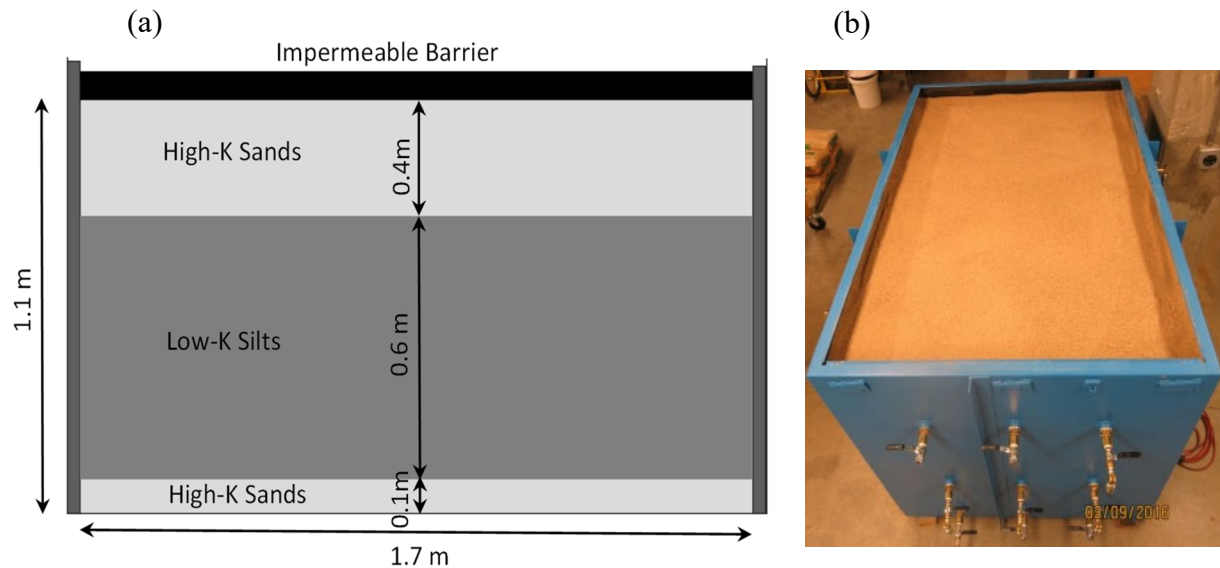


Figure 2-14. (A) schematic of the flow box for testing the low-K HPT, and (B) picture of the flow box constructed in the lab.

With the probe remaining at the bottom of the flow box, the HPT pressure was continuously monitored for two days (**Figure 2-15**). About 15 hours after the start of test, we began to see some large random spikes and drifts in the monitored pressures. Because the spikes and drifts occurred without any probe movement or flow injection, a likely explanation was that there was entrapped air in the injected water, and the entrapped air slowly moved up in the trunkline and caused random change in the pressure readings. The spikes were most likely associated with the air bubble moving through the pressure sensor or bubbles coalescing. We performed a series of injections, but the pressure spikes and drifts resumed 2 hours after injection stops. We determined that these pressure anomalies were probably due to the air entrapped in the source water. As a result, we installed a de-airing system in the flow box (see **Figure 2-12**). **Figure 2-15** shows an example injection flow rate and pressure versus time after the source water is de-aired. It can be seen that the random spikes and drifts in the monitored pressures are largely gone after de-airing the source water.

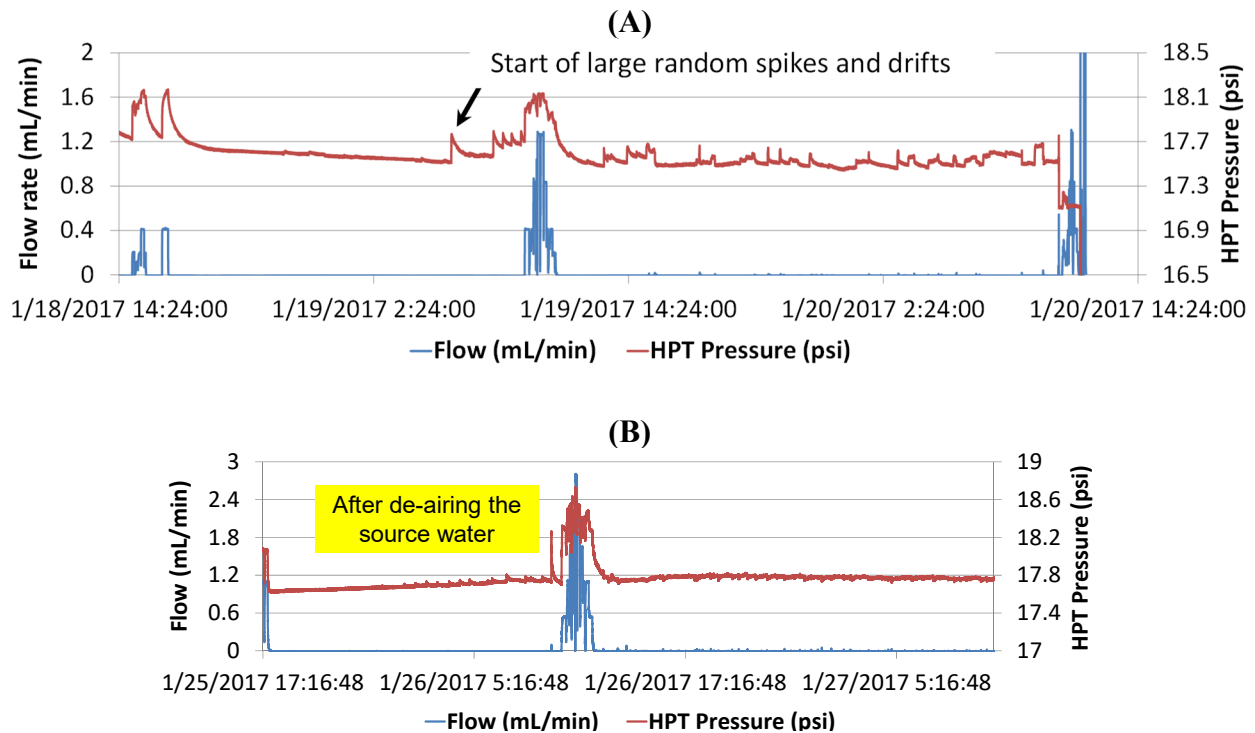


Figure 2-15. (A) injection rate and pressure versus time prior to de-airing the source water, and (B) injection rate and pressure versus time after de-airing the source water.

Figure 2-16 shows three HPT profiles in the lab flow box obtained with the new low-K HPT system. Three different injection rates were used in the silt layer, 4 mL/min for the first test profile, 0.4 mL/min for the second and 0.1 mL/min for the third (in the sands the flow rate was 100 mL/min for the first two profiles, and 0.1 mL/min in the third). The transition from sand to silt was clearly identified by the increase of EC (electrical conductivity) and HPT pressure in all profiles. The low-flow injection system performed well during the tests, and the flow rates were very stable as indicated by the flowmeter recordings. One question resulting from these test profiles, however, was that the HPT pressure did not respond proportionally with the injection rate. As we reduced the flow rate from test 1 to test 3 (left to right in **Figure 2-16**), the HPT pressure did not decrease correspondingly. The likely explanation was that the silts in the box were very soft due to little time for natural compaction and also contained a large amount of entrapped air so that the injection at the higher rate (4 mL/min) could easily cause formation alteration. Due to this concern, testing of the low-K HPT system was quickly shifted from the lab flow box to the field.

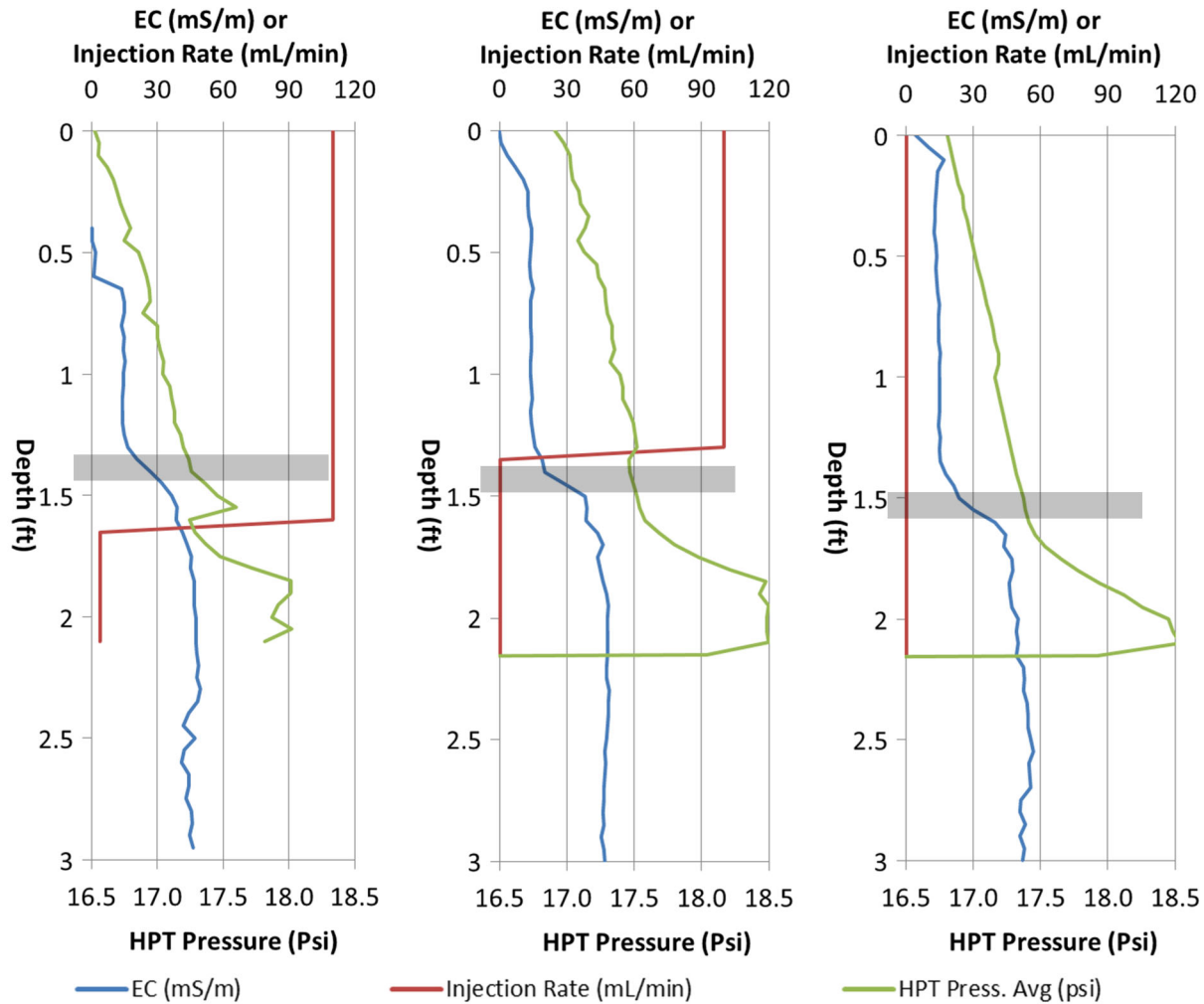


Figure 2-16. Three HPT profiles in the lab flow box obtained with the new low-K HPT system. The HPT injection rate used in the silt layer, from the left to right profile, are 4 mL/min, 0.4 mL/min, and 0.1 mL/min, respectively. The transition of the top sand layer to the middle silt layer is indicated by the increase in both EC and HPT pressure (marked by the shaded intervals).

2.4 LOW-K HPT TESTS AT GEMS

The new low-K HPT system has been tested at the Geohydrologic Experimental and Monitoring Site (GEMS), a long-term experimental area of the Kansas Geological Survey (KGS) located in the Kansas River floodplain and, a short distance (20-min drive) from KGS headquarters (**Figure 2-17**). The flow and transport characteristics of GEMS have been extensively studied (e.g., Butler, 2005; Butler et al., 2002, 2007; Schulmeister et al., 2003; Liu et al., 2012), enabling the field evaluation of HPT to be performed in a relatively controlled setting. The low-K HPT profiles are focused in the upper low-K interval (interbedded clays, silts and sands) at the site extending from the water table (typically at 5-6 m below land surface) to a depth of 12 m (base of clay interval).

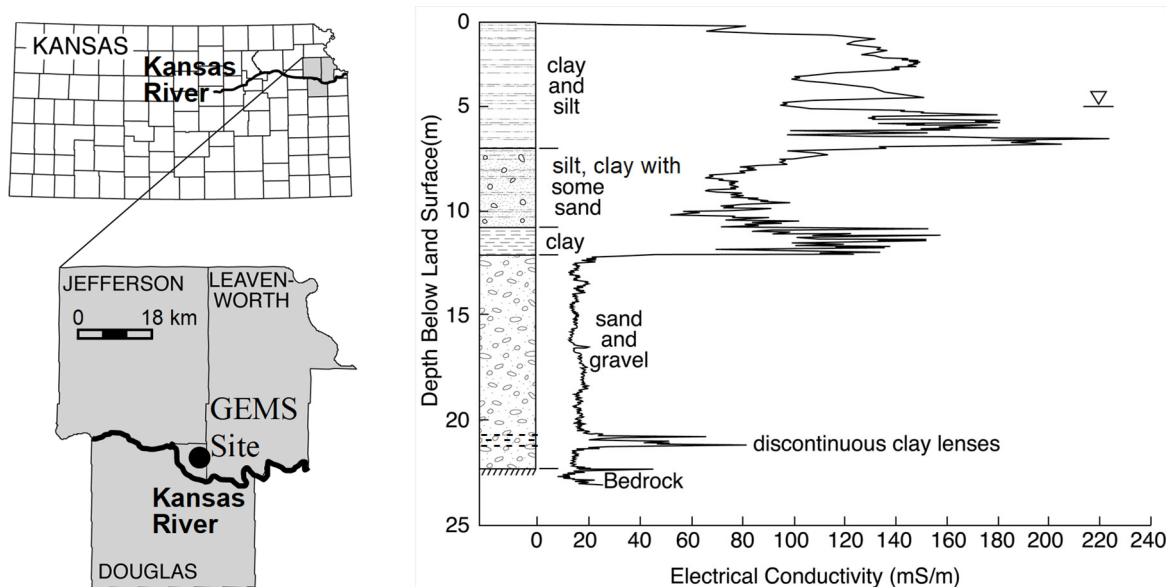


Figure 2-17. Location of GEMS and a profile of the shallow stratigraphy at the site (after Butler, 2005). The EC variation in the upper 12 m is a function of clay content. The water table is shown by the inverted triangle. Testing of the low-K HPT system was performed in the upper silt and clay layer.

A series of low-K HPT profiles were performed at GEMS during the summer of 2017. **Figure 2-18** shows a picture of the HPT operation at the site and the distribution of the profiles performed at GEMS. Totally, 23 profiles were collected in a compact area of 10 ft by 10 ft during twelve field days. Between profiles, different flow rates and probe advancement speeds were used in an effort to determine the best field procedure for conducting low-K HPT profiling.

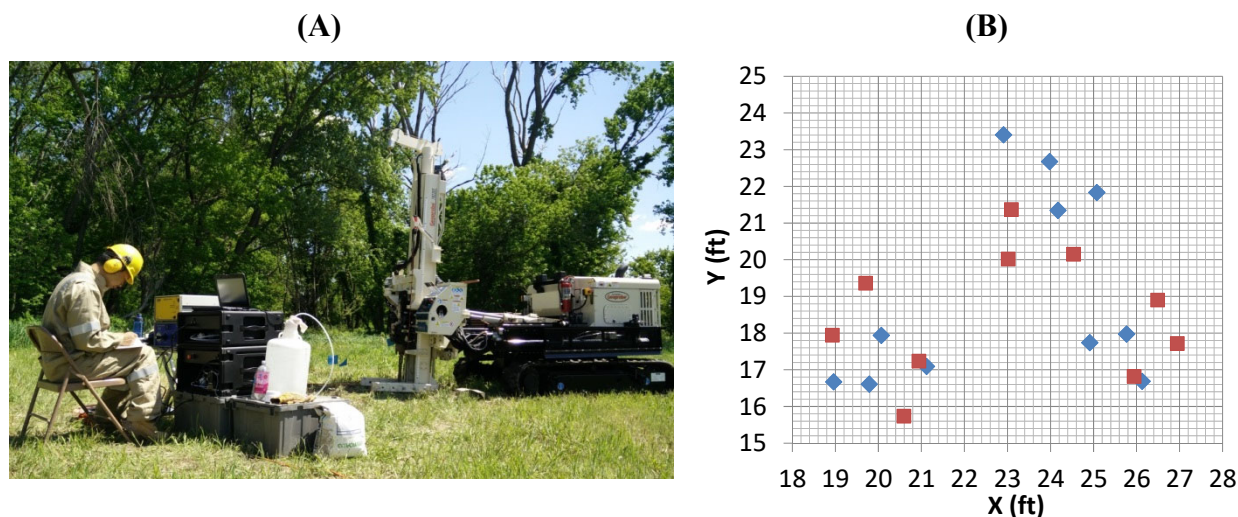


Figure 2-18. (A) Picture of low-K HPT field operation, (B) Distribution of the HPT test profiles at GEMS (different symbols indicate two separate time periods during which the profiles are performed).

Figure 2-19 compares the low-K HPT profiles between three different flow rates, 260, 20, and 5 mL/min. Overall, all the profiles show similar general patterns in both EC and HPT pressure profiles as they are relatively close to each other. Note that the HPT pressure plotted is the total amount of pressure measured by the transducer, which includes hydrostatic background pressure, water injection pressure, and pressure from materials displacement by probe advancement. A close examination of these profiles indicates that although EC and pressure generally agree with each other (higher EC corresponds to higher pressure), there are also exceptions at certain depths. For example, between depth 10 and 12 m, EC becomes elevated but remains lower than EC at depths above 6.5 m; HPT pressure, however, is higher at 10 – 12 m than that at most other depths. This local inconsistency between EC and HPT pressure can be explained by the differences in clay mineralogy (clays at different depths may have somewhat different EC characteristics), as well as more compaction of the formation at 10 – 12 m than at shallower depths (more compaction leads to lower permeability).

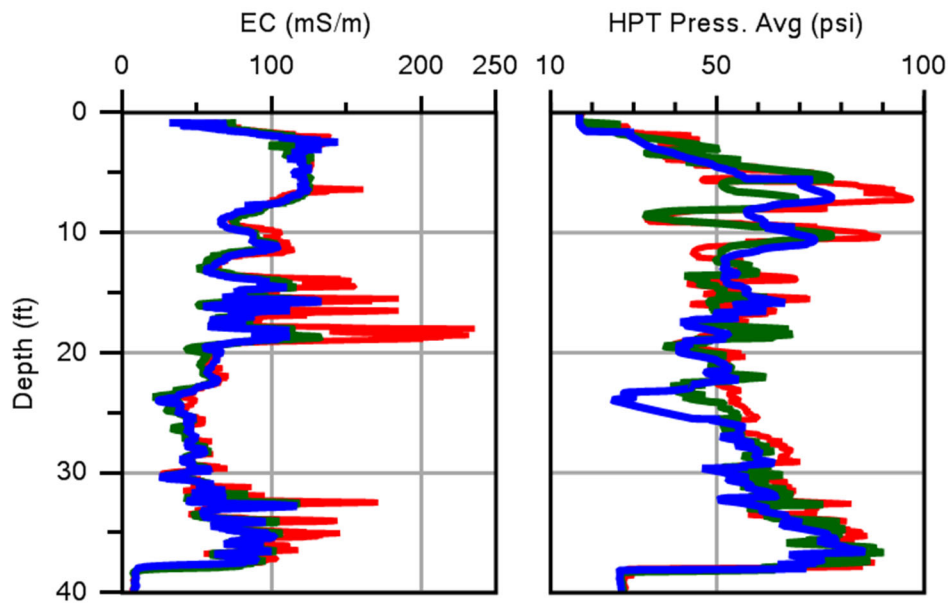


Figure 2-19. Comparison of low-K HPT profiles at three different flow rates. The red, green and blue profiles are for injection rates 260, 20, and 5 mL/min, respectively. The probe advancement speed is fixed at 2 cm/s for all three profiles.

As expected, **Figure 2-19** shows when the injection rate reduces, injection pressure reduces, which leads to a lower HPT pressure measured by the transducer. **Figure 2-20** compares the profiles between two different probe advancement speeds, 2 and 0.5 cm/s. Consistent with previous numerical simulations (**Section 2.2.3**), when the advancement speed reduces, the advancement-generated pressure reduces, which also leads to lower HPT pressure measurements. It should be pointed out that when the advancement speed reduces, the probe spends more time at each 1.5-cm measurement interval while water is continuously injected into the formation. The HPT pressure measurement plotted is the average of pressure responses over the entire duration the probe spends at each interval. Therefore, when the advancement speed is lower, the HPT

pressure consists of more elevated pressure responses from later injection time at each measurement interval. Based on **Figure 2-20**, however, the impact of longer injection time at each measurement interval is much less significant as compared to the reduction of advancement-generated pressure; as a result, the overall pressure is significantly reduced when the advancement speed decreases from 2 to 0.5 cm/s.

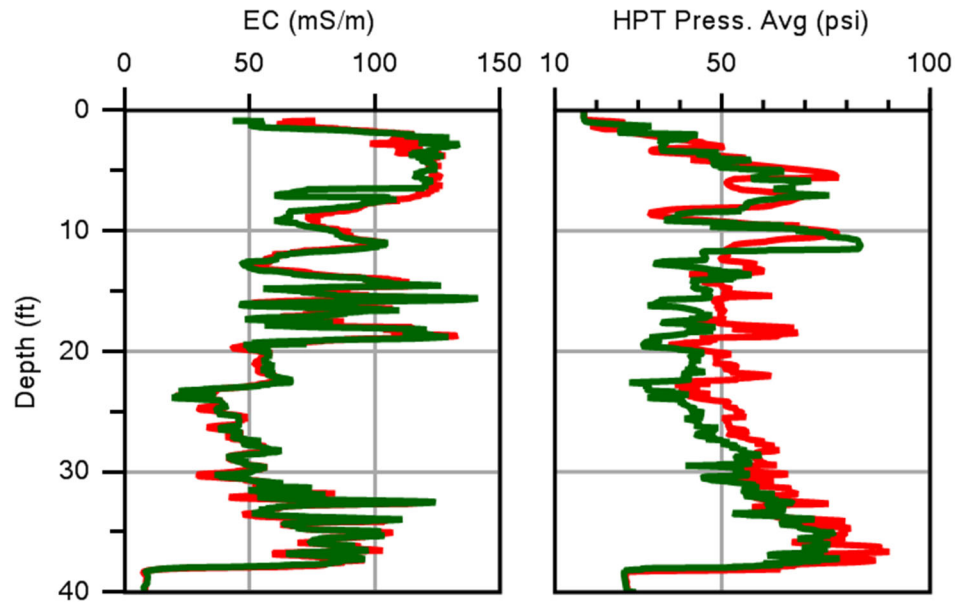


Figure 2-20. Comparison of low-K HPT profiles at two different probe advancement rates. The red and green profiles are for advancement speeds 2 and 0.5 cm/s, respectively. The water injection rate is fixed at 20 mL/min for both profiles.

For a given probe advancement speed and water injection rate, the HPT pressure profile can be converted into K estimates. **Figure 2-21** shows example K estimates from a low-K HPT profile at GEMS. Unlike standard HPT in more permeable zones, the HPT pressure in low-K settings consists of a significant portion of pressure generated from probe advancement that has to be taken into account during K estimation. In **Section 2.2.3**, we have shown that the advancement-generated pressure is dependent on both the speed of advancement and formation K. Formation S_s can also become a significant factor when it is greater than 10^{-3} m^{-1} , but for most unconsolidated sediments, it is smaller than 10^{-3} m^{-1} and can be neglected during HPT profile analysis. Using numerical simulation results from **Section 2.2.3**, for the example HPT pressure profile in **Figure 2-21**, we can estimate both water injection pressure and the pressure generated by probe advancement, as well as the corresponding K. In this example profile, the estimated advancement pressure is larger than the water injection pressure, and the lowest K estimate is $5 \times 10^{-8} \text{ m/s}$, about one order of magnitude smaller than the low end of the reported K range for standard HPT (Geoprobe Systems, 2010).

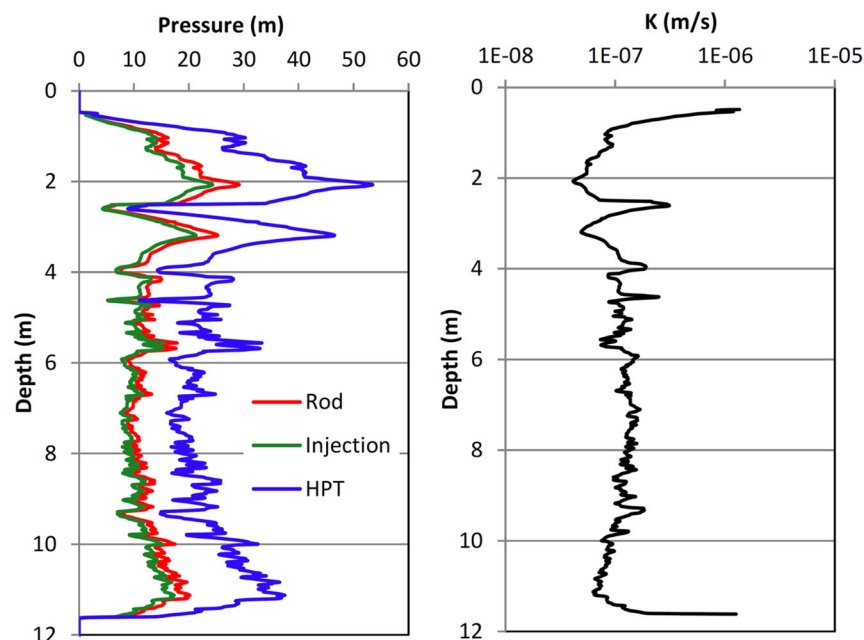


Figure 2-21. An example K profile estimated from the injection pressure and flow rate by the low-K HPT tool at GEMS. The injection rate for this profile is 5 mL/min. “Rod” represents the probe advancement pressure, estimated based on the numerical simulation results presented in **Section 2.2.3**. The injection pressure is computed as the difference between HPT pressure and probe advancement pressure.

In order to assess the accuracy of the K estimates from the low-K HPT tool, we have been performing a series of slug tests at GEMS using small-diameter direct-push installations. **Figure 2-22** shows the slug test K estimates obtained so far, as compared to the low-K HPT profile. Although the K estimates show a similar trend between HPT and slug tests, the variability showed by the slug tests is clearly much larger than that by HPT. Additional slug tests will be performed to assess if the large variability in slug test K estimates with depth is repeatable at different locations.

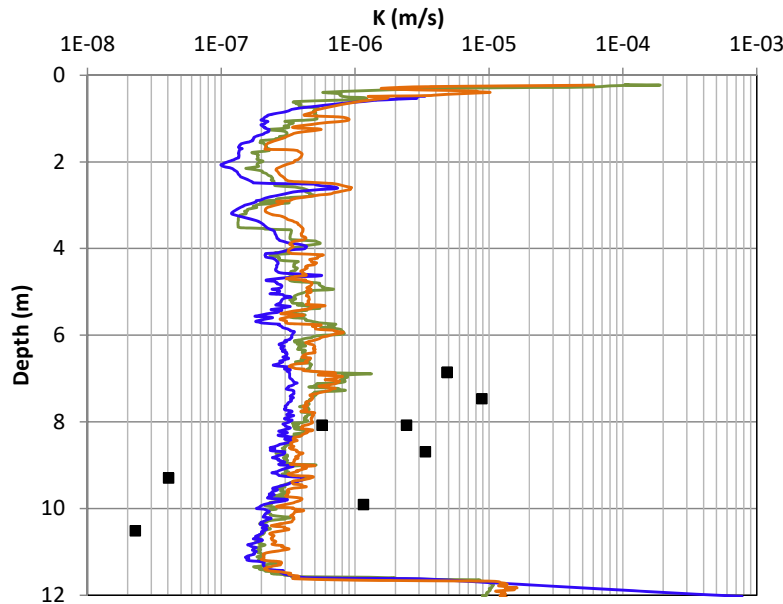


Figure 2-22. Comparison of slug test K estimates with HPT K profiles. The slug test K estimates are plotted as solid squares. Three HPT K profiles are plotted, which show a consistent overall pattern with some local variations.

Based on the field test results performed in this project, a preliminary field operating procedure for the new low-K HPT system has been drafted. This draft is provided as Appendix A of the report. A summary of different field approaches for K estimation is also provided as Appendix B of the report. That summary has been published as an online article to provide environmental site managers an easy access to various field tools that are available for characterizing their sites under different conditions.

(https://www.enviro.wiki/index.php?title=Characterization_Methods_%E2%80%93_Hydraulic_Conductivity)

2.5 A PHYSICALLY BASED EQUATION FOR ESTIMATING K

Over the past two decades, a series of DP-based field approaches (Dietrich and Leven 2009; McCall and Christy 2010; Liu et al., 2012; Maliva 2016) have been developed to characterize small-scale spatial variations in K that control groundwater flow and contaminant transport in heterogeneous aquifers. One of the most effective approaches for directly estimating K is DPIL where water is injected through the probe at flowrate (Q) while monitoring changes in pressure. **Figure 2-23** shows the HPT manufactured by Geoprobe Systems, Inc. (Salinas, KS) for DPIL logging. As the HPT probe is advanced through saturated formation material, water is injected through a port on the side of the probe while simultaneously monitoring injection rate at the surface and pressure closely behind the injection screen. The measured pressure (P_m) is the sum of hydrostatic pressure (P_h), atmospheric pressure (P_a), pressure generated by water injection (P_i), and pressure generated by displacement of aquifer material as the probe is advanced through the aquifer (P_p). HPT profiling has been recently established as an international standard practice by American Society for Testing and Materials (ASTM, D8037) under ASTM designation D8037.

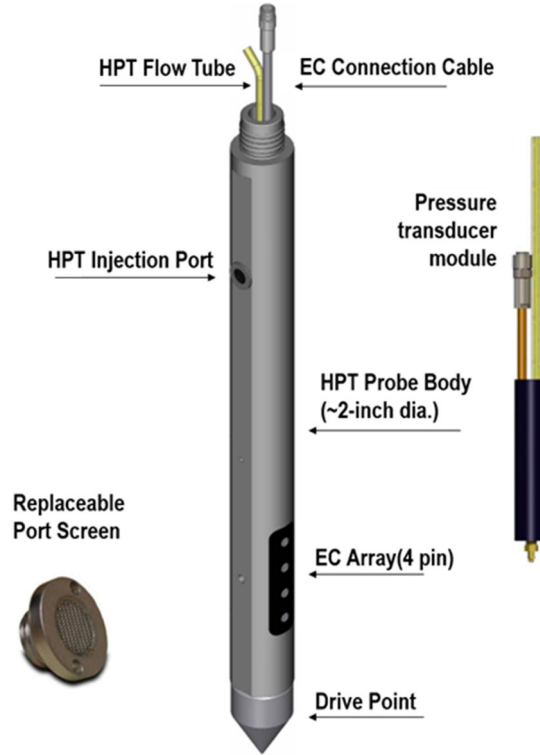


Figure 2-23. Schematic of Hydraulic Profiling Tool (HPT). During HPT profiling, water is injected through the flow tube and out of the screened port, and pressure is measured inside the connection rod right above the injection port. Formation bulk electrical conductivity is measured near the bottom of probe to provide additional information on subsurface conditions (Schulmeister et al., 2003; McCall et al., 2017).

A variety of approaches have been used to relate water injection rate and pressure data acquired during HPT profiling to spatial variations in permeability. Cho et al. (2004) proposed using the ratio of water injection rate to pressure (Q/P) as an index of K . Dietrich et al. (2008), Liu et al. (2009) and Lessoff et al. (2010) generated profiles of K versus depth using site-specific empirical relationships between Q/P and K . McCall and Christy (2010) developed an empirical relationship between Q/P_c and K measured in DP piezometers using pneumatic slug testing in an alluvial aquifer. Estimated K is calculated

$$Est. K = 21.14 \ln \left(\frac{Q}{P_c} \right) - 41.71 \quad (2-5)$$

where Q is the water injection rate through the HPT probe in mL/min and P_c is the corrected pressure, $P_c = P_m - P_h - P_a$. In Eq 2-5, K is a linear function of the natural log of Q/P_c . However, based on numerical simulations by Liu et al. (2019, Figures 5 and 8), K should be a largely linear function of Q/P_c for moderately to highly permeable settings ($K > 10^{-6}$ m/s).

In this section, we present a physically based approach for estimating K from Q and P_c data acquired during HPT profiling. This new approach is based on a series of high-resolution models

of the physical flow processes that take place during probe advance and water injection under different aquifer and HPT operation conditions (Liu et al., 2019). Average K from HPT borings is then compared to K estimates from slug tests in adjoining wells, and an empirical skin factor (C_s) is developed to correct for compaction of aquifer material near the probe.

2.5.1 Developing New Relationship for Estimating K

Section 2.2 presents the results from a series of high-resolution numerical simulations to gain a better understanding of the underlying physical processes controlling pore pressures during HPT profiling. Pressure change observed at the water injection port is the sum of injection-induced pressure and the pressure change generated by probe advance. When the probe is rapidly advanced through lower K aquifer material ($K < 10^{-6}$ m/s), high pressures are generated at the probe tip, which produces a measurable change in pressure at the injection port. If the rate of probe advance is reduced, the pressure generated at the tip is decreased and there is more time for that pressure to dissipate before the injection port pressure sensor arrives at the tip location.

The results presented in **Section 2.2** do not directly evaluate the physical processes that could lead to formation of a lower permeability zone around the HPT probe. When the HPT probe is advanced through saturated soil, high stresses near the probe tip cause local shear failure, and the plasticized soil is forced to the side, resulting in a disturbed zone surrounding the HPT probe. The disturbed zone typically has a diameter (D_d) that is 4 to 6 times the probe diameter (D_p), depending on the soil rigidity index (Burns and Mayne, 1998). In normally consolidated soil, porosity (n) within the disturbed zone can decline as the excess pore pressure is released. Assuming the solid particles displaced by the advancing probe remain within the disturbed zone, the final porosity of soil within this zone will decline by 5 to 20%, depending on initial porosity and D_d/D_p . From the Kozeny–Carman equation (Chapuis and Aubertin, 2003), K is proportional to $n^3/(1-n)^2$, which implies K may decrease by 20-50% within the disturbed zone. K can decline further if sand and clay layers are mixed by shearing of the plasticized soil.

Liu et al. (2019) summarized the impacts of Q , speed of probe advance through the aquifer material (V) and formation properties (K and S_s) on pressure at the injection port in curves relating K/S_s to $Q_p/P_p/S_s$ and $Q/P_i/S_s$ (**Figure 2-24**). Q_p is equivalent to the volume per unit time of groundwater displaced as the HPT probe is advanced through the formation material, $Q_p = V \pi D^2/4$, where D is the HPT probe diameter.

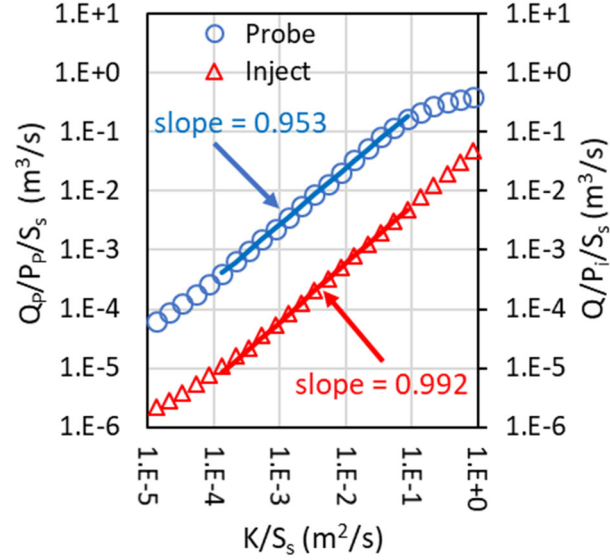


Figure 2-24. Numerical simulation results from Liu et al. (2019) relating hydraulic diffusivity (K/S_s) to pressure generated by HPT probe advance (P_p) and fluid injection through the HPT probe (P_i). Note that the summation of P_p and P_i is the pressure change at the injection port that is measured during field HPT profiling.

Figure 2-24 shows that when K/S_s is between 10^{-4} and $10^{-1} \text{ m}^2/\text{s}$, $\text{Log}(Q_p/P_p/S_s)$ and $\text{Log}(Q/P_i/S_s)$ are linear functions of $\text{Log}(K/S_s)$. In this range,

$$Q_p/P_p/S_s = \alpha_p (K/S_s)^{\beta_p} \quad (2-6a)$$

$$Q/P_i/S_s = \alpha_i (K/S_s)^{\beta_i} \quad (2-6b)$$

where $\alpha_p = 1.982$, $\beta_p = 0.953$, $\alpha_i = 0.0574$ and $\beta_i = 0.992$, based on the best fit lines matched to the simulation data (**Figure 2-24**). Rearranging and solving for the corrected pressure (P_c)

$$P_c = P_p + P_i = Q_p / \{ \alpha_p * S_s * (K/S_s)^{\beta_p} \} + Q / \{ \alpha_i * S_s * (K/S_s)^{\beta_i} \} \quad (2-7)$$

Figure 2-25 shows the relationship between K and P_c at different values of S_s , probe speed V , and Q , for varying P_c . For the considered ranges of parameter values, S_s does not have a measurable impact on the K vs P_c relationship. When $Q \geq 200 \text{ mL/min}$, the impact of V is also negligible. However, for $Q \leq 50 \text{ mL/min}$, varying V has a small but measurable impact. In contrast, varying Q between 50 and 600 mL/min has a substantial impact on the K vs P_c relationship. Most interestingly, the slope of K versus P_c does not change substantially with Q .

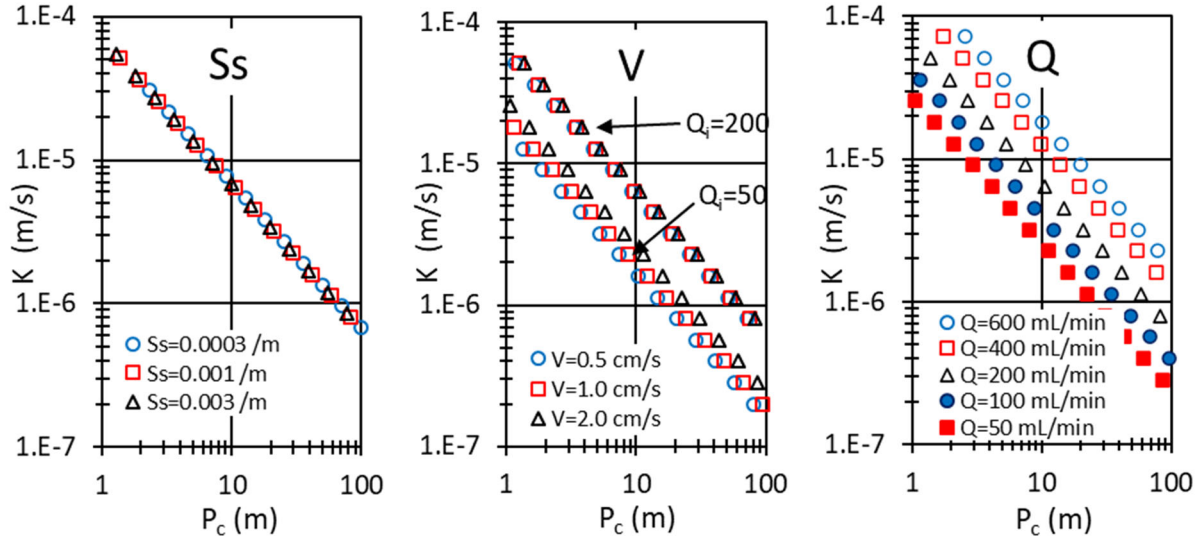


Figure 2-25. K as a function of corrected pressure (P_c) for varying specific storage (S_s), probe speed (V) and injection rate (Q). In all three plots, the base case parameter values are $S_s=0.001/\text{m}$, $V=2 \text{ cm/s}$, and $Q=200 \text{ mL/min}$. In the left plot, S_s is varied between 0.0003 and 0.001 /m; in the right plot, Q is varied between 50 and 600 mL/min. In the middle plot, the probe velocity is varied between 0.5 and 2 cm/s at two different flow rates (200 and 50 mL/min).

K cannot be solved for directly from Eq 2-7 for a set of given P_c , S_s , Q and Q_p values. However, K can be found using an iterative procedure where K values are continuously adjusted until the computed P_c matches the measured value. Instead of this iterative procedure, we propose the use of Eq 2-8 to calculate K from HPT data, using empirical coefficients, C_1 , C_2 and C_3 , that provide results equivalent to Eq 2-7,

$$K = (C_1 V D^2 + C_2 Q) P_c^{C_3} \quad (2-8)$$

S_s was not included in Eq 2-8 since it did not have an appreciable impact on K. To estimate C_1 , C_2 and C_3 , Eq 2-7 is used to estimate P_c for a range of S_s , V , Q and K. S_s was varied between 0.0003 and 0.003 m^{-1} , based on published S_s values for unconsolidated aquifers (Freeze and Cherry, 1979) and S_s values measured in triaxial tests of aquifer material at Tulsa, OK (Borden et al., submitted). These data were sorted to eliminate any parameter combinations that would result in pressures outside the range that can be accurately measured with currently available equipment (0.7 to 70 m head or 1 to 100 psi) resulting in over 1700 unique combinations of K, P_c , Q , V and S_s . The solver function in Microsoft Excel was used to search for values of C_1 , C_2 and C_3 that minimized the normalized root mean squared error (NRMSE) between the reference K and estimated values by Eq 2-8.

Best fit values of C_1 , C_2 and C_3 are presented in Eq 2-9a for metric units (K in m/s, P in m of hydraulic head) and Eq 2-9b for English units (K in ft/d, P in psi),

$$K[\text{m/s}] = (4.061\text{E-}07 V[\text{cm/s}] D^2[\text{cm}] + 4.262\text{E-}07 Q[\text{mL/min}]) / P[\text{m}]^{1.017} \quad (2-9a)$$

$$K[\text{ft/d}] = (0.1235 V[\text{cm/s}] D^2[\text{cm}] + 0.119 Q[\text{mL/min}]) / P[\text{psi}]^{1.017} \quad (2-9b)$$

Figure 2-26 shows a comparison between the reference K in Eq 2-7 and estimated K using Eq 2-9. Overall, Eq 2-9 provides an excellent match with the reference K values. The NRMSE of estimated K is less than 2%, which is considered excellent given that K varies by 3 orders of magnitude.

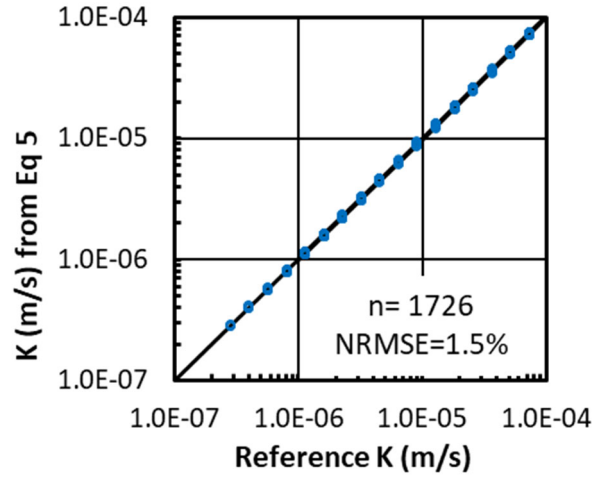


Figure 2-26. Comparison of reference K with estimates generated by Eq 2-9.

Note that Eq 2-9 provides an estimate of aquifer K when there is no reduction of K in the measurement domain by HPT probe advance. However, in field practice, as the formation is pushed aside and compacted during probe advance, reduction of K is likely in the formation close to the probe (Liu et al., 2012). An empirically derived efficiency factor (E) is included in Eq. 2-10 to account for permeability loss in the disturbed zone surrounding the HPT probe.

$$K[\text{m/s}] = E (4.061\text{E-}07 V[\text{cm/s}] D^2[\text{cm}] + 4.262\text{E-}07 Q[\text{mL/min}]) / P[\text{m}]^{1.017} \quad (2-10a)$$

$$K[\text{ft/d}] = E (0.1235 V[\text{cm/s}] D^2[\text{cm}] + 0.119 Q[\text{mL/min}]) / P[\text{psi}]^{1.017} \quad (2-10b)$$

As presented below, E is estimated to be 2.02 for unconsolidated settings across four test sites.

2.5.2 Field Evaluation of K Estimation Relationships

The new K estimation approach is evaluated by comparing HPT results to slug test results from adjoining monitor wells, and to develop the empirical skin factor C_s to account for permeability reduction due to compaction of aquifer material during HPT probe advance.

Slug tests were conducted in 2-inch PVC monitor wells installed by hollow stem auger with a sand pack. The slug test K was obtained by instantaneously adding or removing a weighted slug and measuring head response with a pressure sensor connected to a data logger. Results are analyzed using the Bouwer and Rice (1976) method. Replicate slug-in and slug-out tests were conducted on each well. When the water table intersected the well screen, only the slug-out test

results were used for analysis. When there are multiple slug tests available from a single well, the arithmetic mean is computed and compared to the HPT results.

HPT Profiles of K versus depth were performed at 23 locations within 3 ft of an existing slug test well at four sites: Jacksonville, Selma, Greenville, and Tulsa. At each location, the 1.75-inch HPT Probe (Geoprobe K6050) with Wenner array was advanced at a relatively constant rate of $V=2$ cm/s. Q was held approximately constant for each boring, but Q was varied between borings ($Q=100$ to 500 ml/min) to maintain P_c within a measurable range. Data was acquired using the HPT Flow Controller (K6300), Field Instrument (FI6000) and HPT Acquisition Software. P_c was calculated as the total HPT measured pressure minus the sum of P_h and P_a . P_a was measured using the HPT probe with $Q=0$ at the land surface immediately prior to the start of each boring. P_h was calculated from the measured depth to water in the adjoining monitor well. Profiles of K versus depth were calculated using Eq. 2-10, generating individual K estimates at 0.05 ft intervals. For comparison with the slug test results, the vertically averaged K is calculated as the arithmetic average of the HPT K values over the saturated screened interval of the adjoining slug test well.

Results of the slug tests and HPT profiling are summarized in **Table 2-1** assuming no permeability loss in the disturbed zone ($E = 1.0$). The ratio of vertically averaged HPT K to slug test K (K_{HPT}/K_{slug}) varied from 0.11 to 1.66 with a mean of 0.49 (std. dev. =0.37, 99% conf. limit = 0.28 to 0.71) indicating that on average, K_{HPT} is about half of K_{slug} assuming $E=1.0$. The slope of $\ln K_{HPT}$ versus $\ln K_{slug}$ was not significantly different from 1.0 at the 95% level (Borden et al. 2020). Consequently, the simpler linear relationship, $K_{slug} = E K_{HPT}$ where $E = 1/0.49=2.02$, is adopted here.

Table 2-1. Summary of Slug Test and HPT Results.

Site Location	Well #	Screen Length (ft)	Slug Test K (ft/d)	HPT Boring	Average Q (ml/min)	Average V (cm/sec)	Average HPT K (ft/d)	K_{HPT} / K_{slug}
Jacksonville, FL	MW-7	10	7.1	HPT-2	255	1.7	2.7	0.38
	MW-13	10	2.6	HPT-1	260	2.2	4.3	1.66
Selma, NC	MW-1	5	19.5	MW-1	423	1.3	3.6	0.19
	MW-4	5	17.9	MW-4	401	0.5	4.5	0.25
	MW-17	10	11.6	MW-17	404	0.6	5.4	0.47
	MW-19	10	35.9	MW-19	459	0.5	7.5	0.21
	MW-20	10	73.7	MW-20	420	0.5	8.1	0.11
Greenville, NC	W-8	15	49.5	W-8	189	0.4	17.7	0.36
	W-8	15	49.5	W-8-3	421	0.4	45.5	0.92
	W-12	10	107.7	W-12	407	0.4	19.2	0.18
	W-17	9.7	32.5	W-17	436	0.9	23.2	0.71
	W-53	10	32.2	W-53	456	0.9	26.8	0.83
Tulsa, OK	MW-6	10	1.85	HPTS-01	249	1.9	1.3	0.71
	MW-8	2.5	0.85	HPTS-02	247	2.9	0.6	0.71
	MW-9	1	1.48	HPTS-02	247	2.9	0.8	0.56
	MW-7	10	2.84	HPTS-03	226	1.9	0.7	0.25
	MW-1	10	2.48	HPTS-09	235	3.1	0.6	0.24
	MW-2	10	1.23	HPTS-10	236	1.3	0.5	0.37
	MW-3	10	3.10	HPTS-12	232	2.1	0.6	0.20
	MW-4	10	4.98	HPTS-13	254	1.4	2.7	0.54
	8-20	15	2.38	HPTS-14	270	2.9	2.6	1.08
	MW-5	10	2.86	HPTS-15	231	1.8	0.7	0.23
	MW-5	10	2.86	HPTS-16	224	1.8	0.6	0.20

Figure 2-27 shows a comparison of K measured by slug tests in monitor wells to vertically averaged K estimated using Eq 2-10 with $E = 2.02$. The average K generated by HPT provided an excellent match to the slug test results. The NRMSE of 67% is considered excellent, given the natural variability in slug test results and that the slug test and HPT profiles were located about 3 ft apart.

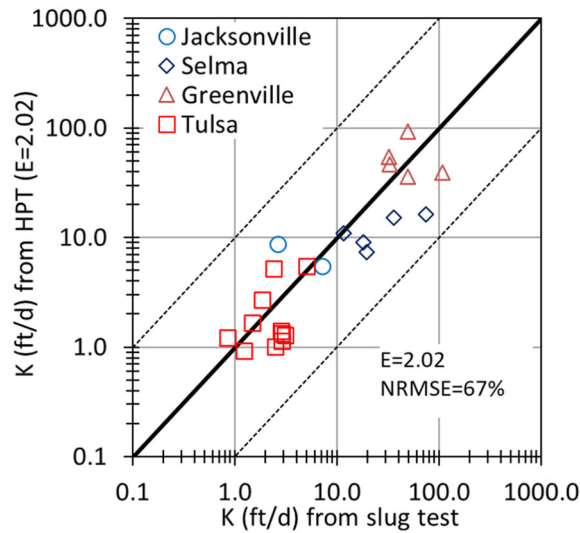


Figure 2-27. Comparison of K estimates from slug tests and HPT profiling using Eq 2-10. The HPT K is vertically averaged over the saturated screened interval of the adjoining slug test well.

2.5.3 Dependence of P_c on Q and V

In both high and low K formations, our ability to reliably measure pressure generated by the HPT tool is the key to accurate K measurement. Temporal variations in atmospheric pressure, shock waves generated by hydraulic hammering, and other factors such as regional groundwater pumping, can all contribute to background noise in HPT pressure measurement, making it difficult to reliably determine P_c within ± 0.5 psi (± 0.35 m). In high K formations, pressure generated by probing is often less than levels that can be reliably measured (1 psi). In lower K formations, pressures in excess of the maximum measurable pressure (100 psi) can be generated due to fluid displaced by the advancing HPT probe and fluid injection. The allowable operating range for K could potentially be expanded by adjusting the HPT rod speed and the injection rate Q. **Figure 2-28** shows the pressure generated by the HPT probe at speeds of $V=2$ and 0.5 cm/s and Q between 50 and 500 mL/min using Eq 2-10 with $E=2.02$. At $V=2$ cm/s and $Q=500$ mL/min, P exceeds 100 psi for $K < 1.2$ ft/d. However, by reducing Q to 50 mL/min, K values down to 0.21 ft/d could be measured. By reducing the probe speed to 0.5 cm/s, K is further extended to 0.14 ft/d. However, reducing the probe speed would greatly increase probing time, so it is typically not recommended unless K is less than 1 ft/d. A significant advantage of our new K estimation equation over previous approaches is that it explicitly incorporates the impact of probing speed that becomes more important when Q is small in lower K settings.

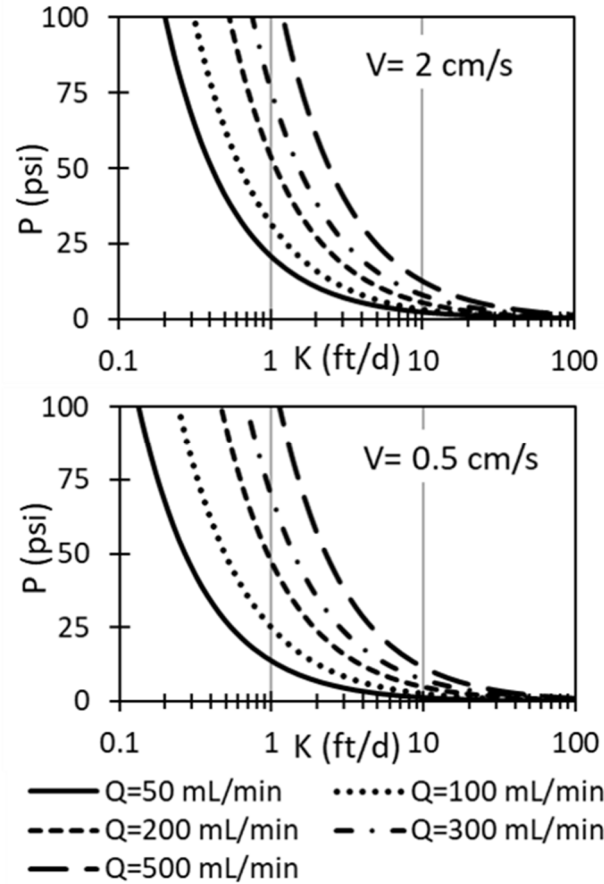


Figure 2-28. Pressure generated for varying Q and K at V=2 and 0.5 cm/s.

2.5.4 Summary

A physically based equation is presented for estimating hydraulic conductivity from data generated during HPT profiling. The new K estimation equation (Eq 2-10) is developed using results from high-resolution numerical simulations spanning a range of formation properties (K and S_s) and HPT operating parameters (advance speed and injection rate). Compared to previous work (Dietrich et al., 2008; McCall and Christy, 2010), our approach explicitly addresses the effect of HPT probe advance speed, which becomes important in less permeable settings ($K < 1$ ft/d) with $Q < 50$ mL/min. When K is lower, the pressure generated by HPT probe advance and water injection can exceed the limit of the pressure sensor, while reducing the injection rate and probe advance speed can reduce the pressure and extend the measurable K range.

The new K estimation equation is evaluated by comparing HPT K estimates to slug test results from 23 wells located at four different field sites. Assuming $E = 1.0$, the average ratio of K_{HPT} / K_{slug} was 0.49 (std. dev. = 0.37, 99% conf. limit = 0.28 to 0.71), consistent with reduced K in the disturbed zone surrounding the HPT probe. Lower K in the disturbed zone is most likely due to soil compaction and/or shear induced mixing of clayey and sandy layers.

Using the best fit hydraulic efficiency factor (E) of 2.02, the HPT results match the slug tests very well. The normalized root mean square error is 67%, indicating the high accuracy of our equation for K estimation under field conditions. Additional research is required to understand the impacts of aquifer characteristics on E .

3.0 SITE CHARACTERIZATION AND NUMERICAL MODEL DEVELOPMENT

Objective: Determine if high-resolution solute transport models, primarily calibrated using DP tools, can provide satisfactory predictions of contaminant mass transfer between high and low K zones.

Two sites were selected for detailed characterization and high-resolution numerical modeling – Air Force Plant 3 (AFP3) in Tulsa, OK and Former Naval Training Center (NTC) Orlando, Operable Unit 2 (OU2) in Orlando, FL.

3.1 AIR FORCE PLANT 3

AFP3 is located northeast of Tulsa, Oklahoma, adjacent to the Tulsa International Airport. Groundwater impacts are believed to result from two vapor degreasers located within or near and upgradient building. The trichloroethene (TCE) vapor degreaser was located sub-grade within a sump while the former 1,1,1-trichloroethane (TCA) degreaser was above grade. Environmental investigations have identified CVOCs and 1,4-dioxane (1,4-D) plumes originating from the former vapor degreaser locations and migrating east-northeast in the direction of groundwater flow towards Mingo Creek.

The research site for this project is a pilot test area where emulsified vegetable oil (EVO) was injected to simulate reductive dechlorination of CVOCs and cometabolic bioremediation of 1,4-D. EVO was injected to simulate conversion to TCE to 1,2-cis-dichloroethene (cDCE), vinyl chloride (VC) and ethene. **Figure 3-1** shows the location of the pilot test area in relation to the CVOCs and 1,4-D plume.

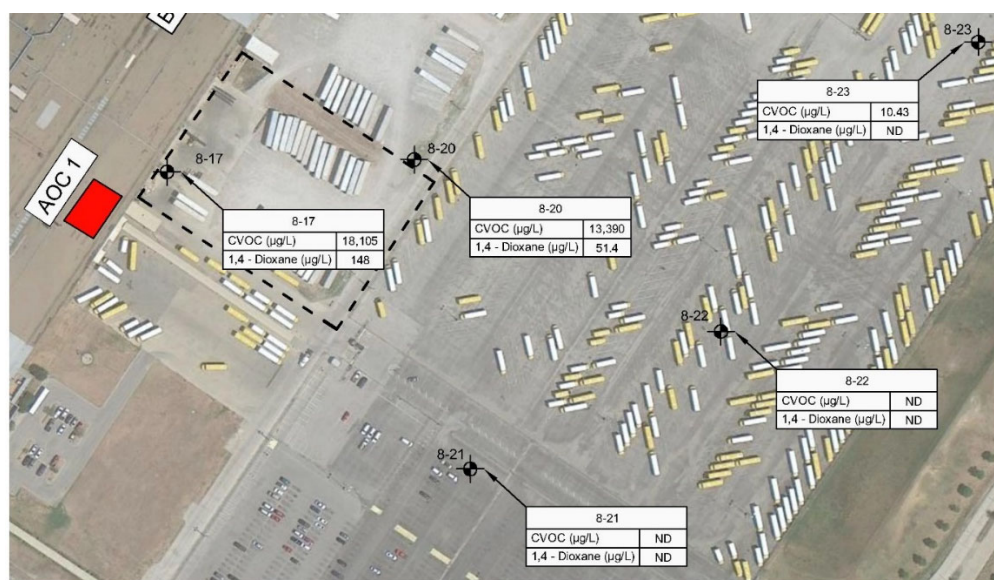


Figure 3-1. Location of pilot test area (dashed box) in relation to CVOCs and 1,4-D plumes.

Shallow groundwater at the site is present in terrace deposits comprised of cohesive silty clays with intermittent sand, silty sand, and clayey silt lenses, overlying the Nowata Shale formation, a black clay shale that is encountered at depths of 20 to 25 feet below ground surface (ft bgs). Depth to groundwater is approximately 10 ft bgs. Groundwater typically flows in an east-northeastern direction towards Mingo Creek Based with an average hydraulic gradient of ~0.01 ft/ft (AECOM, 2012).

3.1.1 AFP3 EVO Pilot Test

In August 2013, a 45-ft long permeable reactive barrier (PRB) was constructed consisting of six injection wells (IW-1, IW-2, IW-3, IW-4, IW-5 and IW-6) installed 7.5 ft on center (**Figure 3-2**). The wells were installed using a hollow stem auger drill rig and constructed of 2" diameter PVC well materials with a 10 ft long, 0.010-slot screen from 10 to 20 ft bgs. A series of monitoring wells were also installed upgradient and downgradient of the barrier to evaluate barrier performance and methane production over time. Four monitoring wells (MW-2, MW-3, MW-4 and MW-5) were positioned 10, 20, 30 and 40 ft downgradient from the center of the barrier along the general direction of groundwater flow. Two monitoring wells (MW-6 and MW-7) were installed 20 ft downgradient of the injection wells IW-1 and IW-6; and one monitoring well (MW-1) was positioned 15 ft upgradient of the barrier. The monitoring wells were also constructed of 2" diameter PVC well materials with a 10 ft long, 0.010-slot screen from 10 to 20 ft bgs. All wells were finished with flush mount surface completions.

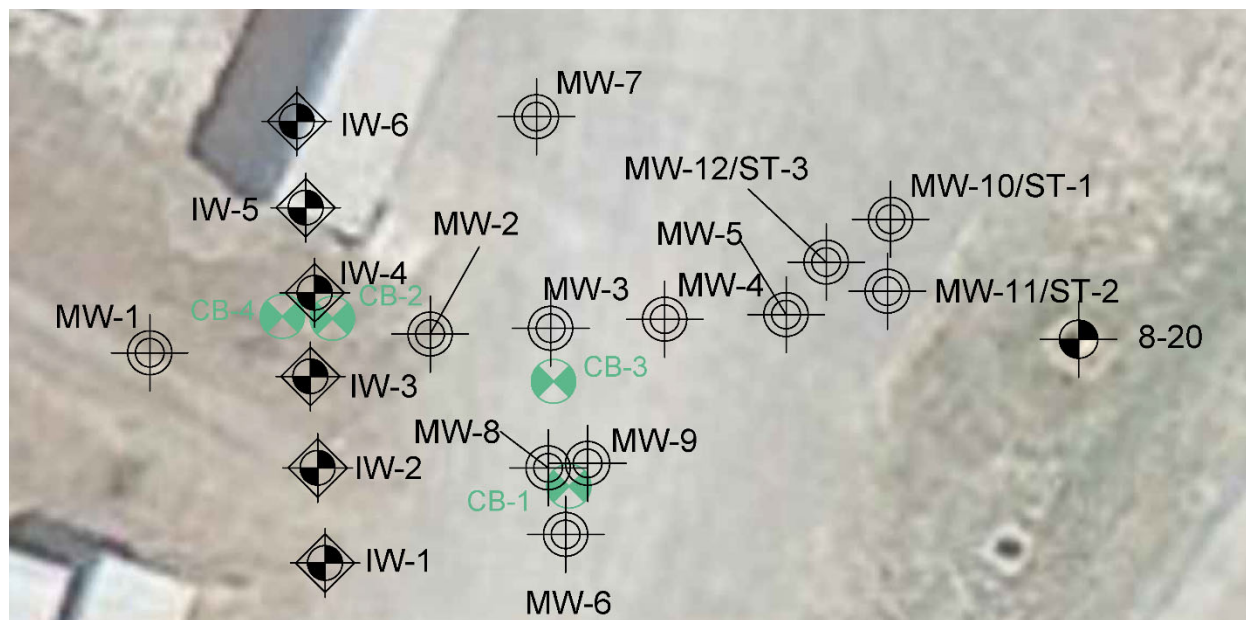


Figure 3-2. Location of monitor and injection wells in the vicinity of EVO pilot test.

A total of 156 gallons of concentrated EVO (EOS-LS™; EOS Remediation, LLC) diluted with approximately 168 gallons of potable water was evenly distributed into the six injection wells. An additional 80 gallons of potable chase water was injected into each well-except injection well IW-5-after substrate addition to clean out the injection wells and well screens and drive residual substrate into the formation. IW-5 may have been damaged during construction resulting in very

low injection flowrates during the substrate injection so only 50 gallons of chase water could be injected into IW-5. 19 liter (L) of a commercial dechlorinating bacterial consortium (BAC-9™; EOS Remediation, LLC) was evenly distributed into the injection wells and chased with about 9 gallons of anaerobic water to increase abundance of *Dehalococcoides* sp. (DHC).

The injection and monitoring wells were periodically sampled over the next several years for CVOCs, light hydrocarbon gases (methane, ethane, ethene), bromide and geochemical indicator parameters.

3.1.1.1 Groundwater Flow

Groundwater elevations in monitoring wells in line parallel to groundwater flow (MW-1, MW-2, MW-3, MW-4, MW-5 and 8-20) are shown in **Figure 3-3** for seven sampling events between August 2013 and June 2015. The groundwater table shifted up and down over about a 1 ft interval and maintained a relatively constant hydraulic gradient of 0.28% (standard deviation=0.09%).

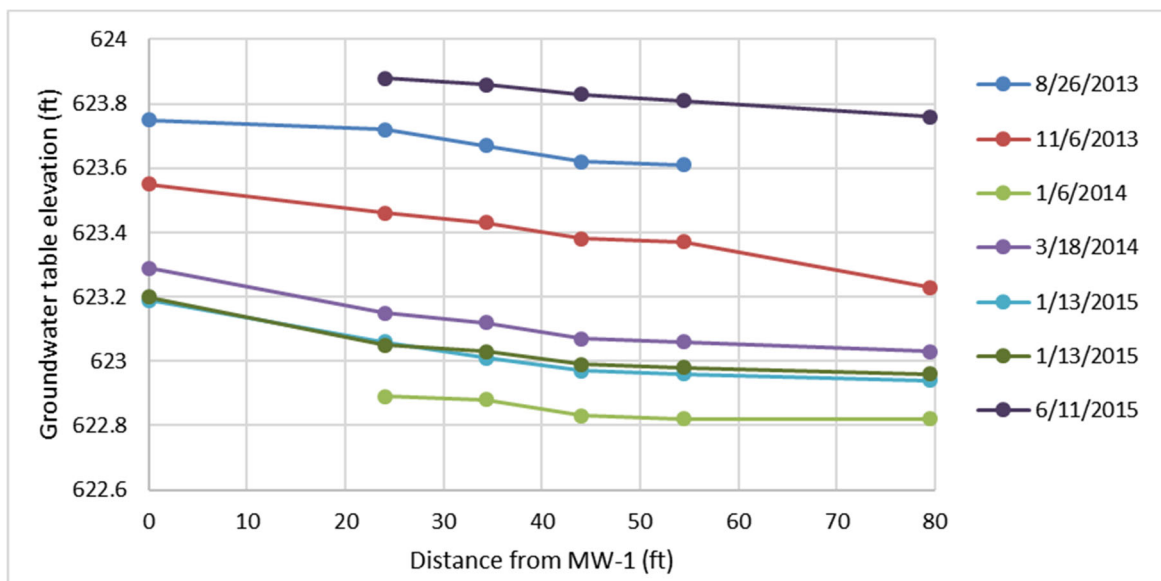


Figure 3-3. Water table elevation during seven monitoring events in line extending from MW-1 to 8-20.

3.1.1.2 Non-Reactive Tracer Test Results

During the substrate injection, 4 lbs of sodium bromide (NaBr) was mixed with the diluted substrate resulting in an average concentration of approximately 500 mg/L NaBr. **Figure 3-4** shows Br concentrations measured in injection and monitoring wells over time. Br concentrations in injection well IW-4 spiked immediately after injection, then slowly declined. As expected, Br concentrations gradually increased in downgradient wells, then slowly decreased as the Br pulse migrated through the aquifer. However, MW-2 (10 ft downgradient) responded more slowly than MW-3 (30 ft downgradient), indicating that MW-2 was somewhat isolated from the main groundwater flow system.

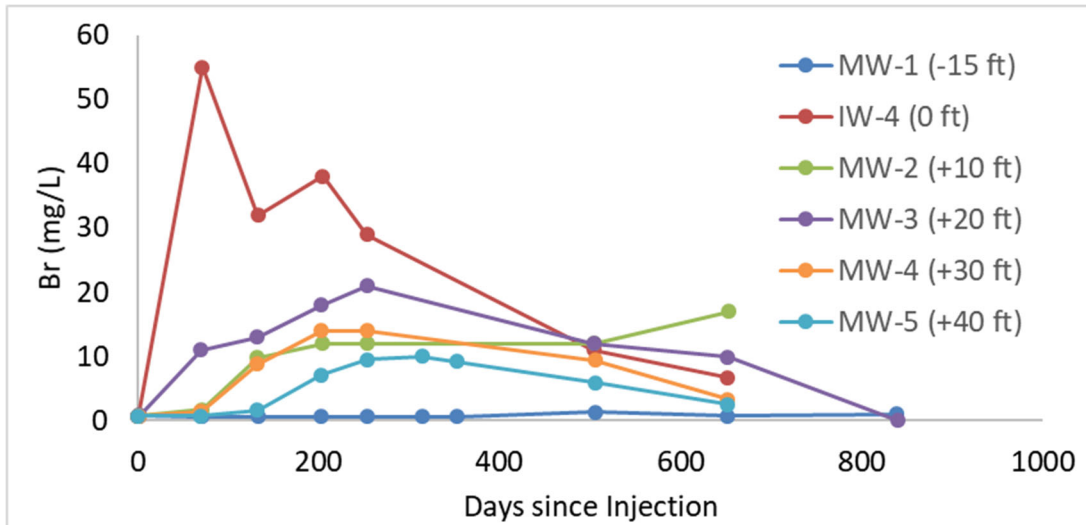


Figure 3-4. Bromide concentration versus time in injection and monitoring wells.

3.1.1.3 CVOC Results

Figure 3-5 shows TCE, cDCE, VC and ethene concentrations versus time in injection and monitoring wells. Addition of EVO and the bioaugmentation culture was very effective in stimulating Enhanced Reductive Dechlorination (ERD), with nearly complete removal of TCE and extensive production of ethene in all injection wells (only data for IW-4 presented). However, TCE declined much more slowly in the downgradient wells. This is not believed to be due to incomplete biotransformation within the EVO treated zone since there was nearly complete conversion to ethene in the injection wells. Instead it appears that TCE is being released from lower permeability zones, causing TCE concentrations to decline more slowly in downgradient wells.

Figure 3-6 shows Chlorine Number (Cl#) and total ethenes versus time in injection and monitoring wells. Total ethenes is calculated

$$\text{Total ethenes} = [\text{PCE}] + [\text{TCE}] + [\text{DCE}] + [\text{VC}] + [\text{ethene}]$$

where [] indicates the molar concentration. Cl# is calculated

$$\text{Cl\#} = (4 * [\text{PCE}] + 3 * [\text{TCE}] + 2 * [\text{DCE}] + 1 * [\text{VC}]) / \text{total ethenes}$$

Upgradient of the PRB in MW-1, Cl# remains constant at 3.0 indicating no significant biotransformation. Cl# declines to near zero in the injection wells (only data for IW-4 shown), indicating essentially complete conversion to ethene. Overtime, total ethenes in IW-4 decline, presumably due to conversion of ethene to methane or carbon dioxide (CO₂). Similar to TCE, total ethenes decline more slowly in downgradient wells, presumably due to back diffusion of TCE out of lower K zones. When total ethene concentrations are fit to an exponential function, effective 1st order decay rates decrease with increasing distance downgradient from 1.49/yr in IW-4 to 0.11/yr at 40 ft downgradient in MW-5.

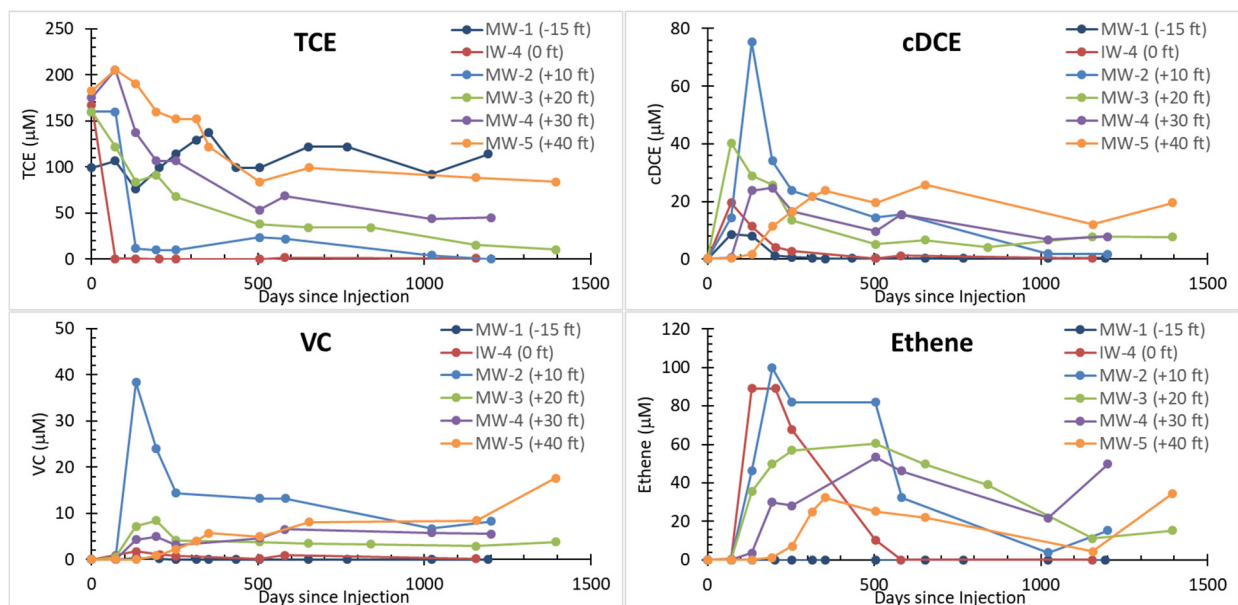


Figure 3-5. TCE, cDCE, VC and ethene concentration versus time in injection and monitoring wells.

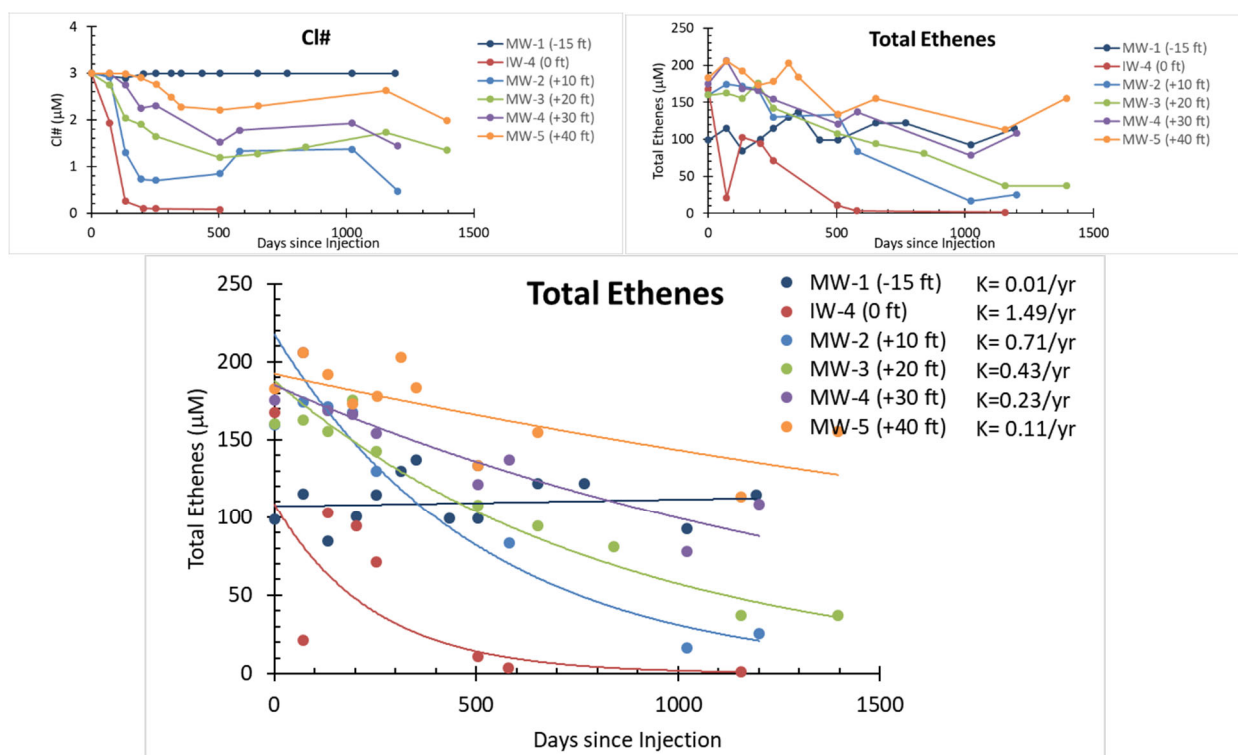


Figure 3-6. Chlorine number (Cl#) and total ethenes versus time in injection and monitoring wells.

3.1.2 AFP3 Site Characterization

The pilot test area was intensively characterized to define spatial variations in aquifer properties and the impact of these variations on transport of non-reactive tracers and groundwater contaminants. Work completed included the following.

- Installation of cone penetrometer test (CPT) borings to measure spatial variations in the physical properties of the aquifer material;
- Installation of a series of HPT borings to measure spatial variations in K;
- Collection of three undisturbed cores for laboratory measurement of K and consolidation;
- Collection of continuous cores to measure vertical changes in lithology and CVOC concentrations; and
- Slug tests in multiple wells to measure the K of both high and low K zones;

3.1.2.1 Cone Penetrometer Test (CPT) Borings

Thirteen CPT borings were advanced in July 2017, either adjacent to previous soil or HPT borings or in other areas of the site to improve the understanding of the site lithology. For the CPT borings, a Type 2 piezocone with 35.7 mm diameter with a cross-sectional area of 10 cm² and sleeve area of 150 cm² was used. The net area ratio (a_n) was 0.8 and the depth of boring was ~25 ft. bgs. The CPT measured three soil parameters (i.e. cone tip pressure – q_c , sleeve friction – f_s , and porewater pressure – u_2) while the rod was advancing at 2.5 cm/s. For each CPT boring, dissipation tests were done at different depths to collect the depth specific permeability information. Soils were classified using **Figure 3-7**.

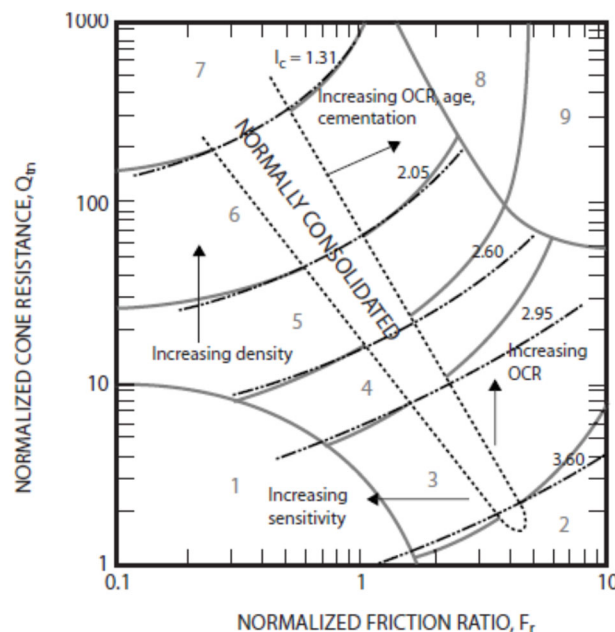


Figure 3-7. Normalized CPT SBT chart. OCR stands for over consolidation ratio. (Robertson, 1990; Robertson and Cabal 2010).

Figure 3-8 shows a typical CPT boring log. At CPT-04, the CPT borings indicate the aquifer material is primarily silt, silty sand and sandy silt. From 10 to 15 ft bgs, the material is classified as silt (clayey silt to silty clay) consistent with the low tip stress and sleeve resistance and increasing pore pressure due to probe advancement. From 15 to 22 ft bgs, the aquifer contains interbedded layers of sand (silty sand to sandy silt) and silt, indicated by the intermediate tip stress and sleeve resistance and lower pore pressure.

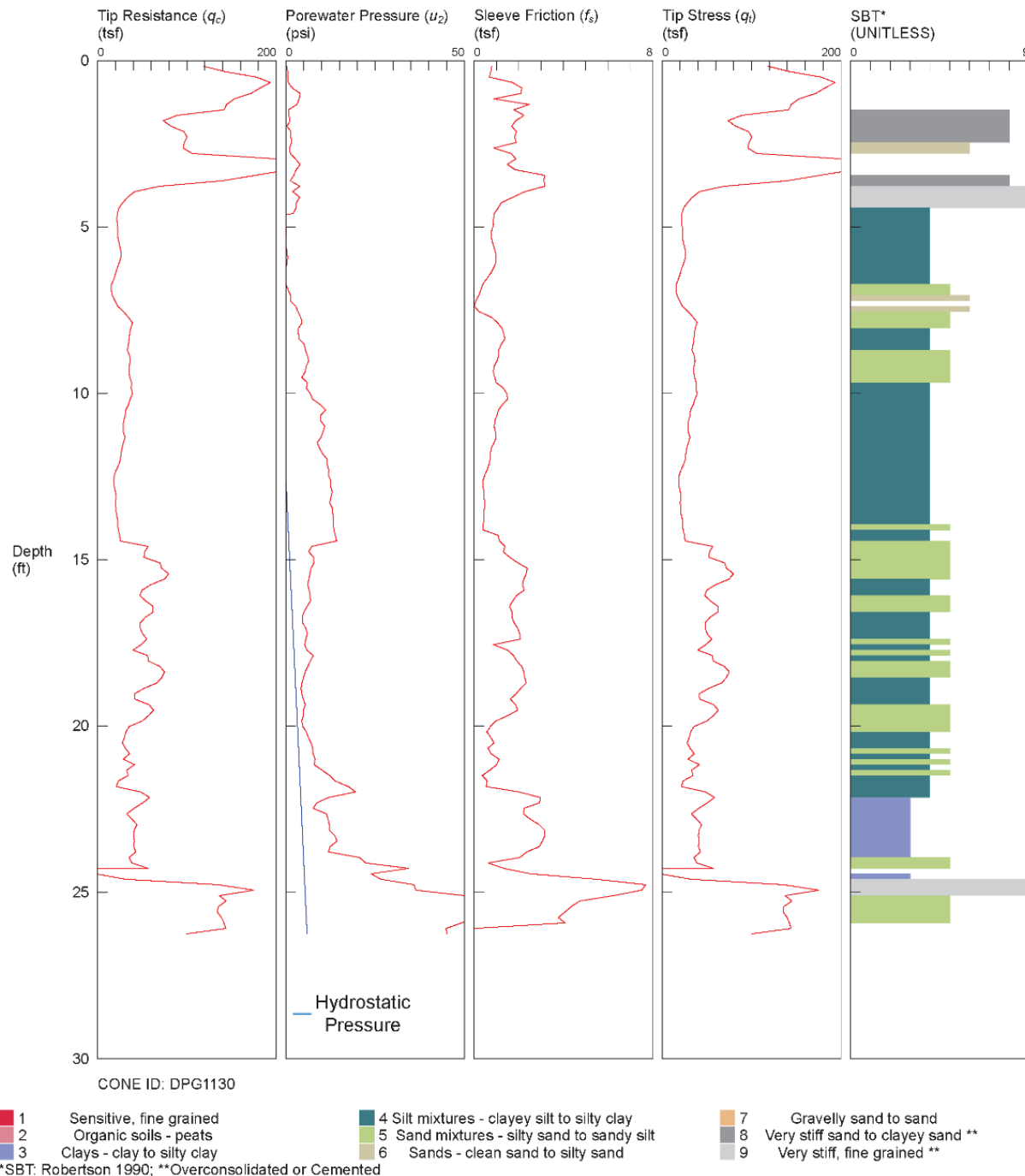


Figure 3-8. CPT Boring Log from CPT-04 location.

Locations of each cross section are shown in **Figure 3-9**. To help integrate and interpret the CPT results, we generated lithologic cross sections generally parallel to groundwater flow (**Figure 3-10**) and perpendicular to groundwater flow (**Figure 3-11**). Both cross sections show interbedded silts and sands extending from the water table at an elevation of ~623 ft above mean sea level (msl) to ~615 ft msl. At about 615 ft msl, there is a 1–2 ft thick continuous zone that is classified as clay based on the CPT tip stress and sleeve resistance. However, visual examination indicates this material is a loose, gravelly sand (**Figure 3-17**). Stiff weathered rock is encountered 1–2 ft below the loose, gravelly sand.

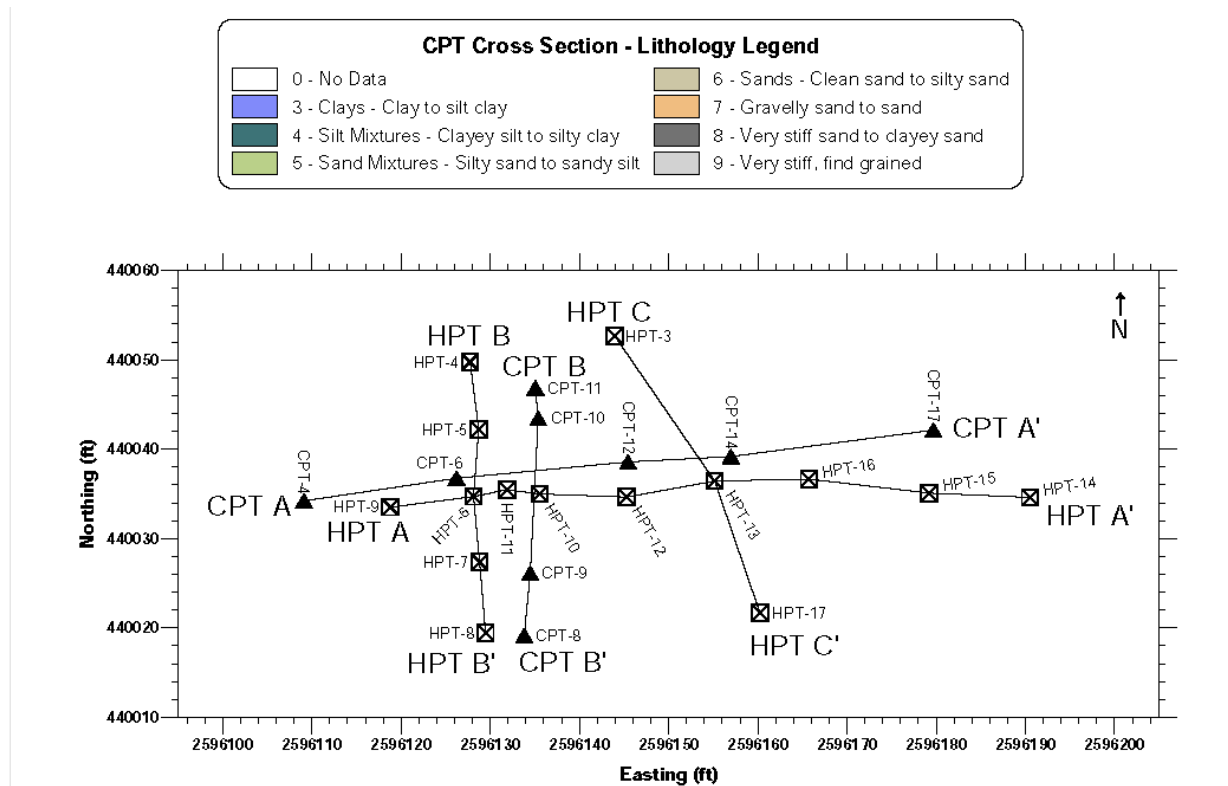


Figure 3-9. Location of the CPT cross-sections and includes the lithologic legend.

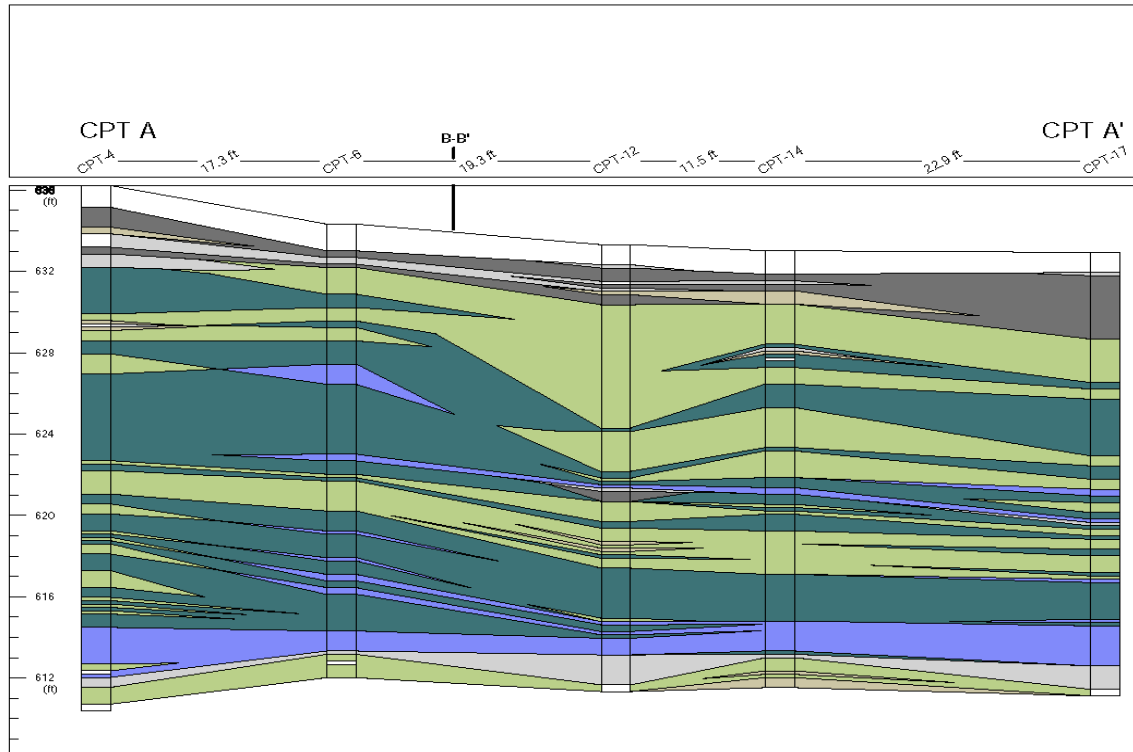


Figure 3-10. CPT Cross-section from CPT A to A' approximately parallel to flow.

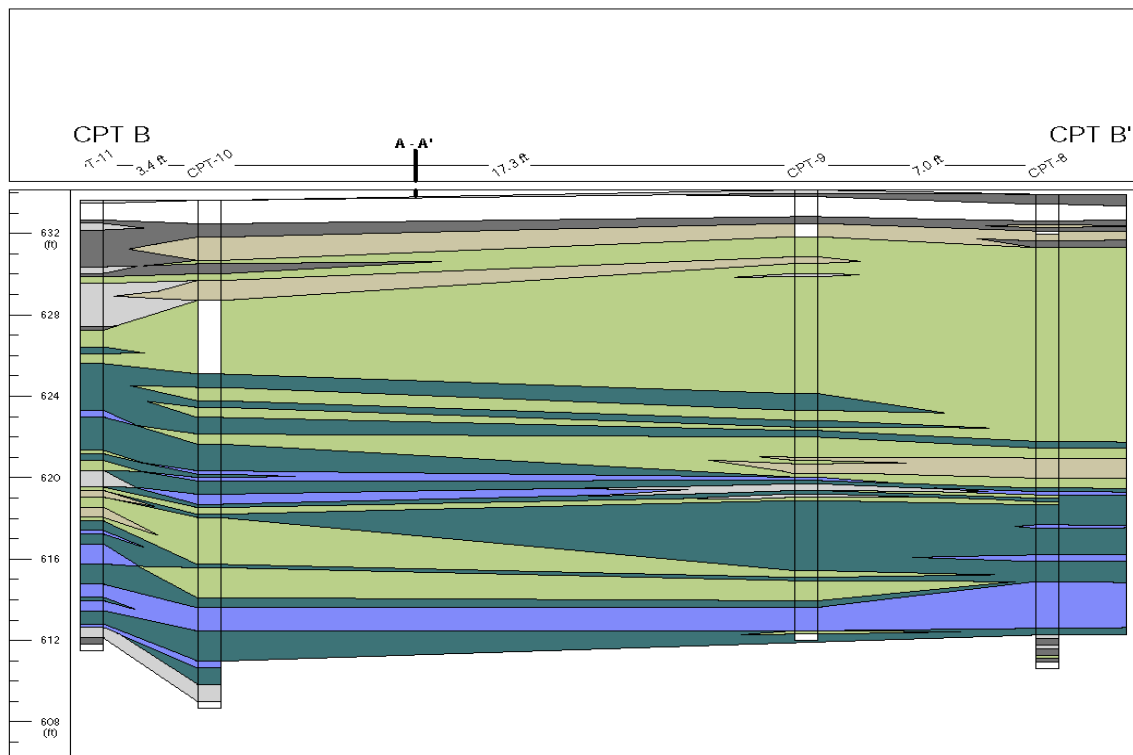


Figure 3-11. CPT Cross-section from B to B' approximately perpendicular to flow.

3.1.2.2 CPT Dissipation Tests

When the CPT penetrometer is advanced, displacement of the soil formation occurs and excess porewater pressure (Δu) is generated. Pressure dissipation tests were run to estimate K by monitoring the decline in pressure versus time. A variety of empirical methods are available which relate K to the time required for pressure to decline to 50% of the maximum (t_{50}). **Figure 3-12** shows results of a typical pore pressure dissipation test. When rod advance was stopped, the pressure increased to 39.71 psi due to over consolidation of the aquifer material, then gradually declined to hydrostatic pressure (u_0) of 2.34 psi, with t_{50} =90 seconds. Using the empirical relationship $K[\text{cm/s}] = (251 * t_{50}[\text{sec}])^{-1.25}$ presented by Perez and Fauriel (1988), $K=4.0\text{E-}6$ cm/s or 0.01 ft/d.

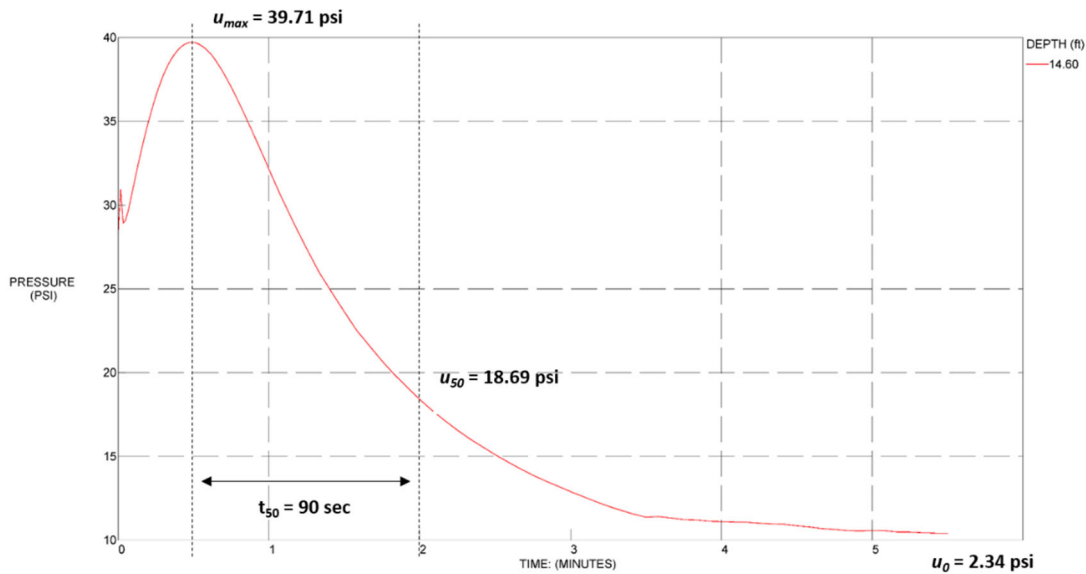


Figure 3-12. Example dissipation test to determine t_{50} .

CPT dissipation tests were run at up to four depths in each CPT boring. Given the low permeability of the aquifer material, it was not practical to run the tests to equilibrium. Instead, dissipation tests were run until the pressure declined by 50% or for 30 minutes, whichever came first. **Table 3-** summarizes the results of the CPT test with K estimated using the relationship presented by Perez and Fauriel (1988). The median K estimated by CPT was ~ 0.001 ft/d with 10% of the values greater than 0.01 ft/d and a maximum estimated K of 0.7 ft/d.

Table 3-1. Estimated K from CPT Dissipation tests

CPT Boring	Depth (ft bgs)	Elevation (ft)	Hydraulic Conductivity (K)		t ₅₀ (sec)
			(cm/s)	(ft/d)	
CPT-2	15.42	622.80	6.0E-09	1.7E-05	15,137
	18.70	619.52	1.3E-07	3.7E-04	1,280
	21.98	616.24	5.1E-06	1.5E-02	68
CPT-4	14.44	622.20	8.3E-08	2.3E-04	1,845
	17.72	618.92	7.4E-07	2.1E-03	321
	21.00	615.64	4.1E-07	1.2E-03	511
	24.28	612.36	8.6E-09	2.4E-05	11,324
CPT-5	12.30	621.00	2.5E-04	7.2E-01	3
	14.60	618.70	3.6E-06	1.0E-02	90
	16.57	616.73	1.2E-07	3.5E-04	1,354
CPT-6	11.65	622.68	2.7E-07	7.6E-04	723
	14.93	619.40	2.0E-07	5.8E-04	899
	18.21	616.12	5.2E-07	1.5E-03	425
	21.49	612.84	1.4E-07	4.0E-04	1,203
CPT-7	11.48	622.07	1.3E-07	3.6E-04	1,305
	14.60	618.95	2.6E-06	7.3E-03	118
	16.57	616.98	1.2E-06	3.4E-03	219
CPT-8	12.47	621.45	4.8E-07	1.4E-03	450
	14.60	619.32	4.0E-07	1.1E-03	520
	18.05	615.87	3.0E-07	8.5E-04	656
CPT-9	16.73	617.40	1.0E-08	2.8E-05	10,005
CPT-11	10.66	622.98	2.9E-07	8.1E-04	685
	17.55	616.09	3.1E-07	8.8E-04	638
	19.19	614.45	1.4E-06	3.8E-03	197
CPT-12	11.98	621.34	1.1E-07	3.1E-04	1,462
	21.98	611.34	1.2E-08	3.4E-05	8,650
CPT-13	11.98	621.21	2.7E-06	7.6E-03	114
	15.26	617.93	1.2E-08	3.3E-05	8,898
	18.54	614.65	8.1E-08	2.3E-04	1,876
CPT-14	11.98	621.04	3.0E-06	8.4E-03	105
	18.54	614.48	5.5E-08	1.6E-04	2,553
CPT-17	11.98	620.96	9.6E-06	2.7E-02	41
	18.54	614.40	3.7E-08	1.0E-04	3,542

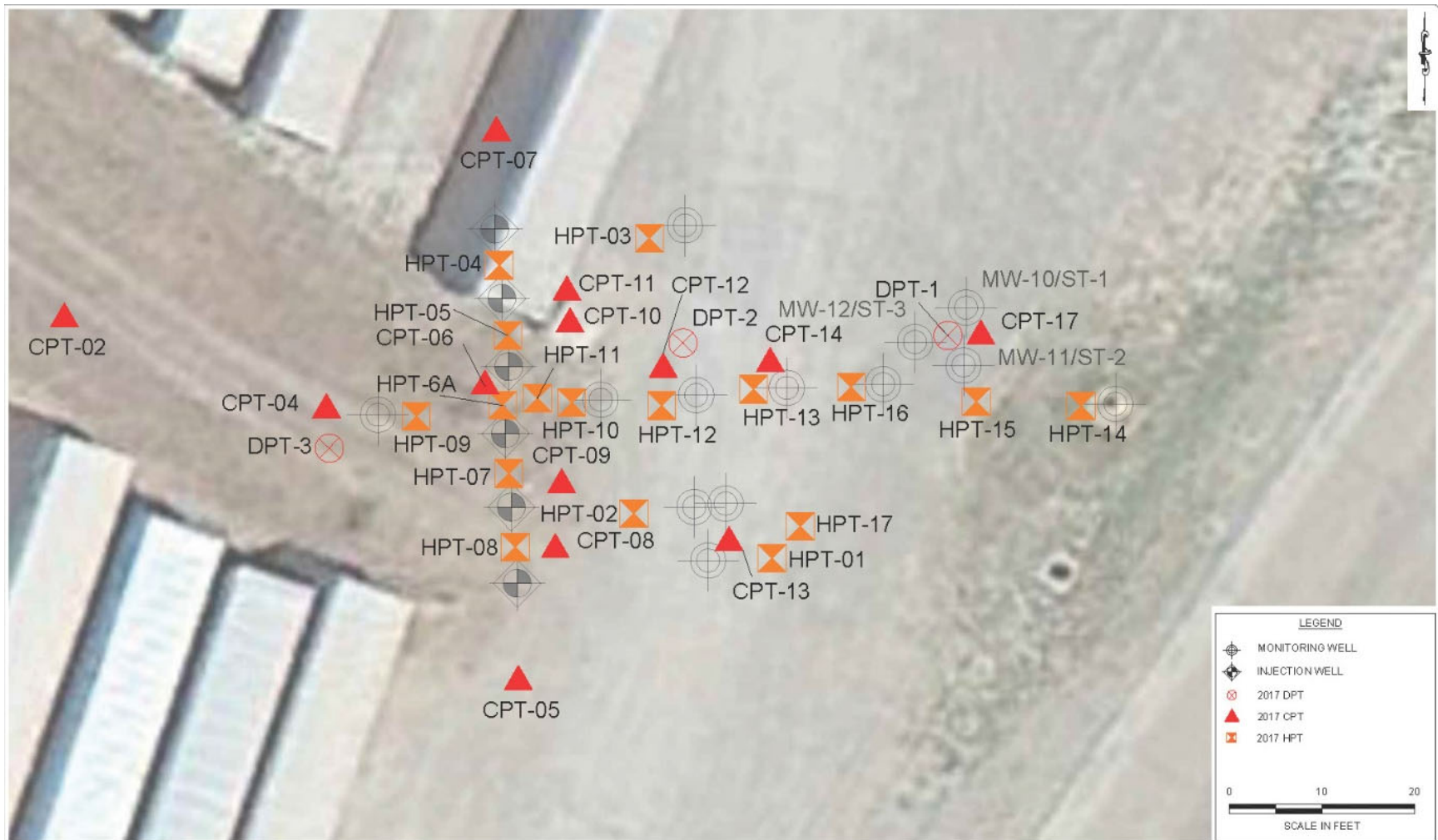


Figure 3-13. HPT and CPT Boring locations.

3.1.2.3 Hydraulic Profiling Tool (HPT) Borings

A series of 16 HPT borings were installed and HPT boring locations are shown in **Figure 3-9** and **Figure 3-13**. The HPT system used in these borings was developed by Geoprobe Systems® and is composed of the Field Instrument (FI6000) that manages overall work, HPT Flow Module (K6300) that controls the flow rate, probe assembly and HPT trunkline that connects probe assembly with Field Instrument and Flow Module. The probe is pushed or hammered into the ground at a constant rate, typically 2 cm/s. As the probe advances, clean water is injected through a screen on the side of the probe into the subsurface at a constant flow rate (Q). The in-line sensor records pressure (P), providing an indication of the hydraulic properties of the soil. At a constant flow rate, a low-pressure response indicates a relatively high permeability zone; conversely, a high-pressure response indicates a relatively low permeability zone. An integrated EC sensor collects soil resistivity data to aid in delineation of the soil stratigraphy. In general, an increase in EC correlates with a decrease in grain size. The EC response is similar to the HPT pressure response (high response generally corresponds with low permeability).

In most of the HPT borings, water was injected at ~250 mL/min which resulted in over pressuring in the lowest permeability zones. Profiles of K versus depth were generated using the relationship developed in **Section 2.5**, which is equal to the average of measured values (**Table 3-2**). In many cases, pressure observed during dissipation tests never reached equilibrium so hydrostatic pressure was calculated from the depth to water in nearby monitoring wells.

Figure 3-14 shows an example HPT log for boring HPT-13. The EC, HPT injection water pressure, HPT injection flow rate, and estimated K are shown versus elevation. In general, the EC and HPT pressure increase with decreasing grain size, and vice versa throughout the boring.

Profiles of estimated K versus elevation are shown in **Figure 3-15** and **Figure 3-16**. Higher K zones were observed in many of the borings, often at similar elevations. However, these higher K zones were sometimes absent in adjoining borings, indicate this zone is not continuous throughout the site.

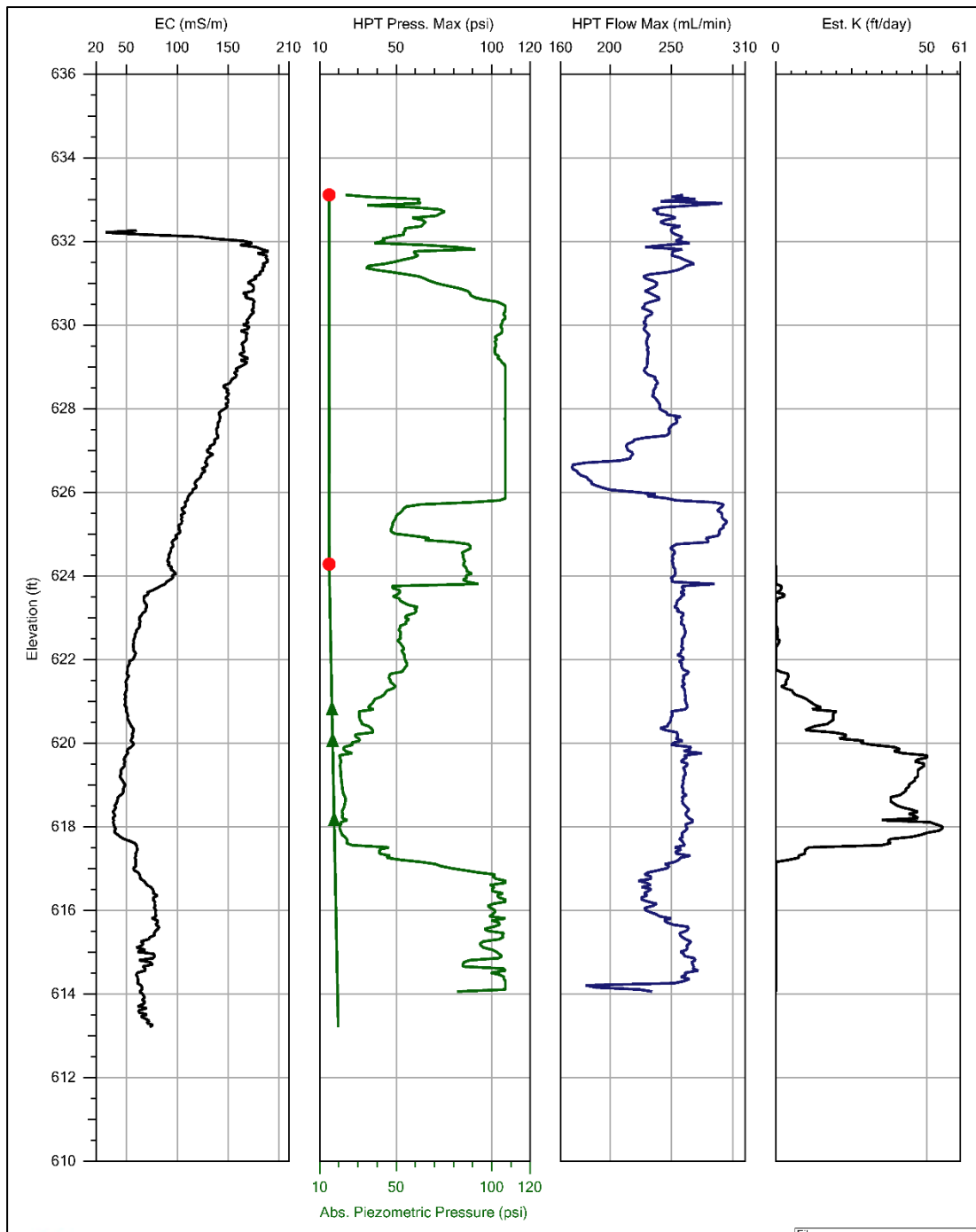


Figure 3-14. HPT Boring Logs from HPT-13. The EC, HPT Pressure, HPT Flow rate, and Estimated K (Geoprobe equation) presented from left to right with elevation.

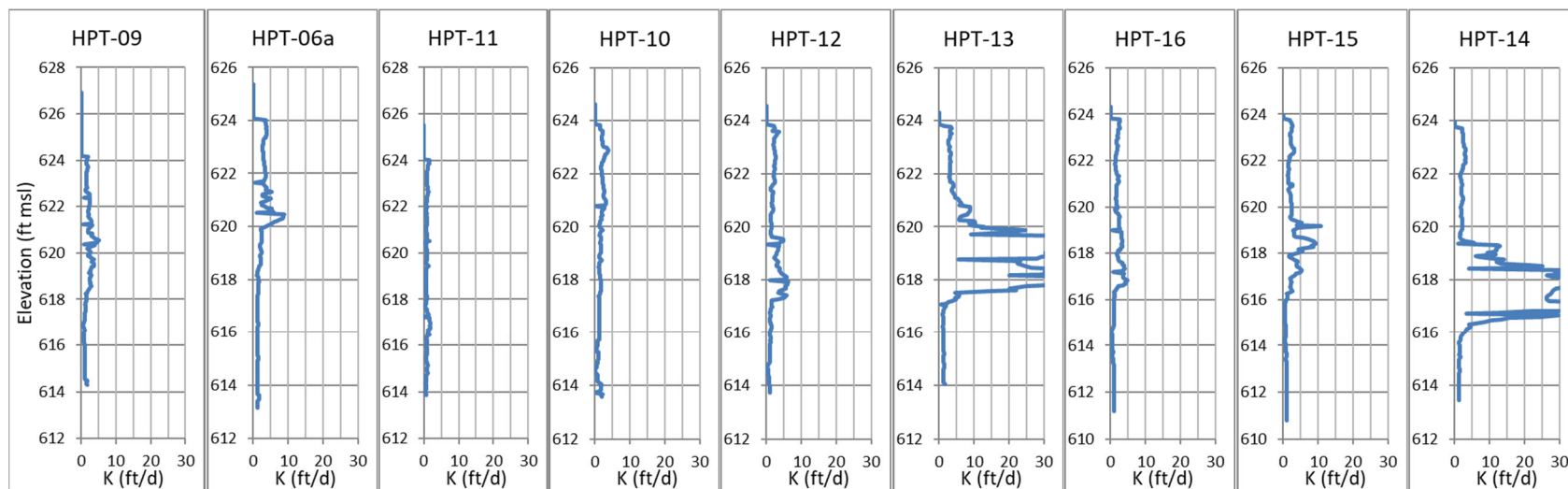


Figure 3-15. Profiles of estimated K from HPT parallel to flow (HPT A- HPT A')

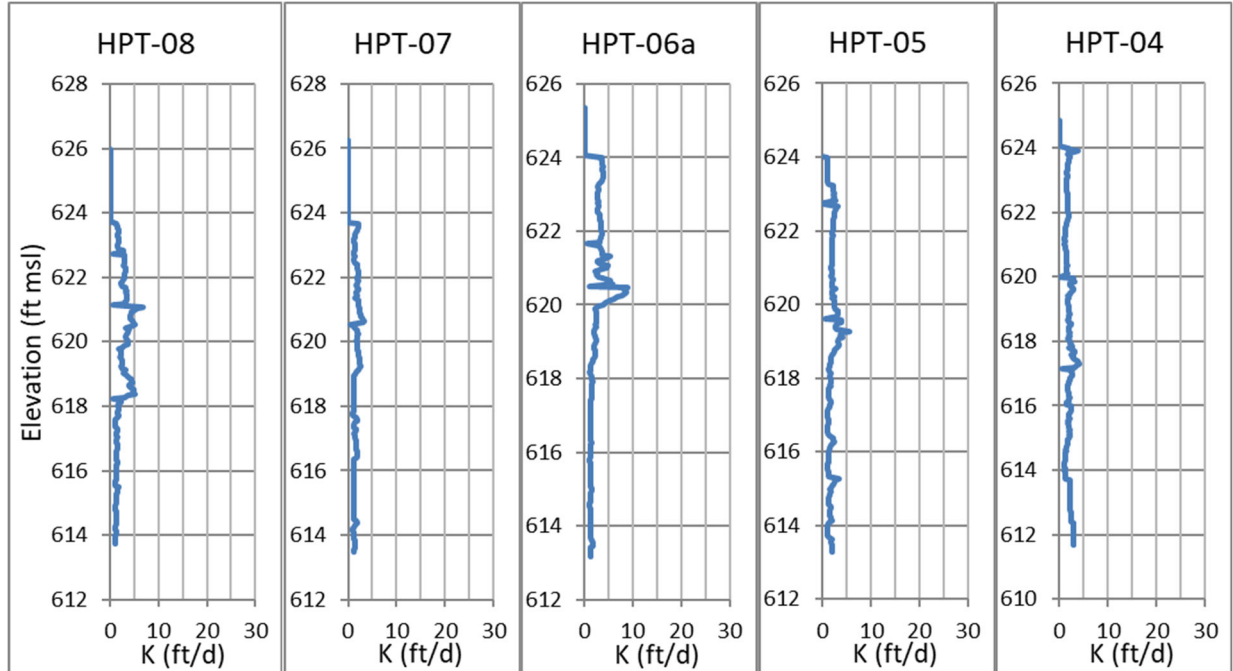


Figure 3-16. Profiles of estimated K from HPT perpendicular to flow (HPT B- HPT B')

3.1.2.4 Characterization of Fine-Grained Material

Three hollow stem auger borings were advanced in a triangle pattern around boring DPT-1 (**Figure 3-13**). One Shelby tube sample was collected from 15-17 ft bgs from each of these borings. After collection of each Shelby tube sample, the borehole was converted to a 2" monitoring well (MW-10/ST-1, MW-11/ST-2 and MW-12/ST-3) with 2 ft screens at the same depth as the Shelby tube sample. Slug tests were conducted in these wells for comparison with the laboratory measurements of K.

Results of the geotechnical laboratory testing are presented in **Table 3-2**. The materials tested consisted of silt, clay and silty-clayey sand. K varied from 0.9 to 3.8E-7 cm/s and compressibility varied from 1.1 to 2.1E-7 /Pa. K values were similar to results of the CPT pore pressure dissipation tests, but 3 orders of magnitude lower than from slug tests on these same boreholes.

Table 3-2. Geotechnical Properties of Undisturbed Samples

Parameter	MW-10	MW-11	MW-12
Color	Brown	Greyish-brown	Brown
Material	Silt	Clay	Silty-clayey sand
Specific Gravity	2.67	2.66	2.75
Moisture Content	23%	18%	21
Porosity	44%	37%	42%
Liquid Limit	n/a	35%	22
Plastic Limit	n/a	13%	17
Plasticity Index	n/a	22%	5
Liquidity Index	n/a	0.2	0.8
Permeability @ 20 °C (m/sec)	3.8E-9	8.8E-10	2.7E-9
K (ft/d)	0.0011	0.0002	0.0008
Compressibility (1/Pa)	2.1E-7	1.1E-7	1.2E-7
Specific Storage (1/m)	2.1E-3	1.1E-3	1.2E-3
Hydraulic Diffusivity (m ² /s)	1.8E-6	8.2E-7	2.3E-6

In addition to the geotechnical characterization, 30 soil samples were submitted for laboratory measurement of organic carbon content (foc) and particle size distribution (**Table 3-3**). Fraction organic carbon (foc) was not correlated ($r^2=0.01$) with median particle diameter (D_{50}) or other soil characteristics. Samples were primarily silt with a substantial clay fraction, and small amount of sand. Soil organic carbon was low varying from the method detection limit (0.03%) to 0.28% with a median of 0.07%.

Table 3-3. Soil Organic Carbon and Particle Size Fraction

		TOC %	Clay %	Silt %	Sand %	D50 (μm)
Mean		0.10%	28.2	65.0	6.9	10.5
Median		0.07%	27.2	64.5	4.0	8.1
Standard Deviation		0.07%	7.6	6.5	8.3	8.1
Minimum		0.03%	16.0	51.9	0.0	2.7
Maximum		0.28%	43.8	78.1	32.0	37.7

The linear equilibrium retardation factor (R) can be calculated as

$$R = 1 + K_{oc} * f_{oc} * \rho_B/n \quad (3-1)$$

where K_{oc} is the organic carbon partition coefficient, f_{oc} is the soil organic carbon content, ρ_B is soil bulk density and n is porosity. Using the published value of K_{oc} for TCE of $94.3 \text{ cm}^3/\text{g}$ from USEPA (1996), f_{oc} of 0.0007 from **Table 3-3**, ρ_B of 1.59 g/cm^3 , and n of 0.41 from **Table 3-2**, the low K retardation factor for TCE is 1.25.

3.1.2.5 Vertical Distribution of CVOCs

Three soil borings (DPT-1, DPT-2 and DPT-3) were advanced with continuous sampling to obtain detailed stratigraphic information (location shown in **Figure 3-13**). From approximately 10 to 20 ft bgs discrete soil samples were collected from the continuous core at either 0.5 or 1.0 ft intervals for laboratory analysis for CVOCs and 1,4-D. DPT lithologic data were used for comparison with HPT/CPT results and to look for potential CVOC and 1,4-D diffusion gradients from higher to lower K lithologies. **Figure 3-17** shows a typical boring log for DPT-2 showing TCE concentrations and visual classification of soil.

Figure 3-18 shows profiles of TCE and DCE concentration and Cl# versus depth in borings DPT-3, DPT-2 and DPT-1. In DPT-3, approximately 20 ft upgradient of the PRB, cDCE is below detection in all samples, consistent with groundwater monitoring data showing no reductive dechlorination prior to EVO injection. TCE concentrations are highest at 614 – 615 ft msl, where a sandy gravel was observed. TCE concentrations gradually decline away from the gravel, consistent with diffusion of TCE into the lower K silts. In DPT-2, ~20 ft downgradient of the PRB, TCE concentrations are very low in the sandy gravel and cDCE is present, resulting in a low Cl# indicative of reductive dechlorination. cDCE was detected 2 – 3 ft into the overlying silt, consistent with cDCE diffusion away from the high K zone. TCE concentrations in the silt immediately above and below the gravel are lower than in DPT-3, indicating ERD has somewhat depleted the TCE in the 4 years since the PRB was installed. In DPT-1, ~50 ft downgradient of the PRB, some cDCE was detected, but TCE concentrations remain elevated and the Cl# is close to 3 indicating minimal impact of ERD at this location.

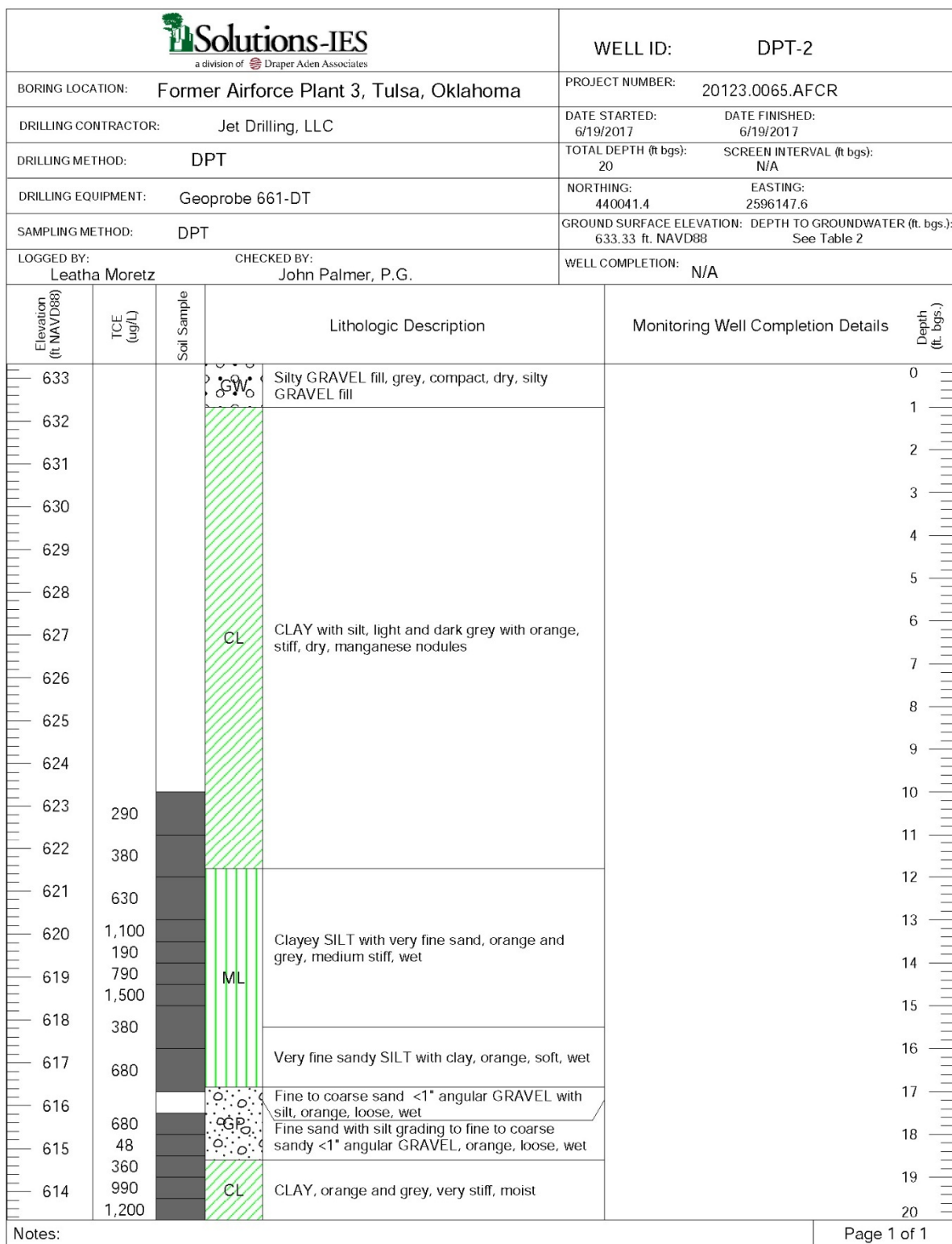


Figure 3-17. Typical boring log showing TCE concentrations and visual classification of soil.

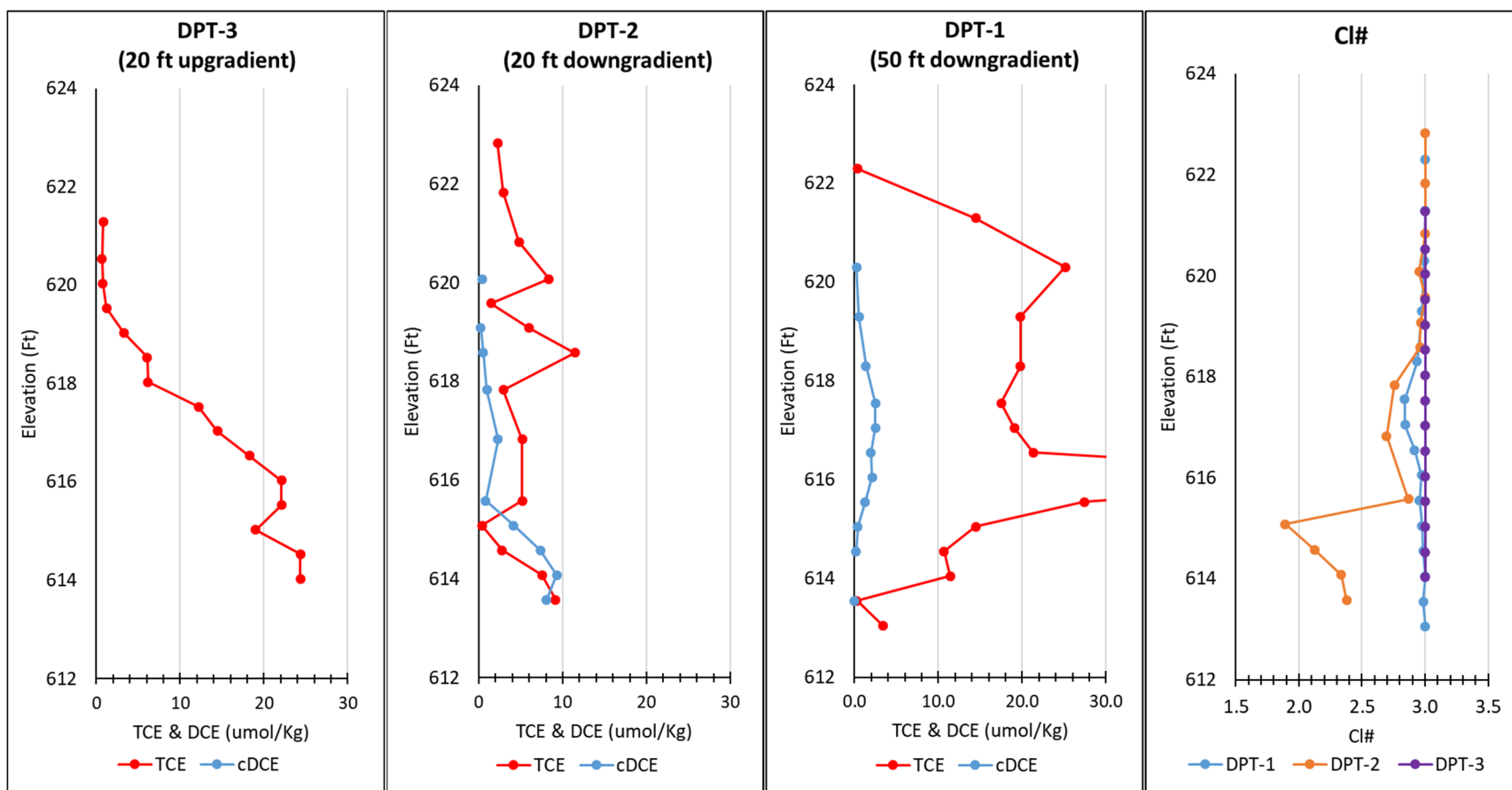


Figure 3-18. Profiles of TCE and DCE concentration and Cl# in soil samples. DPT-3 is 20 ft upgradient of the PRB, DPT-2 is 20 ft downgradient, and DPT-1 is 50 ft downgradient.

3.1.2.6 Slug Tests

Slug tests were conducted on monitoring and/or injection wells with varying screen intervals in 2013, 2015, and 2017. Head data during the slug tests was collected using a transducer sensor and periodic field verification using an electric water level meter. The head data for each slug-in or slug-out was used to calculate a K in ft/d using the Bouwer and Rice (1976) method using Aqtesolv software. The Bouwer and Rice method, for unconfined aquifers with wells both fully submerged and bracketing the water table, uses slope matching of the log of the normalized head (ft/ft) versus the time (sec) to calculate K.

Results of the slug tests are presented in **Table 3-4**. Average K values for each well ranged from 0.2 ft/d in IW-2 to 11.1 ft/d in IW-3 (pre-2013 injection). The monitoring wells MW-10, 11 and 12, installed in June 2017, were all screened with the same 15-17 ft interval (Shelby tube samples discussed in **Section 3.1.2.4** were taken from the same locations) in a silt to sandy silt interval (DPT-1). However, the K values from these wells (located in a triangle pattern 6 ft apart) varied by two orders of magnitude from 1.3 ft/d in both MW-11 and MW-12 to 11.1 ft/d in MW-10.

Table 3-4. Slug Tests Results

Well ID	Slug Test K ft/d
8-20	0.24
IW-2	0.2
IW-3	11.1
MW-1	2.52
MW-2	1.26
MW-3	3.10
MW-4	4.98
MW-5	3.08
MW-6	1.85
MW-7	2.84
MW-8	0.60
MW-9	1.48
MW-10	11.07
MW-11	1.32
MW-12	1.27
Average	2.7

3.1.2.7 Summary of Site Characterization Results

Shallow groundwater in the vicinity of the EVO PRB is present in terrace deposits comprised of cohesive silty clays with intermittent sand, silty sand, and clayey silt lenses overlying the Nowata

Shale formation. Visual evaluation of continuous soil cores indicates the subsurface is primarily clayey silt to very fine sandy silt with 1-2 ft thick zones of sandy gravel.

CPT profiles show the subsurface material primarily consists of interbedded layers of clayey silt to silty clay, with layers of clean sand to silty sand present at some locations. Soil Behavior Type (SBT) analysis of the CPT results indicate that 19% of the material below the water table is clay (clay to silty clay), 47% is silt (clayey silt to silty clay) and 23% sand (silty sand to sandy silt) with minor amounts of clean sand and gravel. CPT dissipation test results indicated K values in the silt and clay zones varied between $1.0\text{E-}08$ to $1.0\text{E-}04$ cm/s with a median value of $3.0\text{E-}07$ cm/s.

Geotechnical laboratory testing indicates the fine-grained soils vary from silty-clayey slightly plastic sand to highly plastic clay. K varied from $0.9\text{E-}07$ to $3.8\text{E-}07$ cm/s which is generally consistent with the CPT dissipation test results.

Slug test results vary from 0.2 to 11.1 ft/d with an average value of 2.7 ft/d indicating moderately transmissive material.

HPT profiles indicate that most of the vertical section is lower K material (<0.1 ft/d). However, more permeable zones make up about one fifth of the vertical thickness. At some depths, there was little pore pressure buildup in some of the sandy zones which is consistent with K values of 10-50 ft/d. There appears to be a reasonably continuous higher permeability unit at 616 – 620 ft msl. However, higher K zones were not observed in several borings, indicating this high K zone is not continuous throughout the pilot test area.

The non-reactive bromide (Br) tracer was observed in downgradient wells, 2 to 7 months after injection, indicating relatively rapidly downgradient transport. The non-reactive transport velocity estimated from Br appearance in downgradient wells varied from 72 to 104 ft/yr with an average transport velocity of 86 ft/yr. The rapid downgradient transport of Br is consistent with the presence of a conductive zone ($K > 10$ ft/d) that extends tens of ft. However, breakthrough and flush out of Br in MW-2 was much slower, consistent with the absence of conductive zones in HPT borings adjoining MW-2.

Injection of emulsified vegetable oil (EOS Pro) and a bioaugmentation culture was very effective in stimulating essentially complete removal of TCE in injection wells. However, downgradient TCE removal was much slower. Effective first-order TCE decay rates steadily decline from 1.67/yr at 10 ft downgradient of the PRB (MW-2) to 0.11/yr at 50 ft downgradient (MW-5).

Sampling of TCE and cDCE in continuous soil profiles indicates transport of dissolved TCE in coarser grained zones followed by slower transport into lower permeability fine grained materials. At 20 ft downgradient of the PRB, TCE has been largely depleted from the sand zones with concurrent production of cDCE. However, TCE depletion in fine grained zones is much more limited.

3.1.3 Flow and Transport Modeling with DP Technologies

Accurate simulation of groundwater flow and transport requires detailed information on spatial variations in hydraulic conductivity. However, until recently, it was not practical to obtain this information. With the recent development of the HPT tool, it may now be possible to cost effectively collect this information and use it to improve model predictions. In this project, a high-resolution numerical model of groundwater flow and solute transport at AFP3 was developed using high-resolution hydrogeologic data obtained from sixteen HPT borings. CPT data was not used for numerical model development, due to inconsistencies between CPT results and visual inspection of soil cores.

3.1.3.1 Geostatistical Analysis

The HPT tool provided high-resolution data on the vertical distribution of K at sixteen locations within the pilot test area. However, development of the high-resolution numerical model requires that K be defined for all cells within the model domain, including cells located some distance away from HPT borings. Estimation of K for every model cell requires some method to interpolate or extrapolate K from the available borings.

In this project, the transitional probability approach developed by Carle (1999) was used to analyze the data collected from the HPT borings, and then use this data to estimate K throughout the model domain. Data processing was performed with the T-PROGS (Carle, 1999) geostatistical analysis tool incorporated into the Groundwater Modeling Software (GMS)(Aquaveo, 2020: <http://aquaveo.com>). In this approach, site characterization data is used to classify aquifer materials into discrete units or facies with homogeneous properties.

For statistical analysis, approximately 3000 values of K from the HPT borings were combined into a single dataset and sorted from low to high to generate a cumulative frequency distribution (CFD) for K (**Figure 3-19**). Results of traditional soil borings and laboratory analyses indicate that the aquifer primarily consists of fine grained, low K material (sandy silt to silty clay) with thinner zones of higher K sand and fine gravel. The CFD presented in **Figure 3-19** is consistent with the soil boring results – there is a small fraction of high K material, while most of the material has a $K < 2$ ft/d. However, there is no obvious cutoff point to separate high and low K material in **Figure 3-19**. For preliminary screening, T-PROGS was used to generate distributions of low and high K material using three different high/low K cutoff points (2.2, 3.2 and 5.4 ft/d shown as blue diamonds in **Figure 3-19**).

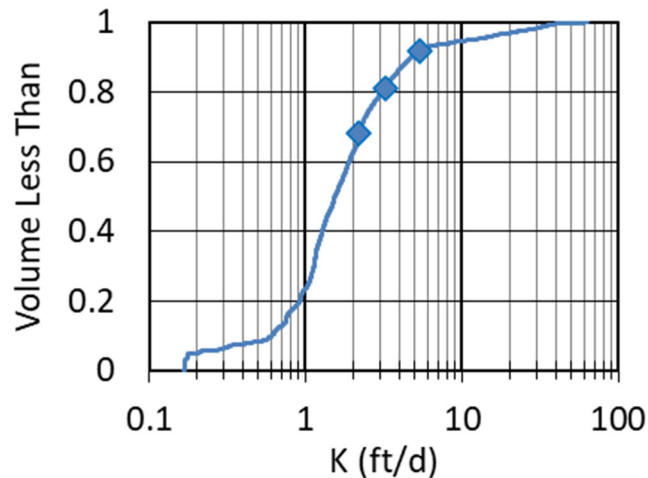


Figure 3-19. Cumulative frequency distribution (CFD) of hydraulic conductivity (K) in HPT borings at AFP3.

Figure 3-20 shows the material distributions generated by T-PROGS in a cross-section parallel to the line of PRB injection wells using three different high/low K cutoff values. Low K material is shown in orange and high K material in white. Overlain on each figure are five soil profiles generated from HPT borings located between injection wells. Visually, the three distributions appear very different. Using a relatively low cutoff value of 2.2 ft/d (30% high K / 70% low K), high K material is broadly distributed throughout the upper portion of the aquifer. Using an intermediate cutoff value of 3.2 ft/d (81% low K / 19% high K), the high K material is present in several small bodies located in the upper middle portion of the aquifer. Using a relatively high cutoff value of 5.4 ft/d (92% low K / 8% high K), high K zones are almost absent from the cross-section.

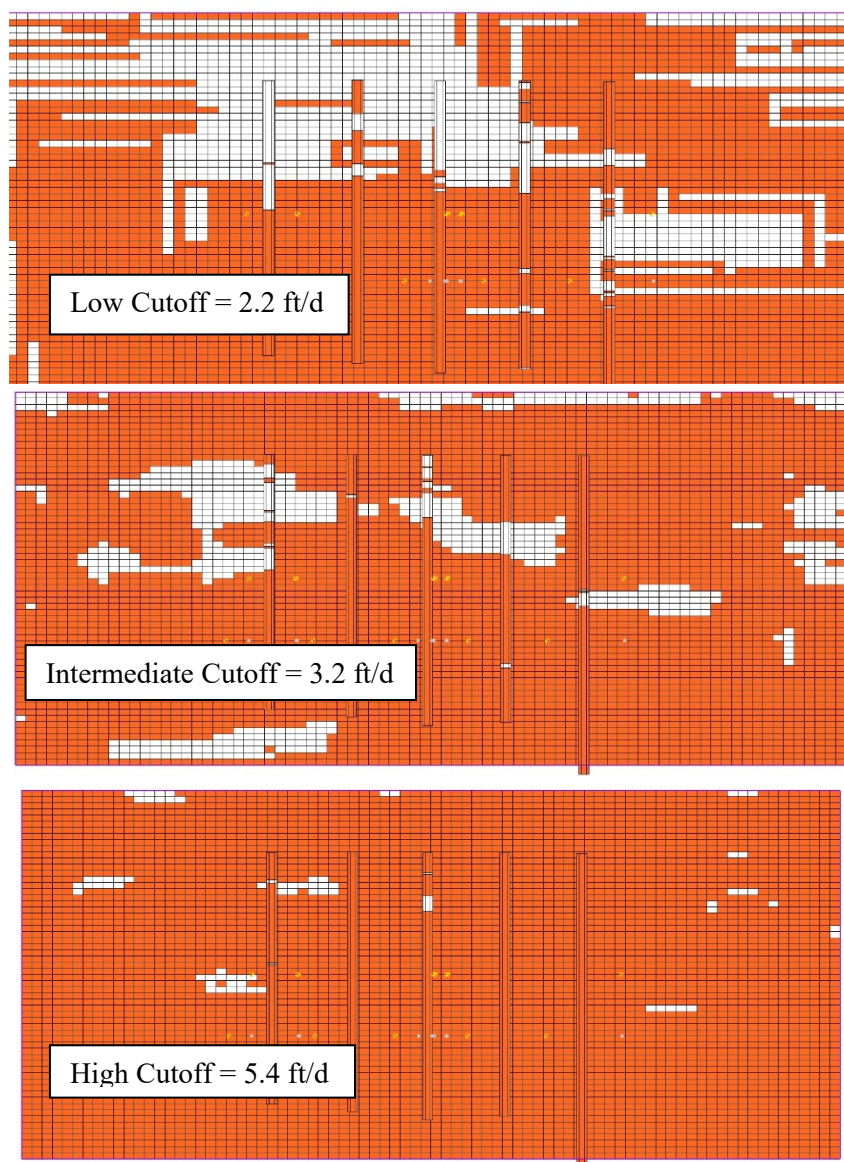


Figure 3-20. Distribution of low K and high K material for different high/low cutoff values. Low K material is shown in orange and high K material in white. Material distribution is overlain by soil profiles generated from HPT borings.

Overall, the material distribution generated using the intermediate cutoff value (3.2 ft/d) was much closer to the conceptual model developed based on soil borings and field observations during the PRB injection and monitoring. Visual inspection of soil cores showed the presence of a thin coarse sand/fine gravel layer of varying thickness in the upper middle portion of the aquifer, consistent with the intermediate cutoff value. During injection, the Br tracer and organic substrate appeared to rapidly migrate through channels or conduits, bypassing some nearby wells, also consistent with the intermediate cutoff value. Based on these results, a high/low K cutoff value of 3.2 ft/d was used in subsequent modeling work.

Figure 3-21 shows plots of transitional probability in the vertical direction versus lag spacing between measurements (dashed line) generated by T-PROGS using the intermediate cutoff value of 3.2 ft/d. A Markov chain model was then fit to this data to provide estimates of average thickness of higher and lower K units. Based on this analysis, the average vertical thickness of the lower K material is 6.01 ft and the average thickness of the higher K material is 1.37 ft.

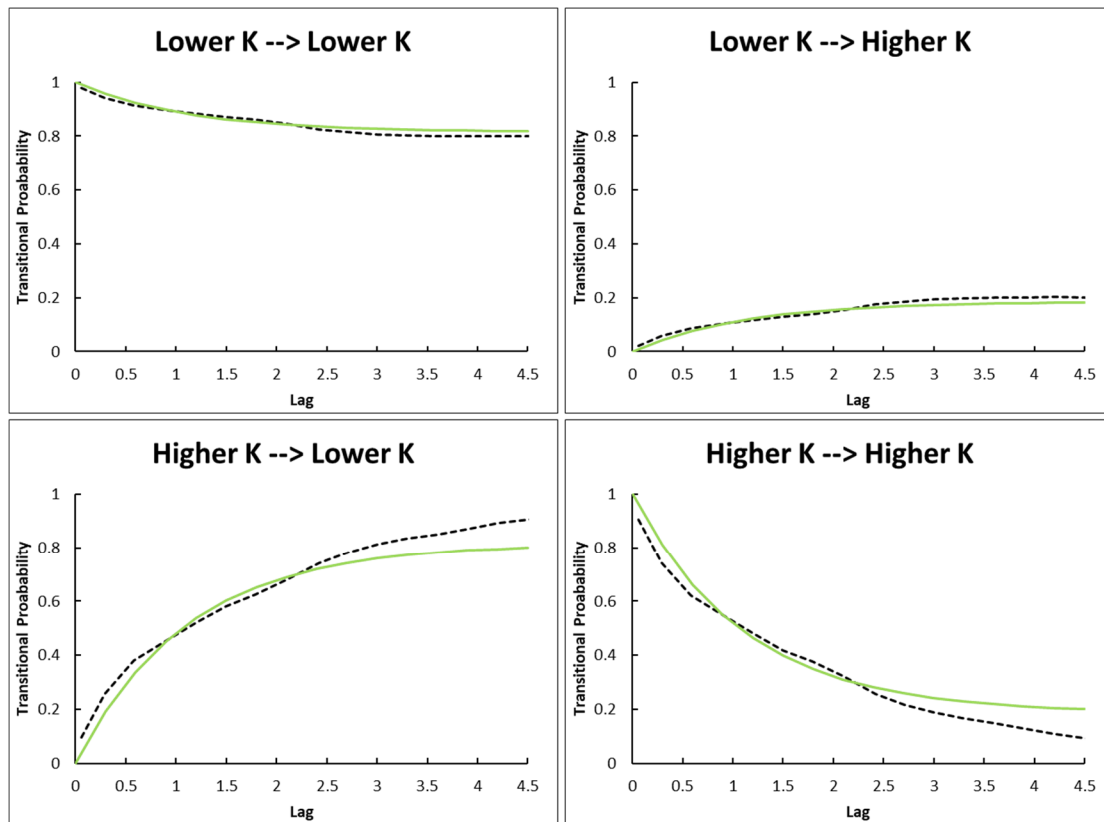


Figure 3-21. Transitional probability plots in vertical direction from T-PROGS. Filled circles is the transitional probability generated from borehole data. Solid line is fitted Markov Chain Model.

It was not possible to estimate the average horizontal length (x and y dimensions) of lower and higher K zones due to the limited number of borings. Following recommendations from the software developer, the ratio of horizontal to vertical lens thickness was assumed to be 10:1. A uniform model grid was established with $\Delta x = \Delta y = 1$ ft and $\Delta z = 0.2$ ft. Once the model grid was defined and average thickness of different materials were measured, the TSIM program within T-PROGS was used to generate five realizations of material properties over the entire model domain.

Figure 3-22 shows five different material distributions (realizations) illustrating potential variations in the location of higher and lower K zones. The lower K zones are presented in red and the higher K zones presented in blue. The yellow indicates high K zones due to the presence of well screen or sand pack. All the realizations have the same general statistical properties (fraction higher/lower K material, average lens dimensions) and were conditioned on the HPT

results so the statistical realizations approximately match the actual HPT results where borings are located. However, away from the HPT boring locations, it is not possible to accurately predict whether a higher or lower K unit is present, only to define the probability that it may be present. As a result, the specific location of higher K channels varies from realization to realization, while the fraction of higher K material is constant. In all the realizations, higher K materials are more common at 2.5 ft to 5 ft below from the top layer of the model (619.9-617.4 ft. msl) which is consistent with the HPT and soil boring results.

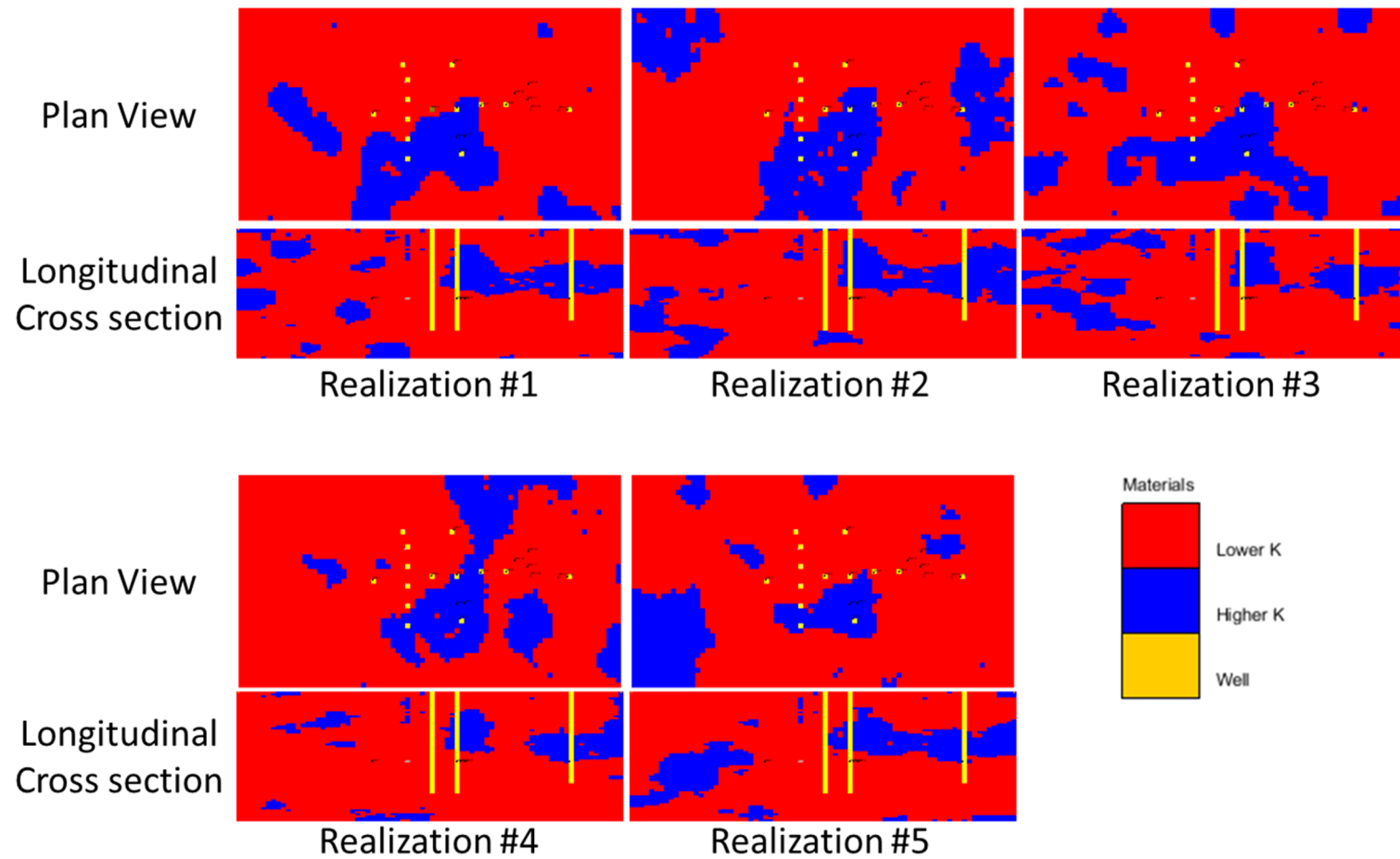


Figure 3-22. Plan view and longitudinal cross-section view of realizations 1 to 5. Plan-view at Layer 12 (620.7 ft. msl). Longitudinal cross section is at the center line of model domain passing through MW-2 and 3.

3.1.3.2 High-resolution Numerical Simulations

A high-resolution numerical model was developed to evaluate whether a model based on HPT data could provide reliable predictions of solute transport. In the first part of this work, the injection and downgradient transport of the bromide tracer test was simulated for each of the five material realizations shown in **Figure 3-22**. Modeling input parameters are presented in **Table 3-5**. The groundwater flow and solute transport were simulated with MODFLOW (McDonald and Harbaugh, 1988) and MT3DMS (Zheng and Wang, 1999), as incorporated into the GMS 10.0 package. The injection flowrate, duration and bromide concentration for each well were set to match the field monitor reports. Detailed injection parameters were listed in **Table 3-6**. The background bromide concentration was set to 0.7 mg/L based on samples collected before the bromide injection test. HPT results indicated that the K of the high permeability zone varied between 10 and 50 ft/d. A K value of 30 ft/d for the high permeability zone provided the best match between simulated and observed Br tracer breakthrough and was used in all MODFLOW/MT3DMS simulations. The presence of multiple monitoring and injection wells could impact solute transport by providing high permeability conduits for vertical migration of tracer and contaminants. To simulate the impact of these wells, the horizontal and vertical K of cells containing well screens were set to 1000 ft/d.

Table 3-5. Bromide Tracer Test Modeling Parameters

Parameters		Value	Unit
Porosity		0.3	-
Effective molecular diffusion coefficient (Dm * porosity)		0.00056	ft ² /d
Hydraulic Conductivity for Material	High K Material	30	ft/d
	Low K Material	0.5	ft/d
	Wells	1000	ft/d
Dispersivity	Longitudinal	0.5	ft
	Transverse	0.05	ft
	Vertical	0.005	ft

Table 3-6. Injection setup at the wells

	Unit	IW-1	IW-2	IW-3	IW-4	IW-5	IW-6
EVO Injection Rate	ft ³ /d	192.5	192.5	192.5	192.5	192.5	192.5
EVO Volume	ft ³	14.7	14.7	14.7	14.7	14.7	4.7
EVO Duration	d	0.076	0.076	0.076	0.076	0.076	0.076
EVO Br Conc	mg/L	565	565	565	565	565	565
Chase Injection Rate	ft ³ /d	192.5	192.5	192.5	192.5	120.3	192.5
Chase Volume	ft ³	11.9	11.9	11.9	11.9	7.5	11.9
Chase Duration	d	0.06	0.06	0.06	0.06	0.03	0.06
Chase Br Conc.	mg/L	0.7	0.7	0.7	0.7	0.7	0.7

Figure 3-23 show the simulated bromide distribution at 0, 1, 2, 3, 6 and 12 months after injection based on the Realization #1 permeability distribution. Br migrates most rapidly downgradient in the southern portion of the model domain due to a high K zone present in this area in realization 1 (see **Figure 3-22**). This causes Br to increase rapidly in MW-3. However, Br stays low in MW-2 due to the absence of higher K material in an HPT boring adjoining MW-2.

Figure 3-24 shows the simulated Br tracer breakthrough curves at injection and monitoring wells for each of the five model realizations and field monitoring results. Model fit was evaluated by calculating the Root Mean Square Error (RMSE) between simulated and observed concentrations for each realization (**Table 3-7**). Most of the model realizations provided a reasonable fit to the monitoring results. However, some realizations clearly performed better than others. This is not surprising since the Br monitoring results reflect the actual K distribution in the aquifer, while the model realizations are a small subset of the infinite number of potential K distributions that could occur.

Overall, realization #1 provided the best fit to the Br breakthrough results with the lowest overall RMSE. Realization #1 also provided a reasonably good fit to the timing of Br breakthrough and peak concentrations in IW-1, IW-6, MW-3, MW-4, and MW-5.

None of the realizations provided a good match to results for IW-3 and MW-2. The relatively poor match for these wells is likely due to an HPT boring (HPT-12) that was installed in this area. This HPT boring indicated there was no high K material. As a result, all the realizations predicted slow Br migration through IW-3 and MW-2. The more rapid Br breakthrough observed MW-2 suggests that there is a high K channel in this area that was not detected by the HPT boring.

Overall, realization #1 provided the best match to the tracer breakthrough results and will be used in subsequent simulations evaluating aquifer cleanup downgradient of the PRB.

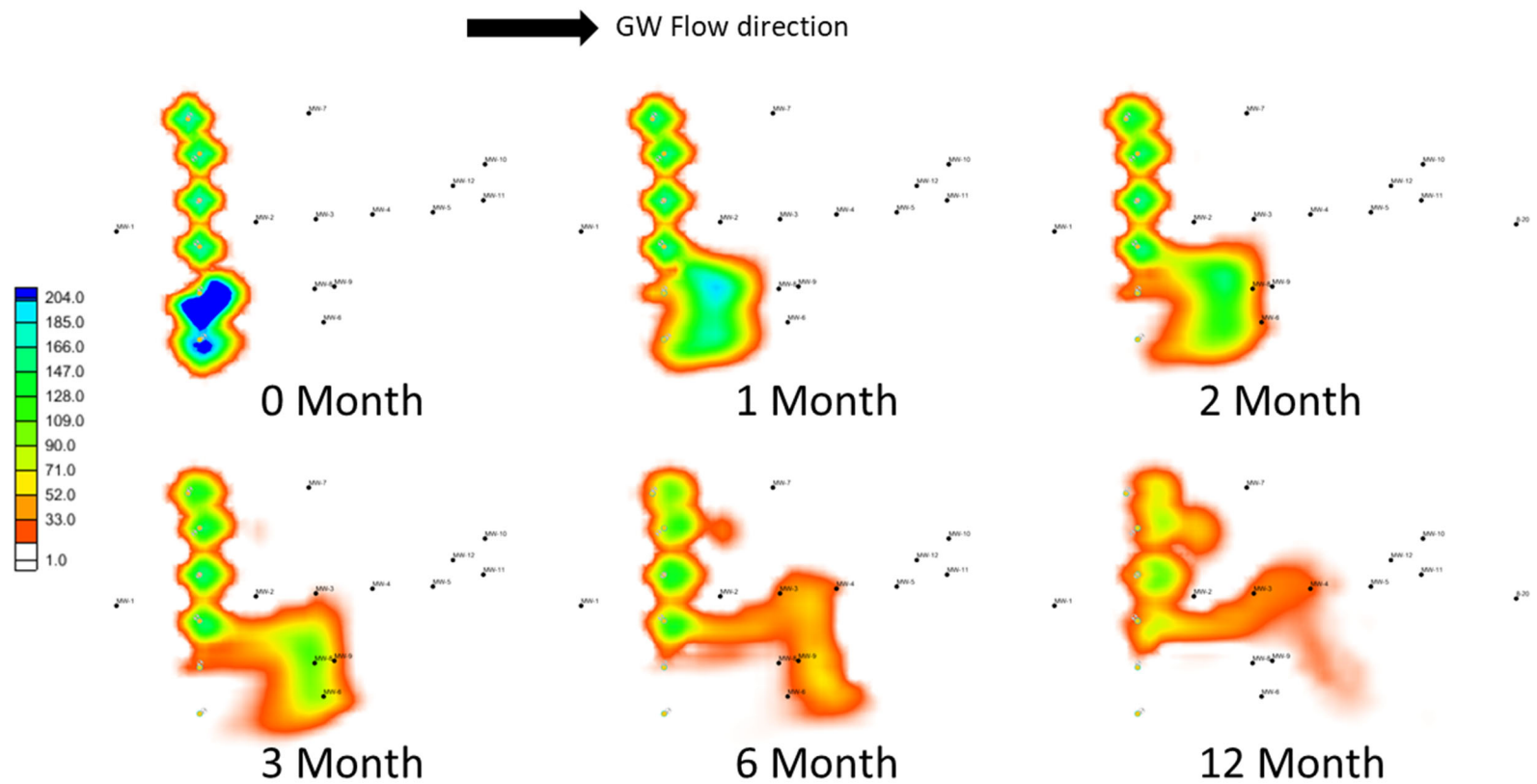


Figure 3-23. Simulated bromide concentration in layer 12 (620.7 ft msl) for realization #1 at 0, 1, 2, 3, 6, and 12 months after Injection.

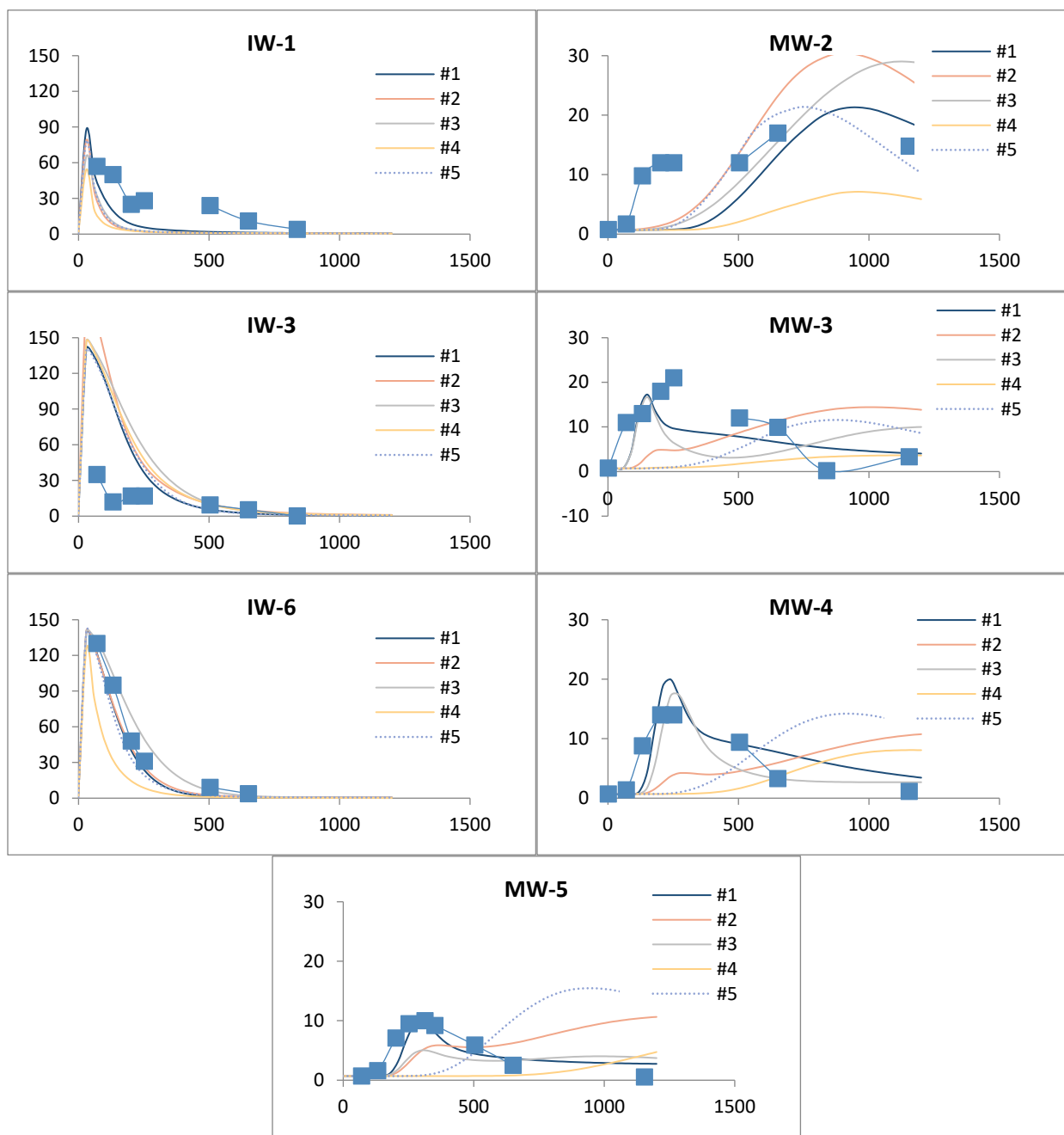


Figure 3-24. Comparison of observed Br concentrations at injection wells (left) and monitoring wells (right) with simulation results for realizations 1 to 5.

Table 3-7. Root Mean Squared Error (RMSE) of realizations.

Realization	#1	#2	#3	#4	#5
Overall	17.1	21.7	20.1	22.4	18.7
IW-1	18.0	22.8	22.0	25.5	22.0
IW-3	45.8	58.5	54.2	50.3	46.3
IW-6	12.1	11.1	11.2	35.1	15.9
MW-1	0.3	0.2	0.2	0.2	0.2
MW-2	6.6	7.1	7.6	8.7	6.3
MW-3	5.9	9.7	7.7	10.6	10.8
MW-4	3.4	6.8	3.1	7.7	8.2
MW-5	1.9	4.8	3.6	5.7	7.1

The calibrated numerical model was then used to evaluate the effect of mass transfer between mobile and immobile zones on downgradient TCE concentrations following installation of the PRB. Transport parameters were identical to the Br tracer simulations using the realization #1 K distribution. The TCE retardation factor was set to 2 for both the higher and lower K zones. The TCE concentration distribution at the start of the simulation was generated by allowing 30 mg/L TCE to migrate into the pilot test area for 50 years. TCE removal within the PRB was simulated by assigning an effective 1st order decay rate of 0.2 d⁻¹ to cells within a 45 ft wide by 7.5 ft long treatment zone.

Figure 3-25 shows the simulated TCE distribution in plan and profile after the initial 50-yr loading period and 5 years after installation of the PRB. After 50 years of contaminant loading, TCE had migrated through the higher K channels and was distributed throughout most of the model domain. However, TCE concentrations remained low in large zones of low K material, when there were no nearby high K channels (e.g. upper right corner of plan view and lower right corner of profile view). At 5 years after PRB installation, TCE concentrations in the higher K channels have declined dramatically. However, substantial TCE concentrations remain in lower K zones.

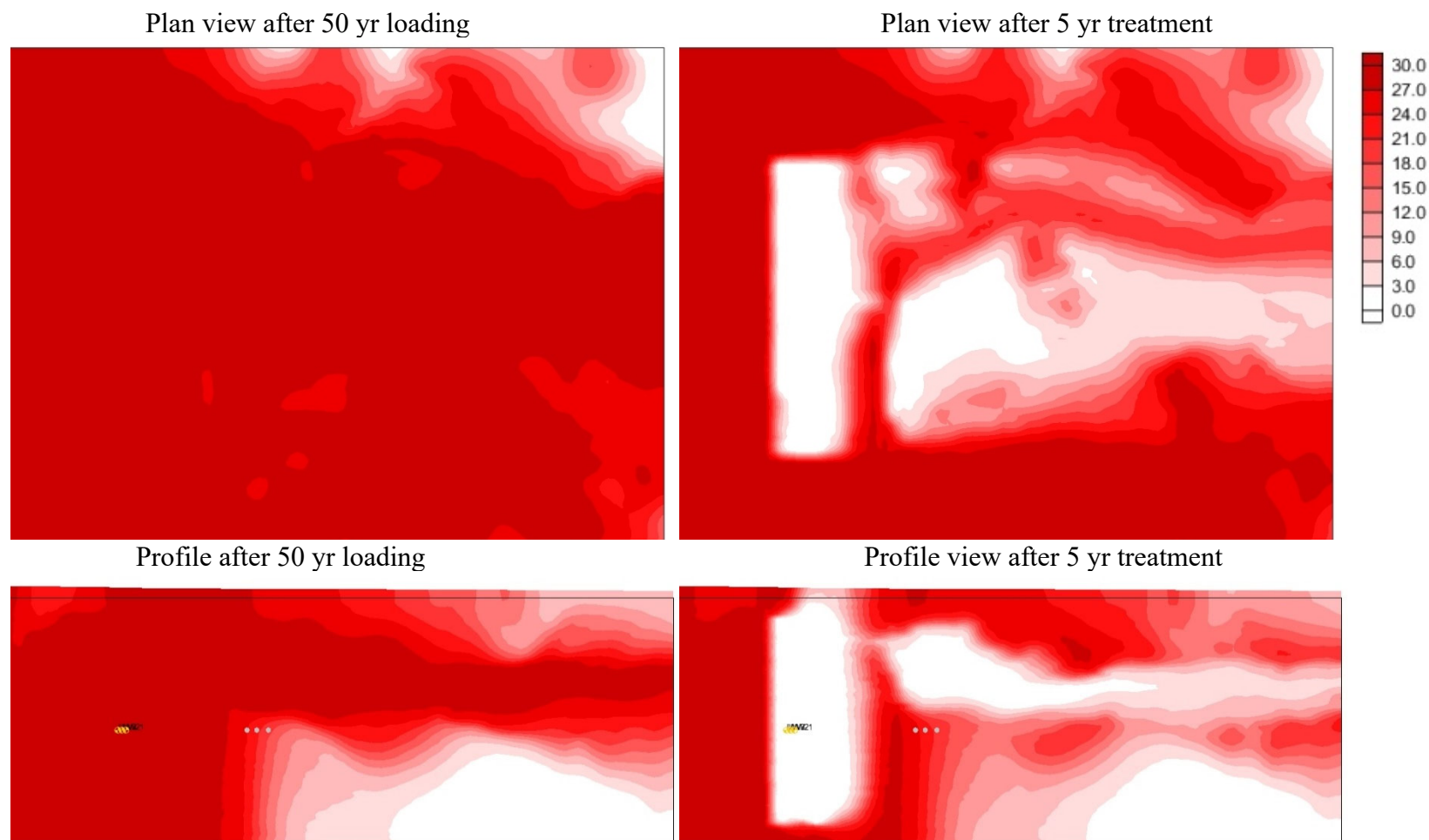


Figure 3-25. Contaminant distribution after 50 years of source loading and 5 years after source removal.

Measured changes in contaminant concentrations in MW-2, MW-3, MW-4 and MW-5 are compared to numerical simulation results in **Figure 3-26**. Measured and simulated concentrations are presented as relative concentrations (C/C_0) to account for differences in measured concentrations in monitor wells prior to PRB installation. The large variations in simulated concentration versus depth make it difficult to directly compare model results with concentration measurements in the wells with 10-ft long screened intervals. In the first approach, we calculated the arithmetic average of TCE concentrations in each model cell intersected by the monitor well screen. In the second approach, the TCE concentrations in each cell were weighted by the steady-state groundwater flow (Q) in that cell.

Figure 3-26 shows both the arithmetic average concentrations and Q-weighted concentrations in MW-2, MW-3, MW-4 and MW-5. The Q-weighted concentrations are generally lower due to the greater weight assigned to cells in high K zones where concentrations decline more rapidly. Concentrations measure in monitor wells during low flow sampling are expected to be generally be closer to the Q-weighted values.

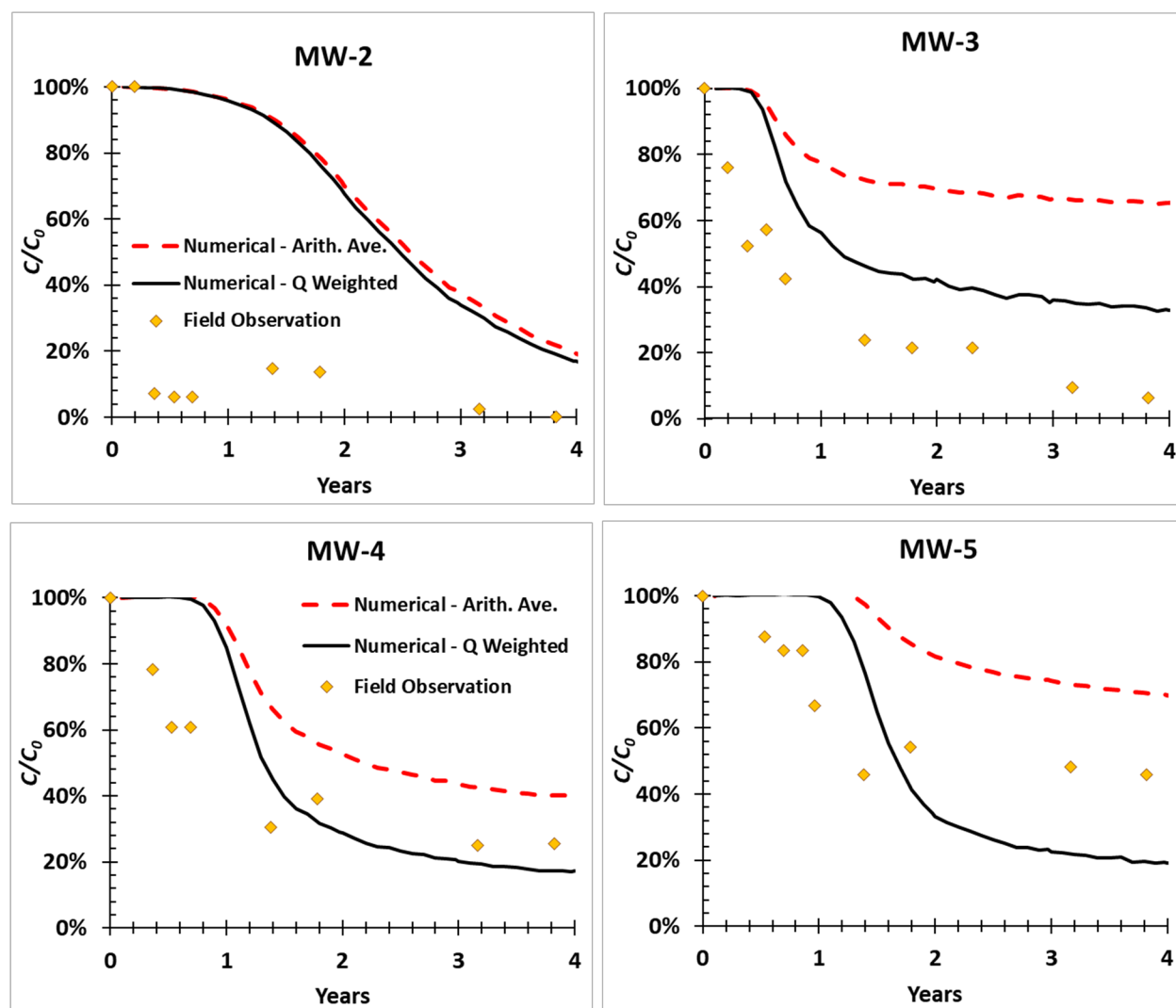


Figure 3-26. Relative concentrations (C/C_0) versus time in downgradient monitor wells following PRB installation.

Overall, the numerical model provided a reasonably accurate prediction of concentration versus time trends in downgradient monitor wells when using a high K/low K cutoff value of 3.2 ft/d. Q-weighted average concentrations more closely matched observed concentrations in MW-3, MW-4 and MW-5. In each of these wells, contaminant concentrations declined relatively rapidly during the first 2 years, then appeared to plateau or decline more slowly due to slower migration through the low K zones. The match between simulated and observed concentrations was relatively poor in MW-2, similar to the Br tracer modeling results. In all the wells, the initial decline in contaminant concentrations lagged observed concentrations, possibly due to an over estimation of the TCE retardation factor in the high K zones.

To evaluate long-term trends, the numerical model was used to simulate TCE concentrations over a 100-year period following PRB installation. For this simulation, the PRB was assumed to extend over the entire pilot test area and to be 100% effective in reducing TCE concentrations discharging from the EVO treated zone. **Figure 3-27** shows simulated Q-weighted average concentrations in MW-2, MW-3, MW-4 and MW-5. TCE concentrations are projected to drop below the MCL in MW-2 within 20 years. However, TCE concentrations in MW-5, 40 ft downgradient, are not projected to decline below 5 µg/L for over 100 years.

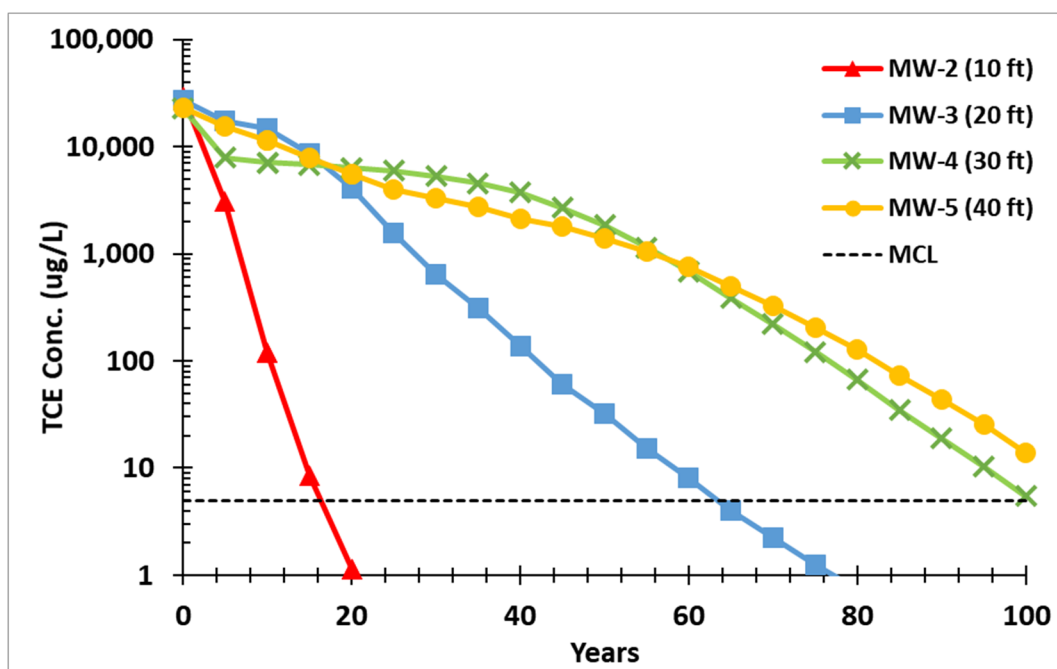


Figure 3-27. Projected long-term trends in Q-weighted TCE concentrations in monitor wells following PRB installation.

3.1.3.3 Semi-Analytical Model

Matrix diffusion can greatly increase groundwater cleanup times following source removal. When contaminants first enter an aquifer, the contaminants will be most rapidly transported through the higher K zones. However, molecular diffusion can slowly transport these contaminants into lower K silts and clays. Once the contaminant source is eliminated, contaminant concentrations in the higher K zones will decline and contaminants will begin to

diffuse back out of the lower K zones, slowing the rate on contaminant cleanup. The extent and importance of matrix diffusion in slowing aquifer cleanup is function of volume and dimensions of both high and low K zones.

There have been many approaches to simulate and understand the back-diffusion process. Numerical models can be used for contaminant transport with matrix diffusion, but this can be time consuming and expensive due to the fine spatial discretization required to generate accurate results (Chapman et al., 2012). Falta and Wang (2017) recently developed a semi-analytical model that uses a combination of analytical and numerical methods to accurately simulate these processes with less computational time.

3.1.3.3.1 REMChlor-MD

The REMChlor-MD model can be used to simulate contaminant transport in the presence of matrix diffusion using the semi-analytical model developed by Falta and Wang (2017). It supersedes REMChlor (Remediation Evaluation Model for Chlorinated Solvents - Falta et al., 2007) which is an analytical solution for simulating contaminant transport and degradation. REMChlor-MD was developed based on the MS Excel. We used a FORTRAN based REMChlor-MD version without the graphical user interface to evaluate long-term cleanup at AFP3.

The REMChlor-MD requires various parameters including model configuration (i.e. domain size, grid size, and a number of cells), aquifer characteristics (i.e. K and porosity), contaminant parameters (i.e. concentration, source size, and retardation factor) and plume degradation and source remediation parameters. These parameters were estimated based on the site characterization results presented in **Section 3.1.2**. The TCE degradation rate was assumed to be zero outside of the EVO treated zone. Typically, the most important parameters are the volume fraction (V_F) of the higher K zone, the diffusion length (L), and the interfacial area (A_{MD}) between higher K and lower K zones.

In our analysis, V_F and the average thickness of the lower K zones were calculated with using the results of the sixteen HPT borings. When most of the formation is higher K material, lower K zones will be bounded above and below by higher K and the diffusion length will be half of the average thickness of the lower K zone. However, at AFP3, most of the formation is lower K material and the lower K zones often contact a single high K zone. As a result, the diffusion length at AFP3 is equal to the average thickness of the low K zone. The T-PROGS analysis presented above indicated that the formation consisted of 18% higher K material and the average thickness of 1.37 ft and lower K zones with an average thickness of 6.01 ft.

3.1.3.3.2 AFP3 PRB Simulation

REMChlor-MD (Muskus and Falta, 2018) was used to simulate contaminant concentrations over time after installation of the PRB at AFP3. Parameter values used in the REMChlor-MD simulations are shown in **Table 3-8**. The contaminant source was 10 ft by 13 ft with a 50-year loading period, followed by complete removal of source following PRB installation. The K of

the higher K zone was adjusted to match the arrival time of the Br tracer at downgradient monitor wells.

Table 3-8. Model Parameters for REMChlor-MD Simulation

Parameters	Value	Site Characterization Methods
Volume Fraction (V_F) (= % High K)	0.18	HPT
Diffusion Length (L)	6.01 [ft]	Integration of HPT Data
Interfacial Area (A_{MD})	$(1-V_F)*V_T = (A_{MD}*L)$	Relationship V_F and L
Cont. Loading Period	50 [yr]	Historic data
Cont. Source Zone	10 [ft]	Width
	13 [ft]	Depth
High K	21.1 [ft/d]	Br-Tracer Test
Porosity	0.3	Direct Push, Shelby Tube
Hydraulic Gradient	0.0028 [-]	Monitoring well

Figure 3-28 presents the concentration breakthrough curves at the 10, 20, 30 and 40 ft. down-gradient of PRB, analogous to the location of the MW-2 through MW-5. Simulation result predicts that TCE concentration will rapidly increase in all wells following the initial release, and then drop rapidly following PRB installation at 50 years. The predicted concentration after 50 years increases with increasing distance down gradient because TCE is continuing to diffuse back out of the lower K layers and down gradient monitor wells have TCE mass from more interfacial area.

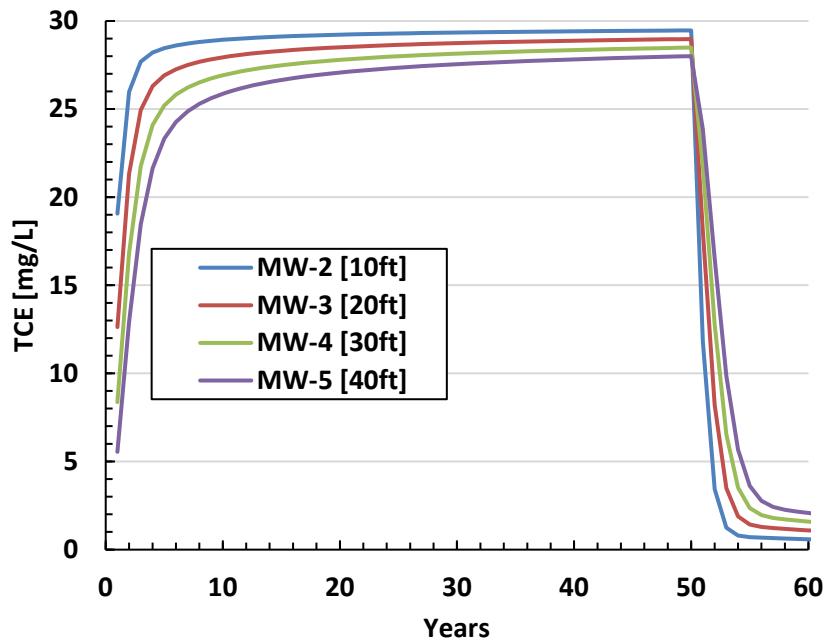


Figure 3-28. TCE concentrations versus time from REMChlor-MD with complete source removal after 50-year loading period.

To provide a more appropriate comparison between simulated and observed concentrations, TCE concentrations were normalized by dividing by the simulated or observed concentration immediately prior to PRB installation (**Figure 3-29**). The semi-analytical model provided reasonably good estimates of the concentration declines in MW-2, MW-3, and MW-4 for the 4-year monitoring period. In MW-5, 40 ft downgradient, model concentrations decline more rapidly than observed after 2 years. The somewhat slower decline in MW-5 could be due to lower K in the transmissive zone, slowing TCE flushing.

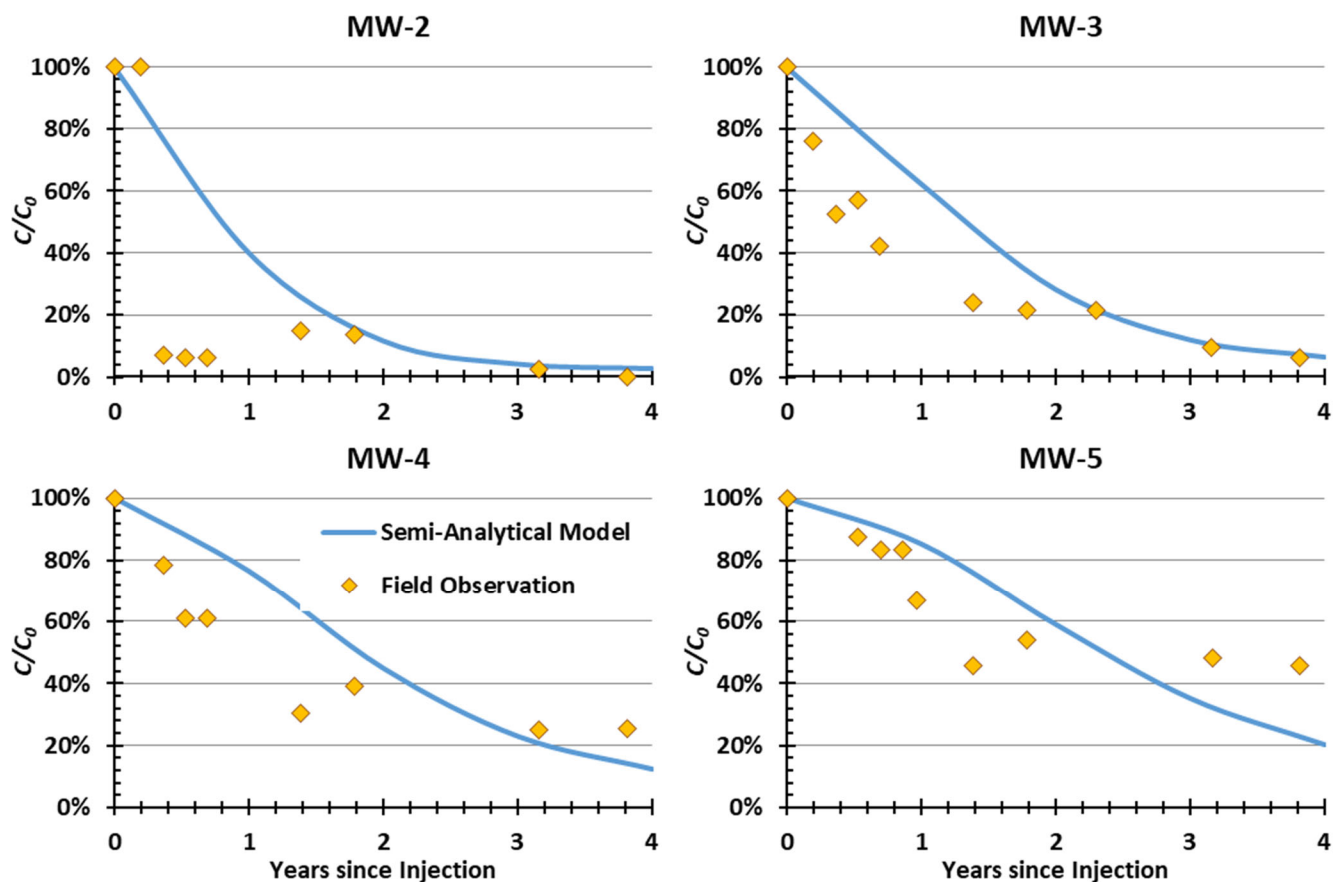


Figure 3-29. The graphs of C/C_0 vs. time at four monitoring well locations.

The relatively good match between the semi-analytical model predictions and field monitoring results suggests that this model provides a reasonable representation of the major physical processes controlling TCE cleanup in the aquifer.

3.2 NTC ORLANDO OU2 OVERVIEW

OU2 located in the southern portion of the McCoy Annex of former Naval Training Center (NTC) Orlando. The various areas were used as a landfill from about 1960 until about 1978. Landfill operations consisted of excavating ditches (100 to 200 ft long by 20 to 25 ft wide by 10 to 15 ft deep) and filling with wastes. Trenches were filled with waste to within 3 or 4 ft of the ground surface and then backfilled with soil and seeded. The estimated volume of waste is more than 1,000,000 cubic yards (yd^3). Landfill waste reportedly included hospital wastes, paint and paint thinner, automobile batteries, airplane parts, low level radioactive waste, and asbestos.

The soils at the site belong to the Smyrna-Bassinger-St. John's and the Smyrna Urban Land complex, which consist of fine sands that are nearly level to gently sloping, and poorly to moderately-well drained (US Department of Agriculture Web Soil Survey). The sediments across the site consist primarily of quartz sand with varying amounts of silt, clay, and shell

fragments that vary both laterally and vertically. The topography at the site is relatively flat. A drainage ditch runs from north to south along the eastern side of the site and appears to form a hydraulic barrier. Groundwater at the site flows to the east/southeast.

The potentiometric surface of the unconfined (water table) aquifer typically occurs at depths of about 6 to 8 ft bgs. Groundwater flow is generally to the east towards the drainage canal with an average hydraulic gradient of ~ 0.002 ft/ft. Based on a 1998 pumping test, the surficial aquifer has an average estimated transmissivity of $602 \text{ ft}^2/\text{d}$, storativity of 0.04, and K of 25 ft/d (Tetra Tech, 2001). Assuming an effective porosity of 0.2, the average groundwater velocity is estimated to be roughly 90 ft/yr .

Two shallow groundwater plumes covering approximately 23 acres have been identified that appear to be discharging from the former landfill and migrating towards a nearby drainage canal. Constituents of concerns (COCs) in groundwater included benzene, TCE, VC, and iron. The plume intersects the adjacent drainage canal, but volatile organic compounds (VOCs) impact to surface water above regulatory standards have not been detected. Installation of an emulsified vegetable oil (EVO) permeable reactive barrier (PRB) was selected to prevent discharge of VOCs to the drainage canal (Tetra Tech, 2003).

3.2.1 OU2 EVO Barrier

An EVO PRB was installed at the site in 2007 (CH2M HILL, 2008) and expanded in 2012 to control migration of TCE and cDCE to the drainage canal (Borden, 2017). **Figure 3-30** shows the location of monitoring wells, injection wells, CPT borings and traditional HPT borings in the northern portion of the PRB near MW-47B, which is the primary focus of this project. **Figure 3-31** shows the location of 15 additional HPT borings (HPT-7 to HPT-21) installed in 2018 to better define the permeability distribution in this area. The low-K HPT tool described in **Section 2** was used in 2018 allowing use of lower injection rates and probe advance speed, reducing the lower range of K measurement.

Figure 3-32 shows the variation in TCE, cDCE, VC and Cl# ethene with time in monitoring wells OU2-43B and OU2-47B, downgradient of the EVO PRB. Following EVO barrier installation in 2012, TCE begins to gradually decline, cDCE slowly increases and there is a modest decline in Cl#. Sampling of the injection wells show essentially complete removal of TCE. The slow decline in TCE in the monitoring wells is surprising since travel time from the barrier to these downgradient wells was estimated to be less than a year.

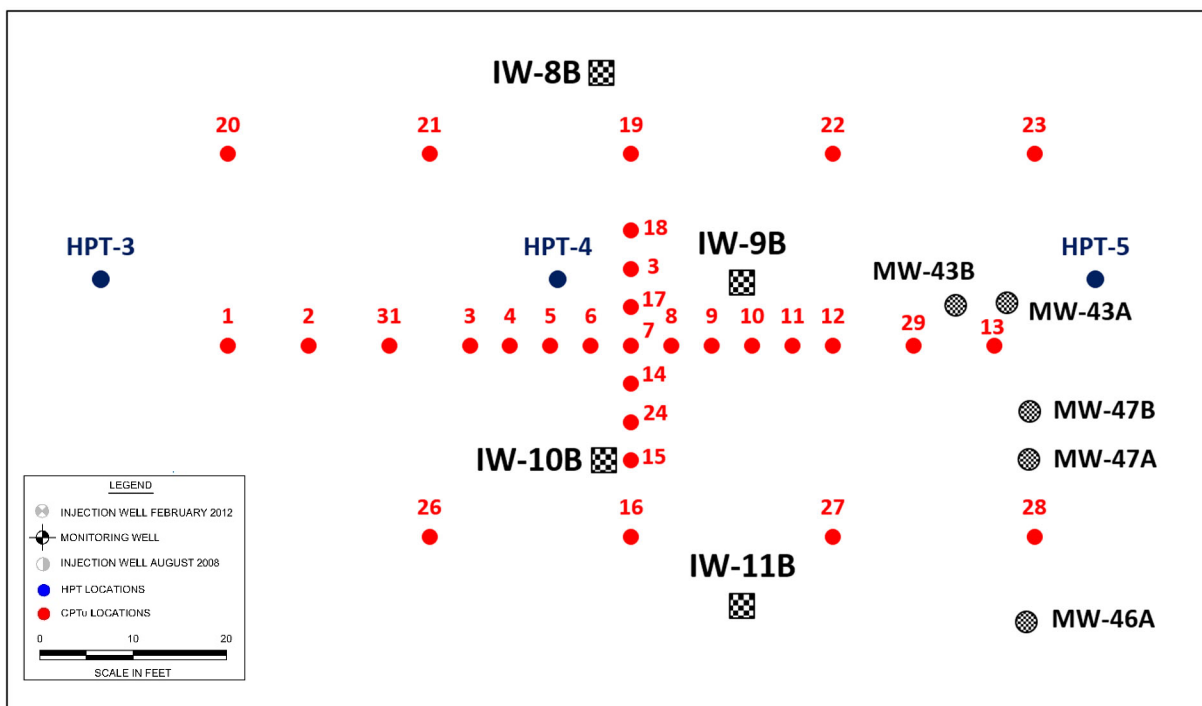


Figure 3-30. CPT and HPT boring locations in the northern characterization area.

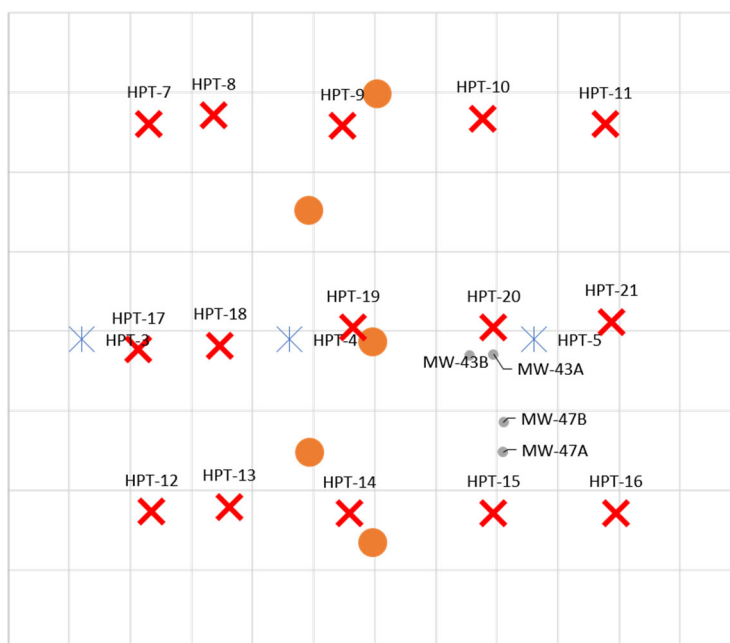


Figure 3-31. HPT Locations (HPT-7 through HPT-21) for January 2018 Fieldwork.

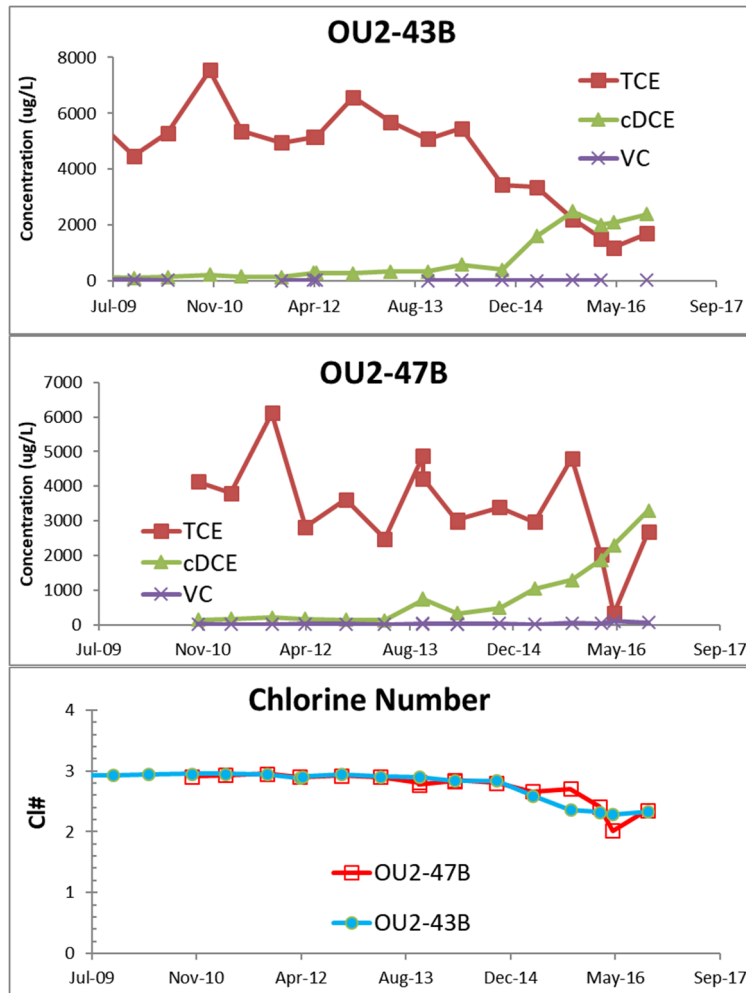


Figure 3-32. Variation in TCE, cDCE, VC and Cl# versus time in OU2-43B and OU2-47B.

3.2.2 OU2 Site Characterization

Figure 3-33 shows the results of the CPT profiling in a cross-section extending from CPT-1 to CPT-13. A clay unit over 10 ft thick is encountered at an elevation of ~47 ft msl or 35 ft bgs. Overlying this clay is interbedded sand and silty sand. These results were interpolated with T-PROGS to estimate material properties throughout the model domain.

Figure 3-34 shows the results of the HPT profiling in a cross-section extending through OU2-17A. Hydraulic conductivity values were first calculated using Eq 2-10. The skin correction factor was adjusted to match the average K of the A zone measured in a prior pumping test (Tetra Tech, 2001). Soils were classified as low K ($K < 1$ ft/d), moderate ($1 < K < 10$ ft/d), high ($10 < K < 100$ ft/d) and very high ($K > 100$ ft/d). These results were interpolated with T-PROGS to estimate material properties throughout the model domain. Overall, the HPT profiles were relatively consistent, showing a higher permeability sand and gravel (10 to 500 ft/d) A Zone underlain by a lower K (0.5 to 20 ft/d) B Zone, then a higher K (5–100 ft/d) C Zone. From 60 to 50 ft msl, K declines from ~ 10 ft/d to <1 ft/d.

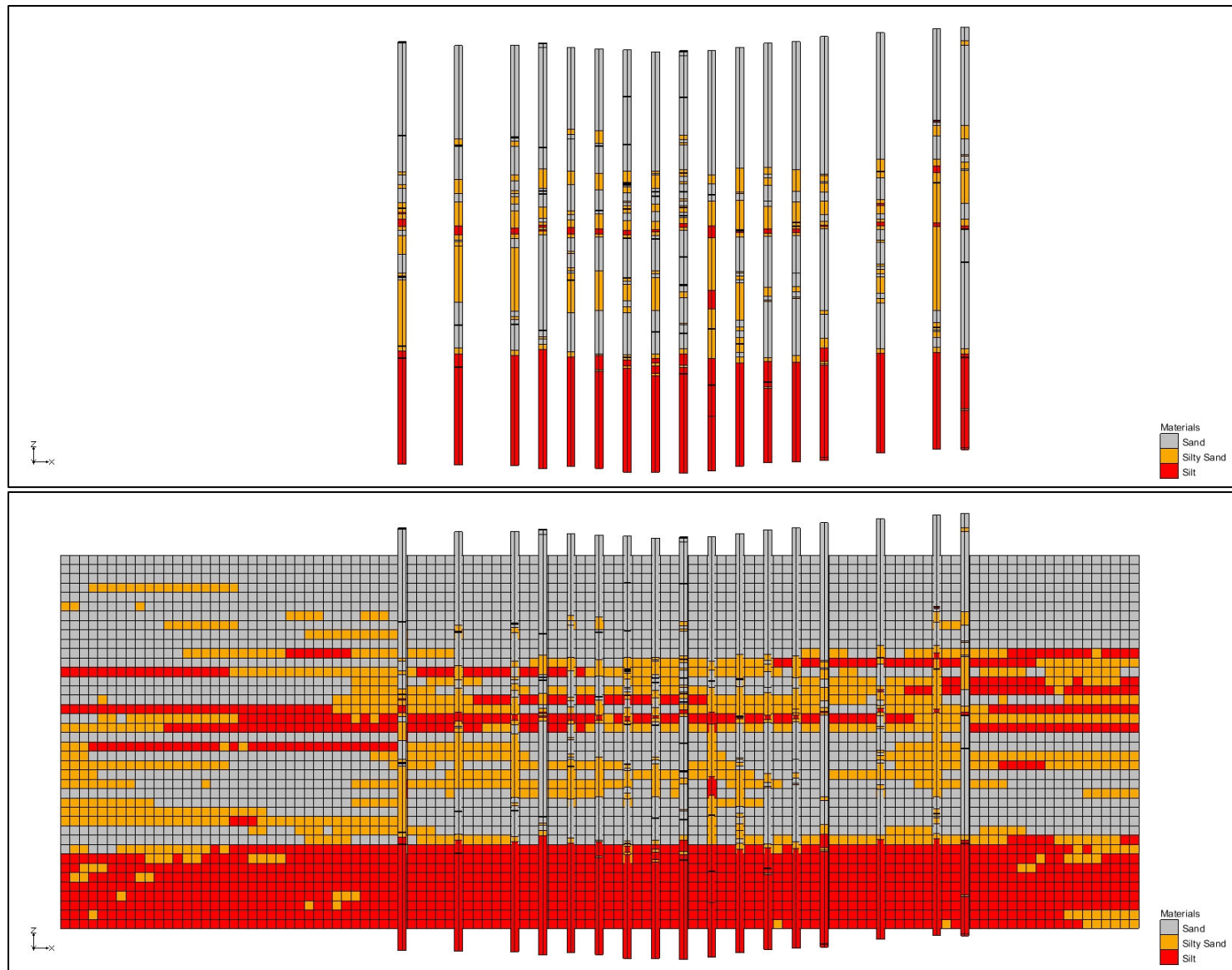


Figure 3-33. CPT borings and interpolated soil units in cross section extending from CPT 1 to 13.

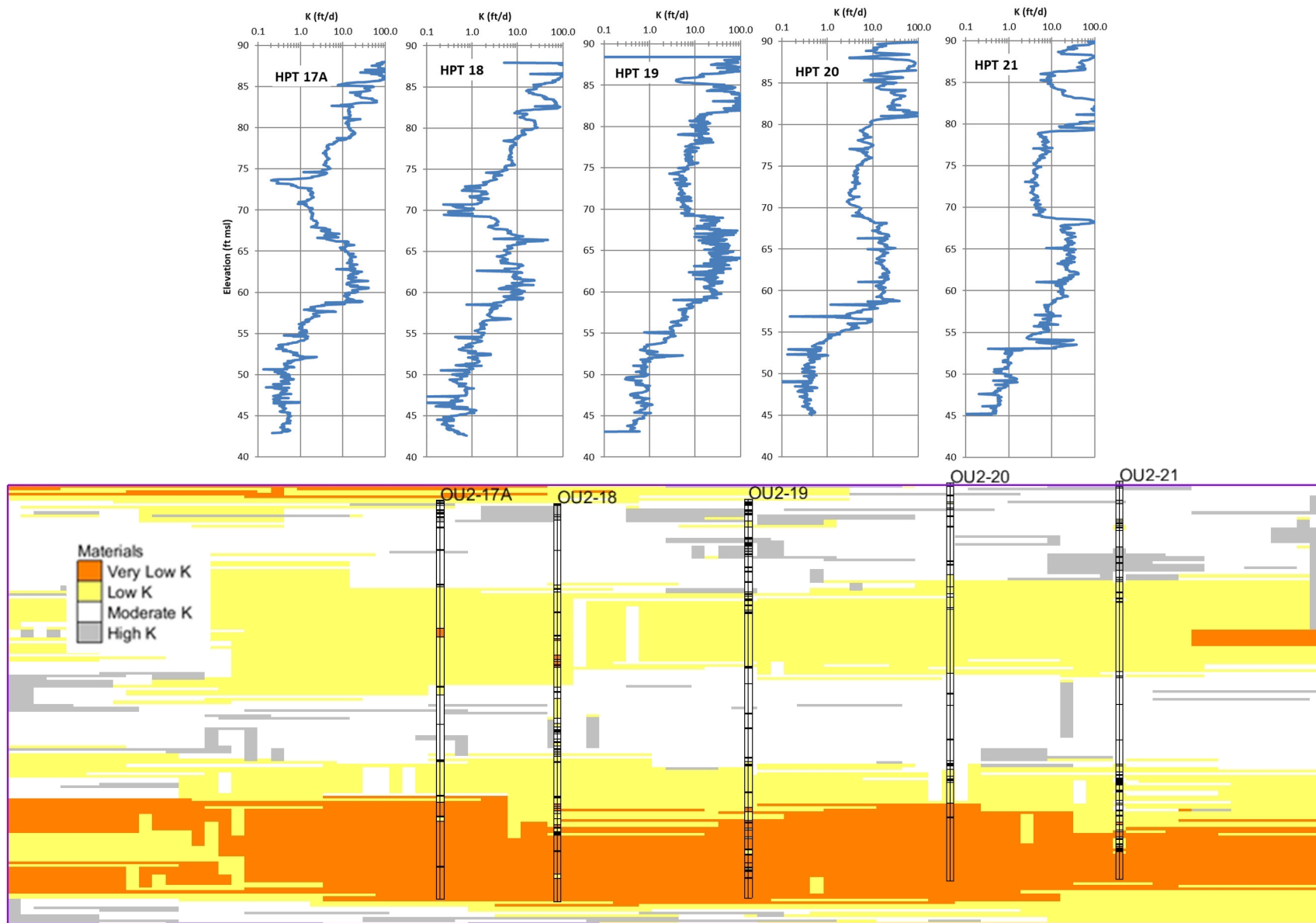


Figure 3-34. HPT borings and interpolated soil units in cross section extending through OU2-17A.

Figure 3-35 shows profiles of EC, K and non-reactive solute transport velocity (V) with elevation. Also shown are lines indicating plus and minus one standard deviation for each parameter. The plotted EC values are for the arithmetic mean. The mean and standard deviation for K are computed with the base 10 Log transformed values. V was calculated assuming an average hydraulic gradient of 0.002 ft/ft and porosity of 0.3. Higher values of EC generally correspond with higher clay content, which results in lower values of K.

As shown in **Figure 3-32**, TCE concentrations declined very slowly with time in OU2-43B and OU2-47B (screened between 50 and 55 ft msl). This was unexpected since the average travel time from the barrier to these wells was estimated to be less than one year. The gradual decline in K with depth from 60 to 50 ft msl may explain the slower than anticipated treatment performance of the EVO barrier.

OU2-43B and OU2-47B were screened in the more highly contaminated interval from 50 – 55 ft msl. The estimated groundwater transport velocity between 50 and 55 ft msl varies between 1 and 10 ft/yr. The travel time from the EVO treated zone to these wells is between 2 and 20 years, with the longest travel times in the deeper zones where TCE concentrations are highest.

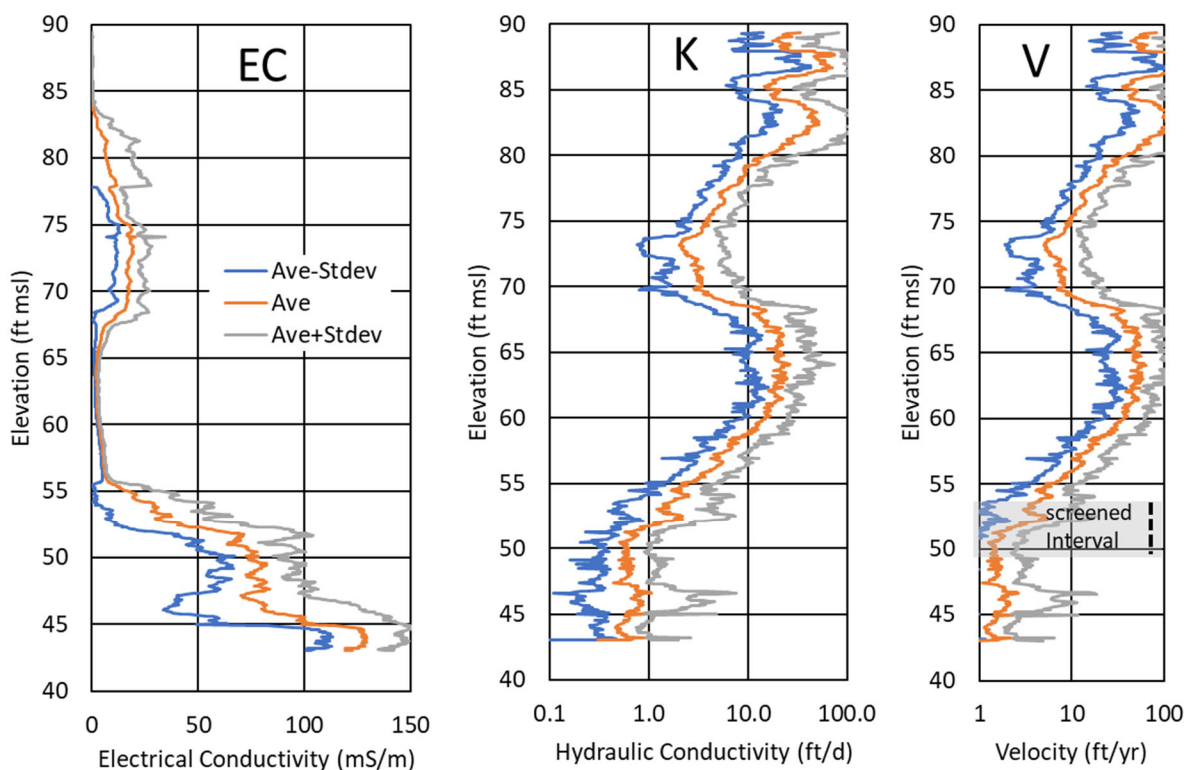


Figure 3-35. Electrical conductivity (EC), hydraulic conductivity (K) and solute transport velocity versus elevation plus and minus one standard deviation.

3.2.2.3 Spatial Distribution of TCE and cDCE

Direct push groundwater samples were collected at four depths (25, 30, 35, and 40 ft bgs) immediately upgradient of the EVO barrier, within the EVO injection zone, and downgradient near OU2-43B in May 2016. These results are compared with K profiles measure by HPT in **Figure 3-36**. Upgradient of the PRB, TCE is the dominant chloroethene with the highest concentrations observed immediately adjoining the clayey silt confining layer and decrease rapidly with distance. Within the EVO injection zone, TCE has been extensively converted to cDCE. Downgradient, TCE concentrations have declined as much.

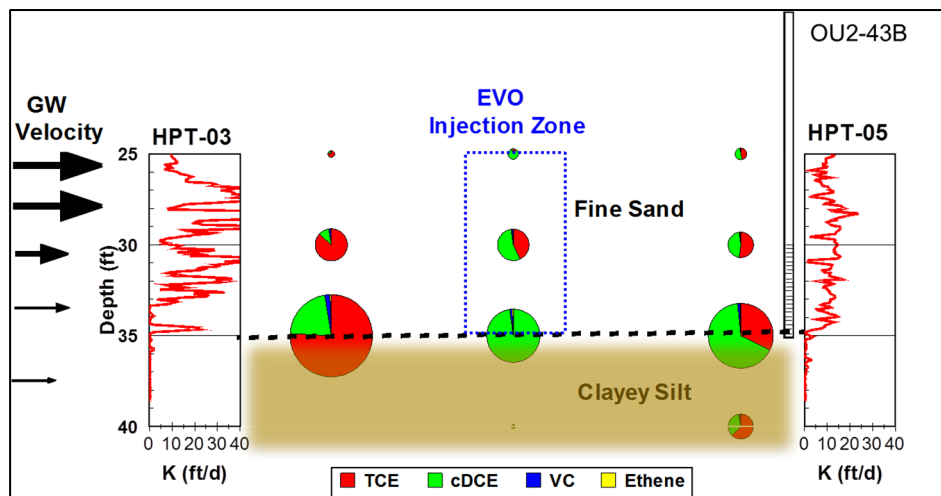


Figure 3-36. TCE, cDCE, VC, and ethene at varying depths upgradient, within, and downgradient of the EVO injection zone. Area in pie chart is proportional to concentration.

3.2.2.4 Back Diffusion

To evaluate the potential for back-diffusion of TCE out of the underlying confining unit, a continuous soil core was collected adjoining OU2-43B from 25 to 40 ft bgs. Subsamples were collected and analyzed for CVOCs and soil particle size distribution. **Figure 3-37** shows the results of this evaluation along with the K profile measured at this location. TCE concentrations were a maximum 2 ft into the confining layer where the clay + silt content was highest. This information will be used to determine if back-diffusion from the confining layer is contributing to slower than desired treatment of the aquifer downgradient of the PRB.

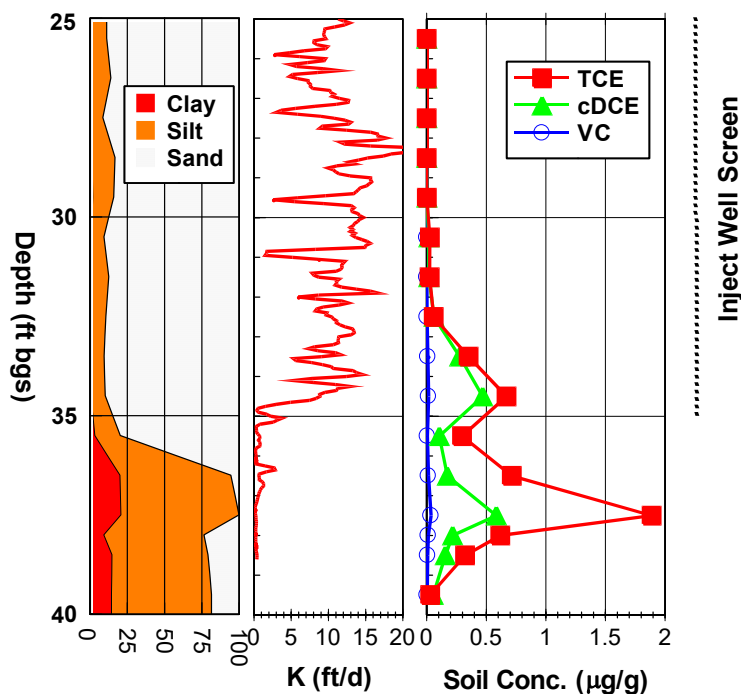


Figure 3-37. Profiles of soil composition, K, and TCE, cDCE and VC concentrations in soil samples collected from a boring adjoining OU2-43B.

The Dandy-Sale (DS) model (Sale et al., 2008) within the Matrix Diffusion Toolkit (MDT) (Farhat et al., 2012) was used to evaluate TCE diffusion into the clayey silt confining layer and back diffusion over time. The TCE release was assumed to reach to occur in 1978 with treatment beginning in 2012 after installation of the EVO PRB. The low K soil organic carbon content was assumed equal to 0.0005 g/g resulting in a TCE retardation factor of 1.07 in the low K zone. Default values from Farhat et al. (2012) were used for all other model parameters.

Figure 3-38 shows the simulated vertical profile of TCE in the confining layer at 10 m downgradient of the EVO PRB compared to measured concentrations in 2016. The DS model provided a relatively good match to the measured concentrations matching the depth and maximum concentration observed.

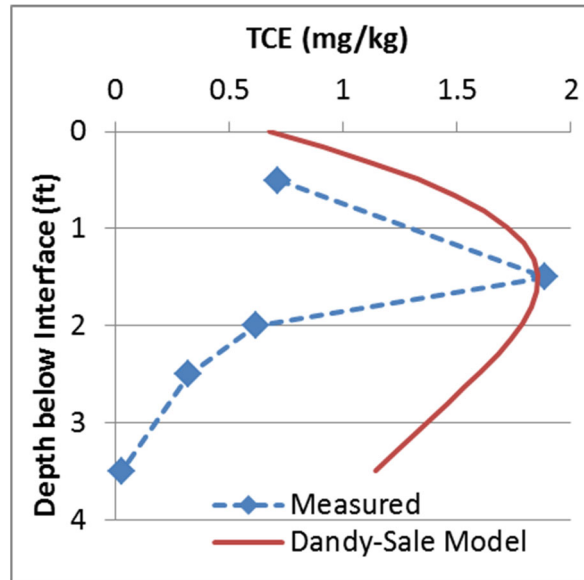


Figure 3-38. Comparison of measured concentrations versus simulated TCE profile generated with Dandy-Sale Model (Sale et al., 2008).

Figure 3-39 shows the simulated mass of TCE entering the drainage canal over time following installation of the EVO PRB in 2012. For comparison, the second y-axis on **Figure 3-39** shows average TCE concentrations in a monitoring well (10-ft screen) installed immediately above the confining layer and adjoining the drainage canal. Mass discharge drops rapidly following installation of the EVO PRB in 2012. However, after 2017, mass discharge declines more slowly as TCE is released from the confining layer by back diffusion downgradient of the PRB and upgradient of the GOAA canal. The total mass released by back diffusion is relatively small due to the short distance from the PRB to the canal (~50 ft). By 2030, TCE concentrations in a monitoring well adjoining the drainage canal are predicted to drop below 5 $\mu\text{g/L}$. In summary, back diffusion from the confining layer, downgradient of the PRB, is not expected to substantially limit the effectiveness of the PRB in reducing TCE discharge to the canal.

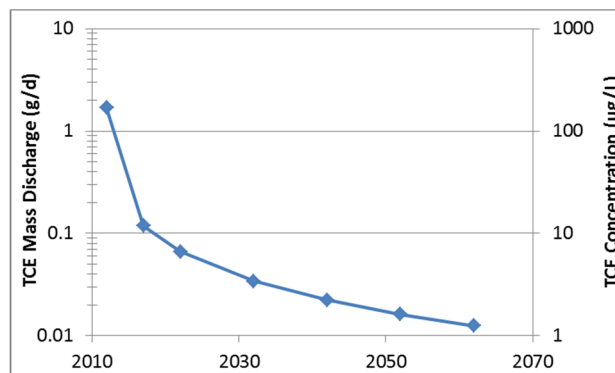


Figure 3-39. Predicted mass discharge and average TCE concentrations in a monitoring well (10-ft screen) installed immediately above the confining layer and adjoining the GOAA canal.

3.3 Flow and Solute Transport Simulation

The groundwater flow and solute transport models MODFLOW (McDonald and Harbaugh, 1988) and MT3DMS (Zheng and Wang, 1999) were used to simulate transport of TCE in the aquifer at OU2 and remediation following EVO injection. Porosity, molecular diffusion coefficient, and dispersivities are the same as shown in **Table 3-5**. The hydraulic gradient was set to 0.002 ft/ft with groundwater discharging to the drainage canal a short distance downgradient of the PRB. The area surrounding OU2-43B and OU2-47B was represented by a 50-layer model with the K in each layer set to the average measured K. The TCE concentration at the upgradient boundary of the C Zone of the aquifer was constant at 8,000 ug/L, beginning 40 years prior to the EVO injection. TCE removal in the PRB was simulated by setting the decay rate in the EVO treated zone to 0.1/d.

Figure 3-40 shows the simulated vertical distribution of TCE in aquifer prior to PRB installation (T=0 yr) and 40 years after PRB installation. Following PRB installation, TCE is effectively flushed from the upper, transmissive portion of the aquifer. However, the monitor well is screened from 50 to 55 ft msl, in a lower K portion of the aquifer, that is not effectively treated following PRB installation.

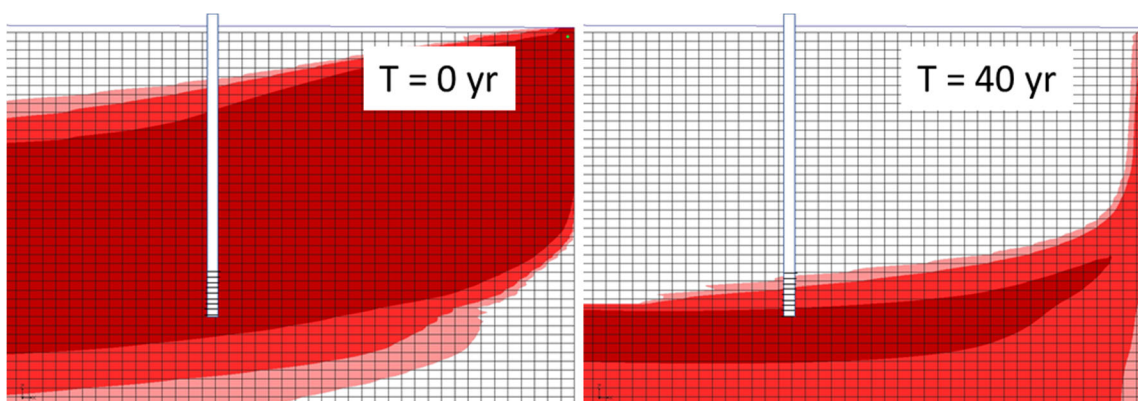


Figure 3-40. Simulated vertical distribution of TCE in aquifer prior to PRB installation (T=0 yr) and 40 years after PRB installation.

Measured TCE concentrations in monitor wells OU2-43B and OU2-47B are compared to simulated concentrations in **Figure 3-41**. These two wells are located close together and are screened over the same vertical interval. Model simulation results were identical for OU2-43B and OU2-175 were identical, so only one line is shown. Simulation results for these wells closely match the measured concentrations in both wells. The arithmetic average and flow-weighted (Q-Wt) average concentrations in the screened interval were similar.

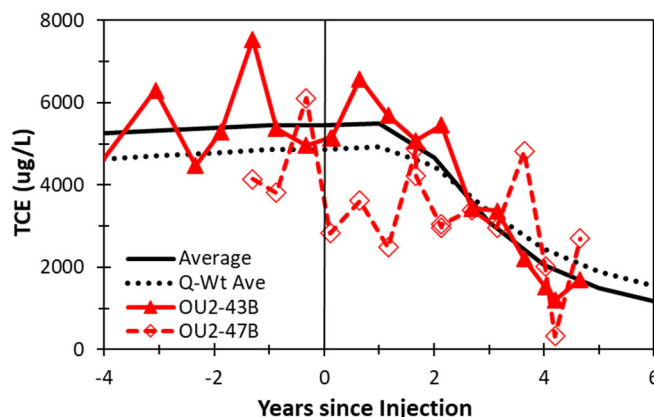


Figure 3-41. Comparison of simulated and observed TCE concentrations in monitor wells OU2-43B and OU2-47B following following PRB installation.

To evaluate long-term trends, the numerical model was used to simulate TCE concentrations over a 40-year period following PRB installation. **Figure 3-42** shows simulated Q-weighted average concentrations in OU2-43B and OU2-47B. TCE concentrations initially decline, then reach a steady-state concentration after about 10 years, due to migration of small amounts of TCE in the lower K zone below where EVO was injected.

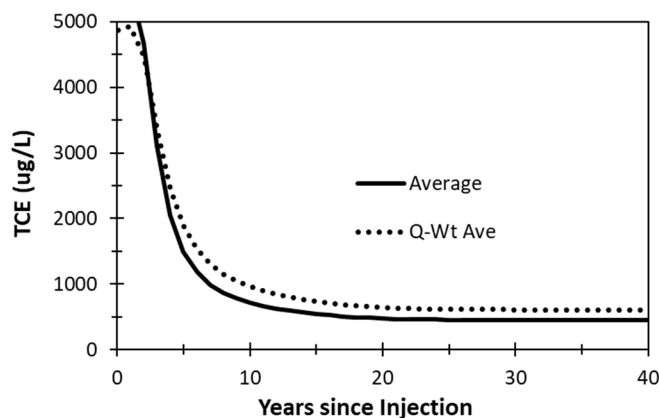


Figure 3-42. Projected long-term TCE concentrations in monitor wells OU2-43B and OU2-47B following PRB installation.

3.4 LESSONS LEARNED

At AFP3 in Tulsa, OK and OU2 in Orlando, FL, permeable reactive barriers (PRBs) were installed by injecting emulsified vegetable oil (EVO) to stimulate biodegradation of trichloroethylene (TCE). At both sites, TCE concentrations rapidly declined to near zero within the PRB. However, downgradient of the PRBs, TCE concentrations declined more slowly than expected. Detailed site characterizations were conducted at both sites, to understand the physical and chemical processes controlling groundwater cleanup, downgradient of the PRBs. These

results were then used to develop high resolution numerical models of groundwater flow and solute transport. Results of this work yielded the following lessons learned.

1. At both sites, large spatial variations in K had a major influence on the groundwater cleanup rate in downgradient monitor wells. TCE was rapidly flushed from higher K zones, but declined much more slowly in lower K zones. In long-screened monitor wells, this gave the appearance of a slow gradual decline in TCE concentrations.
2. Using methods developed in this project, the HPT provided valuable information on spatial variations in K. When this information was used to calibrate high resolution flow and transport models, these models provided reasonably accurate simulations of groundwater cleanup rates in monitor wells.
3. Cone penetrometer testing (CPT) was also used at each site to map soil characteristics. CPT results corresponded with HPT results at both sites. However, the HPT results were more directly useful in model calibration.
4. The mobile-immobile zone modeling approach can be useful for simulating groundwater cleanup. However, at both sites, K varied continuously from high to low. Under these conditions, it can be difficult to identify a sharp cutoff to distinguish between high and low K zones. Additional research is required to identify when use of a mobile-immobile modeling approach is appropriate, and when gradual variations in K control groundwater cleanup times.

4.0 MOBILE-IMMOBILE ZONE MODEL PARAMETER ESTIMATION

Objective: Develop methods to calibrate existing and new mobile-immobile zone models using high-resolution K distributions obtained with DP equipment.

4.1 INTRODUCTION

This task was originally focused on developing parameter estimating methods for three types of mobile-immobile zone models: the dual porosity model, the Matrix Diffusion Tool Kit (Farhat et al., 2012), and the multiple interacting continua (MINC) model. Over the course of this work, and in parallel with project ESTCP ER-201426, we have developed and tested a new modeling approach called the semi-analytic method, that conceptually similar to the MINC method, but simpler, and much more efficient. The semi-analytic method could be implemented in standard finite difference transport codes such as MT3DMS (Zheng and Wang, 1999), and we have built a stand-alone code that uses this method called REMChlor-MD as part of the ESTCP ER-201426 project.

We have recently demonstrated that the semi-analytic method used in REMChlor-MD can accurately reproduce the results of the Matrix Diffusion Tool Kit (Falta and Wang, 2017). For this reason, we believe that the REMChlor-MD model will supersede the Matrix Diffusion Tool Kit, and we do not plan further comparisons with that tool.

Our focus in this project has been on testing the semi-analytic matrix diffusion method, and on developing the parameter estimation methods for using this method with field data collected using the DP tools. The method has been verified by comparison with analytical solutions for matrix diffusion in semi-infinite and finite domains, including cases with parallel fractures and with parent-daughter reactions. The method has been validated by comparison with laboratory experiments for matrix diffusion in a finite layered system, and in a 2D heterogeneous system. The latter experiment allowed us to begin to explore the parameter estimation method for the semi-analytical method.

We have conducted fine-grid 3D numerical simulations using highly heterogeneous grids in MODFLOW/MT3DMS to generate realistic contaminant transport plumes that are strongly affected by matrix diffusion. These simulations use several million gridblocks and take 60-80 hours to run on a fast computer. We then use the REMChlor-MD model to reproduce these results with a few tens of thousands of gridblocks. The REMChlor-MD simulations take about a minute to run on the same computer. These comparisons have allowed us to develop relatively simple methods for estimating the key matrix diffusion parameters needed for the semi-analytical method.

The semi-analytic method has been tested against the dual porosity method for fractured systems. A key feature of the semi-analytic method is that the parameters (V_f , A_{md} , and L) have a direct physical meaning, and can be estimated from direct push and other field data. The dual porosity model also requires the volume fraction (V_f), but it uses a first order mass transfer coefficient, β . In almost all cases, β is treated as a calibration parameter, where its value is adjusted to get a best fit with field data.

The semi-analytic and dual porosity methods were compared to an analytical solution for matrix diffusion in a system of parallel fractures. It was found that the dual-domain method was unable to match the analytical solution at large fracture spacing. In particular, β values that produced a reasonable match of the contaminant loading period were not capable of matching the analytical solution during the unloading (back diffusion) period. In contrast, the semi-analytical method produced good matches with the analytical solutions at all times, and without calibration. With close fracture spacing ($\sim 0.2\text{m}$ or less), the dual porosity model was able to match the analytical solution using a calibrated mass transfer coefficient. The semi-analytical method also matched the analytical solution under these conditions but did not require calibration.

4.2 SEMI-ANALYTICAL MATRIX DIFFUSION METHOD

The semi-analytic method assumes that matrix diffusion between high permeability zones and low permeability zones can be simulated as a 1D process that depends on the distance from the material interface. There are two main cases: a semi-infinite geometry for matrix diffusion from an aquifer into an aquitard, and a finite geometry for matrix diffusion in layered, heterogeneous, and fractured aquifers. The development of the semi-analytical method for the semi-infinite geometry was recently described in Falta and Wang (2017). This section gives the newer derivation for the finite geometry (Muskus, 2017).

The governing one-dimensional matrix diffusion equation assuming decay only in the aqueous phase is:

$$R_l \frac{\partial C_l}{\partial t} = \tau_l D \frac{\partial^2 C_l}{\partial z_l^2} - \lambda_l C_l \quad (4-1)$$

The subscript l refers to the low permeability material. C_l (kg/m^3) is the aqueous concentration, R_l is the retardation factor, τ_l is the tortuosity, D (m^2/s) is the molecular diffusion coefficient, and λ_l (s^{-1}) is the first order decay rate.

Bear et al. (1994), Falta and Wang (2017) and Muskus and Falta (2018) use a fitting function from Vinsome and Westerveld (1980) adapted to the concentration in the low permeability zones:

$$C_l(z_l, t) = (C^{t+\Delta t} + pz_l + qz_l^2)e^{-z_l/d} \quad (4-2)$$

where $C^{t+\Delta t}$ (kg/m^3) is the current concentration at the interface between high permeability and low permeability zones. The concentration penetration depth, d (m), is defined by:

$$d = \frac{\sqrt{\kappa_l t}}{2} \quad ; \quad \kappa_l = \frac{\tau_l D}{R_l} \quad (4-3)$$

The zero level of the concentrations in Eq 4-2 correspond to the initial (uniform) concentration in the low permeability zone, which is usually zero. The fitting parameters p (kg/m^4) and q (kg/m^5) are determined by two conservation of mass laws. The first constraint requires the fitting

function to satisfy the governing equation at the high permeability/low permeability interface (Falta and Wang, 2017):

$$R_l \frac{\partial C_l}{\partial t} = \tau_l D \frac{\partial^2 C_l}{\partial z_l^2} \Big|_{z_l=0} - \lambda_l C_l \Big|_{z_l=0} \quad (4-4)$$

In order to discretize the equation, a first-order finite difference approximation is applied to the time derivative. C_l is replaced with the trial function on the righthand side, which results in:

$$R_l \left(\frac{C^{t+\Delta t} - C^t}{\Delta t} \right) = \tau_l D \left(\frac{C^{t+\Delta t}}{d^2} - \frac{2p}{d} + 2q \right) - \lambda_l C^{t+\Delta t} \quad (4-5)$$

The second constraint is the mass conservation in the low permeability material, and requires the rate of change of total mass in the matrix to equal the mass flux across the interface minus the rate of decay in the matrix. For an ideal infinite aquitard case, the integral of distance into low permeability areas is defined from zero to infinity (Falta and Wang, 2017):

$$R_l \frac{\partial}{\partial t} \int_0^\infty C_l dz_l = -\tau_l D \frac{\partial C_l}{\partial z_l} \Big|_{z_l=0} - \lambda_l \int_0^\infty C_l dz_l \quad (4-6)$$

This research project deals with finite heterogeneities, such as low permeability lenses or layers. Thus, the mass conservation constraint must account for a finite diffusion distance. The characteristic average diffusion length, L (m) corresponds to the depth or vertical distance of diffusion into the low permeability material. The second constraint becomes (Muskus and Falta (2018):

$$R_l \frac{\partial}{\partial t} \int_0^L C_l dz_l = -\tau_l D \frac{\partial C_l}{\partial z_l} \Big|_{z_l=0} - \lambda_l \int_0^L C_l dz_l \quad (4-7)$$

The solution of the concentration integral in Eq 4-7 using the trial function is:

$$I(t) = \int_0^L C_l dz_l = C(t)d + pd^2 + 2qd^3 - (C(t)d + pdL + pd^2 + qL^2d + 2qd^2L + 2qd^3)e^{-L/d} \quad (4-8)$$

Following Pruess and Wu (1988, 1993), this can be written as a weighted function of $C(t)$, p , and q :

$$I(t) = \delta C(t) + \gamma p + \beta q \quad (4-9)$$

where

$$\delta = d - de^{-L/d} \quad (4-10)$$

$$\gamma = d^2 - (dL + d^2)e^{-L/d} \quad (4-11)$$

$$\beta = 2d^3 - (L^2d + 2d^2L + 2d^3)e^{-L/d} \quad (4-12)$$

For the special case of an ideal infinite aquitard, where $L \rightarrow \infty$:

$$\delta = d \quad ; \quad \gamma = d^2 \quad ; \quad \beta = 2d^3$$

corresponding to the definition of $I(t)$ in Falta and Wang (2017). Replacing the derivative in Eq 4-7 with a finite difference approximation of the concentration integral, and substituting C_l with the fitting function in the space derivative and decay term gives:

$$R_l \left(\frac{\delta C^{t+\Delta t} + \gamma p + \beta q - I^t}{\Delta t} \right) = \tau_l D \left(\frac{C^{t+\Delta t}}{d} - p \right) - \lambda_l (\delta C^{t+\Delta t} + \gamma p + \beta q) \quad (4-13)$$

Solving Eq 4-5 for q :

$$q = \frac{R_l}{2\tau_l D} \left(\frac{C^{t+\Delta t} - C^t}{\Delta t} \right) - \frac{C^{t+\Delta t}}{2d^2} + \frac{p}{d} + \frac{\lambda_l C^{t+\Delta t}}{2\tau_l D} \quad (4-14)$$

Multiplying by $2d^2/2d^2$ and rearranging:

$$q = \frac{\frac{(C^{t+\Delta t} - C^t)d^2}{\kappa_l \Delta t} - C^{t+\Delta t} + 2dp + \frac{\lambda_l C^{t+\Delta t} d^2}{R_l \kappa_l}}{2d^2} \quad (4-15)$$

Which is the same expression for q for the infinite aquitard case (Falta and Wang, 2017). Rearranging Eq 4-13:

$$\delta C^{t+\Delta t} + \gamma p + \beta q - I^t = \kappa_l \Delta t \left(\frac{C^{t+\Delta t}}{d} - p \right) - \frac{\lambda_l \Delta t}{R_l} (\delta C^{t+\Delta t} + \gamma p + \beta q) \quad (4-16)$$

$$\left(\beta + \frac{\lambda_l \Delta t}{R_l} \beta \right) q + \left(\gamma + \kappa_l \Delta t + \frac{\lambda_l \Delta t}{R_l} \gamma \right) p + \left(\delta - \frac{\kappa_l \Delta t}{d} + \frac{\lambda_l \Delta t}{R_l} \delta \right) C^{t+\Delta t} = I^t \quad (4-17)$$

Let:

$$A = \beta + \frac{\lambda_l \Delta t}{R_l} \beta \quad (4-18)$$

$$B = \gamma + \kappa_l \Delta t + \frac{\lambda_l \Delta t}{R_l} \gamma \quad (4-19)$$

$$E = \delta - \frac{\kappa_l \Delta t}{d} + \frac{\lambda_l \Delta t}{R_l} \delta \quad (4-20)$$

Then Eq 4-17 can be written as:

$$Aq + Bp + EC^{t+\Delta t} = I^t \quad (4-21)$$

Substituting the expression for q (Eq 4-15) in Eq 4-21.

$$A \left(\frac{(C^{t+\Delta t} - C^t)}{2\kappa_l \Delta t} - \frac{C^{t+\Delta t}}{2d^2} + \frac{p}{d} + \frac{\lambda_l C^{t+\Delta t}}{2R_l \kappa_l} \right) + Bp + EC^{t+\Delta t} = I^t \quad (4-22)$$

Rearranging:

$$\left(\frac{A}{d} + B \right) p = I^t - EC^{t+\Delta t} - \frac{A(C^{t+\Delta t} - C^t)}{2\kappa_l \Delta t} + \frac{AC^{t+\Delta t}}{2d^2} - \frac{A\lambda_l C^{t+\Delta t}}{2R_l \kappa_l} \quad (4-23)$$

Solving for p :

$$p = \frac{I^t - EC^{t+\Delta t} - A \left(\frac{C^{t+\Delta t} - C^t}{2\kappa_l \Delta t} - \frac{C^{t+\Delta t}}{2d^2} + \frac{\lambda_l C^{t+\Delta t}}{2R_l \kappa_l} \right)}{\frac{A}{d} + B} \quad (4-24)$$

Unique values of p and q are calculated in the aquifer gridblocks containing low permeability zones, and they are updated at each time step to represent the changing concentration profile in the low permeability zones. The concentration integral $I(t)$ is recalculated at every time step in every gridblock using Eq 4-9 and it is stored for use in the next time step (I^t). This results in a nearly perfect mass balance.

4.3 MATRIX DIFFUSION MASS FLOW

The matrix diffusion mass flow entering (+) or leaving (-) the high permeability zone is described by Fick's first law of diffusion. Substituting the low permeability material concentration by the trial function:

$$\dot{m} = A_{md} \phi_l \tau_l D \left. \frac{\partial C_l}{\partial z_l} \right|_{z_l=0} = A_{md} \phi_l \tau_l D \left(-\frac{C^{t+\Delta t}}{d} + p \right) \quad (4-25)$$

where ϕ_l is the porosity of the low permeability material and A_{md} (m²) is the matrix diffusion area, defined as the interfacial area between the high permeability and low permeability zones. The equation for p can be rewritten as:

$$p = aC^{t+\Delta t} + b \quad (4-26)$$

With

$$a = \frac{-E - \frac{A}{2\kappa_l \Delta t} + \frac{A}{2d^2} - \frac{A\lambda_l}{2R_l \kappa_l}}{\frac{A}{d} + B} \quad (4-27)$$

$$b = \frac{I^t + \frac{AC^t}{2\kappa_l \Delta t}}{\frac{A}{d} + B} \quad (4-28)$$

And the expression for the mass rate, \dot{m} (kg/s), turns into (Muskus and Faltá (2018):

$$\dot{m} = A_{md}\phi_l\tau_l D \left(\left(a - \frac{1}{d} \right) C^{t+\Delta t} + b \right) \quad (4-29)$$

The matrix diffusion mass flow becomes a concentration-dependent source/sink term added in the numerical transport model gridblocks that contain low permeability materials.

4.4 NUMERICAL FORMULATION

The integral finite difference mass balance equation (Narasimhan and Witherspoon, 1976) for an element i is given in Eq 4-30. Only transmissive zones are considered due to the working assumptions of the semi-analytical method.

$$V_i \frac{dM_i}{dt} = \sum_j F_{ij} A_{ij} + Q_i \quad (4-30)$$

where

V_i = element volume

M_i = mass of contaminant per unit volume

F_{ij} = mass flux entering i from neighbouring elements j

A_{ij} = interfacial area between i and j

Q_i = source/sink term in element i (mass/time)

The mass term in the high permeability material is (Muskus and Faltá, 2018):

$$M = V_f \phi R C \quad (4-31)$$

Here, V_f is the volume fraction of high permeability material in the aquifer, ϕ is the porosity of the high permeability material, and R is the solute retardation factor in the high permeability material.

The right-hand side in the mass balance expression corresponds to the accumulation of mass. Following the conventional approach for numerical modeling, the sum of mass fluxes includes advection and hydrodynamic dispersion (Freeze and Cherry, 1979; Fetter, 2008), and the internal source/sink term includes reactions. With the semi-analytical approach, diffusion is included in the source/sink term as a mass rate and not in the sum of fluxes, like in traditional numerical modeling. Therefore, the internal source/sink term also includes the matrix diffusion mass flow when element i is adjacent to or includes low permeability materials (Faltá and Wang, 2017).

Following Faltá and Wang (2017), the transport equation using the semi-analytical approach was expressed for a three-dimensional system, using Cartesian coordinates. The system assumes uniform groundwater flow in the horizontal direction and dispersion in all three directions (i , j , and k). Additional conditions included first-order decay in the aqueous phase in the high permeability zone, and matrix diffusion with decay in low permeability zones. A uniform grid with spacing of Δx , Δy and Δz was used, along with a finite difference approximation for the

concentration gradients in the dispersive fluxes, and upstream weighting for the advective term. Under these conditions, the transport equation with a fully implicit formulation is equal to:

$$\begin{aligned}
V_f \Delta x \Delta y \Delta z \phi R \left(\frac{C_{i,j,k}^{t+\Delta t} - C_{i,j,k}^t}{\Delta t} \right) = & v_x \Delta y \Delta z (C_{i-1,j,k}^{t+\Delta t} - C_{i,j,k}^{t+\Delta t}) \\
& + \frac{\phi D_x \Delta y \Delta z}{\Delta x} (C_{i-1,j,k}^{t+\Delta t} - 2C_{i,j,k}^{t+\Delta t} + C_{i+1,j,k}^{t+\Delta t}) \\
& + \frac{\phi D_y \Delta x \Delta z}{\Delta y} (C_{i,j-1,k}^{t+\Delta t} - 2C_{i,j,k}^{t+\Delta t} + C_{i,j+1,k}^{t+\Delta t}) \\
& + \frac{\phi D_z \Delta x \Delta y}{\Delta z} (C_{i,j,k-1}^{t+\Delta t} - 2C_{i,j,k}^{t+\Delta t} + C_{i,j,k+1}^{t+\Delta t}) \\
& - \Delta x \Delta y \Delta z \phi \lambda C_{i,j,k}^{t+\Delta t} \\
& + A_{md,i,j,k} \phi_l \tau_l D \left(\left(a - \frac{1}{d} \right) C_{i,j,k}^{t+\Delta t} + b_{i,j,k}^t \right)
\end{aligned} \tag{4-32}$$

where

- v_x = Darcy velocity in the x direction
- D_x = horizontal dispersion coefficient
- D_y = transverse dispersion coefficient
- D_z = vertical dispersion coefficient
- λ = aqueous decay rate in high k material

As defined before, the last term in Eq 4-32 contains the matrix diffusion flux into or out of the high permeability material, multiplied by the interfacial matrix diffusion area to convert to mass rate units. The matrix diffusion term is only applicable to the gridblocks adjacent to or containing low permeability materials. Eq 4-8 produces a simultaneous system of linear algebraic equations with only one unknown, $C^{t+\Delta t}$. REMChlor-MD uses a Gauss Siedel iterative method to solve the resulting system of equations (Muskus and Falta (2018)).

4.5 SEMI-ANALYTICAL METHOD PARAMETERS

There are three geometrical parameters required for the embedded (finite diffusion length) matrix diffusion model: the high permeability volume fraction in the aquifer, V_f , the interfacial area per total volume, A_{md}/V , and the characteristic diffusion length, L .

It is possible to reduce the number of geometrical parameters to two by considering the volume of low permeability material, and how that relates to the interfacial area and diffusion length. The volume of low permeability material is

$$V_{low} = V(1 - V_f) \tag{4-33}$$

From a volume balance, the volume of low permeability material should be equal to the product of the interfacial area and the average diffusion length, or

$$V(1 - V_f) = A_{md} L \tag{4-34}$$

or

$$\frac{A_{md}}{V} = \frac{(1-V_f)}{L} \text{ or } L = \frac{(1-V_f)}{A_{md}/V} \quad (4-35)$$

Using Eq 4-35, if the high permeability volume fraction is known, only the characteristic diffusion length or the interfacial area need to be estimated. We have found that this method provides a good match with data from a laboratory experiment, and from fine-grid numerical simulations.

4.6 SEMI-ANALYTICAL MODEL SIMULATION OF MATRIX DIFFUSION IN A HETEROGENEOUS SAND TANK EXPERIMENT

Doner (2008) carried out a set of laboratory experiments at Colorado State University using a 1.07×0.03×0.84 m tank filled with sand and four suspended clay lenses. A tracer solution was flushed through the sandbox followed by flushing of clean water. Influent and effluent concentrations were monitored throughout the experiments. The setup of the sandbox experiment is shown in **Figure 4-1**.

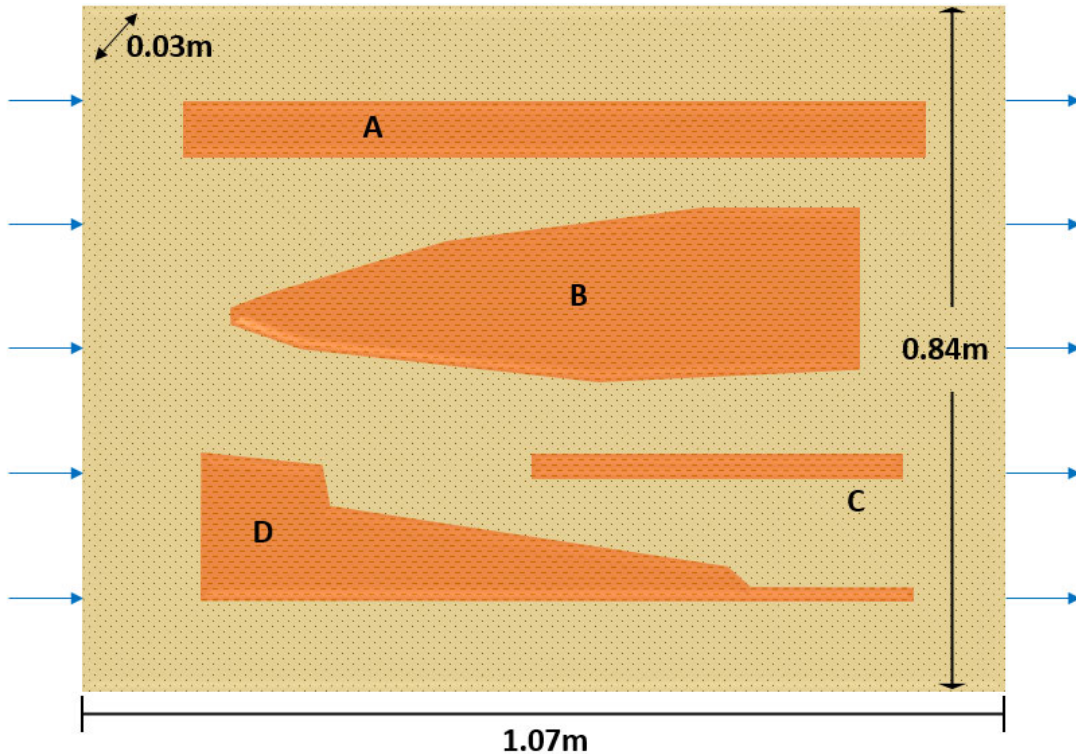


Figure 4-1. Sandbox experiment setup. Adapted from Doner (2008).

More recently, Chapman et al. (2012) simulated this experiment numerically to study the validity of several high-resolution numerical models to simulate diffusion in and out of low permeability

areas. The tested models showed close match to the experimental data, requiring fine grids (~9,000-24,000 gridblocks) and temporal discretization.

The tracer solution used in the experiment consisted of de-aired tap water containing 400 mg/L of fluorescein and 90 mg/L of bromide. The flow rate during the experiment was not constant. During the first 10 days, the solution flowed through the sandbox at a rate of 0.9 mL/min and it was later increased to and held constant at 1.5 mL/min. This inflow was maintained for 22 days and then switched by clean water for 100 more days.

The semi-analytical method was used to simulate this experiment using a 1D grid with 50 gridblocks. These gridblocks represent the sand part of the experiment, and the interaction with the clay lenses is performed with the semi-analytical approximation. The matrix diffusion area was calculated approximating the geometry of the irregular clay lenses. This was accomplished by digitizing the clay lenses from a picture of the experimental setup (Doner, 2008) and scaling the clay dimensions from the sandbox dimensions. The values are shown in **Figure 4-2**.

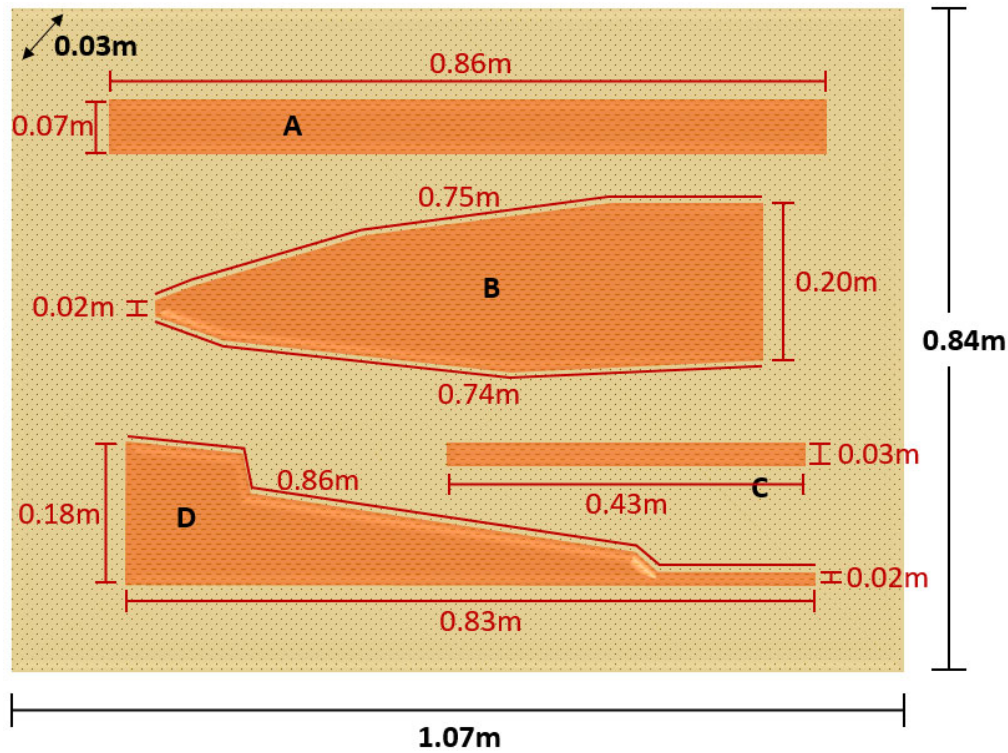


Figure 4-2. Approximate dimensions of clay lenses estimated from Doner (2008).

The matrix diffusion area for every clay lens is the sum of each face length times the thickness of the sandbox. The total matrix diffusion area, A_{md} , is the sum of the individual lens matrix diffusion areas and it was estimated as 0.1923 m^2 . The high/low permeability zone distribution was specified by volume fractions. The volume of sand required for the volume fraction calculation was computed from the overall sand area (0.26 m^2) specified in Chapman et al. (2012). The sand volume fraction, V_f , was 0.711.

The Darcy velocity was calculated as Q divided by the product of Δy and Δz . However, the experiment was carried out with a variable volumetric rate and the current formulation of the semi-analytical method uses a constant value. The value of Q_2 was chosen to be used in the semi-analytical method because it was implemented for a longer period of time during the sandbox testing.

The difference of volumetric flow rates between the experiment and the semi-analytical model will impact the results of the simulation, increasing any existing deviation from the experimental results. By choosing the higher volumetric rate the expected effluent concentrations during the first 10 days of the experiment are achieved at a faster time. Therefore, a shift to the left is expected in the leading edge of the simulated concentration versus time profile.

With the interfacial area estimate, the calculated value for L was 0.0405 m using Eq 4-35. Given that this value is only an estimate, additional simulations were carried out varying the characteristic average diffusion length (while maintaining the relationship in Eq 4-35 to evaluate its effect on the results (Muskus, 2017)). The simulated effluent concentration as a function of time is shown in **Figure 4-3**.

Additional simulations were carried out for diffusion lengths of 3 cm, 5 cm, 6 cm, and 8 cm and compared to the experimental data. Since the characteristic average diffusion length was specified, Eq 4-35 was used to estimate the correspondent matrix diffusion area for each case.

Error! Reference source not found. shows the resulting curves, including the original results ($L = 4.05$ cm) for comparison. It appears that the match with the experimental data is slightly better with a characteristic diffusion length of about 5 or 6 cm rather than the original estimate of 4.05 cm.

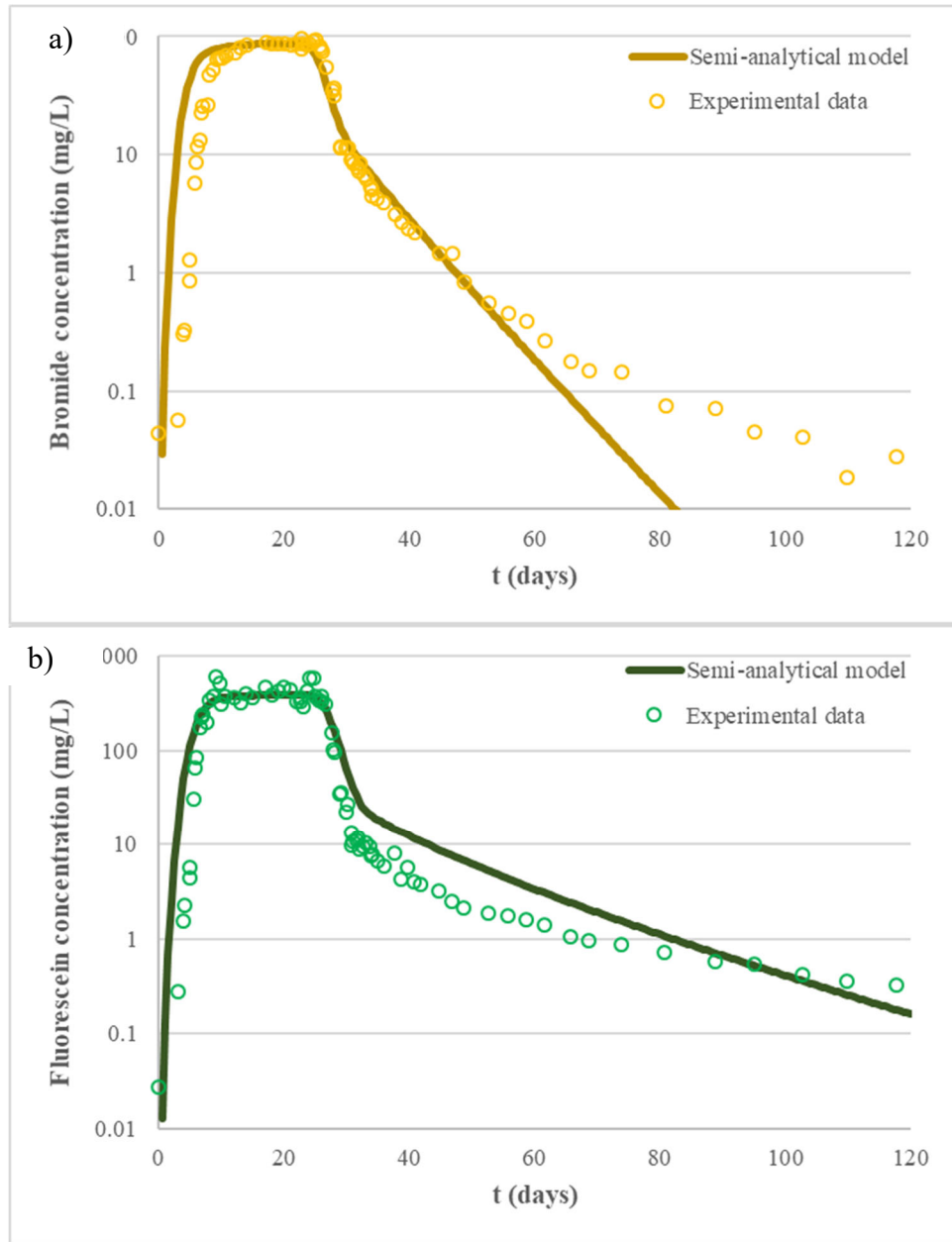


Figure 4-3. Effluent concentration vs time profile comparing the semi-analytical model using 50 gridblocks with experimental data for Doner (2008) for a) bromide and b) fluorescein.

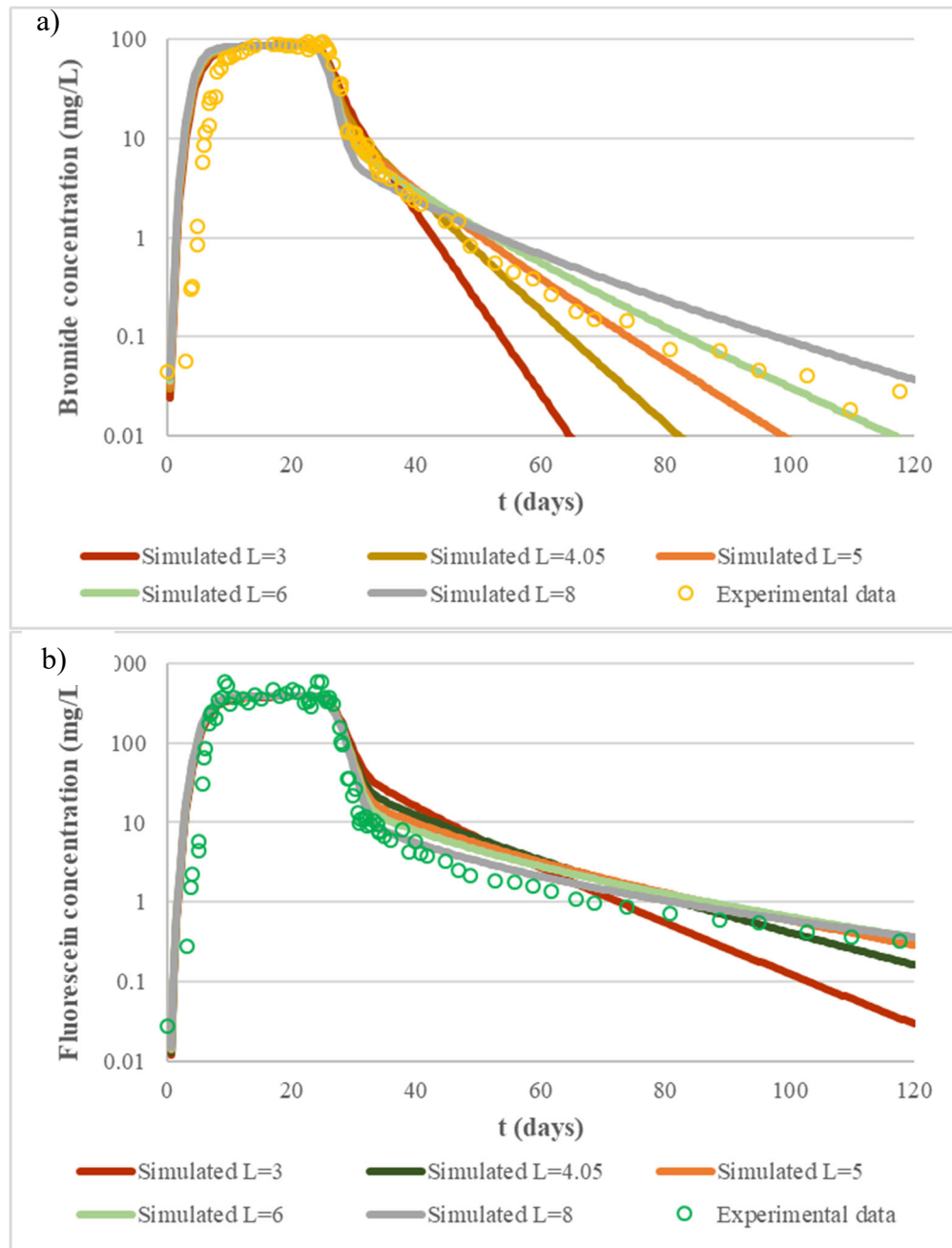


Figure 4-4. Effect of diffusion length on effluent concentration profile for the case of matrix diffusion from suspended low k zones for a) bromide and b) fluorescein.

4.7 USING SEMI-ANALYTICAL METHOD TO REPRODUCE FINE-GRID HETEROGENEOUS NUMERICAL SIMULATIONS

Fine-grid numerical simulations were performed (Muskus and Faltz (2018) using MODFLOW and MT3DMS using a heterogeneous grid generated using the T-PROGS transitional probability geostatistics program (Carle, 1999). A hypothetical site was created modifying the T-PROGS tutorial borehole data (AQUAVEO, 2016), resulting in the 84 boreholes seen in **Figure 4-5**. The boreholes are representative of a sand/clay scenario dominated by clay.

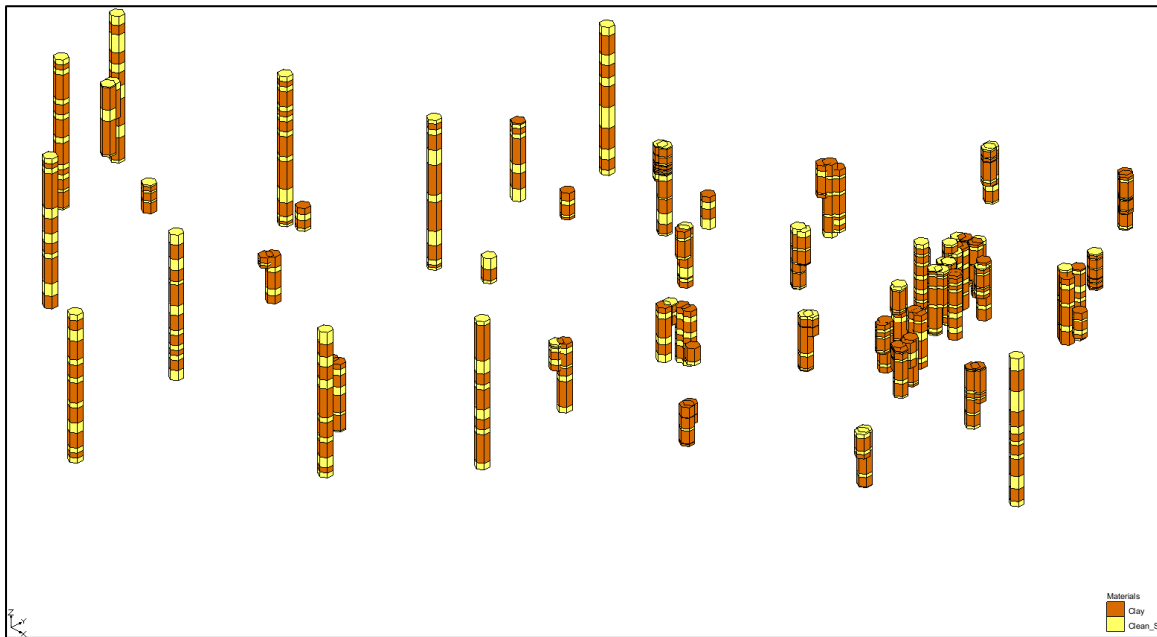


Figure 4-5. Boreholes used for T-PROGS simulation (z magnification = 2).

One T-PROGS material set, called the lense case, is shown in **Figure 4-6** and displays elongated sand zones in the horizontal direction. The vertical magnification was set as 2 in order to have a better view of the material distribution. Different views in GMS allow one to appreciate the heterogeneity of the model.

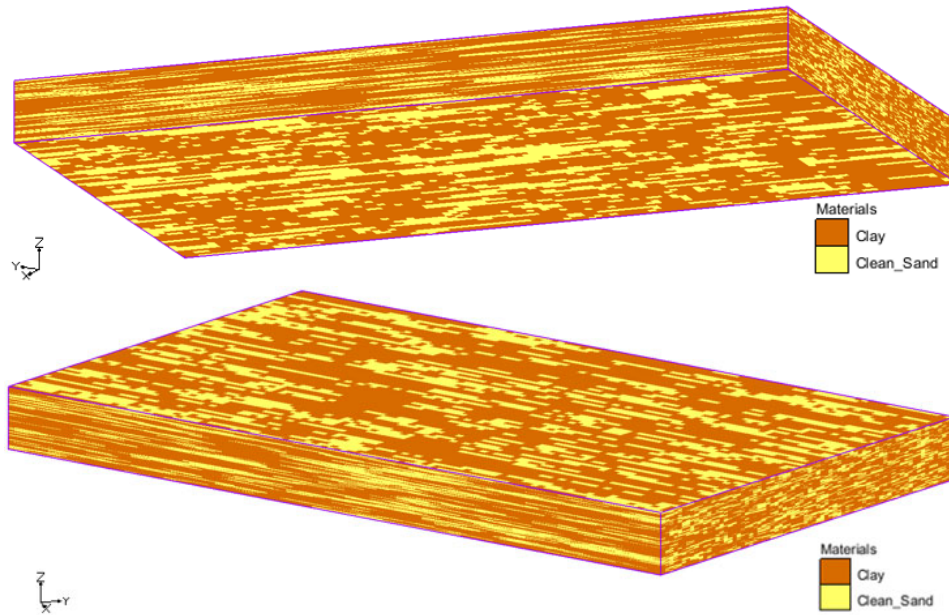


Figure 4-6. Material distribution from T-PROGS for lens case (z magnification=2).

In order to create the flow field, the sand and clay properties were edited by material. The hydraulic conductivity was set as 30 ft/d (9.14 m/d) for the sand and 1.0E-3 ft/d (3.05E-4 m/d) for the low permeability clay. The model contains 400 layers, and a total of 2,828,000 gridblocks.

The flow model is three dimensional, steady-state, heterogeneous, and anisotropic. Two specified head boundary conditions are used to represent the head gradient that causes the flow of groundwater through the model, as shown in **Figure 4-7**.

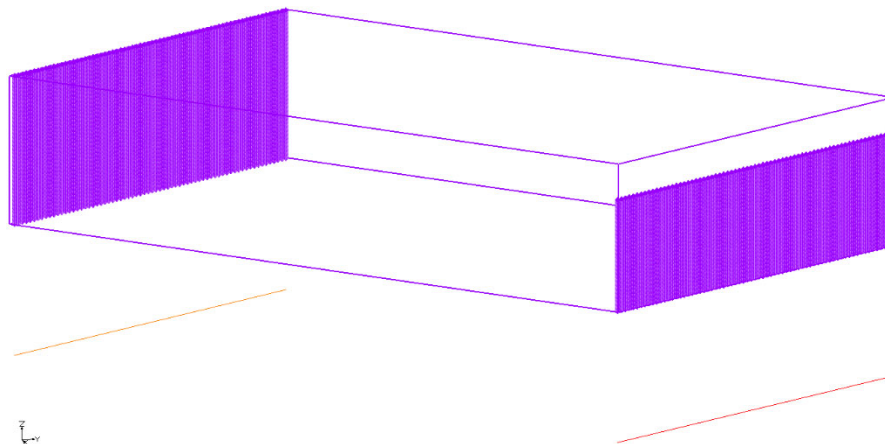


Figure 4-7. Specified head conditions for the flow field in lens case.

The maximum hydraulic head was set equal to the top elevation of the model. Because the grid had a vertical origin in 119.62 ft (36.46 m) the top elevation and thus, maximum hydraulic head was 254.62 ft (77.61 m). The minimum hydraulic head was estimated from the change in head,

which in turn was calculated from the hydraulic gradient needed for a Darcy flux in the sand of 0.09 m/d (107.78 ft/yr). The estimated change in head of 33.66 ft (10.26 m) lead to a minimum hydraulic head calculation of 220.96 ft (67.35 m). The MODFLOW simulation took about 17 minutes in a workstation with an Intel i7 CPU at 3.60 GHz, and provided the head contours shown in **Figure 4-8**.

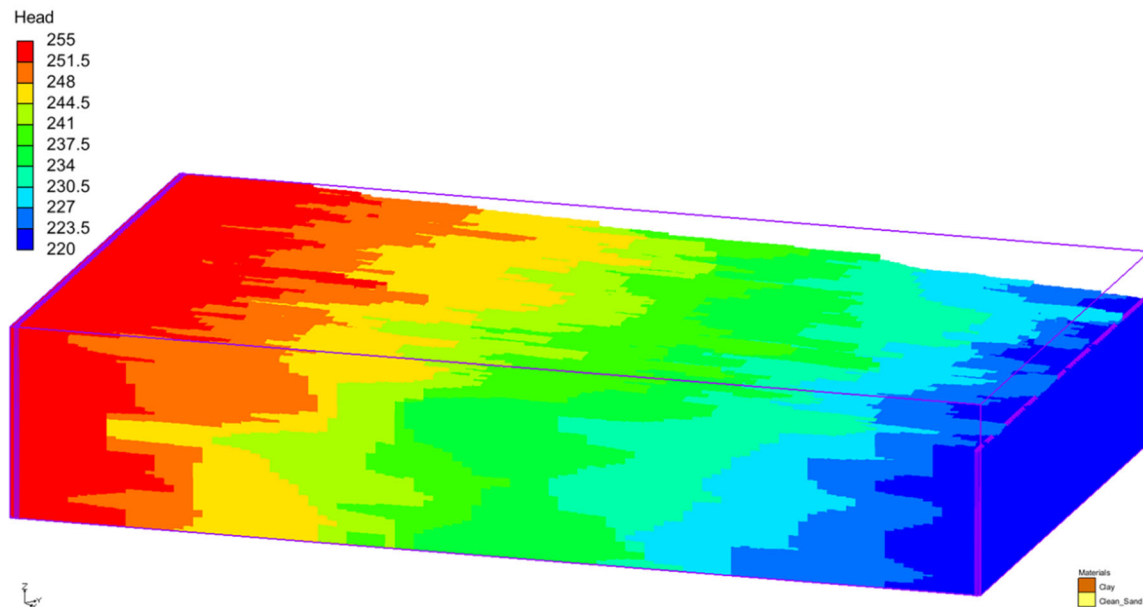


Figure 4-8. Head contours for lens case.

The simulation time for the mass transport model was set to a total of 230 years. A TCE source of 10,000 ppb was placed downstream from the model inlet (column 15) to reduce the observed lateral dispersion of the plume when the source was located in the first column of the model. The contamination source was laid out over a total area of 389.57 ft² (36.19 m²) comprised by two cells in the *y* direction and 20 gridblocks in the *z* direction. The constant concentration condition was set only in the sand cells of the source area, represented in **Figure 4-9** as blue triangles and outlined by the red square. The TCE source was maintained constant for 30 years, at which point it was removed, and followed by advective flushing for 200 years.

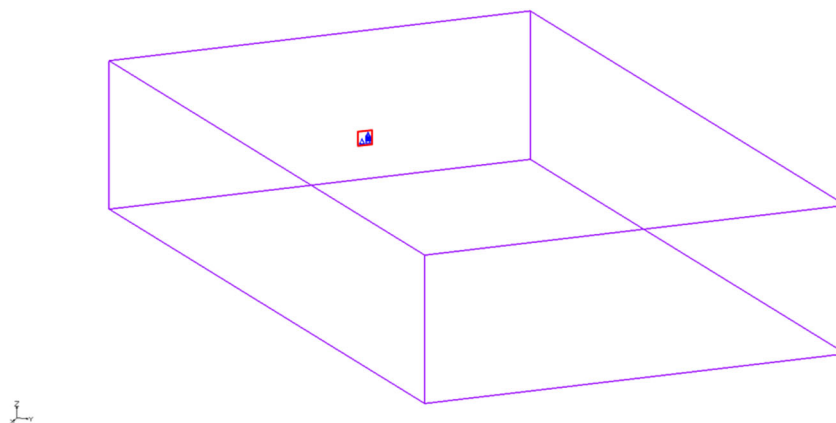


Figure 4-9. Location of TCE source for MT3DMS simulation.

The MT3DMS transport simulations was run with molecular diffusion, but with the dispersivity values set essentially to zero. Although the dispersivities are zero, the high degree of heterogeneity results in a dispersed plume. **Figure 4-10** shows a view of the plume after 30 years; at this time the leading edge has already reached the downstream face. **Figure 4-11** shows the plume at 230 years, after 200 years of flushing. The fine-grid MT3DMS simulation took about 60 hours to run.

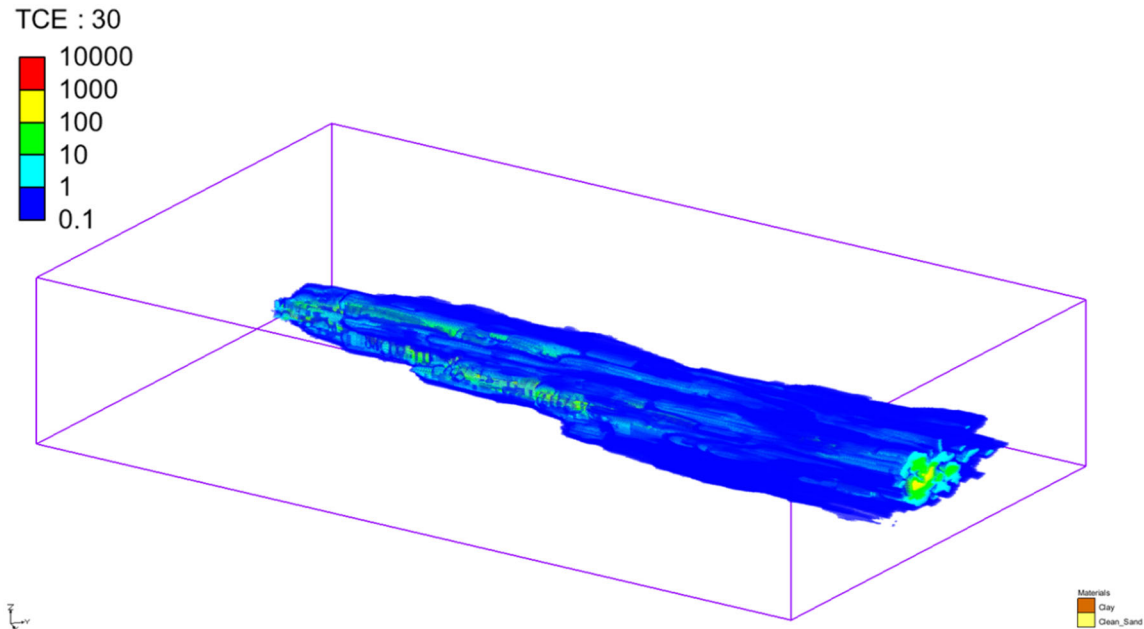


Figure 4-10. MT3DMS simulated TCE concentration distribution after 30 years. Although the source is removed at 30 years, the plume persists due to matrix diffusion in the extensive clay zones.

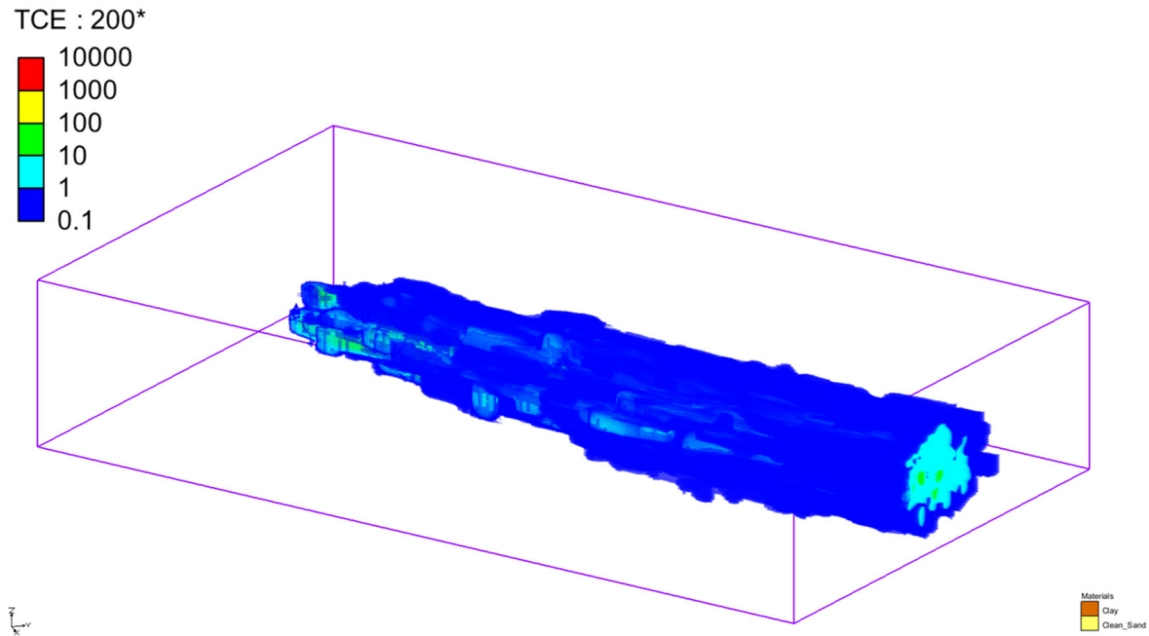


Figure 4-11. MT3DMS simulated TCE concentration distribution after 230 years (200 years of flushing).

The implementation of the semi-analytical method was performed with the FORTRAN formulation of REMChlor-MD. For the embedded heterogeneity case, the semi-analytical method works under the assumption that the high permeability zone is well mixed. Therefore, the REMChlor-MD model uses a homogeneous, uniform velocity in the transmissive zone, with matrix diffusion using the semi-analytical approximation. The macro-scale dispersion caused by the heterogeneity is approximated using longitudinal, transverse, and vertical dispersivity values of 5m, 0.5m, and .005m, respectively. The REMChlor-MD model uses a numerical grid with about 56,000 gridblocks.

Properties such as porosity, tortuosity, and retardation factor in the low permeability zone were set equal to the values in the MT3DMS model. The sand volume fraction is equivalent to the 0.288 sand proportion stated in T-PROGS.

To estimate the characteristic average diffusion length, three randomly selected lateral faces of the model were chosen to determine the average thickness of clay in them. The selected faces for the determination of L corresponded to the rows (x -dir) 30, 68, and 93 in the numerical model.

Each vertical column in the face was treated as a separate borehole and the thickness of clay in each borehole section was measured and recorded. The clay thickness of the total cross-sectional area was calculated as a volumetric weighted average to give more contribution to higher diffusion lengths to the averaged value.

To have a better understanding of how the estimation of L was carried out, consider the borehole shown below in **Figure 4-12**. The volume fraction of the small clay zone is given by its thickness divided by the total thickness of the borehole. The volume fraction of the big clay zone is

calculated in the same manner. The volume weighted average thickness of clay in the borehole is the sum of the individual clay thicknesses weighted by their respective volume fraction, divided by the sum of the fractions.

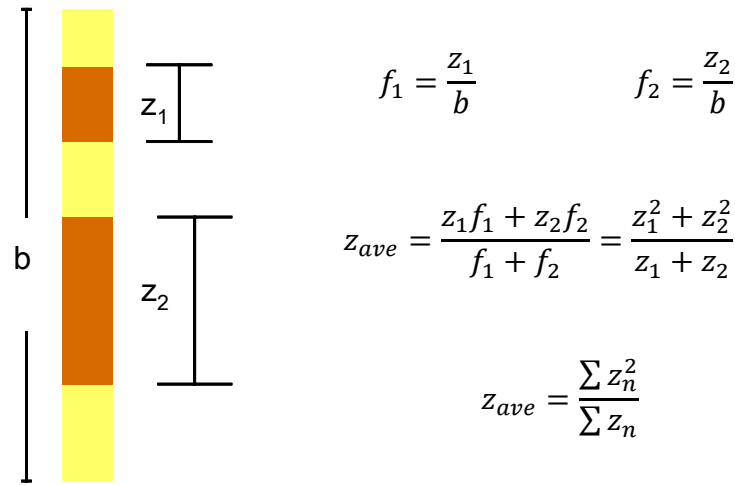


Figure 4-12. Illustration of weighted average L calculation.

Since clay lenses usually have both top and bottom faces in contact with the transmissive zone, diffusion into the clay from both faces is expected to meet in the middle of the low permeability lens. Thus, the characteristic average diffusion length was calculated as half of the average clay thickness for each cross-sectional area in the MT3DMS/MODFLOW model, resulting in an average value of 1.85 m. The interfacial area was then calculated using Eq 4-35.

The total TCE mass discharge at the downstream face was calculated for both models by integrating the mass flux over the y-z plane. The comparison between the heterogeneous fine-grid MT3DMS simulation and the homogeneous coarse-grid REMChlor-MD simulations is shown in **Figure 4-13**, using the estimated (but not calibrated) characteristic diffusion length of 1.85 m.

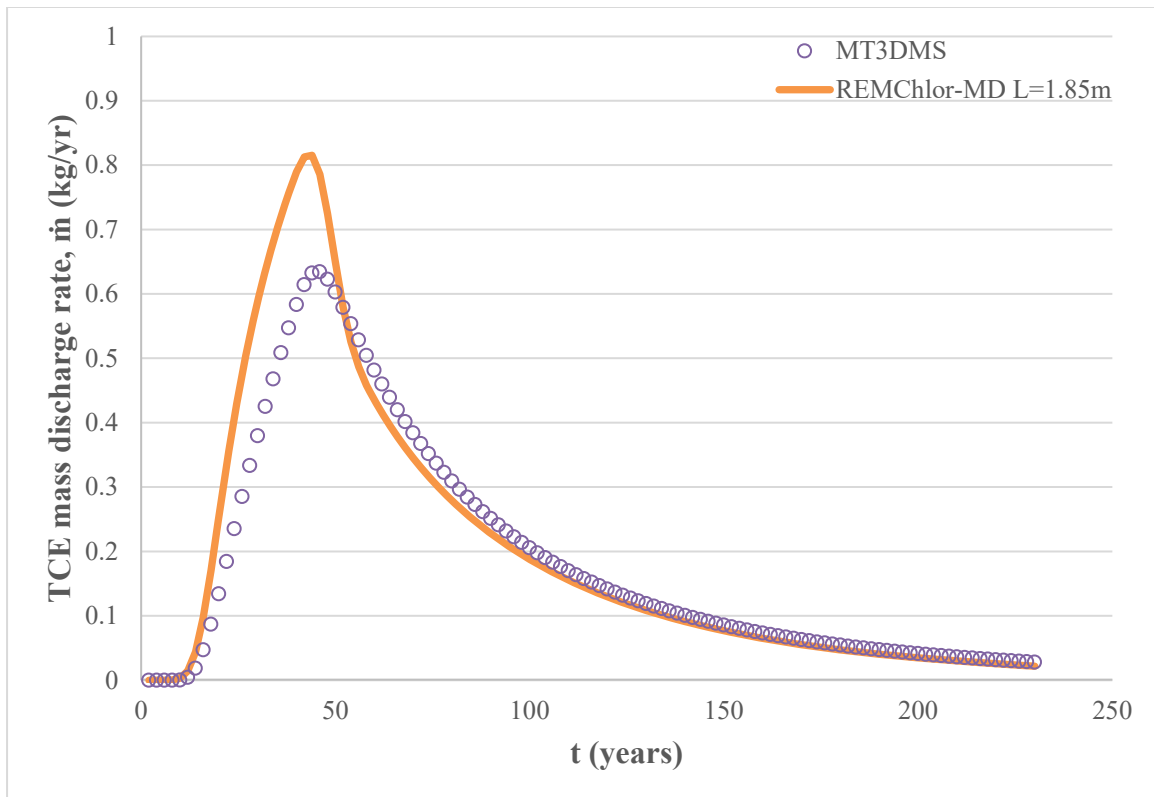


Figure 4-13. TCE mass discharge rate vs time profile comparing the MT3DMS model with REMChlor-MD for lens case with $L = 1.85$ m.

The fit of the mass discharge improved somewhat when the characteristic diffusion length was reduced to 1.5 m (**Figure 4-14**).

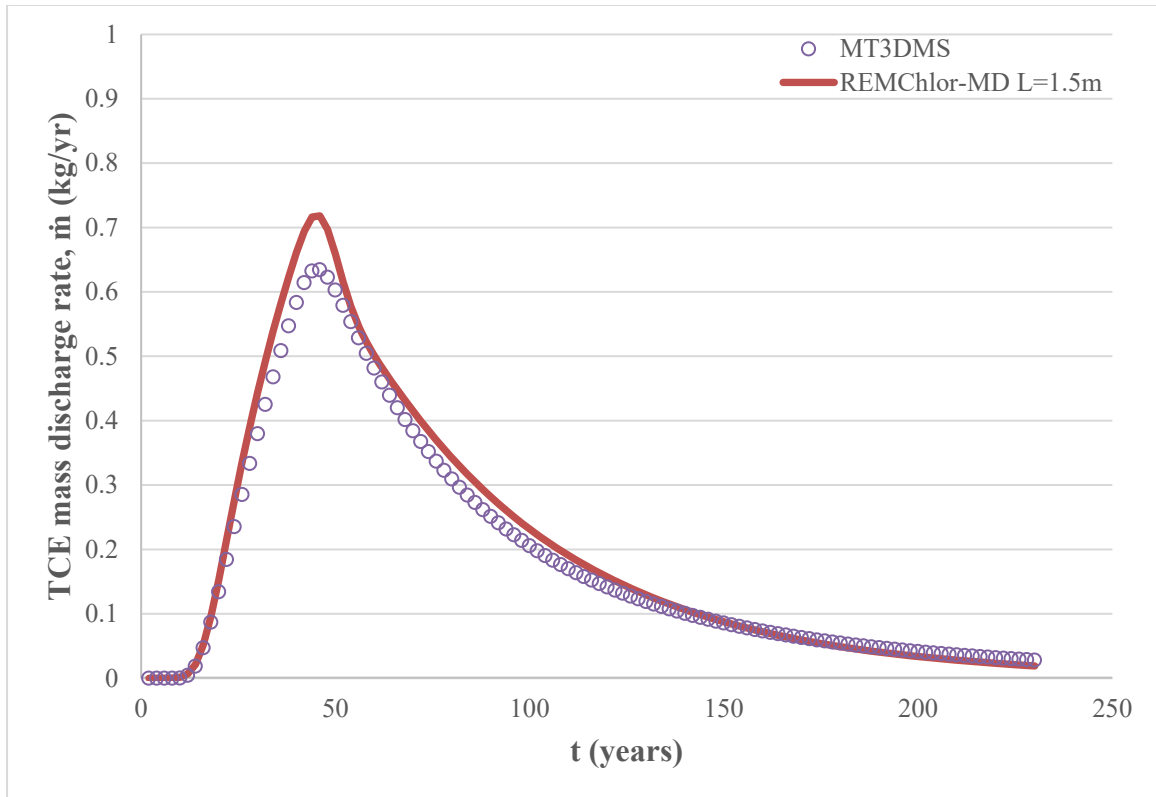


Figure 4-14. TCE mass discharge rate vs time profile comparing the MT3DMS model with REMChlor-MD for lens case with $L = 1.5\text{m}$.

Figure 4-15, Figure 4-16 and Figure 4-17 show a comparison of the fine grid MT3DMS results and the results using the semi-analytical method in REMChlor-MD with a coarse, homogeneous grid at times of 10 years, 30 years, and 130 years, respectively. These figures show a horizontal slice through the center of the source zone, and the diffusion length of 1.5m was used.

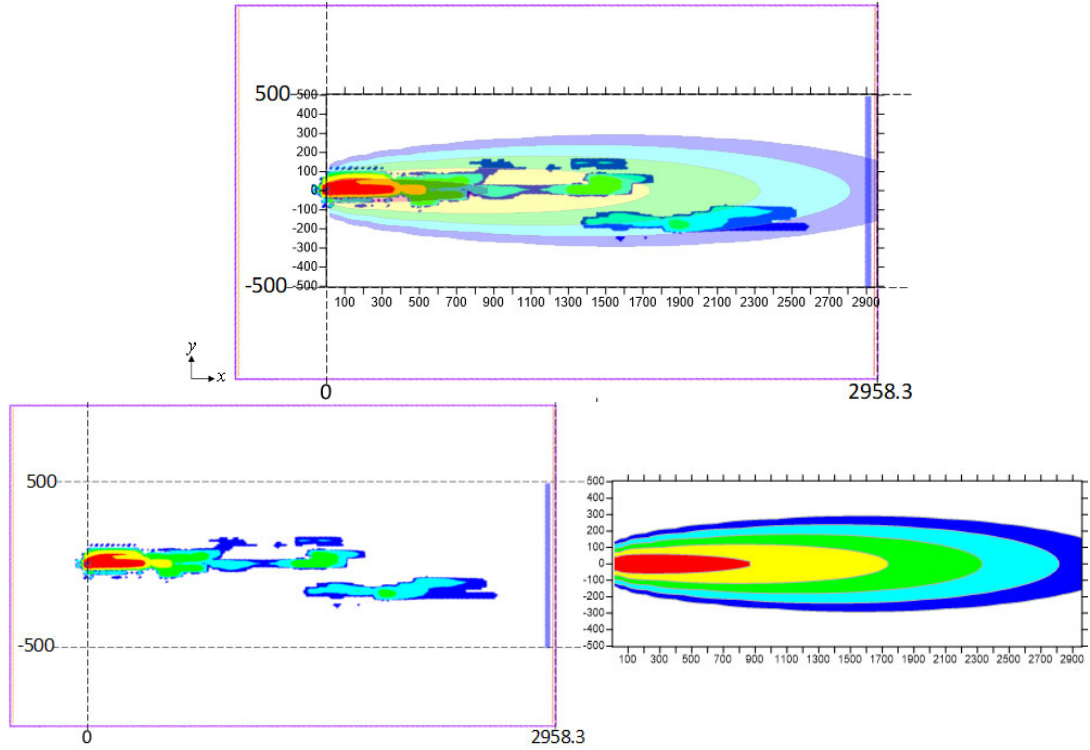


Figure 4-15. Comparison of MT3DMS ($k=200$) and REMChlor-MD (layer #18) models in xy plane at $t=10$ yrs for lens case. Above: REMChlor-MD contours over MT3DMS contours. Below: MT3DMS contours (left) and REMChlor-MD contours (right).

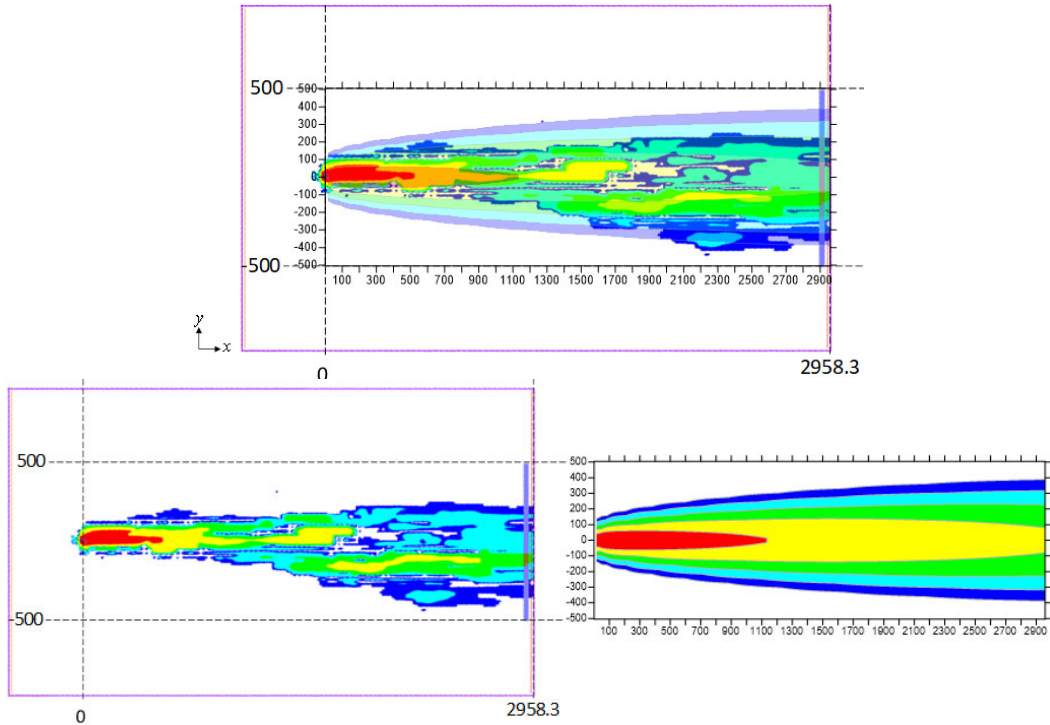


Figure 4-16. Comparison of MT3DMS ($k=200$) and REMChlor-MD (layer #18) models in xy plane at $t=30$ yrs for lens case. Above: REMChlor-MD contours over MT3DMS contours. Below: MT3DMS contours (left) and REMChlor-MD contours (right).

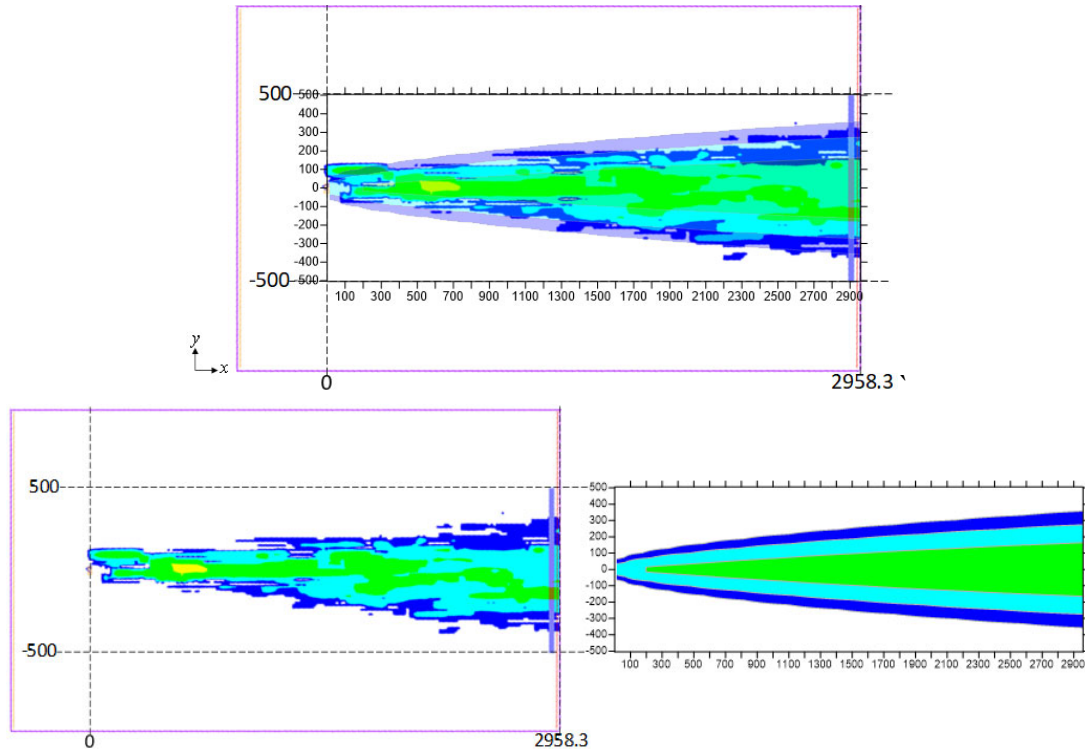


Figure 4-17. Comparison of MT3DMS ($k=200$) and REMChlor-MD (layer #18) models in xy plane at $t=130$ yrs for lens case. Above: REMChlor-MD contours over MT3DMS contours. Below: MT3DMS contours (left) and REMChlor-MD contours (right).

It appears that the new semi-analytical method is capable of reproducing the essential features of the fine-grid heterogeneous flow and transport simulation that is dominated by matrix diffusion. The new method has three geometrical parameters, but these can be reduced to two parameters by assuming a logical relationship between the low permeability zone volume, the interfacial area, and the characteristic diffusion length. It appears that the key matrix diffusion parameters needed for this model, the volume fraction of high permeability material (V_f) and the characteristic diffusion length (L) can be estimated from well logs.

4.8 COMPARISON OF SEMI-ANALYTICAL AND DUAL-DOMAIN METHODS FOR SIMULATING MATRIX DIFFUSION IN PARALLEL FRACTURES

The dual-domain model is implemented as an optional feature in the popular modular 3-D multispecies transport model (MT3DMS) to simulate transport in fractured media or highly heterogeneous porous media (Zheng and Wang, 1999). For use in our simulations, we assumed a homogeneous and constant groundwater velocity field with flow in x -direction with contaminant decay only in the aqueous phase. Given those assumptions, the coupled dual-domain model equations can be written as:

$$V_f \phi_f R \frac{\partial C}{\partial t} + (1 - V_f) \phi_l R_l \frac{\partial C_l}{\partial t} = V_f \phi_f (D_x \frac{\partial^2 C}{\partial x^2} + D_y \frac{\partial^2 C}{\partial y^2} + D_z \frac{\partial^2 C}{\partial z^2}) - v_x \frac{\partial C}{\partial x} - \lambda \phi_f V_f C - \lambda_l \phi_l (1 - V_f) C_l \quad (4-36)$$

$$(1 - V_f) \phi_l R_l \frac{\partial C_l}{\partial t} = \beta (C - C_l) - (1 - V_f) \phi_l C_l \quad (4-37)$$

The subscript l in Eq 4-36 and 4-37 symbolizes parameters of the low permeability domain. Parameters without any subscript or with the subscript f are those of the fracture or a high permeability material. An exception to that subscript convention is made for porosity because φ is typically reserved for total porosity i.e. $\varphi = \varphi_f + \varphi_l$. In Eq 4-36, the volume fraction, V_f , is the same parameter as introduced in the semi-analytical model to specify the degree of heterogeneity (Muskus and Falta, 2018). Specifically, volume fraction is the ratio of the high permeable materials to the total volume. The mobile porosity is defined as the product of the volume fraction and the porosity in the high permeability layers:

$$\varphi_m = V_f \varphi_f \quad (4-38)$$

whereas the immobile porosity is the product of the volume fraction of the low permeability layers and the porosity in those layers:

$$\varphi_{im} = (1 - V_f) \varphi_l \quad (4-39)$$

The sum of the mobile and immobile porosity is the total porosity: $\varphi_m + \varphi_{im} = V_f \varphi_f + (1 - V_f) \varphi_l = \varphi$. Those porosity definitions are consistent with how Zheng and Wang (1999) and others have defined in the literature.

The retardation factor in the low permeability material is R_l . The aqueous mass concentration in the low permeability and high permeability material is C_l and C , respectively. The 3-D dispersion coefficients are D_x , D_y , and D_z . The component in the x-direction of the Darcy velocity is v_x . The decay rate in the low permeability material is λ_l .

In Eq 4-37, the mass transfer between the two domains is moderated by the mass transfer coefficient, β . The mass transfer coefficient is typically a calibrating parameter of the dual-domain model to simulate matrix diffusion. In the case of a fractured system with parallel fractures, a derivation documented by van Genuchten (1985) for transport through soils of line-sheet type aggregates was used to develop a mathematical expression for β :

$$\beta = \frac{3\tau_l D \phi_{im}}{(a/2)^2} \quad (4-40)$$

where, τ_l is the tortuosity in the low permeability material, D is the molecular diffusion coefficient, and a is the fracture spacing. The formula in Eq 4-40 is tested extensively in this work and referred to as the shape factor formula of the first order mass transfer coefficient.

van Genuchten (1985) derived the expression in Eq 4-40 by recognizing that the mass transfer coefficient can be solved for in terms the ratio of the dimensionless time of the parallel fractured system to the dimensionless time of the first order mass transfer equation. An expression of the dimensionless time for the first order mass transfer equation was found by integrating Eq 4-37 for an initial zero concentration in the matrix while keeping the concentration in the fractures at unity. The result of the integration is the first order approximation of the matrix concentration profile whose exponent is the dimensionless time of the first order model. The dimensionless time of the parallel fractured system is analogous to the dimensionless time of the heat conduction in a solid bounded by two parallel plates (Carslaw and Jaeger, 1959). The analytical concentration profile in the matrix of the parallel fractured system is also known from heat conduction. van Genuchten (1985) observed that when the first order approximation of the matrix concentration profile and the analytical solution are plotted together to varying dimensionless time, one could glean from the plot two dimensionless times that would give an equivalent diffusive matrix concentration in the fractured system and in the first order mass transfer model. van Genuchten (1985) called the ratio of the two dimensionless times the shape factor, which in turn, could be used to define a generalized expression for the mass transfer coefficient (Eq 4-40).

Neville (2006) tested the formula in one system of parallel fractures using MT3D and found that in that system, the formula predicted the mass transfer coefficient well, producing concentration profiles that matched the analytical solution (Sudicky and Frind, 1982). Per Bear et al. (2010), the implicit assumption of Eq 4-38 is that the concentration difference between the high permeability and low permeability layers is linear over a characteristic length. That linear assumption is only valid when the concentration difference has reached a quasi-steady state. The time to steady state condition or the characteristic diffusion time, $t_{c,diff}$, can be computed using the characteristic length and the diffusion coefficient: $t_{c,diff} = L^2/D$ (Bear et al., 2010). In a fractured system, the characteristic length can be computed directly using geometry (Farhat et al., 2018):

$$L = (a - b)/2 \quad (4-41)$$

where a is the fracture spacing and b is the fracture aperture. Assuming the contaminant is TCE, the characteristic diffusion time can be computed and plotted for a range of fracture spacing as shown in

Figure 4-18.

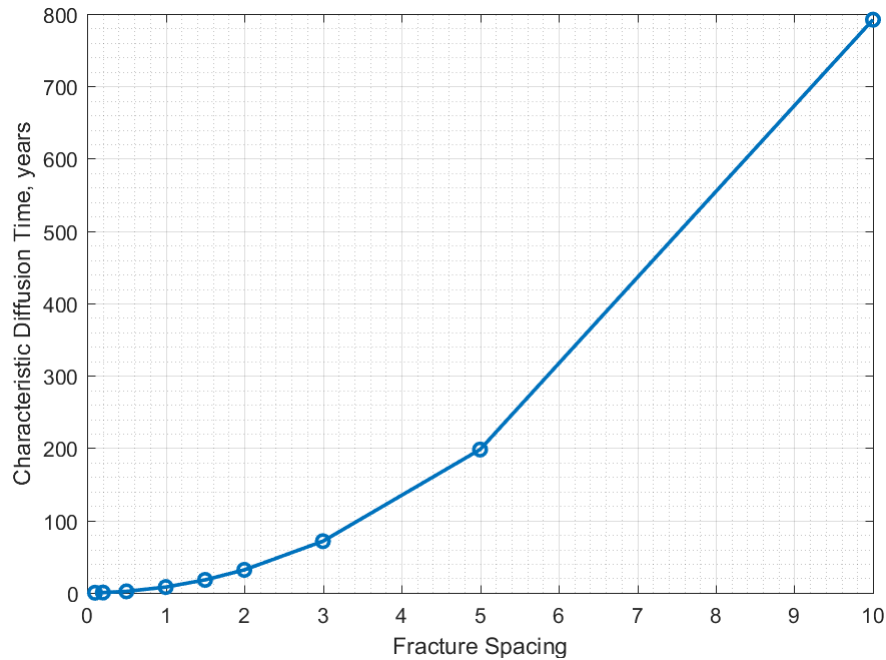


Figure 4-18. Characteristic diffusion time in systems of varying fracture spacing (m).

The implicit linear approximation of the first order mass transfer coefficient is only valid when the concentration difference occurs at times that are significantly greater than the times plotted in the figure above (Bear et al., 2010). When the fracture spacing is large enough, the characteristic time required for the first order mass transfer coefficient to be valid can be unreasonably large. For example, in the fracture spacing case of 10 m and TCE being the contaminant, that time threshold is almost 800 years. That shortcoming of the dual-domain method in comparison to the robustness of the semi-analytical method is the primary focus of the present work.

Muskus and Falta (2018) compared the semi-analytical method against an analytical solution for a fractured porous media system of parallel fractures developed by Sudicky and Frind (1982). Sudicky and Frind (1982) developed the exact analytical solution for one-dimensional transport along parallel fractures. They assumed that the fracture width is significantly smaller than the length and that complete mixing exists in the fractures. The solution solves a coupled equation: one for the advective, diffusive, and dispersive transport in fractures and another equation for only diffusive transport in the matrix. Adsorption and decay are considered in both equations. The coupled equations are solved for using Laplace transform and Crump numerical inversion. Sudicky and Frind (1982) coded the solution in a FORTRAN program called CRAFLUSH, which we used extensively in the present work. The program collects inputs from a modifiable textfile and produce time series of the concentration in the fractures. In a previous test (Muskus and Falta, 2018), where matrix diffusion was assumed to almost completely dominate transport, the semi-analytical model compared favorably.

In the current work, we have expanded the study of matrix diffusion in fractured media with parallel fractures by testing a series of scenarios where the fracture spacing, sorption rates, and solute decay rates were varied. In those test scenarios, the concentration simulated by the semi-analytical and dual-domain models were compared to that of the analytical solution (Sudicky and Frind, 1982).

A one dimensional (1-D) numerical grid with 200 gridblocks of 1 *m* long in the x-direction was created. A range of fracture spacings from 0.1 *m* to 10 *m* was tested but the fracture aperture was fixed at $b = 100 \mu m$. Using an equivalent porous media approach, the flow model's equivalent hydraulic conductivity was computed as the product of the volume fraction and the conductivity of the matrix. The pore velocity in the fracture was held at 100 *m/yr*, and the intrinsic permeability in the fracture was assumed to be dependent on the fracture aperture, $b^2/12$. The hydraulic gradient was computed as the ratio of the fracture Darcy velocity to the fracture hydraulic conductivity, equaling 0.0004.

The material porosities were set at $\phi_f = 1$ and $\phi_l = 0.1$ for the fracture and the matrix, respectively. The mobile and immobile porosities were computed using Eq 4-38 and Eq 4-39. **Figure 4-19** and **Figure 4-20** show the trends in porosity, equivalent Darcy flux, and equivalent hydraulic conductivity values as the fracture spacing increases:

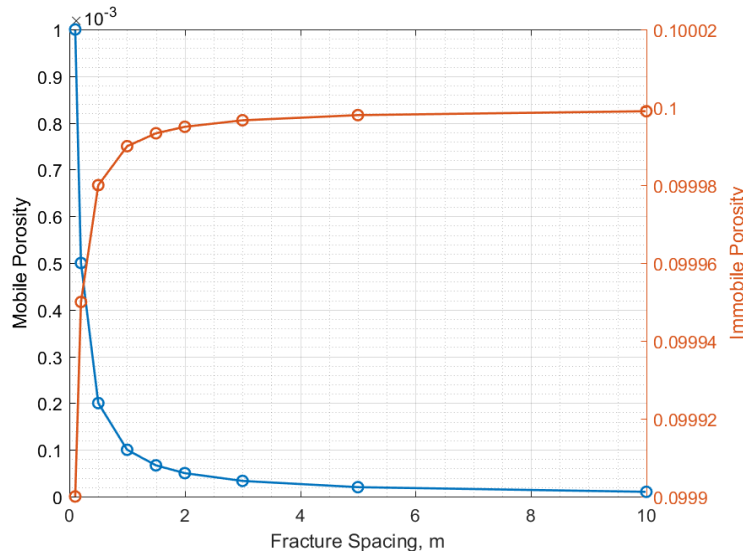


Figure 4-19. Mobile porosity and immobile porosity as fracture spacing increases.

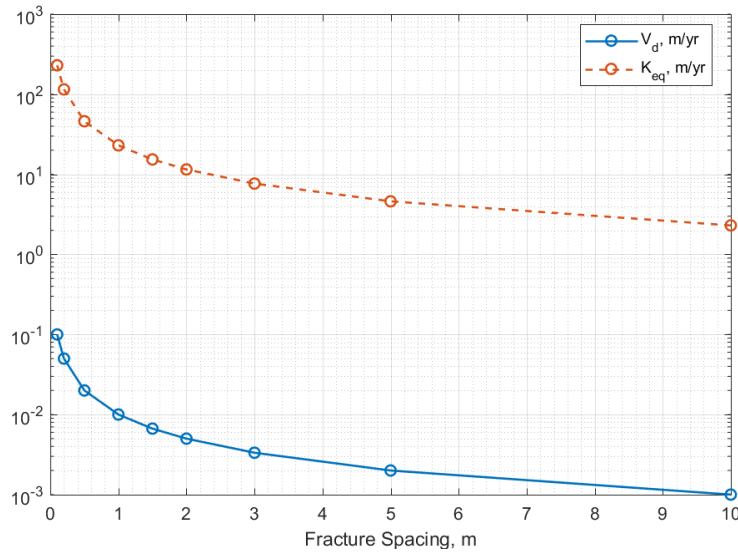


Figure 4-20. Darcy velocity and hydraulic conductivity as fracture spacing increases.

As the fracture spacing increases, there is more low permeability material in the system so the mobile porosity decreases while the immobile porosity increases. The Darcy flux is the largest when the fractures are close together and vice versa. The range of the equivalent hydraulic conductivity tested spans from 230 *m/yr* for a fracture spacing of 0.1 m to 2.3 *m/yr* for a fracture spacing of 10 m.

For each fracture spacing case, the pore velocity is a direct input in the analytical model (Sudicky and Frind, 1982) whereas, the semi-analytical model requires a Darcy flux as an input (Farhat et al., 2018). For the dual-domain model as implemented in MT3DMS (Zheng and Wang, 1999), the Darcy flux is not a direct input so an equivalent flow field must be generated first using MODFLOW (Harbaugh, 2005). A total of nine flow fields were generated, one for each fracture spacing case. Each flow field was then used to simulate an equivalent Darcy velocity in the dual-domain transport model. A flow field can be generated by setting head boundary conditions at the upstream and downstream of each flow model using an equivalent hydraulic conductivity.

After a flow model ran successfully in MODFLOW, a source concentration of 100 *mg/l* of trichloroethylene (TCE) was introduced at the upstream front of the fractured system. Advective loading of the source was enforced by setting the dispersivities in the source cells to a small value. The source was maintained for 50 years in each fracture spacing model and following source removal, clean water was flushed through the system for another 50 years.

The timestep used was 0.05 years. A longitudinal plume dispersivity of 0.5 *m* or half of the gridblock spacing in the x-direction was used in the analytical solution. In the semi-analytical and dual domain models, advection terms were solved for by the standard finite difference scheme with upstream weighting, which has an inherent numerical dispersivity value of 0.5 *m*, same as the value used in the analytical model (Sudicky and Frind, 1982).

Initially, neither decay nor adsorption was considered as fracture spacing was varied. Then, the fracture spacing was varied as the solute half-life decreases from no decay condition to 10 years, 5 years, and 1 year. Finally, the fracture spacing was varied as the retardation factor was increased from 1 (no retardation) to 2 and 5. The retardation factor in the high and low permeability areas were set as equal to each other in our work because that is the underlying assumption in the current implementation of the dual-domain model in MT3DMS (Zheng and Bennett, 2002).

The following table summarizes the modeling parameters used for the fractured media experiments:

Table 4-1. Parameters used in fractured media experiments

Parameter	Fracture	Matrix
Fracture aperture, μm	100	-
Porosity, ϕ_i	1.0	0.1
Tortuosity, τ	1.0	0.1
Retardation factor, R	1 or 2 or 5	
Pore velocity, m/yr	100	0
Diffusion coefficient, m^2/s	0.0316	
Longitudinal dispersivity, α_x	0.0*	-
Decay rate, 1/yr	0 or 0.0693 or 0.1386	
Loading period, yr	50	
Flushing period, yr	50	

*numerical dispersivity is 0.5

To qualitatively evaluate the effectiveness of the dual domain and the semi-analytical models in matching the analytical solution, fracture concentration profiles over distance from source were plotted. Both linear and log-scale concentrations were considered to analyze concentration profile behaviors at high and low range.

Concentration profiles were plotted at four time windows, which were selected to study the system behavior before and after source removal and at high and low concentration gradient. To quantitatively evaluate the models, the root mean square errors (RMSEs) of the semi-analytical and dual-domain concentrations in comparison to the analytical solutions were computed for concentration profiles at each time window. The details on how to compute the RMSE is available in the literature (Singh et al., 2007). Those RMSEs were normalized by the difference between the source concentration and the typical method detection limit (MDL) of dissolved TCE, 0.001 mg/l .

Because the regulatory standard for TCE can be as low as the MDL, the concentration profiles were plotted on the log scale to ensure the simulated concentrations are accurate at low ranges. RMSEs of the log of the simulated and analytical concentration were also computed to gauge the difference in orders of magnitude between the analytical solutions and the model outputs. Those RMSEs were normalized by dividing by 5 or the difference between the log of the source concentration and the TCE detection limit.

Average NRMSEs at linear scale and average NRMSEs at log scale were computed and are referred to as the marginal NRMSEs. The average of those values i.e. the average marginal NRMSEs were also computed to have a single metric to compare the effectiveness of the semi-analytical and the dual-domain models in various fractured systems and under different conditions of plume decay and retardation.

Because of the simplified geometry of the parallel fractured system, all diffusion modeling parameters of the semi-analytical method were computed directly. For dual-domain, the first order mass transfer coefficient can be computed using the shape factor formula. To demonstrate the sensitivity of the shape factor formula to fracture spacing, a mass transfer coefficient was computed using Eq 4-40 prior to calibration for each fracture spacing case. The calibration process was implemented by trial and error to seek the mass transfer coefficient that has the lowest average marginal NRMSEs over different orders of magnitude.

The **Figure 4-21** shows the concentration profiles in four tested fracture spacing cases, and it highlights how the fracture spacing influences the shape of the concentration profiles in the fractures. The figure includes concentration profiles in blue and red from the early time and late time of the loading period respectively. The yellow and purple profiles are from the early time and late time of the unloading period.

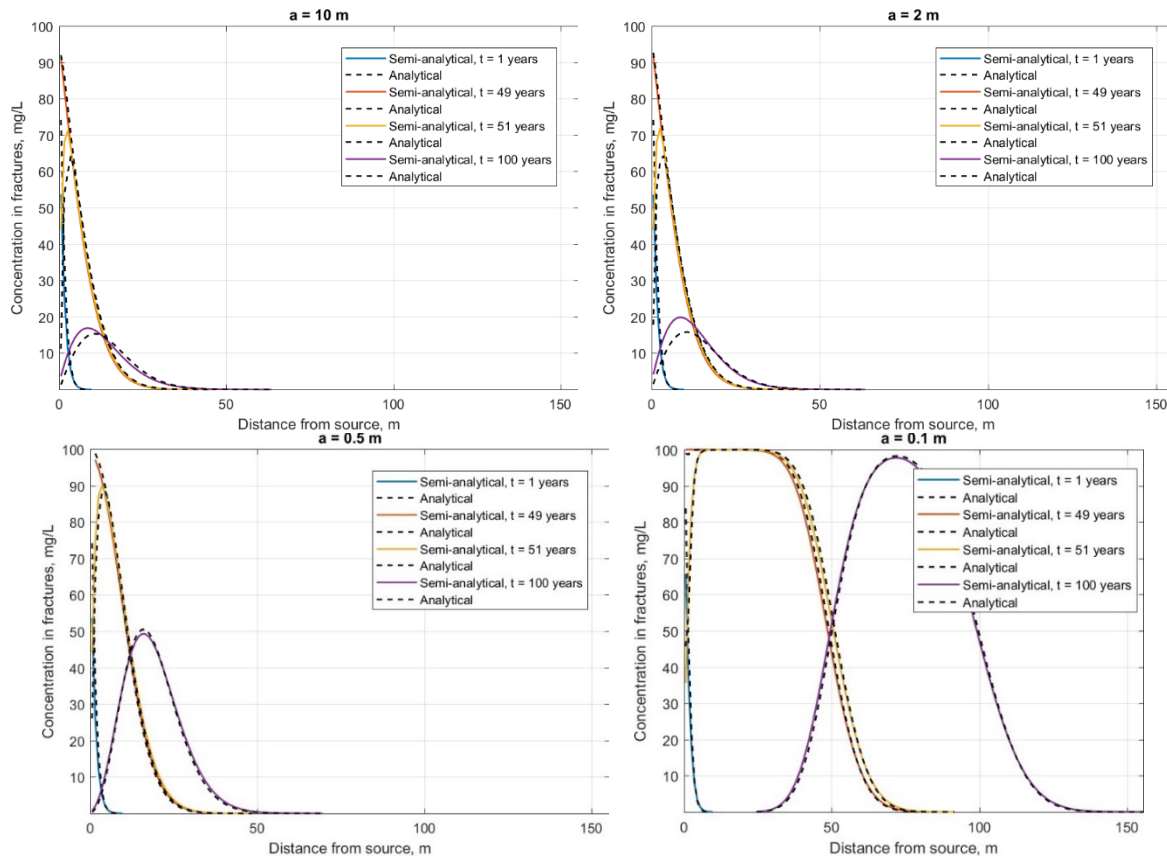


Figure 4-21. Concentration profiles for fracture spacing of 10m, 2m, 0.5m, and 0.1m.

The 1-year profiles (blue lines) of the loading period for the four fracture spacing cases are similar to one another. The semi-analytical method was able to match the exponential shape of the analytical loading curve. At 1 year, both the analytical and the semi-analytical concentration profiles in blue were below the detection limit at 10 m from the source in the six fracture spacing cases. At 49 years, the concentration gradient between the matrix and the fractures was less steep so the drop in the concentration profiles in orange became more gradual over distance. Solute at source concentration was in the fractures for nearly 40 m before the concentration dropped. A clear advective front developed at 50 m from source as the plume was moving at the equivalent seepage velocity of 1 m/yr. Dispersion carried some of the plume mass beyond the advective front, while leaving some behind so the 49-year profile retains a sinusoidal shape.

In the 51-year profiles (yellow lines), an apparent rebound of the concentration in the fractures indicated the effect of back diffusion. At the smallest fracture spacing of 0.1 m, the concentration in the fractures rebounded and remained at peak value for almost 30 m before being flushed out by the clean water front. At that fracture spacing, the matrix volume was minimal so there was less available storage area for the mass, leaving more of it in the fractures for a longer distance from the source. The peak concentration in the 100-year profiles (purple lines) of the unloading period showed another rebound of matrix diffusion at 50 years after source removal. The peak concentration for the profile was initially low but it gradually increased with the fracture spacing to nearly as high as the source concentration at $a = 0.1$ m. As diffusive effects became less dominant with decreasing fracture spacing and matrix volume, the shape of the 100-year profiles

became more symmetrical. As seen in the fracture spacing case of 0.1 m, the shape of the 100-year profile was Gaussian, typical of an advective-dispersive system.

The analysis of the concentration profiles indicated good match between the analytical solution and the semi-analytical method. Peak concentrations simulated by the semi-analytical method were initially off by a minor amount at large fracture spacing cases during the un-loading period but as the spacing was decreased, the match became much closer. While the semi-analytical fitting function can give an adequate approximation of the concentration in the low permeability layers, the method is not exact, especially in highly diffusive systems and when the concentration gradient is steep following the source removal.

Before comparing the semi-analytical results with the dual-domain simulation results, it was verified that the dual-domain and the semi-analytical method produce the same outputs when matrix diffusion is not considered (**Figure 4-22**). The objective was to isolate the simulation of the diffusion process from the simulation of other transport processes when comparing the two methods.

The case of 0.1 m fracture spacing is shown without matrix diffusion using the semi-analytical and the dual-domain method. To simulate the no diffusion scenario, the semi-analytical method's matrix diffusion area A_{md} , and the dual-domain mass transfer coefficient β , were set to zero.

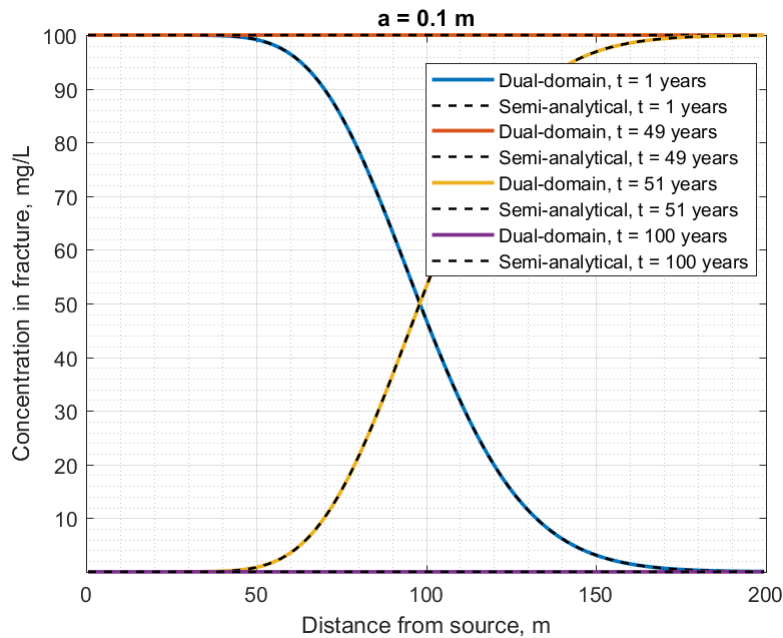


Figure 4-22. Concentration profile without diffusion for fracture spacing $a = 0.1$ m

After one year, a mixing zone developed with the advective front at approximately 100 m from the source. Without diffusion into the embedded low permeability layers, the advective front was 50 m further downstream in comparison to the case with diffusion (see **Figure 4-21**). At later time in the loading period, without diffusion, the concentration profile was at steady state after

49 years. Had matrix diffusion been present as in **Figure 4-21**, the shape of the concentration profile would not have been steady because the mass was still being loaded into the matrix. Following source removal, the 51-year profile mirrored the 1-year profile over the y-axis as the system switched from being loaded with a source to being flushed with clean water. Without matrix diffusion, the contaminant was completely removed from the system 50 years post-source removal.

The semi-analytical and dual-domain profile were identical, indicating that the two methods only differ in the way they simulate diffusive transport. Although only the fracture spacing case of 0.1 *m* is shown here, the same analysis was repeated for all fracture spacing cases with the same result.

After verifying that the dual-domain and semi-analytical model produce identical concentration profiles when diffusion was not considered, diffusion was considered at each fracture spacing. For the semi-analytical method, the matrix diffusion area was changed from zero to a computed value. For the dual-domain model, the mass transfer coefficient was computed first using the shape factor formula. Then, additional values of the mass transfer coefficient were tested to gauge the effect of the coefficient on the concentration profile and to calibrate a better fit of the dual-domain profile to the analytical solution via trial and error.

The **Figure 4-23** shows concentration profiles at each of the four time periods over distance from source for the largest fracture spacing of 10 *m*. The analytical solution is shown in dashed black line, whereas the semi-analytical simulation is shown in blue dash- dotted line. The dual-domain simulations are shown in color solid lines. The mass transfer coefficient with five significant figures is the coefficient computed by the shape factor formula while the rest are iterations of the coefficient from calibration. The mass transfer coefficient iteration that produced the best average marginal NRMSE value is plotted as asterisks.

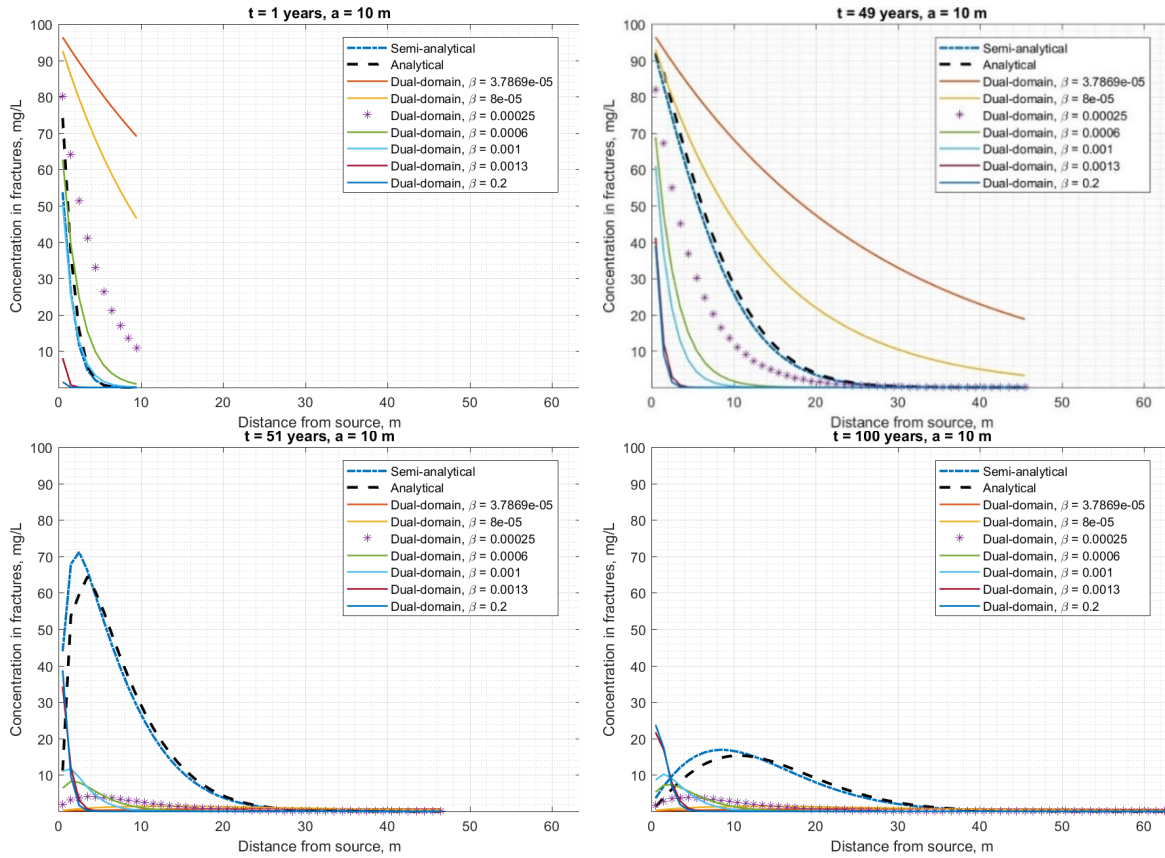


Figure 4-23. Comparison of analytical, semi-analytical, and dual domain concentration profiles for a fracture spacing of 10 m at 1, 49, 51, and 100 years.

In **Figure 4-23**, the concentration profiles using the mass transfer coefficient as computed by the shape factor formula were plotted immediately after the semi-analytical and the analytical profiles in solid orange lines. That mass transfer coefficient was unable to produce profiles that match the analytical solution for all four time periods. For the case of 10-m spacing, the first order mass transfer model is invalid because of its time-dependent steady-state assumption. As shown previously, the case of 10-m spacing requires 800 years to reach steady-state, which makes the dual-domain model impractical for many common simulations such as the one being considered here, where the concentration profiles are evaluated over the span of 100 years.

Even after calibration, the dual-domain model was still unable to match the analytical solution because a calibrated mass transfer coefficient that quantitatively placed the dual-domain concentrations close to the analytical solution during the loading period could not match the analytical solution during the unloading period. As observed by Guan et al. (2008) and others in the literature, because the mass transfer coefficient is a time-dependent parameter, it is not possible to have one parameter that works for all time periods.

For fracture spacing case of 2 m (**Figure 4-24**), the characteristic diffusion time is only 30 years so the mass transfer coefficient as predicted by the shape factor formula is expected to match analytical solutions better at later times during loading and unloading periods.

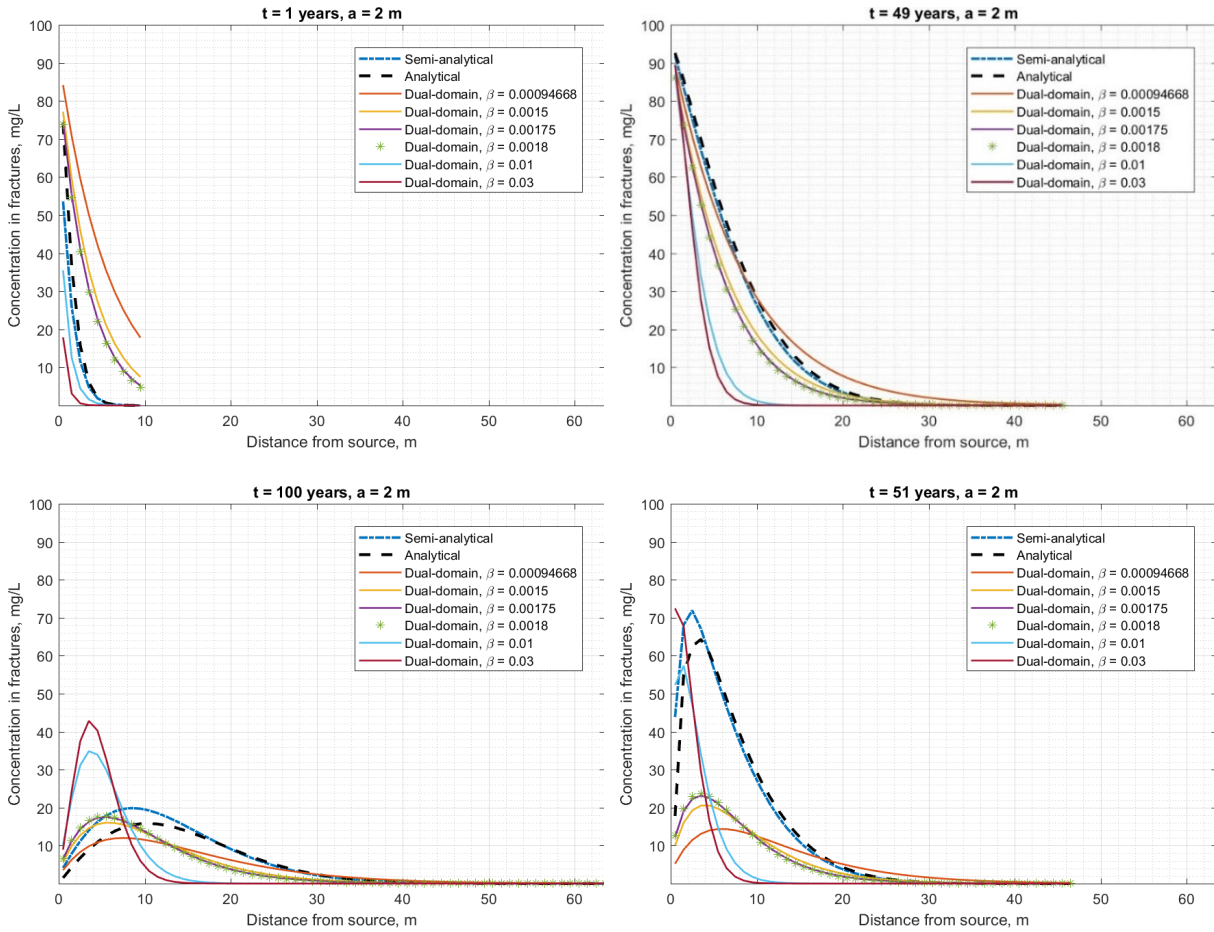


Figure 4-24. Comparison of analytical, semi-analytical, and dual domain concentration profiles with a fracture spacing of 2 m at 1, 49, 51, and 100 years.

The orange line is the concentration profile produced by the mass transfer coefficient computed using the shape factor. It matched relatively well with the analytical solution at 49 years and 100 years. It did not match the analytical solution at 1 year and 51 years because the characteristic diffusion time had not been reached. The semi-analytical method does not require the quasi-steady state assumption to work. It matched analytical solution well at all time windows.

The profile of the calibrated mass transfer coefficient value was plotted in green asterisk line. The calibration improved the fit at later times but the dual-domain model was unable to match the analytical solution using one mass transfer coefficient for all time periods.

For a fracture spacing case of 0.1 m (**Figure 4-25**), the characteristic diffusion time is fast at 0.08 years, which is almost two orders of magnitude less than the 1-year time window of analysis. So, the dual domain model is expected to match the analytical solution well at all four time periods.

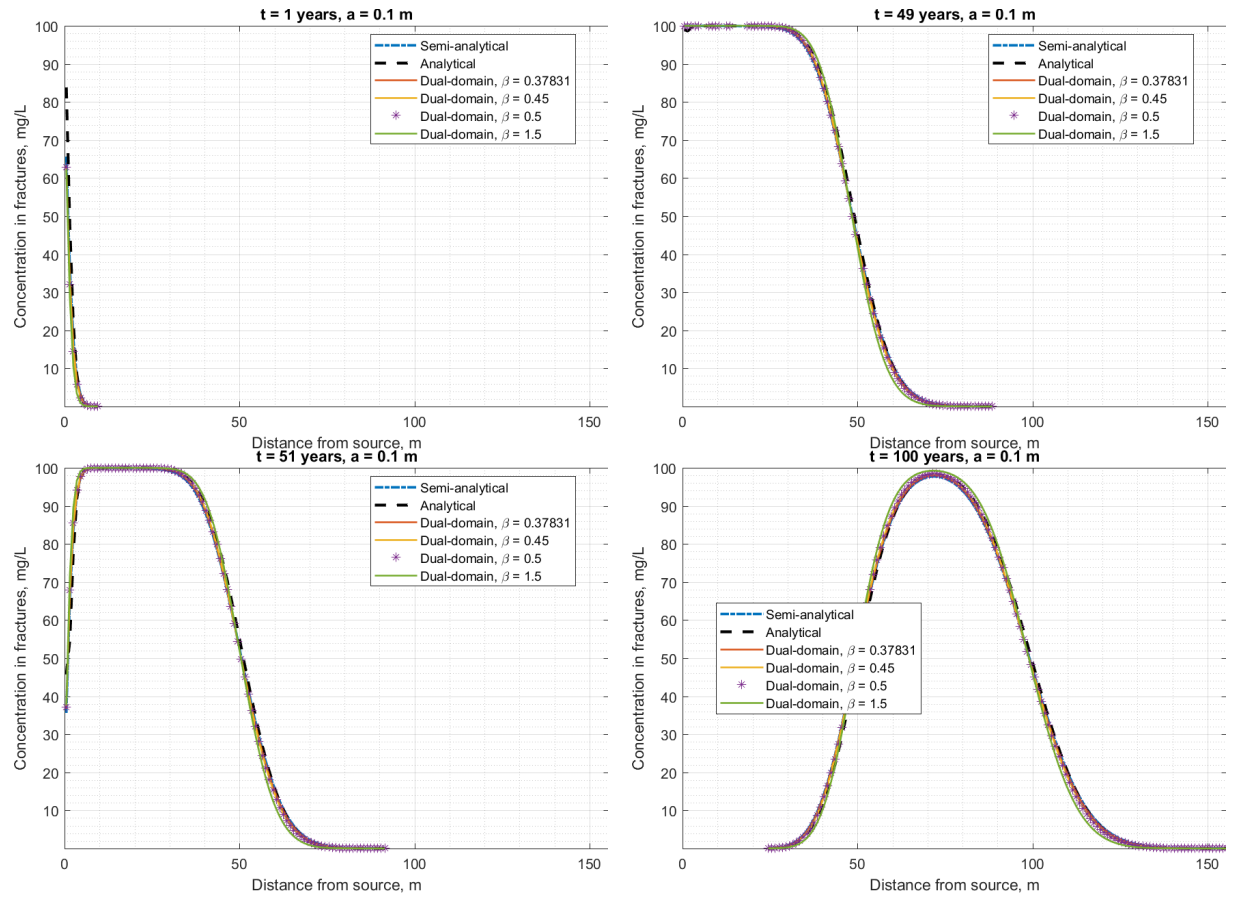


Figure 4-25. Comparison of analytical, semi-analytical, and dual domain concentration profiles with a fracture spacing of 0.1m at 1, 49, 51, and 100 years.

At linear scale, all of the concentration profiles shown matched well with the analytical solution. The best fit mass transfer coefficient for this case was 0.5/yr, which is not far off from the value of 0.378/yr predicted by the shape factor formula.

Following analysis of the concentration profiles at linear scale, we also plotted the profiles at log scale to study the performance of the semi-analytical and the dual-domain method at low concentration range and at distance far from the source. Results indicated that the semi-analytical did not only match the analytical solution well at linear scale but also at log scale. Meanwhile, the inability of the dual-domain method to match the analytical solution at large fracture spacing was underlined when the profiles were plotted on log scale. We repeated the concentration profile comparison for six other fracture spacing cases in the range between 0.1 m and 10 m.

Figure 4-26 summarizes the change of the average marginal NRMSEs for both the semi-analytical and the dual-domain models.

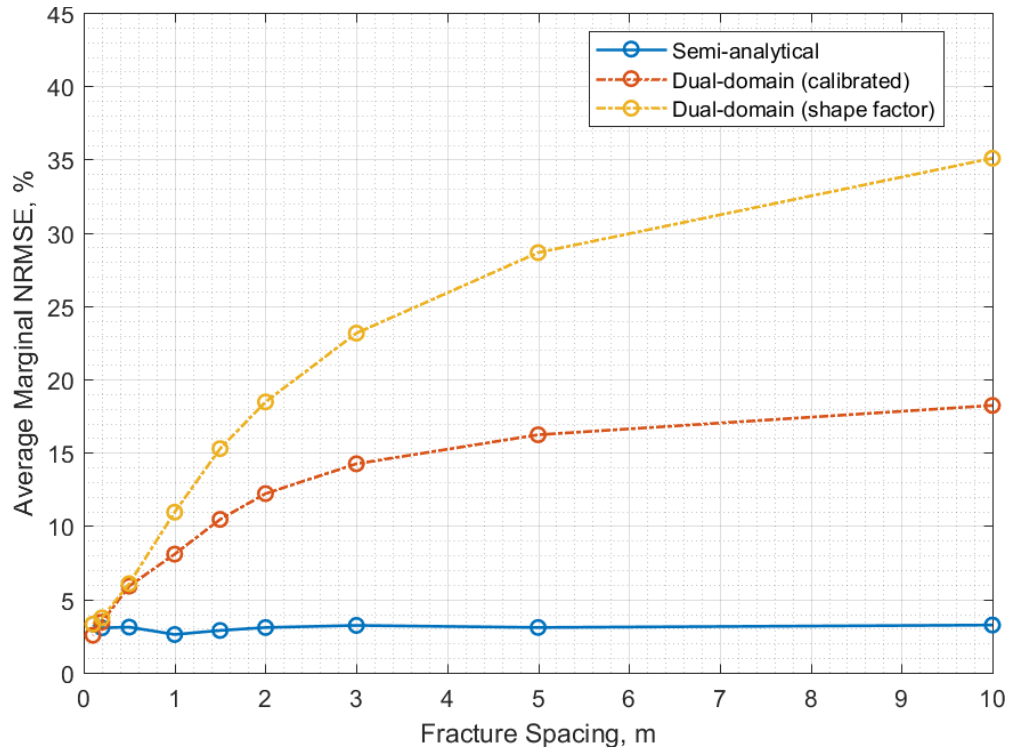


Figure 4-26. Average marginal NRMSEs comparison between semi-analytical and uncalibrated dual-domain models over fracture spacing range between 0.1 *m* and 10 *m*.

The NRMSE values for the semi-analytical method was consistent over the range of fracture spacing at 3.5% or less. In contrast, the mass transfer coefficient computed by the shape factor formula only worked without calibration at fracture spacing less than 1 *m*. At the largest fracture spacing, the error was tenfold that of the semi-analytical method without calibration. The effectiveness of the mass transfer coefficient based on the shape factor is limited by the quasi-steady state assumption which can only be satisfied at small fracture spacing.

5.0 ESTIMATING THE IMPACT OF MATRIX DIFFUSION ON CLEANUP TIME

Objective: Develop simplified methods for estimating the impact of matrix diffusion on cleanup time.

5.1 INTRODUCTION

Extensive research over the past thirty years (Mackay et al., 2000; Liu and Ball 1999; Chapman and Parker 2005; Parker et al., 2008) has demonstrated that diffusive mass transfer can have a major impact on contaminant transport in the subsurface. As a plume advances through an aquifer, dissolved contaminants will diffuse from high K zones into low K zones, slowing the rate of contaminant migration in the high K zone. However, once the contaminant source is eliminated, contaminants will diffuse out of low K zones, slowing the cleanup rate in the high K zone (Grisak and Pickens 1980).

There are multiple numerical and analytical models that can be used to simulate diffusive mass transfer processes and their impacts on large scale contaminant migration. Chapman et al. (2012) demonstrated that the numerical models HydroGeoSphere (Therrien et al., 2010), FEFLOW (Trefry and Muffels, 2007), and MODFLOW/MT3DMS (Zheng and Wang, 1999) are capable of simulating back diffusion process and accurately predict concentration changes over 3 Orders-of-Magnitude (OoM). However, a fine vertical discretization is required to accurately simulate back diffusion (Farhat et al., 2020), greatly increasing simulation time.

Falta and Wang (2017) present a semi-analytical approximation for simulating transient matrix diffusion for use in numerical contaminant transport simulators. In this approach, the contaminant concentration profile in extensive low K zones is represented with a fitting function that is adjusted at each timestep. The resulting matrix diffusion fluxes are added to the numerical model as linear concentration-dependent source/sink terms, eliminating the need for fine discretization of the low K region and greatly reducing computation time. Muskus and Falta (2018) extend this approach to simulate matrix diffusion in finite thickness low K zones embedded within a numerical gridblock and allow for coupled parent-daughter decay reactions with multiple species. The embedded low K zones have a finite average thickness, volume fraction and interfacial area with the high permeability domain. Simulation results generated with this method closely matched matrix diffusion results from laboratory experiments with layered systems and irregularly shaped low K lens, fine grid numerical simulations, and analytical solutions for matrix diffusion in fractured rock and with parent-daughter decay reactions.

Implementation of any modeling project requires a substantial investment of time and resources to obtain site specific information on model parameters, run the model, and interpret the results. In this work, we conduct an extensive sensitivity analysis to identify the aquifer characteristics that have the greatest impact on site cleanup time and develop simplified methods that can provide preliminary estimates of the time after complete source removal to reach 1, 2 or 3 OoM reductions in contaminant concentrations for a range of aquifer conditions.

5.2 APPROACH

We employ the modeling approach developed by Muskus and Falta (2018) and incorporated in REMChlor-MD (Falta et al., 2018) to evaluate the effect of matrix diffusion on aquifer cleanup times for a range of site conditions. **Figure 5-1** shows typical results generated with REMChlor-MD, showing the change in contaminant concentrations in a monitor well located 100 m downgradient from a contaminant source in a homogeneous aquifer for two different boundary conditions and two different solute transport velocities. For the zero (0 BD) low K boundary condition and $V = 105$ m/yr, contaminant concentrations in the well reach close to 100% of the source concentration within a few years after the release, and then decline rapidly after source removal at 50 years. When one (1 BD) low K boundary is present, contaminant concentrations also rise rapidly, and then decline following source removal. However, once the contaminant declines by 2 OoM (99%), concentrations in the monitor well begin to decline more slowly as contaminants diffuse out of the underlying low K zone into the transmissive aquifer. Concentrations patterns are similar for $V = 10.5$ m/yr. However, the impacts of back diffusion are greater for $V = 10.5$ m/yr, due to the longer travel time (T_i) from the source to the monitoring point. This simple example illustrates the impacts that diffusive mass transfer between high and low K zones can have on cleanup times following source removal. In a homogeneous aquifer with no low permeability boundaries, contaminant decline rapidly following source removal. However, in the presence of a low K boundary, the time to reach 2 OoM (99%) or 3 OoM (99.9%) reductions in contaminant concentrations can be much greater.

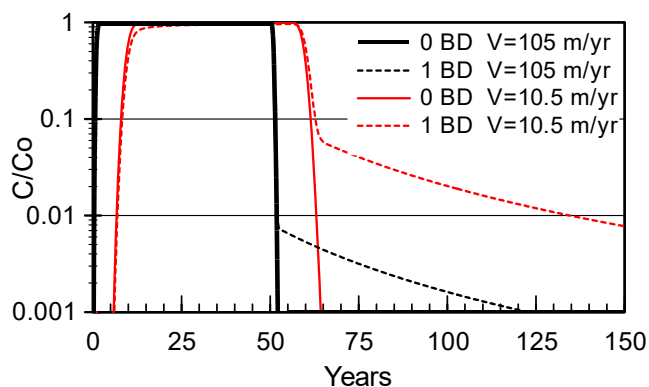


Figure 5-1. Example contaminant breakthrough and flush out curves for homogeneous aquifer with zero (0 BD) and one (1 BD) low K boundaries and aquifer transport velocity (V) = 105 and 10.5 m/yr.

In this work, we conduct an extensive sensitivity analysis using the semi-analytical modeling approach developed by Falta and Wang (2017) to simulate contaminant migration through a hypothetical aquifer and calculate the time (T) to reach 1 OoM (90%), 2 OoM (99%) and 3 OoM (99.9%) reductions in contaminant concentration. OoM reductions are calculated based on the contaminant concentration at a specified distance downgradient from the source, at the time the source is eliminated. Concentrations at the downgradient monitoring points are somewhat lower than the source concentration due to less than complete breakthrough, prior to source elimination.

Two general conditions are evaluated: (a) a heterogeneous aquifer containing one or more embedded low K zones with a defined thickness, interfacial area, and volume fraction; and (a) homogeneous aquifer of thickness B bounded below and/or above by semi-infinite low K boundaries(**Figure 5-2**). The semi-infinite low K boundaries are thick low K zones where the solute diffusing into this zone does not reach the end of the layer within the simulation period. In contrast, low K zones embedded within the heterogeneous aquifer are sufficiently thin that contaminants diffusing into these zones may encounter boundaries or contaminants diffusing from the other side within the simulation period. In all cases, advection through low K zones was assumed to be zero.

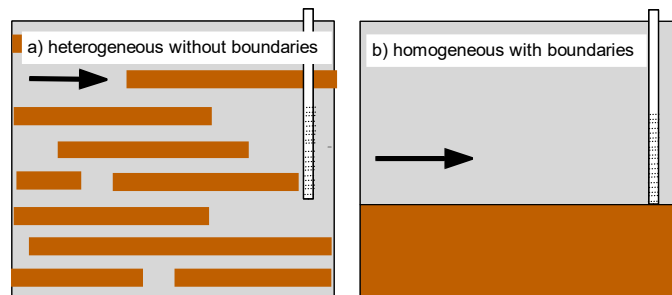


Figure 5-2. Aquifer conditions evaluated: a) heterogeneous aquifer with no low K boundaries; and a) homogeneous aquifer with semi-infinite low K boundaries.

Parameters examined in the sensitivity analysis included K of high K zone, distance to the monitoring point (X), high K zone non-reactive solute transport velocity (V), high-K travel time ($T_t = X/V$), aquifer thickness (B), number of semi-infinite low K boundaries (BD), maximum distance in aquifer to low K boundary (B/BD), aquifer high K volume fraction (V_F), time to flush one pore volume through aquifer ($T_{PV} = T_t/V_F$), number of interfaces between high and low K zones in heterogeneous aquifer (# interface), low K diffusion length (D_L), contaminant loading period prior to source removal, high K retardation factors (R_H), and low K retardation factor (R_L). A total of ~28,000 simulations are run generating values of T for 1, 2 and 3 OoM reductions for a range of parameter values. JMP Pro (Sall et al., 2017) was used to conduct standard least squares regressions to identify the parameters that had the greatest influence on cleanup time.

To focus on the effects of diffusive mass transfer between high and low K zones, the source area extends over the full width and depth of the aquifer. Transverse and vertical dispersivity are zero to minimize the impact of source width on simulation results. Contaminants degradation rates are zero in both the high and low K zones, so only the effects of source removal are evaluated. Diffusion Coefficient (D_m) was $9.1E-10$ m²/s in all simulations, a representative value for TCE. The model domain was 200 m long, 20 m wide and 3 m thick with $\Delta x=1$ m, $\Delta y=20$ m and $\Delta z=3$ m. Preliminary work showed the model discretization in the y and z direction had no detectable impact on simulation results. Monitoring wells with 3 m (~10 ft) long screens are located at 25, 50, 75, 100, 125 and 150 m downgradient of the source. For homogeneous aquifers with boundaries, monitor wells screens are located immediately adjoining the low K boundary. The model was run for 1000 yr after source removal. When cleanup times are greater than 1000 yr, these results are not included in the analysis.

A fifty-year loading period was selected for the base case, which is equivalent to a spill occurring in 1960 with complete (100%) source removal in 2010. The base case aquifer thickness was 3 m (~10 ft), equivalent to the length of common monitoring well screens. Hydraulic gradient, porosity and tortuosity are 0.001, 0.3 and 0.7, respectively. Parameter ranges examined in the sensitivity analysis are presented in **Table 5-1**. Given this range of values, the non-reactive solute transport velocity varied from 10.5 to 840 m/yr. When solute travel time to the monitoring point was less than 0.25 yr, these simulations are not included from the analysis.

We did not conduct an extensive evaluation of the impact of D_m , high K porosity, and low K zone porosity on cleanup time. A limited preliminary evaluation indicated that typical variations in these parameters did not have a dramatic impact on cleanup time. However, additional work is needed to better understand this process.

Table 5-1. Parameter Values Evaluated in Sensitivity Analysis.

Parameter	Values Evaluated
Contaminant Loading Period (yr)	10, 25, 50, 100
High K Volume Fraction, V_F	0.1, 0.2, 0.4, 0.6, 0.8, 0.9
Number of Interfaces, $\#_{inter}$	1, 2, 4, 6, 8
High K Hydraulic Conductivity, K_H (cm/s)	0.01, 0.02, 0.03, 0.05, 0.10, 0.20, 0.40, 0.80
Monitoring Location (X)	25, 50, 75, 100, 125, 150
High K Retardation Factor, R_H	1, 2, 5, 10
Low K Retardation Factor, R_L	1, 2, 5, 10
Aquifer Thickness, B (m)	0.5, 1, 2, 3
# Low K Boundaries (BD)	0, 1, 2

Results are first presented for the cleanup of a non-reactive tracer (contaminant does not sorb to aquifer) with a 50 yr loading period. In later sections, the effects of sorption and contaminant loading period are discussed.

5.3 REGRESSION ANALYSIS FOR NON-REACTIVE TRACER

The statistically significant parameters ($p < 0.001$) that have the greatest impact on cleanup time in heterogeneous aquifers without low K boundaries are T_{PV} and D_L . T_t and V_F are not significant when T_{PV} was included. Number of interfaces and V_F are not significant when D_L was included. The parameters with the greatest impact on cleanup time in homogeneous aquifers with low K boundaries are T_t and B/BD. High K velocity and distance to monitoring point are not statistically significant when T_t is included. Similarly, B and BD are not significant when the parameter B/BD is included. The best fit multiple regression equation for estimating cleanup time (T) has the following form.

$$\ln(T) = C_1 + C_2 \cdot \ln(T_{PV}) + C_3 \cdot \ln(D_L) + C_4 \cdot \ln(T_i) + C_5 \cdot \ln(B/BD) \quad (5-1)$$

Best fit values for C_1 to C_5 are shown in **Table 5-2** along with the correlation coefficient (r^2) and RMSE. Both arithmetic and Ln transformed values of each parameter were evaluated. However, Ln transformed values are much better predictors of cleanup time and are incorporated into Eq 5-1.

Cleanup times calculated with REMChlor-MD (T_{MD}) and Eq 5-1 (T_{Reg}) are compared in **Figure 5-3** for a heterogeneous aquifer without low K boundaries, and for a homogeneous aquifer with one or two low K boundaries. The mean \pm standard deviation of the ratio T_{Reg}/T_{MD} are provided in **Table 5-2** as an additional measure of model goodness of fit. Overall, Eq 5-1 provides a reasonably good estimate of cleanup times generated by REMChlor-MD. Most regression estimates are within a factor of 2 of the REMChlor-MD values.

Table 5-2. Regression Coefficients for Estimating Non-Reactive Solute Cleanup Time.

Coefficient	Parameter	Heterogeneous with zero low K boundaries			Homogeneous with one or two low K boundaries		
		1 OoM	2 OoM	3 OoM	1 OoM	2 OoM	3 OoM
C_1	--	0.084	2.272	3.248	0.626	3.012	5.399
C_2	$\ln(T_{PV})$	1.093	0.738	0.593	--	--	--
C_3	$\ln(D_L)$	-0.080	0.558	0.817	--	--	--
C_4	$\ln(T_i)$	--	--	--	1.259	1.058	0.572
C_5	$\ln(B/BD)$	--	--	--	-0.668	-1.011	-0.546
r^2		0.93	0.98	0.97	0.93	0.92	1.00
RMSE		0.316	0.17	0.21	0.35	0.36	0.01
T_{Reg}/T_{MD} Mean \pm Std Dev.		1.06 ± 0.42	1.01 ± 0.17	1.02 ± 0.20	1.05 ± 0.34	1.09 ± 0.57	1.00 ± 0.01

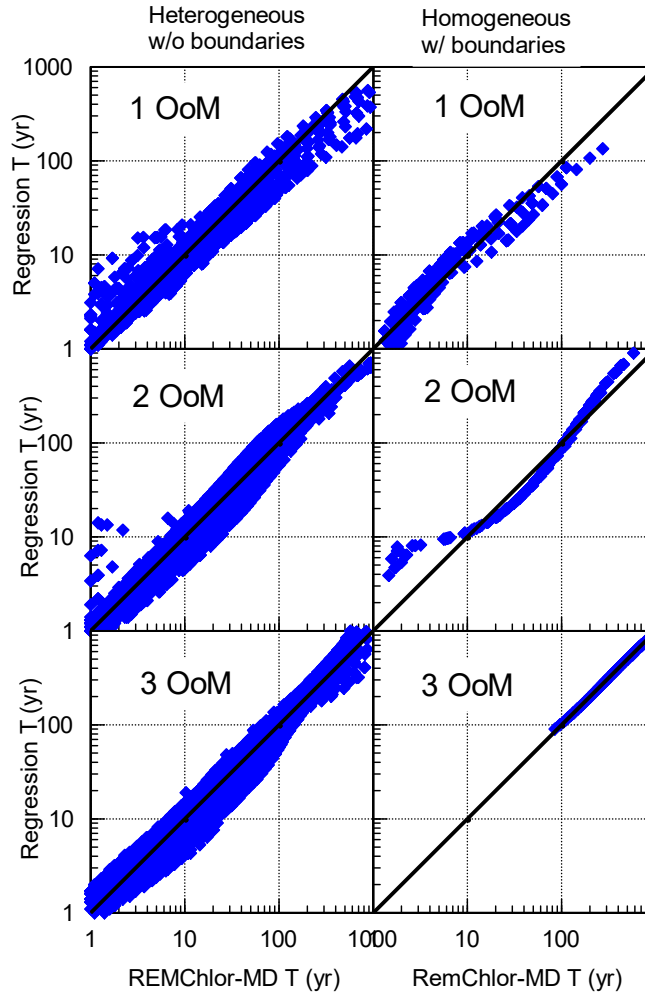


Figure 5-3. Comparison of cleanup times calculated with RemChlor-MD and simplified regression equations for heterogeneous aquifer without low K boundaries and homogeneous aquifer with low K boundaries.

5.3.1 Heterogeneous Aquifer without Low K Boundaries

Figure 5-4 shows a series of curves generated with Eq 5-1 for heterogeneous aquifers without low K boundaries. These curves show the cleanup time (T) and normalized cleanup time (T/T_{PV}) for 1, 2 and 3 OoM reductions in contaminant concentration for varying T_{PV} and diffusion length (D_L). As expected, cleanup time increases with T_{PV} for all cleanup levels. For $T_{PV} > 5$ yr, the time to reach 1, 2 and 3 OoM reductions are 1.2-1.6 T_{PV} , 1.5-6 T_{PV} , and 2-15 T_{PV} , respectively. Greater values of D_L reduce the time to reach 1 OoM cleanup, but increase the time to reach 2 and 3 OoM cleanup. For 2 and 3 OoM cleanup, T/T_{PV} increases rapidly for $T_{PV} < 2$ yr, indicating cleanup time is mass transfer limited for $T_{PV} < 2$ yr.

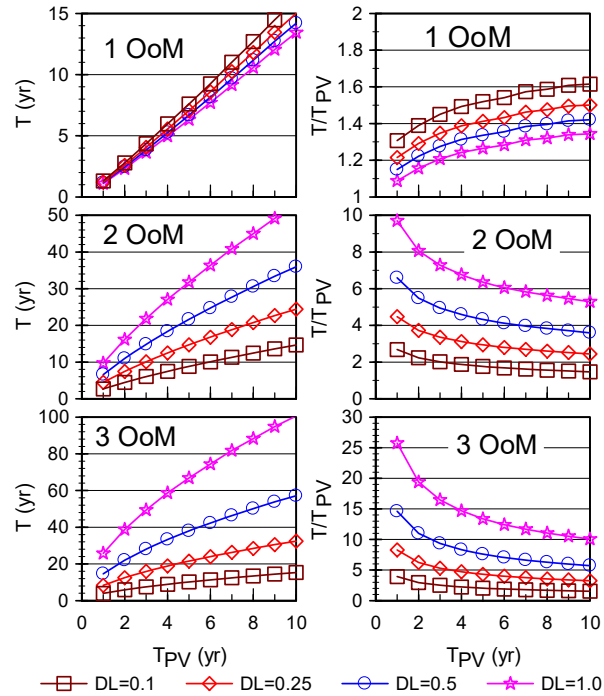


Figure 5-4. Cleanup time (T) and normalized cleanup time (T/T_{PV}) in a heterogeneous aquifer without low K boundaries for 1 OoM (90%), 2 OoM (99%) and 3 OoM (99.9%) reductions in contaminant concentrations for complete source removal after a 50-year loading period.

5.3.2 Homogeneous Aquifer with Low K Boundaries

Figure 5-5 shows a series of curves generated with Eq 5-1 for homogeneous aquifers with low K boundaries. The curves relate estimated cleanup time (T) and normalized cleanup time (T/T_t) for 1, 2 and 3 OoM reductions in contaminant concentration as a function of Travel Time (T_t) to the monitoring location in the high K zone and aquifer thickness divided by the number of low K boundaries (B/BD). Cleanup time increases with increasing T_t for all cleanup levels since more time is required to flush one pore volume (PV) of groundwater through the aquifer. For $T_t > 5$ yr, the time to reach 1, 2 and 3 OoM reductions are 1-6 T_t , 5-50 T_t , and 40-150 T_t , respectively. Cleanup time is greater for smaller B/BD for all cleanup levels since diffusive flux is greater relative to advective flux for thinner aquifers.

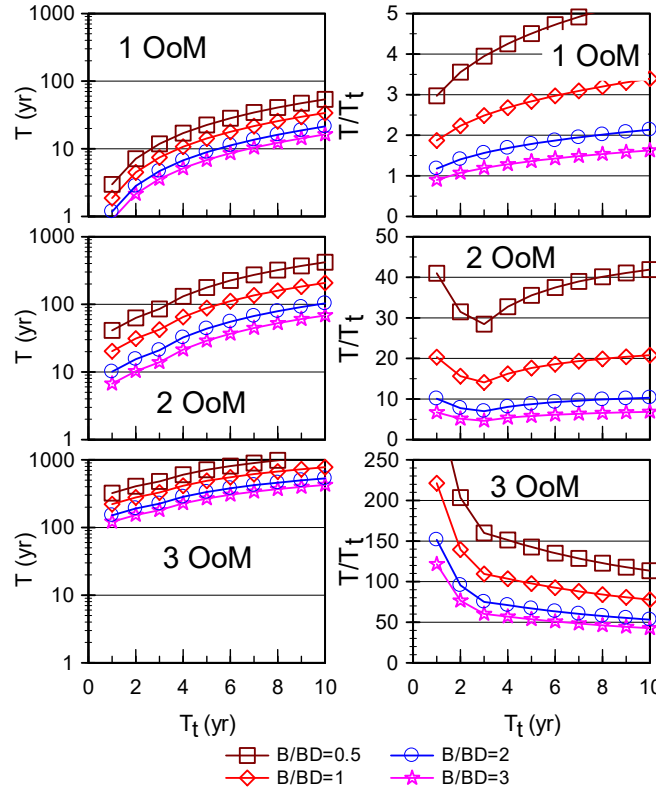


Figure 5-5. Effect of travel time (T_t) and aquifer thickness divided by number of low K boundaries (B/BD) on cleanup time (T) and normalized cleanup time (T/T_t) in a homogeneous aquifer with low K boundaries for 1 OoM (90%), 2 OoM (99%) and 3 OoM (99.9%) with a 50 year loading period.

Overall, cleanup times are much longer for homogeneous aquifers bounded by thick low K zones compared to heterogeneous aquifers without low K boundaries. This effect is most dramatic for thin aquifers bounded above and below by thick low K zones. The time to reach 3 OoM cleanup will often exceed $100 T_t$ for a 1 m thick aquifer bounded above and below by thick low K zones. For a 3 m thick aquifer bounded by an underlying low K aquitard, time to reach 3 OoM $\sim 50 T_t$.

5.4 CONTAMINANT LOADING PERIOD

Sensitivity analyses were conducted to evaluate the effect of varying the contaminant loading period on cleanup time (T) for 1, 2 and 3 OoM (90%, 99%, 99.9%) reductions in concentration. Multiple regression analyses showed that there was limited interaction between loading period and other parameters (V , X , T_t , V_F , D_L , T_{PV} , B , BD , B/BD) and the effect of varying the loading period could be represented by the Cleanup Time Ratio (CTR) for sorption where

$$CTR_L = \frac{\text{Cleanup Time with varying Loading Period}}{\text{Cleanup Time with 50-year Loading Period}} \quad (5-2)$$

Figure 5-6 shows cumulative density functions for CTR_L in heterogeneous and homogeneous aquifers for 1, 2 and 3 OoM reductions. In heterogeneous aquifer, varying the loading period has a limited impact on cleanup time. For 1 2 and 3 OoM cleanup levels, CTR_L is commonly close to 1. This indicates that loading period has a limited impact on cleanup times in aquifer that are not bounded by thick low K zones. In homogeneous aquifers with one or two low K boundaries, loading period had a somewhat greater impact on cleanup time. Longer loading periods increased cleanup times, with the greatest impacts for 3 OoM cleanup. However, the overall impact of loading period on cleanup time was modest.

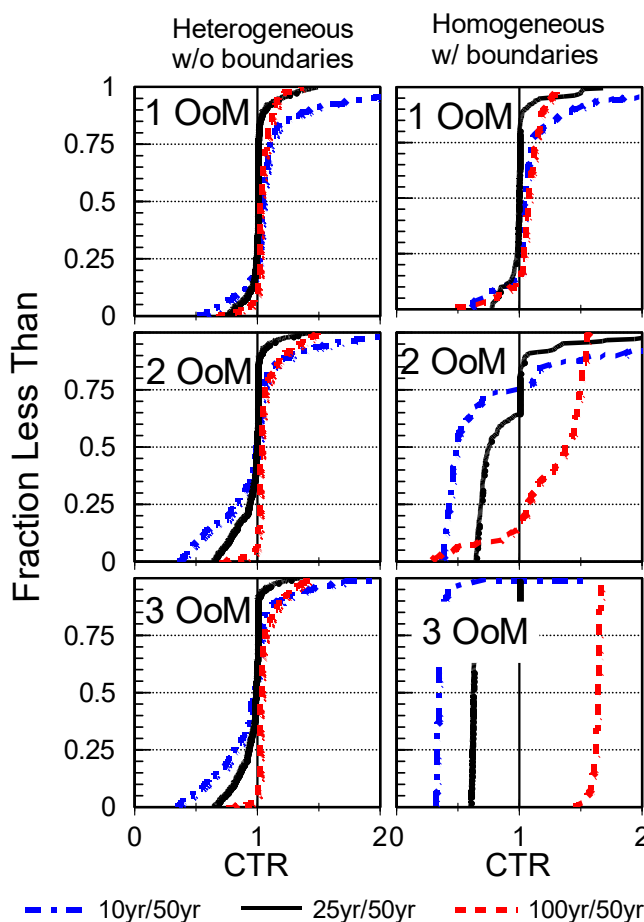


Figure 5-6. Cleanup time ratio (CTR) for 10, 25 and 100 yr loading periods in homogeneous and heterogeneous aquifers.

5.5 CONTAMINANT SORPTION

Sensitivity analyses are also conducted to evaluate the effect of varying the linear-equilibrium retardation factor for the high K zone (R_H) and low K zone (R_L) on cleanup time (T) for 1, 2 and 3 OoM (90%, 99%, 99.9%) reductions in concentration. Multiple regression analyses showed that there was limited interaction between R_H and R_L and other parameters (V , X , T_i , V_F , PV , D_L , B , BD , B/BD) and the effect of varying R_H and R_L could be represented by the Cleanup Time Ratio for Retardation (CTR_R) where

$$CTR_R = \frac{\text{Cleanup Time with varying } R_H \text{ and } R_L}{\text{Cleanup Time with } R_H = R_L = 1} \quad (5-3)$$

Both arithmetic and Ln transformed values of R_H and R_L are evaluated as predictors of CTR_R . Ln transformed values are much better predictors of CTR_R ($p < 0.001$) and are incorporated into Eq 5-4.

$$\ln(CTR_R) = C_1 + C_2 \ln(R_H) + C_3 \ln(R_L) \quad (5-4)$$

Best fit values of C_1 , C_2 and C_3 are shown in **Table 5-3** along with r^2 , RMSE, and the mean and standard deviation of the ratio of regression generated CTR_R divided by REMChlor-MD generated CTR_R (regression/REMChlor). Most regression estimates are within a factor of 2 of the REMChlor-MD values.

Table 5-3. Regression Coefficients for Estimating Clean Time Ratio for Retardation (CTR_R).

Coefficient	Parameter	Heterogeneous without Low K Boundaries			Homogeneous with Low K Boundaries		
		1 OoM	2 OoM	3 OoM	1 OoM	2 OoM	3 OoM
C_1	--	-0.028	-0.008	0.005	-0.052	-0.042	-0.003
C_2	$\ln(R_H)$	0.386	0.165	0.102	0.133	0.380	0.324
C_3	$\ln(R_L)$	0.527	0.708	0.746	0.755	0.354	0.053
r^2		0.71	0.77	0.83	0.82	0.57	0.55
RMSE		0.42	0.36	0.30	0.32	0.45	0.27
Regression/REMChlor Mean \pm Std Dev.		1.09 ± 0.47	1.07 ± 0.48	1.05 ± 0.39	1.05 ± 0.33	1.09 ± 0.39	1.02 ± 0.13

Figure 5-7 shows a series of curves generated with Eq 5-4 for heterogeneous and homogeneous aquifers. The curves relate estimated CTR_R for 1, 2 and 3 OoM reductions for different values of R_H and R_L . For all conditions evaluated, CTR_R increased with both R_H and R_L . However, the increase in CTR_R was generally less than the values of R_H and R_L . For example, increasing both R_H and R_L to 10, increased CTR_R by roughly a factor of 8 for 1 and 2 OoM cleanup in a heterogeneous aquifer. Generally, cleanup times in heterogeneous aquifers are more sensitive to R_H and R_L than for homogeneous aquifers with low K boundaries.

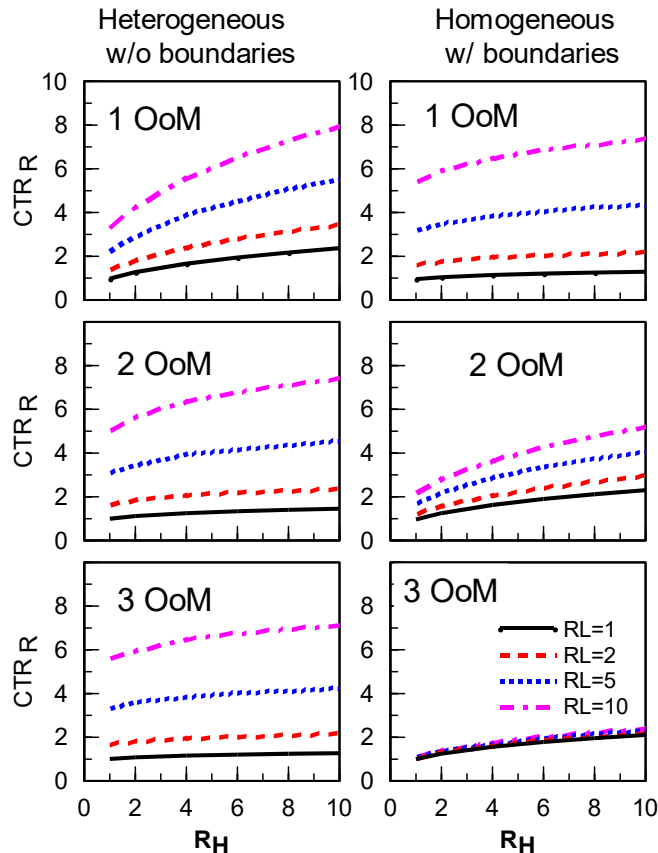


Figure 5-7. Effect of varying R_H and R_L on the Cleanup Time Ratio for Retardation (CTR_R) for homogeneous aquifers with low K boundaries and heterogeneous aquifers without low K boundaries.

5.6 IMPLICATIONS FOR REMEDIATION SYSTEM DESIGN

These results indicate that at many sites matrix diffusion will dramatically slow aquifer cleanup following source removal. In many cases, tens to hundreds of pore volumes of groundwater must migrate through the aquifer before contaminant concentrations decline by 3 OoM. Active remediation of the entire plume is generally not practical due to the large volume of impacted aquifer material. An alternative approach is to install one or more permeable reactive barriers (PRBs), subdividing a long contaminant plume into a series of shorter sections. Using this approach, the travel time through each section is reduced, reducing the overall cleanup time for the aquifer.

To illustrate this approach, we consider two sites with 500 m long contaminant plumes. The first site is a 3 m thick heterogeneous aquifer containing several 0.5 m thick low K layers ($D_L=0.25$ m), where the flux averaged groundwater velocity ($V \cdot V_F$) is 50 m/yr. The second site is a 3 m thick homogeneous aquifer bounded below by a thick low K aquitard (low K boundary) where the uniform groundwater velocity (V) is 50 m/yr. Groundwater contamination at both sites will be treated by installing a PRB immediately downgradient of the source and one or more equally spaced PRBs in the downgradient plume. We assume that the PRBs completely remove all

contaminants that migrate through them, but do not accelerate contaminant degradation in the downgradient aquifer. Cleanup time is calculated using Eq 5-1.

Figure 5-8 shows the impact of installing one or more PRBs on the time to reach 1, 2 and 3 OoM reductions in contaminant concentrations throughout the plume at each site. At the heterogeneous site without low K boundaries, concentrations will be reduced by 3 OoM in 32 years. Installing a 2nd PRB halfway down the plume reduces the 3 OoM cleanup time to 22 years. Installation of additional PRBs further reduces cleanup time, but the incremental benefits of each additional barrier progressively decline.

For the homogeneous aquifer overlying a low K aquitard, cleanup times are much longer. With a single PRB installed downgradient of the source, 830 years will be needed for natural flushing to reduce contaminant concentrations will decline by 3 OoM. With installation of four additional PRBs spaced 100 m apart, 330 years will be required to reach 3 OoM reductions throughout the plume.

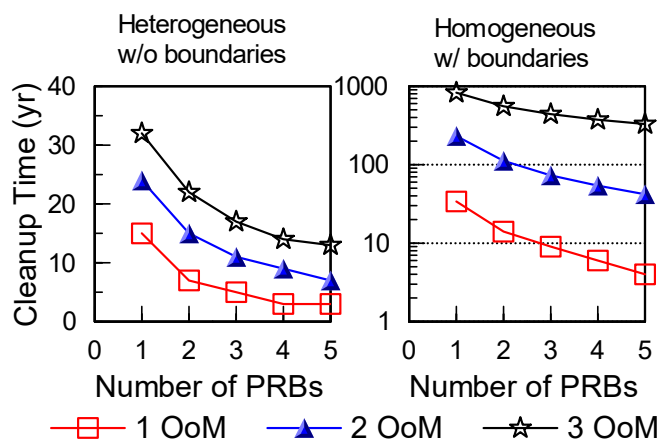


Figure 5-8. Impact of installing multiple PRBs on overall cleanup time.

5.7 SUMMARY

Matrix diffusion can greatly extend the time to reach cleanup goals following source removal. The factors with the greatest impact on cleanup time are the cleanup goals (1, 2 and 3 OoM concentrations reductions) and the time to flush one pore volume through the aquifer ($T_{PV} = T_t/V_F$). In homogeneous aquifers, $V_F=1$ and $T_t = T_{PV}$.

In heterogeneous aquifers containing embedded low K zones, the parameters with the greatest impact on cleanup time are T_{PV} and diffusion length (D_L). For $T_{PV}>5$ yr, the time to reach 1, 2 and 3 OoM reductions are 1.2-1.6 T_{PV} , 1.5-6 T_{PV} , and 2-15 T_{PV} , respectively. Greater values of D_L reduce the time to reach 1 OoM cleanup, but increase the time to reach 2 and 3 OoM cleanup. For 2 and 3 OoM cleanup, T/T_{PV} increases rapidly for $T_{PV}<2$ yr, indicating cleanup time is mass transfer limited for $T_{PV}<2$ yr.

Overall, cleanup times are longer for homogeneous aquifers bounded by thick low K zones compared to heterogeneous aquifers without low K boundaries. In these aquifers, the parameters

with the greatest impact on cleanup time are T_t and aquifer thickness divided by the number of low K boundaries (B/BD). For $T_t > 5$ yr, the time to reach 1, 2 and 3 OoM reductions are 1-6 T_t , 5-50 T_t , and 40-150 T_t , respectively. Cleanup time is greater for smaller B/BD for all cleanup levels since diffusive flux is greater relative to advective flux for thinner aquifers.

Contaminant loading period had a relatively modest impact on cleanup time. In both heterogeneous aquifers and homogenous aquifers with low K boundaries, shorter loading periods reduced cleanup times, but the impact was modest with different loading periods changing cleanup time by less than a factor of 2.

Sorption of contaminants to high and low K aquifer material had a moderate impact on cleanup time. For all conditions evaluated, cleanup time increased with R_H and R_L . However, the increase in cleanup time was generally less than the values of R_H and R_L . For example, increasing both R_H and R_L to 10, increased CTR_R by roughly a factor of 8 for 1 and 2 OoM cleanup in a heterogeneous aquifer. Generally, cleanup times in heterogeneous aquifers are more sensitive to R_H and R_L than for homogeneous aquifers with low K boundaries.

Overall, these results demonstrate that matrix diffusion can dramatically extend the time to reach remediation goals after complete source removal. The overall cleanup time can be somewhat reduced by installing one or more Permeable Reactive Barriers (PRBs), subdividing a long contaminant plume into a series of shorter sections. In one example, installing one PRB separating a 500 ft long plume into two 250 ft long sections reduced the time to reach a 3 OoM reduction by about one-third. Installation of additional PRBs further reduces cleanup time, but the incremental benefits of each additional barrier progressively decline.

6.0 REFERENCES

- AECOM, 2012. Draft Optimized Exit Strategy Plan for LF006 and OT010, Air Force Plant 3, Tulsa, Oklahoma. Prepared for Air Force Center for Engineering and the Environment, August.
- AQUAVEO, 2016. GMS 10.2 Tutorial. T-PROGS.
- Aquaveo, 2020. The Department of Defense Groundwater Modeling System, GMS v10.0.14. Aquaveo, South Jordan Utah.
- ASTM, D8037. Standard Practice for Direct Push Hydraulic Logging for Profiling Variations of Permeability in Soils, ASTM International, West Conshohocken.
- Bear, J., Nichols, E., Kulshrestha, A., and Ziagos, J., 1994. Effect of Contaminant Diffusion into and out of Low-Permeability Zones. Lawrence Livermore National Laboratory Report UCRL-ID-115626.
- Bear, J., Cheng, and A.H.D., 2010. Modeling Groundwater Flow and Contaminant Transport. volume 23. Springer, Dodrecht [u.a.].
- Berkowitz, B., Cortis, A., Dentz, M., and Scher, H., 2006. Modeling non-Fickian transport in geological formations as a continuous time random walk. Reviews of Geophysics, 44(2), RG2003, doi:10.1029/2005RG000178.
- Boggs, J.M., Young, S.C., Beard, L.M., Gelhar, L.W., Rehfeldt, K.R., and Adams, E.E., 1992. Field study of dispersion in a heterogeneous aquifer, 1, overview and site description. Water Resource Research, 28(12), 3281-3291.
- Borden, 2017. Post-Remediation Evaluation of EVO Treatment - How Can We Improve Performance? (ER-201581). Environmental Security Technology Certification Program, Alexandria, Virginia.
- Borden, R.C., Cha, K.Y., and Liu, G., Submitted for Review, A Physically Based Approach for Estimating Hydraulic Conductivity from HPT Pressure and Flowrate, Groundwater, April 2020.
- Bouwer, H., and Rice, R.C., 1976. A slug test for determining hydraulic conductivity of unconfined aquifers with completely or partially penetrating wells. Water Resources Research, 12(3), 423-428.
- Burns, S.E. and Mayne, P.W., 1998. Monotonic and dilatatory pore-pressure decay during piezocone tests in clay. Canadian Geotechnical Journal, 35(6): 1063-1073.
- Butler, J.J. Jr., Healey, J.M., McCall, G.W., Garnett, E.J., and Loheide II, S.P., 2002. Hydraulic tests with direct-push equipment. Groundwater, 40(1), 25-36.
- Butler, J.J. Jr., 2005. Hydrogeological methods for estimation of hydraulic conductivity. In: Hydrogeophysics, ed. Y. Rubin and S. Hubbard, Springer, The Netherlands, 23-58.
- Butler, J.J. Jr., Dietrich, P., Wittig, V., and Christy, T., 2007. Characterizing Hydraulic Conductivity with the Direct-Push Permeameter, Groundwater, 45, 409-419.
- Butler, J.J. Jr., 2009. Pumping tests for aquifer evaluation – Time for a change? Groundwater 47(5), 615-617.
- Chapuis, R.P. and Aubertin, M., 2003. On the use of the Kozeny Carman equation to predict the hydraulic conductivity of soils. Canadian Geotechnical Journal, 40(3): 616-628.
- Carle, S.F., 1999. T-PROGS: Transition probability geostatistical software. University of California, Davis, CA 84.
- Carslaw, H.S., and Jaeger, J.C., 1959. Conduction of heat in solids. 2nd ed., Clarendon Press,

- Oxford.CH2M HILL, 2008. Technical Memorandum - Biobarrier Injection Pilot Study Summary, Operable Unit 2, Naval Training Center Orlando Florida. NAVFAC Southern Division.
- Chapman, S.W., and Parker, B.L., 2005. Plume persistence due to aquitard back diffusion following dense nonaqueous phase liquid removal or isolation. *Water Resources Research*, 41(12), W12411.
- Chapman, S.W., Parker, B.L., Sale, T.C., and Doner, L.A., 2012. Testing high resolution numerical models for analysis of contaminant storage and release from low permeability zones. *Journal of Contaminant Hydrology*, 136–137, 106-116.
- Cho, H.J., Fiacco, Jr. R.J., Horesh, M., Picard, J., Pitkin, S., Madera, E., and Rasmussen, E., 2004. Evaluation of the Waterloo Profiler as a dynamic site investigation tool. In *Proceedings of the Fourth International Conference on Remediation of Chlorinated and Recalcitrant Compounds*, ed. A.R. Gavaskar and A.S.C. Chen. Paper 1B-07. Columbus, Ohio: Battelle Press.
- Dagan, G., and Neuman, S.P., 1997. *Subsurface Flow and Transport: A Stochastic Approach*. Cambridge Univ. Press, Cambridge, UK.
- Dietrich, P., Butler, J.J. Jr., and Faiss, K., 2008. A rapid method for hydraulic profiling in unconsolidated formations. *Groundwater* 46(2), doi: 10.1111/j.1745-6584.2007.00377.x, 323-328.
- Dietrich, P., and Leven, C., 2009. Direct push-technologies. In: *Groundwater Geophysics*, ed. R. Kirsch, Springer, Berlin, Heidelberg.
- Doner, L.A., 2008. Tools to Resolve Water Quality Benefits of Upgradient Contaminant Flux Reduction. (Unpublished Master's Thesis). Colorado State University, Fort Collins, Colorado.
- Elsworth, D., 1993. Analysis of piezocone data using dislocation based methods. *Journal of Geotechnical Engineering-ASCE*, 119(10), 1601-1623.
- Elsworth, D., and Lee, D.S., 2005. Permeability determination from on-the-fly piezocone sounding. *Journal of Geotechnical and Geoenvironmental Engineering*, 131(5), doi: 10.1061/(ASCE)1090-0241(2005)131:5(643), 643–653.
- Falta, R.W., Stacy, M.B., Ahsanuzzaman, W.M., and Earle, R.C., 2007. Remediation Evaluation Model for Chlorinated Solvents (REMChlor). EPA/600/C-08/001.
- Falta, R.W., and Wang, W., 2017. A semi-analytical method for simulating matrix diffusion in numerical transport models. *Journal of Contaminant Hydrology*, 197, 39-49.
- Falta, R.W., Farhat, S.K., Newell, C.J., and Lynch, K., 2018. A Practical Approach for Modeling Matrix Diffusion Effects in REMChlor. Clemson University Clemson United States.
- Farhat, S.K., Newell, C.J., Sale, T.C., Dandy, D.S., Wahlberg, J.J., Seyedabbasi, M.A., McDade, J.M., and Mahler, N.T., 2012. Matrix Diffusion Toolkit. Environmental Security Technology Certification Program, Arlington, Virginia.
- Farhat, S.K., Newell, C.J., Falta, R.W., and Lynch, K., 2018. REMChlor-MD toolkit user's manual. URL: <https://www.serdp-estcp.org/Program-Areas/Environmental-Restoration/Contaminated-Groundwater/Persistent-Contamination/ER-201426>.
- Farhat, S.K., Adamson, D.T., Gavaskar, A.R., Lee, S.A., Falta, R.W., and Newell, C.J., 2020. Vertical Discretization Impact in Numerical Modeling of Matrix Diffusion in Contaminated Groundwater. *Groundwater Monitoring & Remediation*, 40(2), p52-64
- Fetter, C.W., 2008. *Contaminant Hydrogeology*, 2, illustrated, reprint ed. Waveland Press, Incorporated.

- Freeze, R.A., and Cherry, J.A., 1979. Groundwater. Prentice-Hall, Englewood Cliffs, NJ.
- Geoprobe, 2010. Tech Guide for Calculation of Estimated Hydraulic Conductivity (Est. K) Log from HPT Data. Salina, Kansas
- Geoprobe, 2015. Geoprobe® Hydraulic Profiling Tool (HPT) System, Standard Operating Procedure technical bulletin No. MK3137.
- Grisak, G.E., and Pickens, J.F., 1980. Solute transport through fractured media: 1. The effect of matrix diffusion. *Water Resources Research*, 16(4), pp.719-730.
- van Genuchten, M.T., 1985. A general approach for modeling solute transport in structured soils, in: *Hydrogeology of Rocks of Low Permeability*, International Association of Hydrogeologists.
- Guan, J., Molz, F.J., Zhou, Q., Liu, H.H., and Zheng, C., 2008. Behavior of the mass transfer coefficient during the MADE{2 experiment: New insights. *Water Resources Research*, 44. doi:10.1029/2007WR006120.
- Harbaugh, A.W., 2005. MODFLOW-2005, The U.S. Geological Survey Modular Ground Water Model{the Ground-Water Flow Process. Technical Report. URL: <https://pubs.usgs.gov/tm/2005/tm6A16/>.
- Haslauer, C.P., Bárdossy, A., and Sudicky, E.A., 2017. Detecting and modelling structures on the micro and the macro scales: Assessing their effects on solute transport behavior. *Advances in Water Resources*. 107, 439-450, doi: /10.1016/j.advwatres.2017.05.007.
- Lessoff, S.C., Schneidewind, U., Leven, C., Blum, P., Dietrich, P., and Dagan, G., 2010. Spatial characterization of the hydraulic conductivity using direct-push injection logging. *Water Resources Research*, 46, W12502, doi:10.1029/2009WR008949.
- Liu, C., and Ball, WP, 1999. Application of inverse methods to contaminant source identification from aquitard diffusion profiles at Dover AFB, Delaware, *Water Resources Research*, 35(7):1975-1985
- Liu, G., Zheng, C., and Gorelick, S.M., 2004. Limits of applicability of the advection-dispersion model in aquifers containing connected high-conductivity channels. *Water Resources Research*, 40, W08308, doi:10.1029/2003WR002735.
- Liu, G., Butler, J.J. Jr., Bohling, G.C., Reboulet, E., Knobbe, S., and Hyndman, D.W., 2009. A new method for high-resolution characterization of hydraulic conductivity. *Water Resources Research*, 45, W08202, doi:10.1029/2009WR008319.
- Liu, G., Butler, J.J. Jr., Reboulet, E.C., and Knobbe, S., 2012. Hydraulic conductivity profiling with direct push methods. *Grundwasser* 17(1), doi: 10.1007/s00767-011-0182-9.
- Liu, G., Borden, R.C., and Butler, J.J. Jr., 2019, Simulation assessment of direct push injection logging for high resolution aquifer characterization. *Groundwater*, 57(4), 562-574, doi: 10.1111/gwat.12826.
- Mackay, D.M., Wilson, R.D., Brown, M.J., Ball, W.P. Xia, G. and Durfee, D.P., 2000. A controlled field evaluation of continuous vs. pulsed pump-and-treat remediation of a VOC-contaminated aquifer: site characterization, experimental setup, and overview of results. *Journal of Contaminant Hydrology*, 41(1-2), 81-131.
- Maliva, R.G., 2016, Direct-Push Technology. In: *Aquifer Characterization Techniques*, Springer Hydrogeology, Springer, Cham.
- McCall, W., Nielsen, D.M., Farrington, S., and Christy, T.M., 2005. Use of direct-push technologies in environmental site characterization and ground-water monitoring. In: *The practical handbook of environmental site characterization and groundwater monitoring*, 2nd ed., ed. Nielsen, D.M., p. 345–472. CRC Press, Boca Raton.

- McCall, W., and Christy, T.M., 2010. Development of a hydraulic conductivity estimate for the Hydraulic Profiling Tool (HPT), The 2010 North American Environmental Field Conference & Exposition: Conference Program with Abstracts: Session VII.
- McCall, W., Christy, T.M., and Evald, M.K., 2017. Applying the HPT-GWS for Hydrostratigraphy, Water Quality and Aquifer Recharge Investigations. *Groundwater Monitoring and Remediation* 37(1), p. 78-91
- McDonald, M.G., and Harbaugh, A.W., 1988. A Modular Three-Dimensional Finite-Difference Ground-Water Flow Model. U.S. Geological Survey Techniques of Water Resources Investigations, Book 6, p. 586.
- Muskus, N., 2017. Evaluation of a Semi-Analytical/Numerical Method for Modeling Matrix Diffusion Effects in Groundwater Chemical Transport. MS Thesis. Clemson University, Clemson, SC, 183 pp.
- Muskus, N., and Falta, R.W., 2018. Semi-analytical method for matrix diffusion in heterogeneous and fractured systems with parent-daughter reactions. *Journal of Contaminant Hydrology*, 218, 94-109.
- Narasimhan, T., and Witherspoon, P., 1976. An integrated finite difference method for analyzing fluid flow in porous media. *Water Resources Research*, 12, 57-64.
- Neville, C.J., 2006. Solute transport in fractured-porous media: dual porosity simulations with MT3D. URL: https://www.sspa.com/sites/default/files/images/stories/documents/MT3D_Transport-in-fractured-rock.pdf.
- Parez L., and Fauriel R., 1988. Advantages from piezocone application to in-situ tests, *R'évue Française de Géotechnique*. 44, 13–27 (in French).
- Parker, B.L., Chapman, S.W., and Guilbeault, M.A., 2008. Plume persistence caused by back diffusion from thin clay layers in a sand aquifer following TCE source-zone hydraulic isolation. *Journal of Contaminant Hydrology*, 102(1-2), 86-104.
- Pruess, K., and Wu, Y., 1988. A semi-analytical method for heat sweep calculations in fractured reservoirs. LBL-24463.
- Pruess, K., and Wu, Y., 1993. A New Semi-Analytical Method for Numerical Simulation of Fluid and Heat Flow in Fractured Reservoirs. *SPE Advanced Technology Series* 1, 63-72.
- Robertson, P.K., 1990. Soil classification using the cone penetration test. *Canadian Geotechnical Journal*, 27 (1), 151-8.
- Robertson, P.K., and Cabal K.L., 2010. Guide to Cone Penetration Testing for Geotechnical Engineering, Gregg Drilling & Testing, Inc.
- Sale, T.C., Zimbron, J.A., and Dandy, D.S., 2008. Effects of reduced contaminant loading on downgradient water quality in an idealized two-layer granular porous media. *Journal of Contaminant Hydrology*, 102(1), 72-85.
- Sall, J., Stephens, M.L., Lehman, A., and Loring, S., 2017. JMP start statistics: a guide to statistics and data analysis using JMP. Sas Institute.
- Schulmeister, M.K., Butler, J.J. Jr., Healey, J.M., Zheng, L., Wysocki, D.A., and McCall, G.W., 2003. Direct-push electrical conductivity logging for high-resolution hydrostratigraphic characterization, *Groundwater Monitoring & Remediation*, 23(3): 52-62.
- Singh, V.P., Jain, S.K., and Tyagi, A.K., 2007. Risk and Reliability Analysis. American Society of Civil Engineers, Reston, VA. URL: <http://ascelibrary.org/doi/book/10.1061/9780784408919>, doi:10.1061/9780784408919.

- Sudicky, E.A., and Frind, E.O., 1982. Contaminant transport in fractured porous media: Analytical solutions for a system of parallel fractures. *Water Resources Research*, 18, 1634-1642. URL: <https://www.osti.gov/biblio/5756552>, doi:10.1029/WR018i006p01634.
- Tetra Tech (Tetra Tech NUS), 2001. Remedial Investigation Report for Operable Unit 2, McCoy Annex Landfill, Naval Training Center, Orlando, Florida (Rev. 2). Naval Facilities Engineering Command Southern Division.
- Tetra Tech (Tetra Tech NUS), 2003. Final Feasibility Study Report, Operable Unit 2, McCoy Annex Landfill Naval Training Center, Orlando, Florida (Rev. 1). Naval Facilities Engineering Command Southern Division.
- Therrien, R., McLaren, R.G., Sudicky, E.A., and Panday, S.M., 2010. HydroGeoSphere: a three-dimensional numerical model describing fully-integrated subsurface and surface flow and solute transport. Draft User's Manual. Groundwater Simulations Group, Waterloo, Ontario.
- Trefry, M.G., and Muffels, C., 2007. FEFLOW: a finite-element ground water flow and transport modeling tool. *Groundwater* 45(5), 525-528.
- US EPA, 1996. Soil Screening Guidance: Technical Background Document, EPA/540/R-96/018, Washington, DC.
- Vinsome, P., and Westerveld, J., 1980. A simple method for predicting cap and base rock heat losses in thermal reservoir simulators. *Journal of Canadian Petroleum Technology*, 19(3).
- Zheng, C., and Wang, P.P., 1999. MT3DMS: A Modular Three-Dimensional Multispecies Transport Model for Simulation of Advection, Dispersion, and Chemical Reactions of Contaminants in Groundwater Systems; Documentation and User's Guide. SERDP-99-1.
- Zheng, C., and Bennett, G.D., 2002. Applied contaminant transport modeling. 2nd ed., Wiley-Interscience, New York.
- Zheng, C., Bianchi, M., and Gorelick, S.M., 2011. Lessons learned from 25 years of research at the MADE site. *Groundwater*, 49, 649-662, doi:10.1111/j.1745-6584.2010.00753.x.

APPENDIX A

Field Operating Procedure of Low-K Hydraulic Profiling Tool (HPT)

A.1 Background

The standard HPT is a commercial product manufactured by Geoprobe that can be used for measuring hydraulic conductivity (K) at a range of 0.03 to 25 m/d in unconsolidated formations (**Figure A1**). The operation procedure of the standard HPT can be found at <http://geoprobe.com/literature/hpt-sop>. Users should carefully read the standard HPT procedure before performing low-K HPT in the field. Most of the field procedures are identical between the standard and low-K HPT operations. In this document, the differences between the two systems are highlighted while similarities to the standard HPT are omitted or briefly discussed.

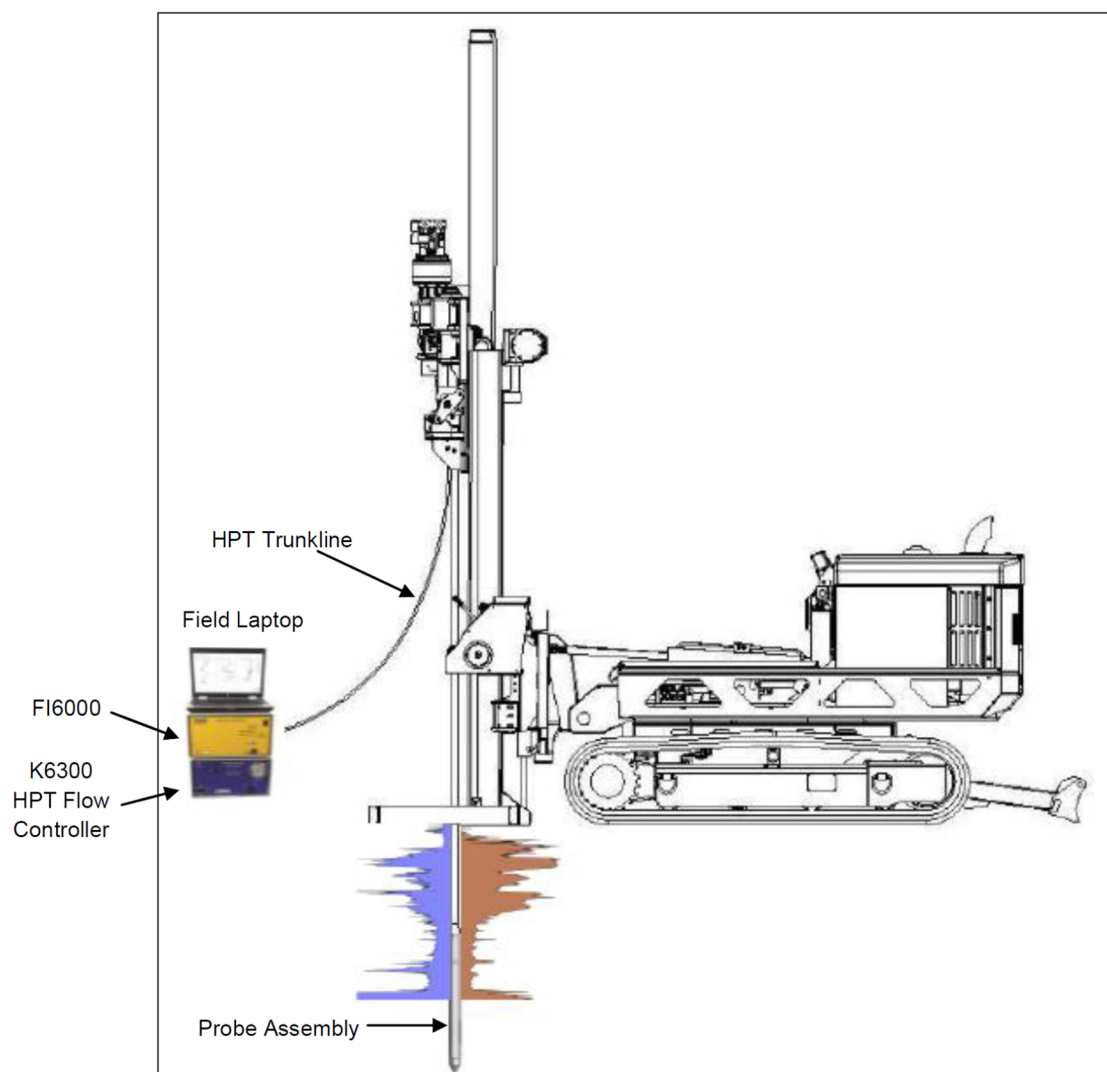


Figure A1. Standard HPT components (from HPT Standard Operating Procedure by Geoprobe).

A.2 Low-K HPT

In order to extend the HPT into low-K settings, water injection rate has to be reduced. As a result, a separate low-flow control box has been developed (**Figure A2**). It consists of a de-airing system, a water pump, and a flow controller and meter. The low-flow controller has a flow rate range of 2 to 100 mL/min. The source water needs to be de-ionized to ensure the safe and accurate operation of the flow controller. Due to the low flow rates used, the air trapped in the injected water was found capable of producing a significant impact on the pressure readings in certain situations. As such, the de-airing system was installed, and initial lab tests indicated it could largely reduce the impact of air trapping in the injected water.



Figure A2. Low-flow control box.

The low-flow control box is connected to the water injection tube in the HPT trunkline. The injection rate is saved into an excel file using a USB connection cable between the flow controller and field laptop, although in the future it will be more desirable to modify Geoprobe's DI data acquisition software so that the injection rates can be directly read by the software. The standard HPT flow control box and field instrument are still needed in for low-K HPT profiling as the EC and pressure data from the downhole probe are transmitted into the field laptop through them. Other than the water injection rate, all HPT data are collected through the standard HPT system and software.

A.3 Field equipment setup

The equipment setup for the low-K HPT is largely similar to that for the standard HPT (**Figure A3**). All instruments needed for the standard HPT operation must be set up in place as instructed

in the standard HPT operation manual. This includes threading the HPT trunkline through the connection rods, setting up the laptop, field instrument, flow controller, and string pot, and positioning the DP rig at the logging location. For the injection tube in the trunkline, instead of directly plugging into the standard HPT flow controller, it is now connected to a low-flow manifold where the injection can be set to either the standard HT flow controller or the low-flow control box (see H in **Figure A3**). The DI source water tank is also connected to a manifold which sets the injection into either the standard HT flow controller or the low-flow control box. The manifold setup allows the user to switch between low-flow mode (injection rate less than 100 mL/min) and standard flow rates (injection rate greater than 100 mL/min) during field HPT profiling on the fly, depending on whether the probe is in low-K formations or not.

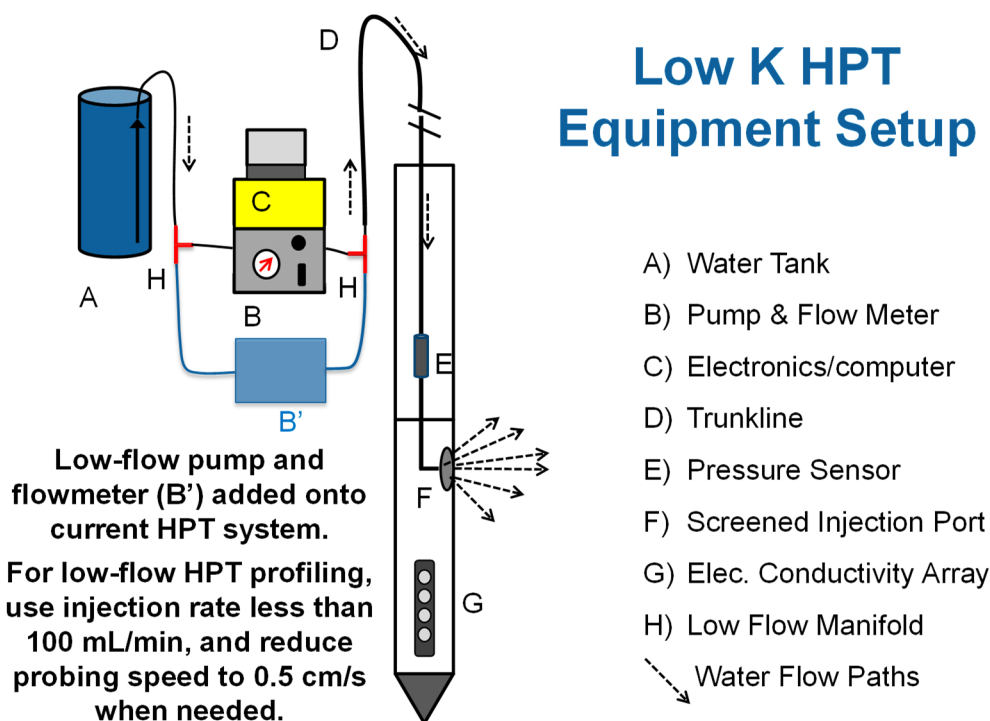


Figure A3. Low-K HPT equipment setup during field profiling.

The tubes for connecting various parts of the low-flow control box need to be installed correctly on the back of the box. From the DI source water tank, a tube with a filter at one end is used to connect the source water to the input port of the pump (marked as “DI in”). The “trunkline” port is for supplying water to the injection tube in the HPT trunkline. An additional tube with a valve may be used as transition between the trunkline port and the trunkline so that the valve can be used to turn the injection on or off as an additional control to the pump on/off switch. Between the de-airing system and source water tank, a tube (the port labeled as “Bypass”) is used for carrying the de-aired water back to the source water tank.

A.4 Pre-logging preparation

Once all the instruments are connected, the de-airing system and low-flow pump should be turned on as early as possible to allow the air initially in the tubes and trunkline to be purged out. The de-airing system is turned on by pressing the power switch and opening the air valve

(turning horizontal). The low-flow pump is turned on by pressing the power switch and opening the valve on the trunkline. During this period the flow rate should be set to a high value (e.g., 100 mL/min) to speed up the air purging of the trunkline. Note that the above step is only needed for the first log of the day, or after any part of the surface tubing is disconnected and air is trapped. After the air purging of trunkline is completed, the flow rate should be changed to the value that will be used for downhole logging. The bypass valve on the front of control box should be adjusted so that the entry pressure shown on the flow controller is approximately 60 psi. This high entry pressure will help the flow controller maintain a steady flow rate despite the potentially large back pressure during downhole profiling in low K zones.

After the air purging of trunkline, two programs need to be started in the laptop: a) the program for recording the flow rates from low-flow controller, and b) Geoprobe's DI acquisition software. Similar to the standard HPT, the quality assurance (QA) tests of the EC and pressure sensors need to be performed before and after each log. The instructions of QA tests are referred to the standard HPT operation manual. The pre-log QA tests of a log can be skipped if the log immediately follows the previous log without changes in the screen or transducers; in this case the post-log QA tests of the previous log can be used as substitute for the pre-log QA tests of the current log.

A.5 Running the low-K HPT log

After passing the QA tests for both EC and pressure sensors, the low-K HPT system is ready for downhole logging. To facilitate the merging of flow rate data from the low-flow controller with the pressure data collected by DI acquisition software, turn on time recording for the entire duration of the log (the software treats it as running a dissipation test). Before driving the probe into the ground, make sure the flow is on and the string pot for depth measurement is connected. For the low-K HPT system, in order to reduce the impact of the pore water pressure increase generated by rod advancement, it is recommended the rod advancement rate be kept nearly constant at 0.5 cm/s instead of the normal rate of 2 cm/s. In addition, to reduce the time of rod change, always have the next connection rod ready nearby. Do not move trunkline during the active probe movement as this may cause artificial pressure fluctuations in the log data.

Before recording the depth log, drive the HPT probe down at approximately 0.5 cm/s until the injection screen intersects the surface. Then quickly click the trigger button in the DI acquisition software and resume driving the probe down at a rate of 0.5 cm/s. After the trigger button is clicked, one person needs to make sure the depth data begin to show up on the computer screen as the probe is advanced.

During the connection rod change, one person adds the rod while another person gets the next rod ready and nearby. Continue this process until the desired depth is reached. Stop the log by triggering off and ending time recording. While tripping out the probe, use a higher flow rate (e.g., 100 mL/min) to prevent screen clogging. Perform the post-logging QA tests as instructed in the standard HPT operation manual.

For continuous low-K HPT logging, no dissipation tests are recommended for two reasons. First, it will take an extremely long time for the pressure to dissipate. Second, the long suspension of

rod during dissipation tests will produce a large impact on the pore water pressure field generated by rod advancement. That impact will be difficult to filter out in post-log data analysis. Without the dissipation tests, it is more reasonable to assume the excess pressure by rod advancement has a similar impact at different depths, given that the rod advancement speed does not vary much, and that rod change is quick.

A.6 Low-K HPT log analysis

Unlike the standard HPT data from Geoprobe's DI acquisition software, the flow rates are recorded in a separate file. Thus, the first thing in the post-log data analysis is merge the separate flow rate data with the time data file from the DI acquisition software (file type .TIM). This can be accomplished by comparing the time information between the two data sources. The flow rate file has the exact time for each flow rate measurement, while the time data file from the DI software has a total elapsed time (in seconds) since logging starts. The log start time can be found in the information file (file type .NFO; note this is the log start time, not the QA test time).

After the flow rate data are incorporated into the .TIM file, flow rates need to be estimated for each sampling depth in the depth log file from the DI acquisition software (file type .HPT). This can be accomplished by linear interpolation for each depth in the .HPT file using the flow rates and depths in the .TIM file. Alternatively, the user can use the .TIM file to generate a new depth file of flow rates and HPT pressure without interpolation; however, this approach will not necessarily produce the same depth resolution as in the .HPT file.

In terms of K estimation from the HPT depth log data, it is still a work in progress. Two approaches appear promising at this point. First, similar to the standard HPT, an empirical relation may be developed that can be used to directly transform the HPT injection rate/pressure ratio into K. This approach will require a series of independent K data to establish the relation at a given site. A potential difficulty of this approach is the dependency of the HPT rate/pressure ratio on specific storage. However, if the specific storage does not vary significantly at the site, its impact on K estimation will likely be minimal. Second, numerical simulations can be performed for the HPT profiling process under the probe advancement speed and water injection rate used in the field. By varying the K and specific storage (S_s) in the simulations, an empirical relation may be developed between the HPT pressure and injection rate and K for a given specific storage and probe speed. This empirical relation can then be used for estimating K from the HPT depth data, assuming that information about specific storage can be obtained via other means. More details about the numerical analysis approach are given in the following section.

A.7 K estimation from low-K HPT depth log

Using COMSOL (a software for multi-physics simulations), numerical simulations for HPT profiling have been performed under 5 rod advancement speeds (5, 7, 10, 15, 20 mm/s) and different K and specific storage (K ranging from $1\text{E-}8$ to 0.00025 m/s, S_s from $7.5\text{E-}5$ to 0.05 m⁻¹). Based on the simulations, a series of empirical curves can be determined that 1) relate the probe advancement-induced pressure measured at the HPT screen to hydraulic diffusivity (K/S_s) at a given probe advancement speed, 2) relate the ratio of injection rate over injection-induced

pressure measured at the HPT screen to hydraulic diffusivity. Error! Reference source not found. shows the empirical relations at the probe advancement speed 5 mm/s.

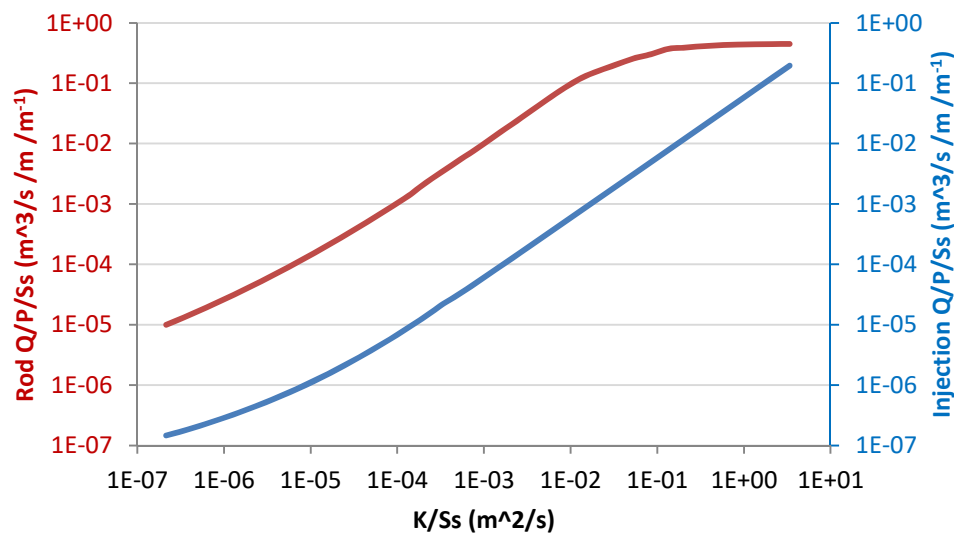


Figure A4. Simulated relations for hydraulic diffusivity versus rod advancement-induced pressure measured at the HPT screen (red curve), and for diffusivity versus the ratio of water injection rate over injection-induced pressure (blue curve). The simulated probe speed is 5 mm/s. Rod Q is the equivalent water injection rate from rod advancement, calculated as the product of the cross-section area of the HPT probe and advancement speed.

Using the simulated relations such as Error! Reference source not found., K can be estimated from the HPT depth logs assuming information about specific storage is known. This is done through the following steps:

Step 1. Open the time data file (.TIM) and scroll the data to obtain the average HPT pressure before the HPT screen goes into the ground (this value should be around 17 psi). Enter that value into the first row of Excel file “getinputfromfielddata” (Error! Reference source not found.). Enter the depth to water in the low-K zone into the second row; this depth to water information can be obtained typically from a monitoring well that is screened in the low-K zone. On the third row of “getinputfromfielddata”, enter the depth to water in the aquifer underlying the low-K zone. These three rows of data are used to calculate the hydrostatic background pressure at different depths in the low-K zone (including the zone above the water table). Alternatively, we can use the water level measurements at two different depths of the low-K zone, if available, to determine the hydrostatic pressure.

Pressure before probe into ground (psi, from time data):		16.8694					
Depth to water in the low-K (m):		3.9377					
Depth to water in the high-K (m):		5.6827					
Depth (ft)	HPT Press.	Hydrostatic	HPT Flow Avg (mL/min)	Depth (m)	CorrectP (n	Q (m ³ /s)	Ss (1/m)
0	16.861	16.8694	5	0	-0.00591	8.33333E-08	0.00164
0.05	16.908	16.8694	5	0.015244	0.027145	8.33333E-08	0.00164
0.1	16.864	16.8694	5	0.030488	-0.0038	8.33333E-08	0.00164
0.15	16.857	16.8694	5	0.045732	-0.00872	8.33333E-08	0.00164
0.2	16.855	16.8694	5	0.060976	-0.01013	8.33333E-08	0.00164
0.25	16.861	16.8694	5	0.07622	-0.00591	8.33333E-08	0.00164
0.3	16.858	16.8694	5	0.091463	-0.00802	8.33333E-08	0.00164

Figure A5. The first few example of an example Excel file “getinputfromfielddata”.

Step 2. Open the depth log file (.HPT) in Excel. Copy and paste the depth, HPT average pressure, and HPT average flow rate into Excel file “getinputfromfielddata”. Make sure to cut or expand the rows of data at the lower end of the file as appropriate (each log may have a different number of data rows). On the specific storage column (labeled as Ss (1/m)), enter the specific storage information at different depths. Copy and paste the columns “Depth (m)”, “CorrectP (m)”, “Q (m³/s)” and “Ss (1/m)” into file “Fieldprofile.txt”. Update the first two rows in “Fieldprofile.txt” for each log.

Step 3. Run the Matlab program “Kestimate.m” for K estimation. Make sure “Fieldprofile.txt” and the simulation files at different rod speeds (“modelresults_05.txt”, “modelresults_07.txt”, “modelresults_10.txt”, “modelresults_15.txt”, “modelresults_20.txt”) are all copied into the same work directory of “Kestimate.m”. The estimated K values are printed in the file “Kestimate.out”. Also included in “Kestimate.out” are the estimated pressures from rod advancement and HPT water injection, respectively. If the HPT pressure measurement is larger than the simulated maximum pressure, a default value of -2 will be used for the estimated K; a default value of -1 will be used if the pressure measurement is smaller than simulated minimum pressure. Error! Reference source not found. shows an example K profile estimated for the low-K layer at a Kansas Geological Survey field site in Kansas River valley.

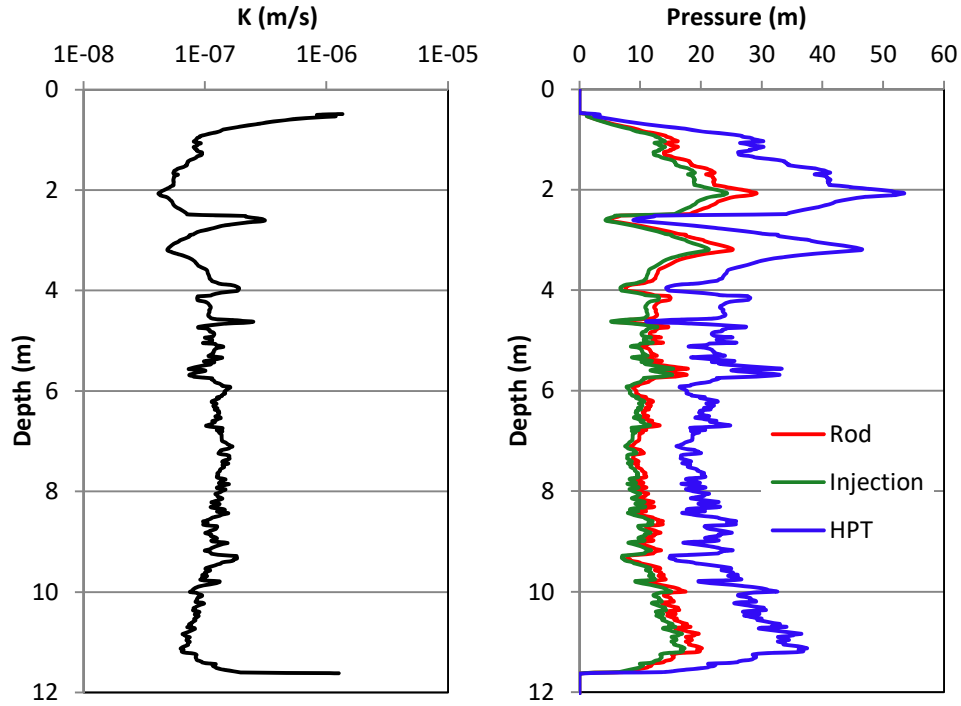


Figure A6. Example profiles of estimated K (left) and pressures (right) from HPT logging at the GEMS. The HPT pressure is calculated as the field pressure measurement minus the estimated hydrostatic background pressure. The rod pressure is the estimated pressure from rod advancement at a speed of 5 mm/s. The sum of rod pressure and injection pressure is equal to the HPT pressure.

APPENDIX B

Hydraulic Conductivity Characterization Methods

Hydraulic conductivity (K), a parameter that describes the ease with which water flows in the subsurface, is widely regarded as one of the most important hydrogeologic parameters for environmental site investigations. Mathematically, it is defined as the ratio of velocity over the hydraulic gradient in the direction of flow. The delineation of the spatial distribution of K has been the key for understanding the fate and transport of contaminants and for designing effective remediation systems at many sites of groundwater contamination ^{[1] [2] [3] [4]}. A variety of methods have been developed to acquire information about K. While traditional methods, such as pumping and slug tests, have proven useful over the years, recently developed approaches based on direct-push (DP) technology hold great promise for characterizing K at the resolution, accuracy, and speed needed for site investigations in unconsolidated settings.

Related Article(s):

- [Direct Push \(DP\) Technology](#)
- [Geophysical Methods](#)

CONTRIBUTOR(S): [Gaisheng Liu](#) and [Jim Butler](#)

Key Resource(s):

- Hydrogeological methods for estimation of spatial variations in hydraulic conductivity^[5]
- Hydraulic conductivity profiling with direct push methods^[6]

B.1 Introduction

Hydraulic conductivity is mathematically defined as the parameter in Darcy's Law (**Figure B1**),

$$Q = -K \times i \times A, \quad (\text{B-1})$$

where Q is the flow rate across area A of a porous medium, K is hydraulic conductivity, and i is the hydraulic gradient, which can be computed as

$$i = (h_1 - h_2)/L, \quad (\text{B-2})$$

where h_1 and h_2 are the hydraulic heads at the ends of the experimental domain and L is the total length.

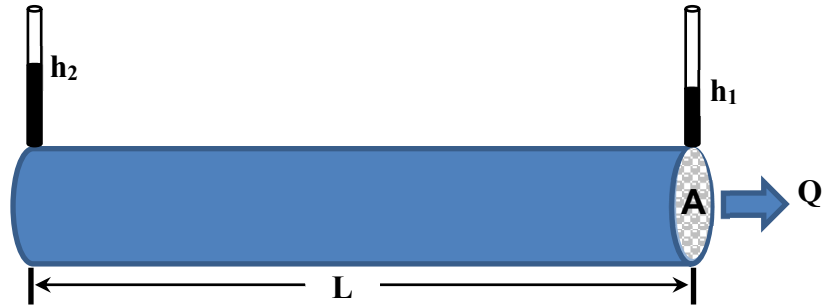


Figure B1. Schematic of Darcy's Law flow experiment.

Hydraulic conductivity is dependent on the properties of both water and the porous medium,

$$K = k \times \rho \times g / \mu, \quad (\text{B-3})$$

where k is the intrinsic permeability of the medium, a parameter that is solely dependent on the geometry of the interconnected pores, g is the gravitational constant, and ρ and μ are the density and dynamic viscosity of the pore water, respectively.

Many approaches have been developed to characterize K ^[5]. These approaches can be grouped into two general categories based on how the K estimates are obtained: (1) hydraulic methods that involve water injection or extraction and the measurement of the induced pressure response, and (2) indirect methods that rely on empirical correlations, often site-specific in nature, between K and other more readily evaluated formation properties (e.g., resistance to electric current). Because hydraulic methods can be directly related to the mathematical definition of K through Darcy's Law, K estimates obtained with those methods are generally considered to be more reliable than those obtained with indirect methods.

Other classifications of K characterization approaches are possible. For example, approaches can be divided into those based on data collected in the field and those based on measurements on core samples in the laboratory. In the latter case, there can be considerable uncertainty about how representative the core sample is of field conditions.

Field-based approaches can be further subdivided based on whether the measurement is conducted in the subsurface or on the surface. Subsurface measurements provide the most reliable information about K variations at the scale needed for environmental site investigations. Nearly all field-based hydraulic methods are performed in the subsurface and require either boreholes or direct push (DP) installations for extracting or injecting water and monitoring the induced head changes. Compared to methods that rely on existing wells, DP approaches can be applied essentially wherever K information is needed, thus greatly expanding the spatial coverage of K measurement in the field. DP approaches, however, are generally limited to use in relatively shallow (20-30 m from land surface) unconsolidated settings.

Field K measurements can also be performed on the land surface or in an aircraft; most of these are geophysical approaches that involve measuring electrical, magnetic, or seismic properties of

the formation and then transforming them into K estimates using empirical relations. The biggest advantage of surface or airborne approaches is their minimal site disturbance, as no subsurface boring is needed. However, the resolution that can be provided is limited, as the measurements are typically affected by conditions over a relatively large volume of the formation. Geophysical methods can also be performed in boreholes. Borehole geophysical methods can provide a much higher resolution description of K than surface-based methods.

The scale of measurement is an important factor to consider when assessing various approaches. For water-supply investigations, a single estimate of K averaged over a large volume of an aquifer will usually suffice; such an estimate is commonly obtained via pumping tests in a well. For water-quality investigations, however, K estimates over a large measurement volume are often of limited value^[7]. In that case, small-scale K measurements that provide information about localized geological controls on groundwater flow and transport are usually required to obtain reliable predictions of contaminant behavior and to design effective remediation systems.

In this article, we focus on the approaches that can be used to obtain small-scale, localized measurements of K for environmental site investigations. Only the more commonly used approaches are discussed. Some other approaches, such as dipole flow tests^{[8] [9]}, tracer tests^[10], or hydraulic tomography^{[11] [12]}, will not be discussed due to their limited application in practice.

B.2 Hydraulic Testing Approaches

B.2.1 Pumping Tests

The pumping test is the most common method for determining K over a relatively large volume of an aquifer in water-supply investigations^[7]. During a typical test, the pumping rate is kept constant, although it can be varied in time to obtain better signal-to-noise ratios in the acquired data^[13]. In the constant-rate approach, a well, preferably centrally located at the site, is pumped while induced head changes are monitored at that and nearby wells. The head changes, along with the pumping rate, can then be used to estimate aquifer parameters using different models of the well-aquifer configuration^{[14] [15]}. Pumping test analyses can be facilitated using software packages like AQTESOLV (Aquifer Test Solver), which has been developed for analyzing different types of aquifer tests^[16].

Pumping tests are primarily performed to obtain large-scale volumetric averages of aquifer parameters as well as information about aquifer boundaries. However, one form of the pumping test, the step-drawdown test, is specifically directed at getting information about the efficiency of the pumping well. The K estimate from a pumping test is an average over a large volume of the formation and does not provide information at the scale of most relevance for issues involving contaminant transport (e.g., meters or less). Thus, pumping tests may be of limited value for environmental site investigations^[7].

B.2.2 Slug Tests

The slug test is one of the most common methods for determining K at the scale of relevance for environmental site investigations^{[17] [18]}. Slug tests are typically performed in existing wells,

although tests can also be performed in temporary installations such as DP rods. In this approach, a near-instantaneous head change is applied in the well or DP rods and the subsequent head recovery is used to estimate K . The initial head change can be introduced using a solid object (slug), compressed gas (pneumatic system), or by the addition/removal of a certain amount of water^[17]. The recovery data can be analyzed using different models of the well-formation configuration^{[16] [17]}. In contrast to pumping tests, slug tests provide a K estimate that is primarily a function of the materials in the vicinity of the screened interval of the test well.

Although a slug test is very simple in principle, considerable care must be taken in all stages of a test^{[5] [17] [18]}. Because test responses are highly sensitive to the materials immediately adjacent to the test well, that well must be appropriately developed before a test is performed. Otherwise, the K estimate can be biased by a low- K zone (skin) that can form during well construction. In high- K formations, the head recovery is rapid. In this situation, the time associated with test initiation must be minimized; pneumatic methods, which involve pressurizing and depressurizing the air column above the water, are typically recommended. In addition, due to the relatively high flow velocity, the impact of pipe hydraulics on pressure readings should be considered when analyzing slug test data from high- K zones^[19]. In low- K formations, slug test can take an extremely long time to complete, although test time can be significantly reduced by decreasing the effective casing radius (portion of well in which the water level is changing)^[17].

Slug tests can be configured to obtain information about vertical variations in K along the screened (open) interval of a well. Test intervals are isolated with straddle packers and slug tests are performed within that isolated interval. The straddle packers can be incrementally moved along the screened interval of a well to characterize the vertical variation of K at a relatively high-resolution. Using a two-packer tool (**Figure B2**), slug tests have been performed in a number of 0.25-m intervals in a well at the Geohydrologic Experimental and Monitoring Site (GEMS) in the Kansas River valley^[5]. At each isolated interval, multiple tests are performed, initiated with different head changes, following recommended test guidelines^{[17] [18]}. An example data set is presented in **Figure B2**. The multi-level slug test K estimates compare favorably with estimates obtained using other approaches (**Figure B3**).

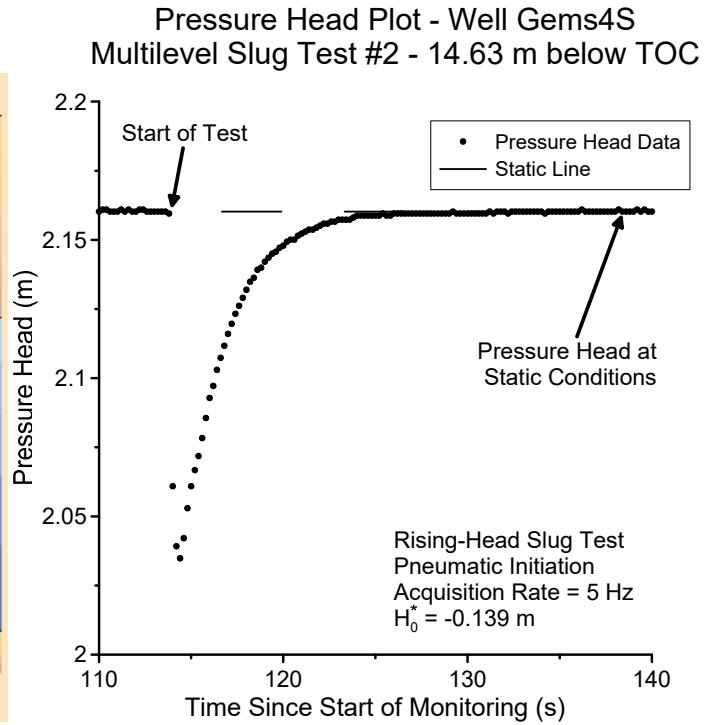
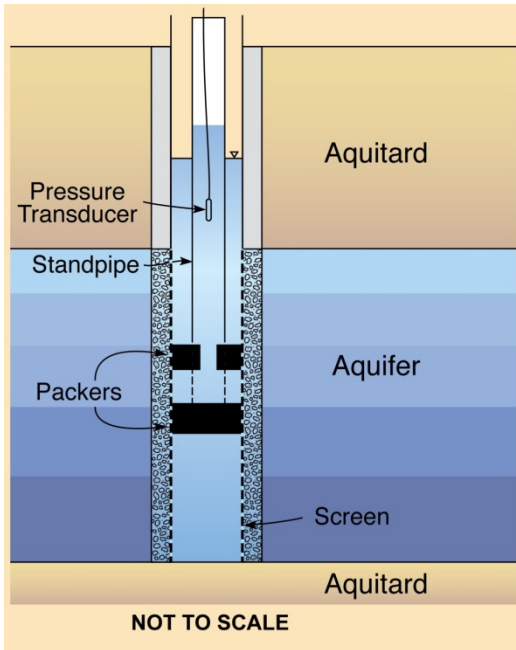


Figure B2. (A) Schematic of a falling-head slug test (water flows from well into aquifer) performed in a multi-level slug-test system. Head change is introduced in standpipe, which is directly connected to the interval isolated by the straddle packers (not to scale). (B) Example data plot from a multilevel slug test at GEMS. Test is initiated by sudden depressurization of a pressurized air column^[19].

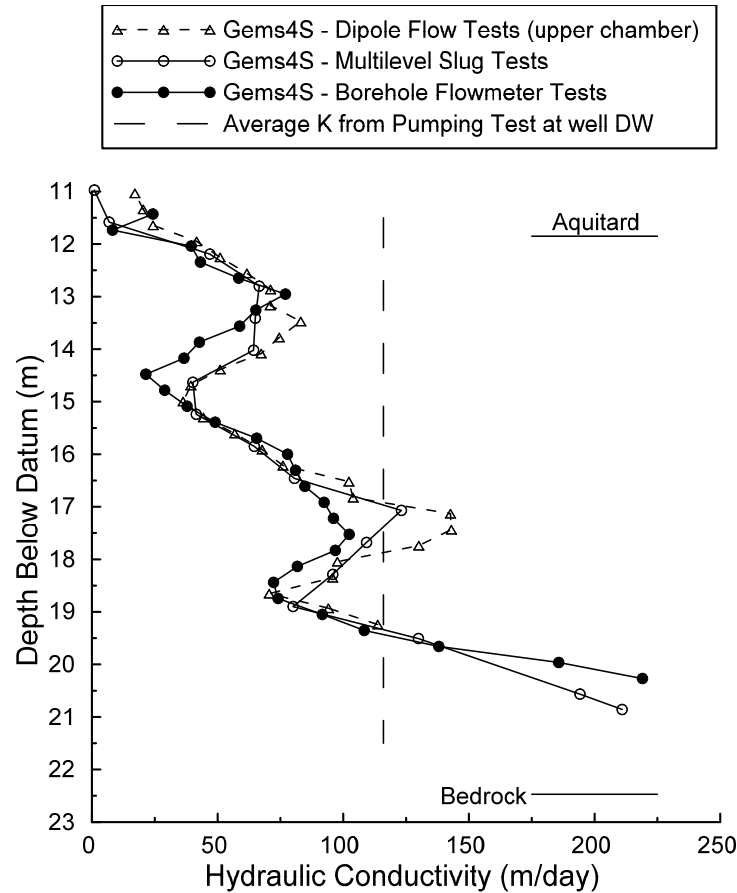


Figure B3. K estimates from different field methods at GEMS^[5]. Well DW is located 2 m east of GEMS4S.

In addition to existing wells, slug tests can also be performed in DP installations so that K estimates can be obtained virtually at any location in unconsolidated formations. Various approaches have been developed that allow slug tests to be performed at one or multiple levels in a single DP hole^{[20] [21] [22] [23]}. In McCall et al. (2002)^[22], a pair of nested rod strings were driven to the test interval; a solid drive point was attached to the end of inner rod string for advancement. Upon reaching the test depth, the drive point and inner rod string were retracted, and a screen was lowered to the bottom of outer rod string. The outer rod string was pulled up while the screen was held in place, leaving the screen exposed to the surrounding formation. After the slug test was completed in the exposed screen, the screen was removed and the inner rod string with the attached solid drive point was reinserted; the nested rod strings were then driven to the next test depth. In low-K formations such as silts and clays, the formation materials may not collapse completely back to the screen when the outer rod string is pulled back. In this case, the diameter of the borehole can be estimated and used in place of the screen diameter, or the problem can be avoided by using a coring tube of similar size to the screen to create a hole below the end of the outer rod string. Instead of setting the screen by pulling up the outer rod string, the screen can be directly inserted into the hole for slug testing. Regardless of how the screen is set into the formation, it is always recommended that the screen be appropriately developed before slug tests are performed. In low-K formations, development may be limited to

scraping the sides of the cored hole with a steel brush and removing the silty water from the screen with a low-flow pump.

Sellwood et al. (2005)^[23] proposed a modification of the approach by McCall et al. (2002)^[22] to lessen profiling time and gain more information about subsurface stratigraphy. Instead of performing slug tests on the way down, slug tests were performed at different depths as the outer rod string was pulled up (**Figure B4**). This way, the number of changes between the outer and inner rod strings was minimized (i.e., only one change needed at the bottom of the profile). Furthermore, an electrical conductivity (EC) probe was attached to the inner rod string so that EC data could be collected as the rod strings were advanced; the EC data could then be used for selecting the intervals for slug tests as the rod strings were retracted. This approach, called hydrostratigraphic profiling, enabled the collection of information on electrical and hydraulic conductivity to be obtained at a speed and resolution that had previously not been possible.

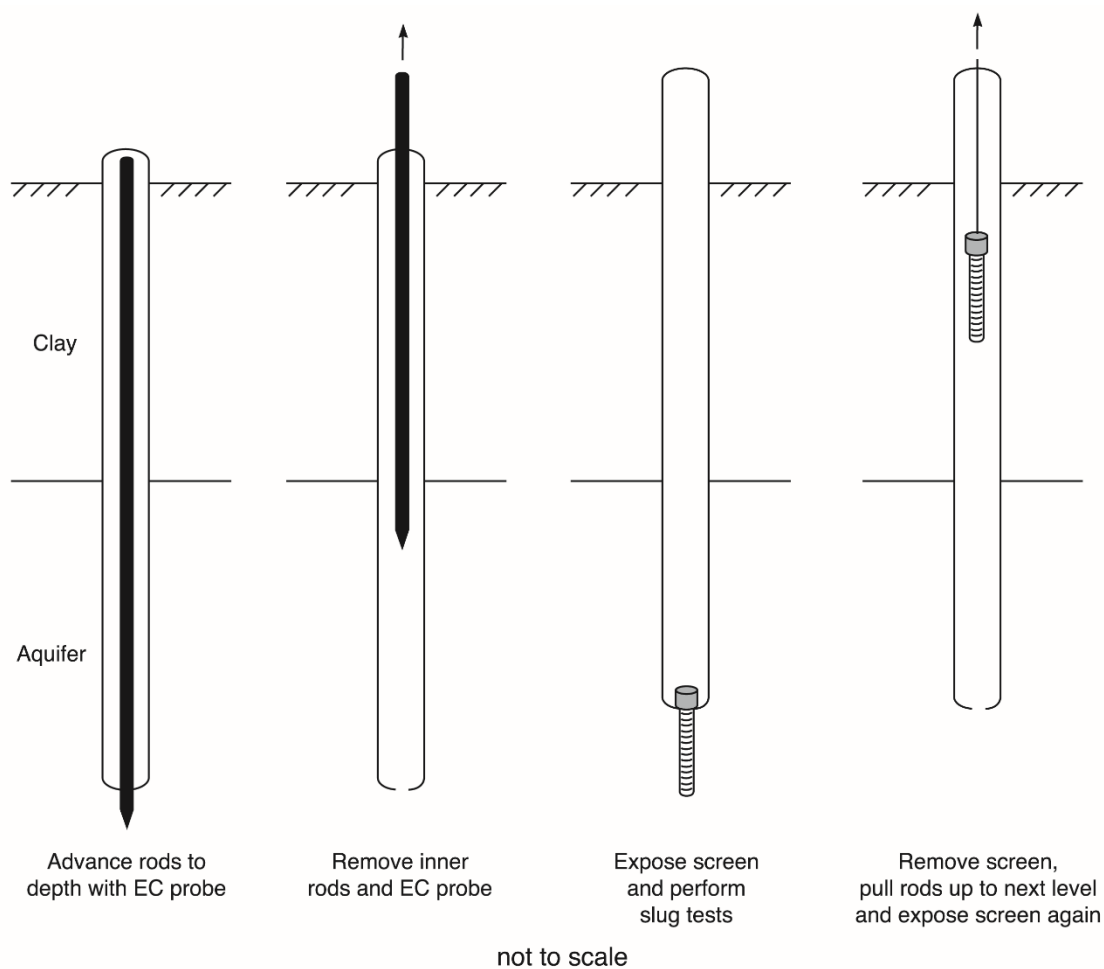


Figure B4. Schematic illustrating hydrostratigraphic profiling, the combination of electrical conductivity (EC) and multilevel slug test profiling^[23].

B.2.3 Borehole Flowmeter Profiling

Borehole flowmeter profiling is one of the most efficient approaches for characterizing the vertical variations of K ^[24]. This approach involves pumping a well at a constant rate while measuring the vertical flow rate within the screened interval (**Figure B5**). A flowmeter is initially positioned at the bottom of the screen. After the pump is turned on and the pumping rate stabilizes, the flowmeter is gradually moved up, often in an incremental fashion with short stops although continuous profiling is also done. After the entire screened interval is measured, the profile of vertical flow rates versus depths can be used for K estimation. Typically, two profiles are performed, one prior to pumping and one during pumping. The profile obtained during pumping is corrected with the profile prior to pumping to remove the impacts of ambient flow in the well. Due to the difficulty of detecting small difference in flow rates, the K estimates from flowmeter profiling are subject to more noise in less permeable settings^[25]. In addition, the results of flowmeter profiling are sensitive to in-well hydraulics, such as the impedance of flowmeter to vertical flow and disturbance by the pump intake when it is too close to the measurement interval^[5].

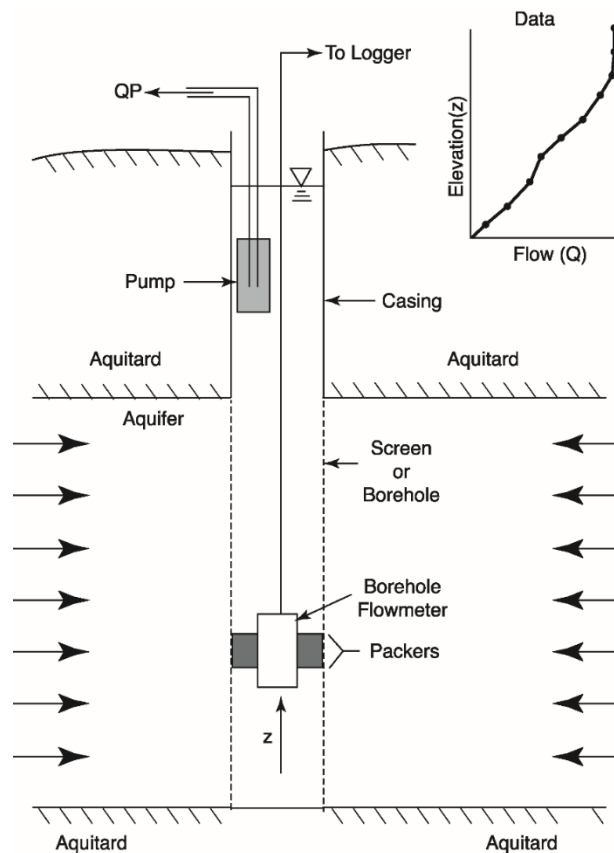


Figure B5. Schematic diagram showing the borehole flowmeter profiling procedure^[24].

Different types of flowmeters have been used for borehole profiling^[26]. For example, electromagnetic flowmeters are often used in environmental site investigations due to their lower flow rate detection limit and lower head loss (high head loss across the flowmeter can cause flow bypass through the filter pack of the well). However, they may be more expensive than other

options and have certain practical limitations as well^[27]. Heat pulse flowmeters are also used for profiling in less-permeable settings.

The most common method of estimating K from borehole flowmeter profiles is based on the assumption that the lateral flow rate of an interval (zone between flow-rate measurements) is proportional to the K and thickness of that interval in a well fully screened in a perfectly layered aquifer,

$$K_i/K_a = (\Delta Q_i/Q_t) / (\Delta B_i/B_t) \quad (B-4)$$

where K_i is the K of test interval i ; K_a is the average K for the entire screened interval; ΔQ_i is the net lateral inflow across interval i , which can be calculated by subtracting the flow rate at the bottom of the interval from that at the top and taking ambient flow, if any, into account; Q_t is total pumping rate; ΔB_i is the thickness of interval i ; B_t is the total thickness of aquifer. K_a can be obtained from pumping or slug tests at the same well, although it is generally recommended that slug tests be used, as the average K in the immediate vicinity of the well may differ from that determined from a pumping test in a laterally heterogeneous aquifer^[5].

Figure B3 compares the results of borehole flowmeter profiling and multilevel slug tests at GEMS. Despite some local differences, the K estimates from borehole flowmeter profiling and multilevel slug tests are quite similar at that well.

B.2.4 DP Injection Logging

DP technology has shown great promise for characterization of K variations in shallow unconsolidated formations at the resolution, accuracy, and speed that are critically needed for practical investigations^{[28] [29] [30]}. Over the last few decades, a series of DP methods and probes have been developed for obtaining information about vertical variations in K^{[5] [6] [31]}.

DP Injection Logging (DPIL) is one of the most powerful approaches for K characterization (in terms of resolution and speed of acquisition) and is also one of the most widely used techniques in environmental site investigations^{[6] [32]}. This approach consists of advancing a probe with a single screened port (**Figure B6**). Water is injected continuously through the screen while the probe is advanced and the pressure response to injection is monitored behind the screen or at the surface. The profile of the ratio of injection rate to injection pressure is closely related to vertical variations in K. However, factors other than the hydraulic conductivity can potentially affect the pressure response (e.g., injection line losses, probe advancement speed, formation alteration, and variations in specific storage), so DPIL ratios only provide relative information about K variations. Methods are needed for transforming DPIL ratios into actual K estimates; these methods typically involve correlations with nearby K data.

There are currently two variants of DPIL: discontinuous^{[31] [33]} and continuous^{[29] [34] [35]} modes. In discontinuous DPIL mode, probe advancement is briefly halted at the desired depth and the injection rate is then varied in a stepwise fashion while injection rates and pressures are measured. In continuous DPIL mode, injection rate and pressure are measured as the probe is continuously advanced. Compared to continuous DPIL, discontinuous DPIL has a few advantages^[6]: (1) pore water pressure changes generated by probe advancement, which can be

difficult to characterize, have little influence on the measured injection pressures; (2) background hydrostatic pressures have no influence on the measured responses; and (3) use of multiple injection rates at each depth allows a better assessment of the formation response to injection. However, due to the need to halt advancement, discontinuous DPIL requires significantly more time than continuous DPIL, and, as a result, resolution below 10 – 20 cm is rarely possible. In common practice, continuous DPIL is generally preferred due to its speed (a 20-m profile requires about 2 hours) and resolution (one measurement per 1.5 cm vertical interval). A continuous DPIL probe, supplemented with an EC sensor, is commercially available from Geoprobe Systems under the tradename of the Hydraulic Profiling Tool (HPT; **Figure B6**).

The HPT is most effective in moderately permeable formations with a K range of 0.03 to 10 m/d, although the detection range can be improved by modifying equipment and operating procedures^[6]. In standard HPT practice, the probe advancement rate is 2 cm/s and the continuous water injection rate is about 300 mL/min. In high K formations (e.g., $K > 10$ m/d), the injection pressure response to the standard injection rate is generally too small to be reliably measured. A larger injection rate can be used to increase the pressure signal. However, the line loss between the transducer and injection screen, which increases with the injection rate quadratically, may become significant and require additional step tests to remove its impact^[6]. On the other hand, in low K formations (e.g., $K < 0.03$ m/d), the pressure increase from probe advancement and water injection may become so large that it will cause formation alterations and exceed the upper measurement limit of the transducer. A recent study has demonstrated that by reducing both probe advancement speed and flow injection rate, HPT can be applied to formations with K as low as 0.003 m/d^[36].

Transforming DPIL profiles into K estimates is based on empirical relationships^{[29] [31] [35] [37]}. Although a general relationship has been presented^[37], site-specific calibrations are typically used to improve the reliability of K estimates. The site-specific calibrations can be performed by comparing the DPIL profiles to nearby K estimates obtained via other means^{[31] [33]} or by a modeling approach that directly combines the DPIL data with collocated hydraulic tests^[35]. **Figure B6** shows a series of K profiles from continuous DPIL at an alluvial aquifer in Mississippi^[35].

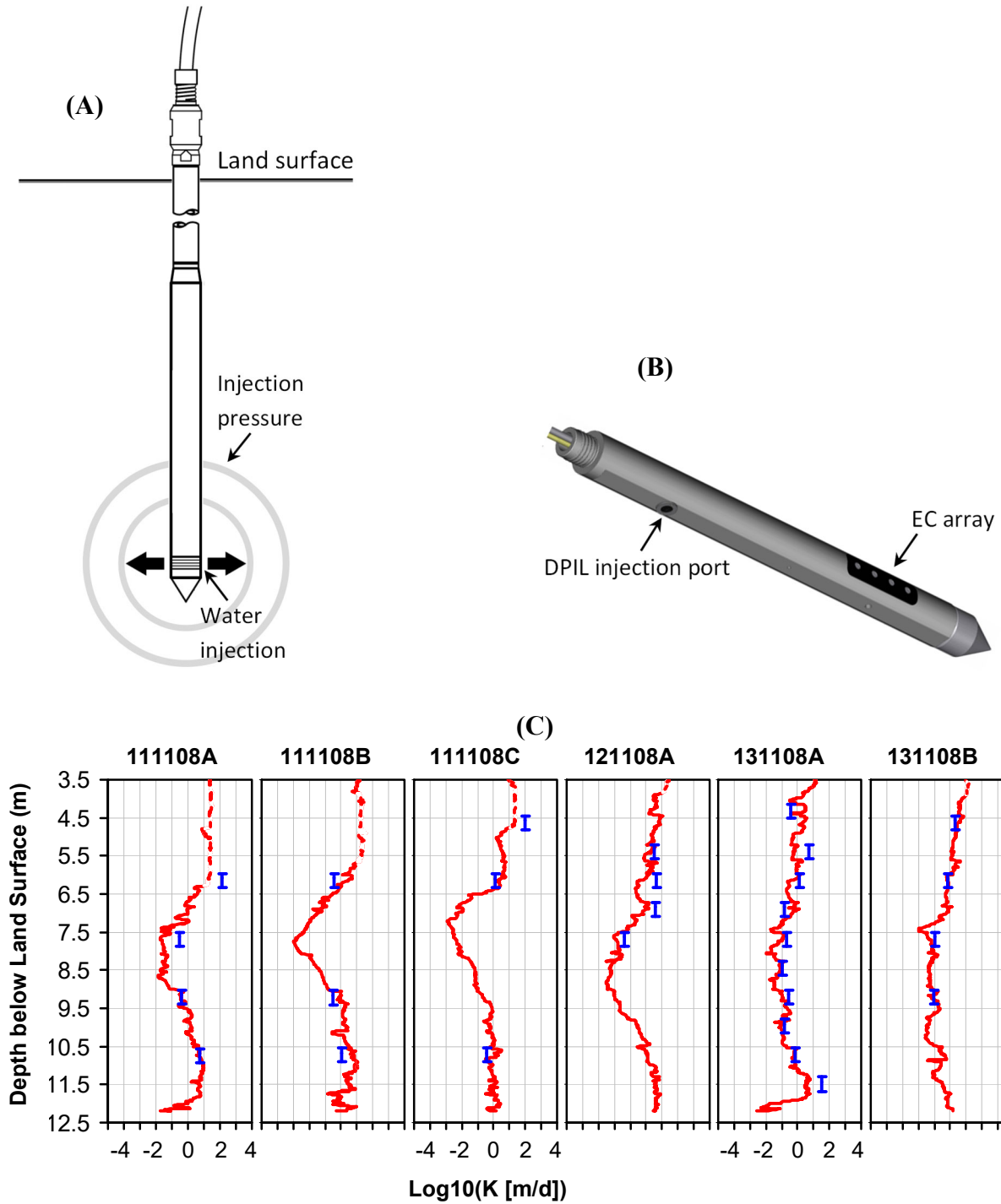


Figure B6. (A) Schematic of the DPIL with a screen attached to the probe rod at its lower end^[6], (B) Artistic rendering of the HPT^[33] (continuous DPIL probe combined with an EC Wenner array), and (C) Six example DPIL (red curve) K profiles calibrated by collocated DPP tests (blue bars) at the MacroDispersion Experiment (MADE) site, Columbus, MS^[35]. In (C), the dashed curves represent the upper K limit for continuous DPIL under the given tool operating procedure.

There are two major assumptions invoked for estimating K from DPIL profiles^{[6] [36]}. First, near-rod material compaction from probe advancement has a similar impact on K at all depths of the profile. Second, the impact of formation specific storage is either similar across the profile or can be ignored. Both assumptions appear to be valid for sands and gravels. In silts and clays, particularly those with high compressibility, considerable caution must be used to assess the viability of these assumptions.

B.2.5 DP Permeameter

The Direct Push Permeameter (DPP) consists of a short cylindrical screen with two pressure transducers inset into the probe at short distances above the screen (**Figure B7**)^{[5] [6] [38]}. The DPP probe is advanced to a depth at which a K estimate is needed and then a series of short-term injection tests are performed; K is typically estimated from the spherical form of Darcy's Law using the injection rate and the injection-induced pressure responses at the two transducers. The resulting estimate is a weighted average over the interval (approx. 0.4 m in **Figure B7**) between the screen and the farthest transducer; material outside of that interval has little influence^[39]. Horizontally, the DPP shows little sensitivity to conditions greater than ~ 0.5 m away from the tool. The DPP test procedure only requires that steady-shape (constant hydraulic gradient) flow conditions be attained; true steady-state conditions are not required, which can lead to a significant reduction in the measurement time. A DPP test sequence generally requires 10–15 minutes per measurement interval in moderate to high-K formations^[38].

Figure B7 shows an example DPP test sequence at GEMS^[6]. Three tests with different rates are used to assess the reliability of the K estimates. The first injection rate is typically based on the expected K value in the test interval (e.g., 800 mL/min for sands). Depending on the magnitude of the pressure response in the first test, the second injection rate can be set higher or lower than the first (if pressure response is high in the first test, the flow rate in the second test is reduced, and vice versa). The third flow rate is set similar to that in the first test to check if similar pressure response can be obtained. The K values computed using Darcy's Law are 66.0, 63.1 and 65.4 m/d, respectively, for the three tests in **Figure B7**. A set of consistent K estimates is the goal; a lack of consistency could indicate DPP system instability or formation alteration. **Figure B8** shows the comparison of DPP K estimates with those obtained from DP multilevel slug tests at GEMS^[38]. The results from DPP profiling have proven extremely useful for transforming collocated DPIL profiles into K estimates^{[25] [35]}.

The most significant advantage of the DPP is that, unlike all other hydraulic tests discussed here, screen clogging and near-rod compaction have a very small impact on K estimates. The insensitivity to the zone of compaction is a result of head-equalizing crossflow between the thin compacted zone and the surrounding formation^{[38] [39]}. The limited lateral sensitivity of the DPP (less than 0.5 m from the probe) is also one of its primary advantages, as it allows the tool to provide high-resolution profiles of vertical K variations in the immediate vicinity of the probe.

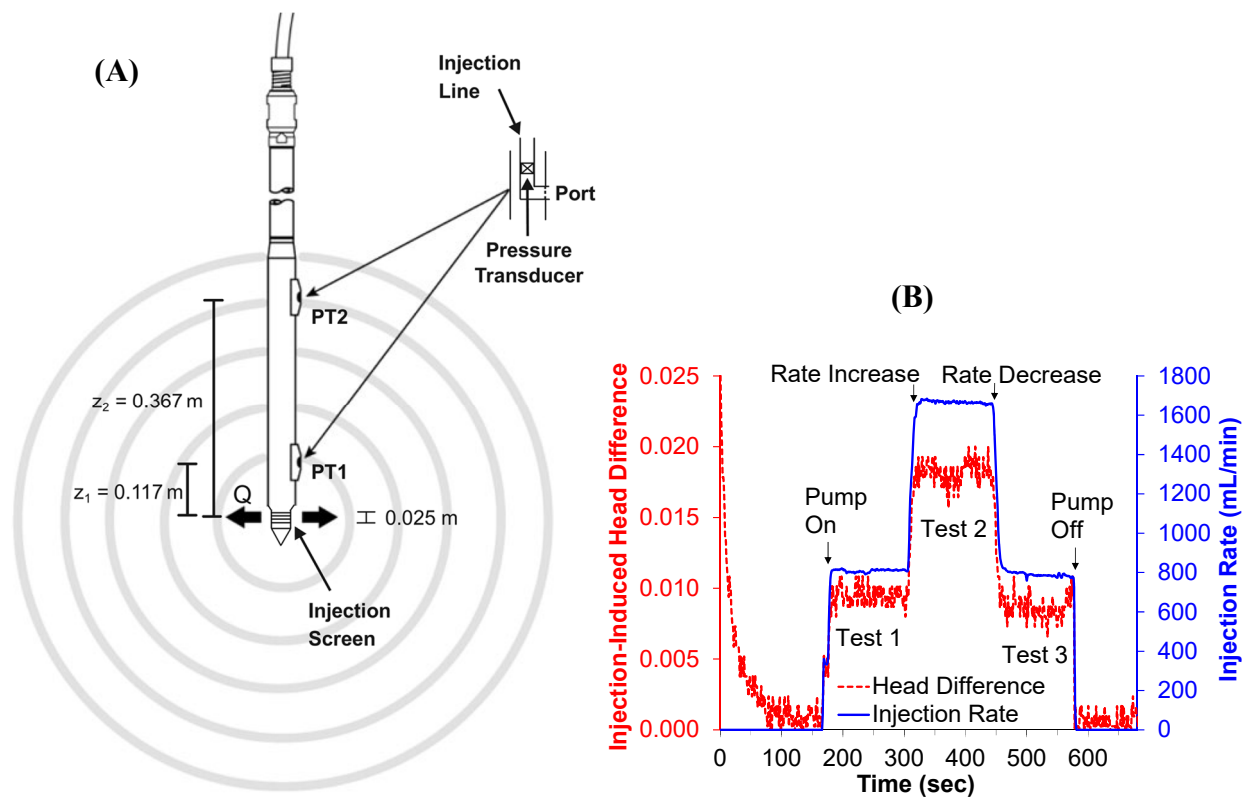


Figure B7. (A) Schematic of the DPP (not to scale), and (B) example DPP test sequence at GEMS^[6].

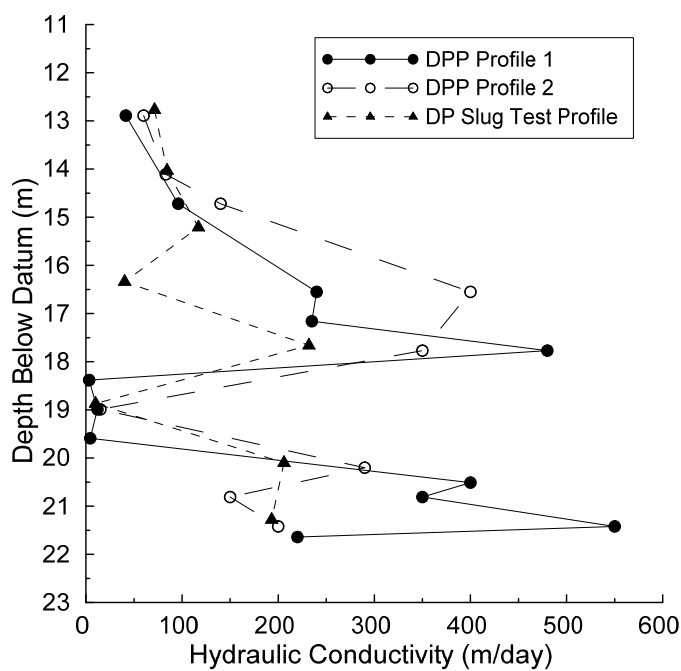


Figure B8. Comparison of DPP and DP multilevel slug test K profiles at GEMS^[5]. The slug test profile is located 2 m northwest of DPP profile 1 and 2 m southeast of DPP profile 2.

B.2.6 Laboratory Permeameter Tests on Core Samples

Laboratory permeameter tests of sediment or core samples collected during drilling are also used for acquiring information about formation K. Different hydraulic systems can be used, depending on the expected K value of the sample. In general, when the sample K is high, constant heads are used for both the influent and effluent tubes to maintain a constant hydraulic gradient across the sample; when K is low, falling heads are used for the influent tube with either constant or rising heads in the effluent tube. By measuring both the hydraulic gradient and flow rate, Darcy's Law can be used to calculate the sample K. In laboratory permeameter tests, considerable care must be given to all stages of the work, including sample preparation and installation into the test cell, use of appropriate ambient stress for materials with high swell potential, de-airing of the hydraulic system and sample, mobilization and resettling of fine materials, head losses in the tubes, non-Darcian flow, and biochemical reactions due to changes in temperature and pore water composition^{[40] [41]} (Klute and Dirksen, 1986; ASTM d5084).

As discussed earlier, the question of how representative samples are of field conditions should always be considered when assessing the K estimates from laboratory analyses. Larger-scale preferential flow features, such as macropores and fractures, are usually not captured adequately by the samples, so K estimates from laboratory permeameter tests should be considered as the lower end of the range for field values. Field-based characterization methods of K are preferred over laboratory-based methods in most environmental site investigations.

B.3 Indirect Approaches

B.3.1 Geophysical Methods

Estimates for formation K can also be inferred from the measurement of more readily evaluated geophysical properties using empirical, often site-specific, relationships. The geophysical properties that may be used for K estimation include, but are not limited to, electrical conductivity (EC) (or the reverse, electrical resistivity), the hydrogen response to nuclear magnetic resonance (NMR), and natural gamma radiation. In addition to K estimation, geophysical methods have also been used for many purposes in environmental site investigation, assessment and monitoring (see related article - [Geophysical Methods](#)).

Borehole EC logging measures vertical variations in the bulk EC of surrounding formation, which can then be used to estimate K based on empirical relationships^{[42] [43]}. EC has been adapted to DP equipment for more efficient assessment of subsurface conditions than the approaches that rely on existing wells^[44]. Variations in the EC of saturated media are primarily a function of pore-fluid chemistry, clay content, and total porosity. If variations in pore-fluid chemistry can be neglected, EC profiling can be used to delineate the major hydrostratigraphic features, and thus large-scale variations in K^[45]. However, when electrically conductive clay is absent, EC profiling generally provides little information about vertical variations in K in silts, sands and gravels.

Borehole natural gamma logging provides a record of natural gamma radiation versus depth. This radiation is quantified by counting the gamma particles passing through a scintillation

crystal in a certain time interval. A high natural gamma reading is generally associated with clay-rich intervals, while a low reading is generally associated with sands and gravels^[46]. Like EC logging, natural gamma logging provides an effective measurement of formation characteristics when clay is present, but is of less use in silts, sands and gravels.

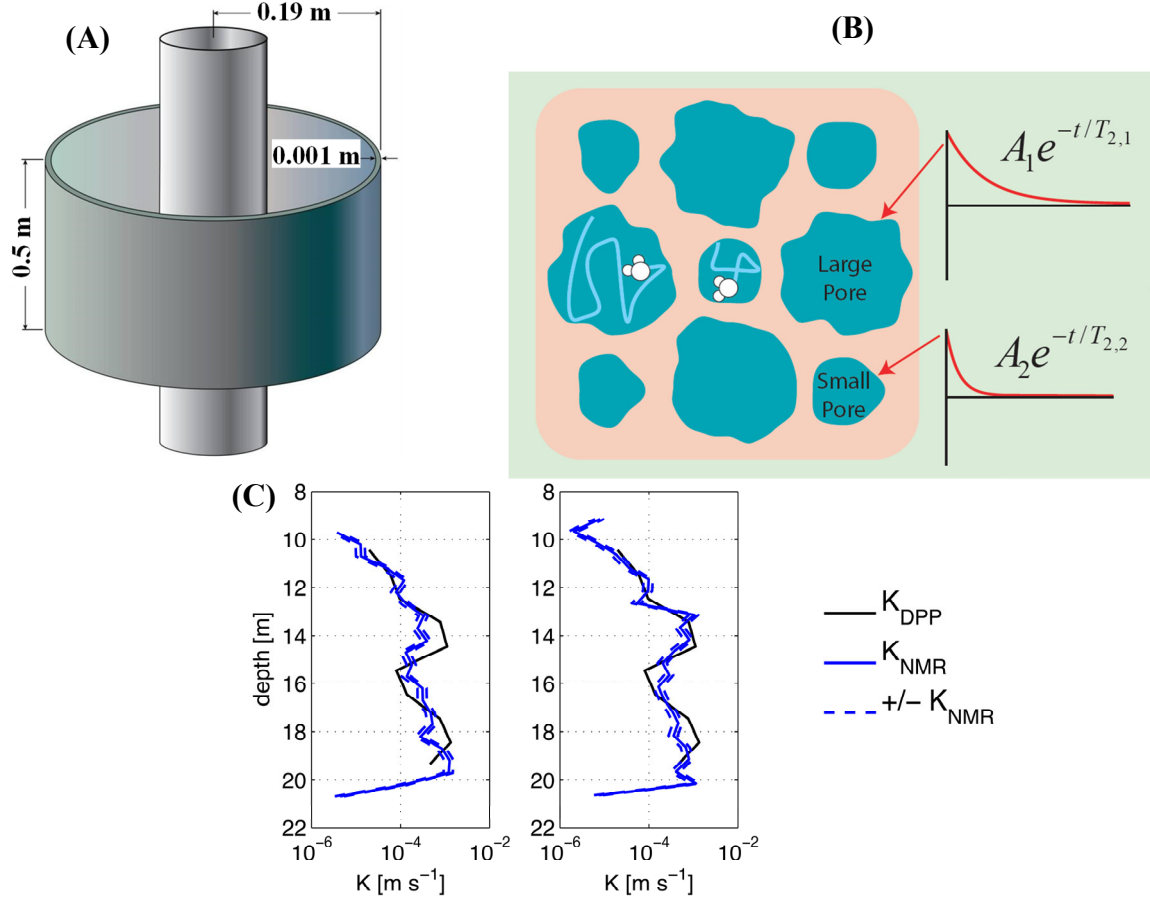


Figure B9. (A) Measurement domain around a NMR borehole probe, (B) NMR responses as a function of pore size^[48], and (C) Comparison of NMR and DPP K estimates at two GEMS locations^[49]. In (B), A is the initial magnetization, T_2 is NMR relaxation time. In (C), the dash lines show the range of the NMR K estimates due to the uncertainty in the empirical parameters used in the pore size - K relationship.

Efforts have been made to adapt nuclear magnetic resonance (NMR) profiling, a widely used borehole technique in the petroleum industry, to environmental site investigations^{[47] [48] [49]}. This approach involves measuring the response of hydrogen atoms (protons) to a series of imposed magnetic fields at radio frequency. The response is a function of, among other things, the pore-size distribution of material in a thin cylindrical ring centered on the probe (**Figure B9** and **Figure B9**). K is then estimated from the pore-size distribution information using different empirical relationships, all of which have their origins in the Kozeny-Carman equation^[49]. **Figure B9** compares the NMR with DPP K estimates at GEMS.

The NMR logging tools used in the petroleum industry are typically too large for use by the hydrological community (e.g., tools are typically well over 10 ft long and have a diameter larger than 5 inches). The equipment costs are also prohibitively high for hydrological users. After recent technology advancements, NMR measurement can be made much more effectively both at the surface and in a borehole, including with DP equipment^{[47] [48] [49]}. The equipment costs are significantly decreased compared to those used in the petroleum industry. The measurement time is reduced down to a few minutes per interval. The vertical sampling interval of most current logging tools is about 0.5 m. Different tools diameters are available, with the smallest being deployable in a 2-inch well. Due to these improvements, NMR has been increasingly used by environmental site investigators worldwide.

B.3.2 Cone Penetrometer profiling

Cone Penetrometer (CPT) profiling is one of the most common approaches for quantifying the mechanical properties of unconsolidated sediments by geotechnical engineers. CPT profiling measures the mechanical resistance on the tip of a conical probe and on a sleeve immediately behind the tip as the probe is advanced into the subsurface. These measurements are often supplemented by pore water pressure measured behind the cone tip due to its impact on mechanical responses to advancement. These quantities are used to determine the sediment class of the material, from which K can be estimated using empirical relationships. The resulting values, however, only provide order of magnitude estimates of formation K^[50].

CPT profiling can be periodically suspended to perform pore pressure dissipation tests to obtain information about the consolidation properties of the formation at selected depths. Hydraulic conductivity can be estimated from these dissipation tests using relationships between K and the consolidation properties of the formation. Generally speaking, the K estimates from dissipation tests tend to be more reliable than those from continuous logging. Robertson (2009)^[51] suggests that it is possible to combine continuous profiles and dissipation tests to improve the quality of CPT K estimates¹.

There are a few practical challenges with CPT profiling. First, it is difficult to keep the porous element for pore pressure measurement fully saturated while the probe is driven through the vadose zone. Clogging of the porous element may also be a concern at sites with a significant amount of fine materials. Similar to DPIL, formation alteration can produce a significant impact on the pore pressure. However, unlike the HPT where the pressure port is located further away from the tip, the porous element is immediately behind the tip so that the impact of probe advancement on the CPT pore pressure measurement will be much greater than with the HPT.

B.3.3 Laboratory Grain Size Analyses on Core Samples

Formation K can also be estimated from laboratory grain size analyses on sediment or core samples. A number of empirical and theoretical relationships have been developed for estimation of K from grain-size statistics. For example, K can be computed using the relationship developed by Hazen^[52],

$$K = C \times (d_{10})^2, \quad (\text{B-5})$$

where d_{10} is the particle diameter at which 10% of the sample's mass is comprised of particles with a diameter less than this value; C is an empirically-defined coefficient depending on grain size and sorting (the value of C varies with the units for K , and has a large range of published values reported by different researchers).

More theoretically based relationships between grain sizes and K have been developed from the Kozeny-Carman equation that relates formation K with porosity and grain sizes assuming the porous space can be modeled as tortuous tubes of different diameters. For example, the following relationship can be used to estimate K ^[53],

$$K = [n^3/(1 - n)^2] \times [(d_m)^2/180], \quad (\text{B-6})$$

where n is porosity, d_m is the geometric mean grain size calculated as $(d_{84} \times d_{16})^{0.5}$, K is in m/d and d_m is in mm. The K estimates from Kozeny-Carman approaches are generally considered to be more accurate than those from the Hazen equation, although both approaches have a number of significant limitations in practice^[54].

B.4 Choosing the Right Approaches

Due to the large uncertainty associated with core sample representativeness, field-based approaches are preferred for acquiring information about K in environmental site investigations. Under certain conditions, such as sites that are primarily composed of low- K silts and clays, hydraulic testing may be time consuming so that only a limited number of measurements can be obtained in the field. In this case, coring and subsequent laboratory analyses can be used as a complement to increase the spatial coverage of K across the site.

For field-based approaches, hydraulic tests provide more reliable K estimates than indirect approaches such as geophysical methods. However, geophysical methods are generally more time efficient and can provide more information about the spatial continuity of subsurface flow and transport features. There is a growing interest in the joint use of hydraulic tests and geophysical methods, so that high-resolution characterization of K can be obtained across the entirety of a site, rather than just in the immediate vicinity of the limited number of boreholes.

Pumping tests provide K estimates averaged over a large volume of formation and do not provide information at the scale relevant to solute transport, so they are not recommended in environmental site investigations directed at getting information about spatial variations in K . Slug tests can be used to obtain high-quality K estimates at the relevant scale, but considerable care must be exercised in all stages of the work, including the proper development of the measurement interval prior to the tests. Borehole flowmeter profiling is sensitive to in-well hydraulics and generally does not provide high-quality K estimates in less permeable settings.

DP methods have great promise for becoming the primary K characterization tool in environmental investigations of relatively shallow unconsolidated formations. Because the tools are small in diameter and no materials are removed during advancement, DP methods generate much less site disturbance than traditional borehole techniques (e.g., rotary drilling). Essentially

all the K methods that have been developed for use in wells can be adapted to DP equipment. Two of the most promising DP K methods are DP injection logging and the DP permeameter. DP injection logging is quick and high-resolution, but is considered to only provide relative information on K because factors other than K can also affect the pressure response. The DPP provides very reliable K estimates and is more time efficient than other formal hydraulic test methods. The most significant advantage of DPP is that a low-K zone formed by advancement-induced compaction has little impact on the estimated K due to head-equalizing crossflow between the thin compacted zone and the surrounding formation.

B.5 Summary

A variety of methods are available for characterizing K in environmental site investigations. These methods can be grouped into hydraulic methods, which involve water injection or extraction and the measurement of the induced pressure response, and indirect methods, which rely on empirical correlations, often site-specific in nature, between K and more readily evaluated formation properties. Compared to indirect methods, hydraulic methods provide more reliable K estimates, although indirect geophysical methods can provide more information about the spatial continuity of subsurface features. Characterization approaches can be further classified based on whether the measurement is performed in the field or on laboratory core samples. Due to the uncertainty about how representative core samples are of site conditions, field approaches are usually preferred. In particular, two DP-based approaches, DP injection logging and the DP permeameter, are considered to have the greatest promise to become the primary K characterization tool in environmental site investigations in shallow unconsolidated settings. DP injection logging is quick and high-resolution, while the DPP provides very reliable K estimates that are not significantly impacted by a compacted zone around the probe. Finally, given the advantages of the different approaches, site investigators may find that a combination of methods will provide the best solution for high-resolution K characterization.

B.6 References

1. Boggs, J.M., S.C. Young, L.M. Beard, L.W. Gelhar, K.R. Rehfeldt, and E.E. Adams, 1992. Field study of dispersion in a heterogeneous aquifer, 1, overview and site description. *Water Resour. Res.* 28(12), 3281-3291.
2. Dagan, G., and S.P. Neuman, 1997. *Subsurface Flow and Transport: A Stochastic Approach*. Cambridge Univ. Press, Cambridge, UK.
3. Fogg, G.E., S.F. Carle, C. Green, 2000. Connected network paradigm for the alluvial aquifer system. In: Zhang, D., Winter, C.L. (eds.): *Theory, Modeling, and Field Investigation in Hydrogeology: A Special Volume in Honor of Shlomo P. Neuman's 60th Birthday*. Geological Society of America Special Paper 348, pp. 25-42.
4. Haslauer, C.P., A. Bárdossy, and E.A. Sudicky, 2017. Detecting and modelling structures on the micro and the macro scales: Assessing their effects on solute transport behavior. *Advances in Water Resources* 107, 439 -450, doi: /10.1016/j.advwatres.2017.05.007.
5. Butler, J.J., Jr., 2005. Hydrogeological methods for estimation of hydraulic conductivity. In: *Hydrogeophysics*, ed. Y. Rubin and S. Hubbard, Springer, The Netherlands, 23-58.
6. Liu, G., J.J. Butler, Jr., E.C. Reboulet, and S. Knobbe, 2012. Hydraulic conductivity profiling with direct push methods. *Grundwasser* 17(1), doi: 10.1007/s00767-011-0182-9.
7. Butler, J.J., Jr., 2009. Pumping tests for aquifer evaluation – Time for a change? *Ground*

Water 47(5): 615-617.

8. Kabala, Z.J., 1993. The dipole flow test: A new single-borehole test for aquifer characterization, *Water Resour. Res.*, 29(1), 99-107.
9. Zlotnik, V.A., and B.R. Zurbuchen, 1998. Dipole probe: Design and field applications of a single-borehole device for measurements of small-scale variations of hydraulic conductivity, *Ground Water*, 36(6), 884-893.
10. Datta-Gupta, A., S. Yoon, D.W. Vasco, and G.A. Pope, 2002. Inverse modeling of partitioning interwell tracer tests: A streamline approach, *Water Resour. Res.*, 38(6), 1079, doi:10.1029/2001WR000597.
11. Yeh, T.C.J., and S. Liu. 2000. Hydraulic tomography: Development of a new aquifer test method. *Water Resources Research* 36, no. 8: 2095-2105.
12. Bohling, G.C., and J.J. Butler, 2010. Inherent limitations of hydraulic tomography, *Ground Water*, 48(6), 809-824, doi:10.1111/j.1745-6584.2010.00757.x.
13. Rasmussen, T.C., K.G. Haborak, and M.H. Young, 2003. Estimating aquifer hydraulic properties using sinusoidal pumping at the Savannah River Site, South Carolina, USA, *Hydrogeology Journal*, vol. 11, pp. 466-482.
14. Batu, V., 1998. *Aquifer Hydraulics*, Wiley, 727 pp.
15. Kruseman, G. P., and N. A. de Ridder, 1990. *Analysis and Evaluation of Pumping Test Data – ILRI Pub. 47*, The Netherlands: International Institute for Land Reclamation and Improvement.
16. Duffield, G.M., 2007. *AQTESOLV for Windows Version 4.5 User's Guide*, HydroSOLVE, Inc., Reston, VA.
17. Butler, J.J., Jr., 1998. *The Design, Performance, and Analysis of Slug Tests*, Lewis Pub., 252 pp.
18. Butler, J.J., Jr., G. Duffield, and D. Kelleher, 2009. *Field Guide for Slug Testing and Data Analysis*, Midwest Geosciences Group, 4 pp.
19. Butler, J.J., Jr., E.J. Garnett, and J.M. Healey, 2003. Analysis of slug tests in formations of high hydraulic conductivity, *Ground Water*, 41(5), 620-630.
20. Hinsby, K., P.L. Bjerg, L.J. Andersen, B. Skov, and E.V. Clausen, 1992. A mini slug test method for determination of a local hydraulic conductivity of an unconfined sandy aquifer, *Jour. Hydrology*, 136, 87-106.
21. Butler, J.J., Jr., J.M. Healey, G.W. McCall, E.J. Garnett, and S.P. Loheide, II, 2002. Hydraulic tests with direct-push equipment, *Ground Water*, 40(1), 25-36.
22. McCall, W., J.J. Butler, Jr., J.M. Healey, A.A. Lanier, S.M. Sellwood, and E.J. Garnett, 2002. A dual-tube direct-push method for vertical profiling of hydraulic conductivity in unconsolidated formations, *Environ. & Eng. Geoscience*, 8(2), 75-84.
23. Sellwood, S.M., J.M. Healey, S. Birk, and J.J. Butler, Jr., 2005. Direct-push hydrostratigraphic profiling: Coupling electrical logging and slug tests. *Ground Water* 43(1), 19-29.
24. Molz, F.J., R.H. Morin, A.E. Hess, J.G. Melville, and O. Guven, 1989. The impeller meter for measuring aquifer permeability variations: Evaluation and comparison with other tests, *Water Resour. Res.*, 25(7), 1677-1683.
25. Bohling, G.C., G. Liu, S. Knobbe, E.C. Reboulet, D.W. Hyndman, P. Dietrich, and J.J. Butler, Jr., 2012. Geostatistical analysis of centimeter-scale hydraulic conductivity variations at the MADE site, *Water Resources Research*, 48, W02525, doi: 10.1029/2011WR010791.

26. Young, S.C., and H.S. Pearson, 1995. The electromagnetic borehole flowmeter: Description and application, *Ground Water Monit. and Remed.*, 15(2), 138-146.
27. Boman, G.K., F.J. Molz, and K.D. Boone, 1997. Borehole flowmeter applications in fluvial sediments: Methodology, results, and assessment, *Ground Water*, 35(3), 443-450.
28. Dietrich, P., and C. Leven, 2005. Direct push technologies. In: Kirsch, R. (ed.) *Groundwater Geophysics*, pp. 321-340. Springer, Berlin.
29. McCall, W., D.M. Nielsen, S.P. Farrington, and T.M. Christy, 2006. Use of Direct-Push Technologies in Environmental Site Characterization and Ground-Water Monitoring; in *Practical Handbook of Environmental Site Characterization and Ground-Water Monitoring*, 2nd Edition. Taylor & Francis Group, New York, NY. pp. 345-471. doi: 10.1201/9781420032246.ch6.
30. Leven, C., H. Weiß, T. Vienken, and P. Dietrich, 2011. Direct-Push-Technologien – effiziente untersuchungsmethoden für die untergrunderkundung. *Grundwasser* 16(4), 1-14. doi:10.1007/s00767-011-0182-9.
31. Dietrich, P., J.J. Butler, Jr., and K. Faiss, 2008. A rapid method for hydraulic profiling in unconsolidated formations. *Ground Water* 46(2), doi: 10.1111/j.1745-6584.2007.00377.x, 323-328.
32. Maliva, R.G., 2016. Direct-Push Technology. In: *Aquifer Characterization Techniques*, Springer Hydrogeology, Springer, Cham.
33. Lessoff, S.C., U. Schneidewind, C. Leven, P. Blum, P. Dietrich, and G. Dagan, 2010. Spatial characterization of the hydraulic conductivity using direct-push injection logging. *Water Resources Research* 46, W12502 (2010). doi:10.1029/2009WR008949.
34. McCall, W., T.M. Christy, T. Christopherson, and H. Issacs, 2009. Application of direct push methods to investigate uranium distribution in an alluvial aquifer. *Ground Water Monit. Remediat.* 29(4), 65-76.
35. Liu, G., J.J. Butler, Jr., G.C. Bohling, E. Reboulet, S. Knobbe, and D.W. Hyndman, 2009. A new method for high-resolution characterization of hydraulic conductivity. *Water Resources Research* 45, W08202, doi:10.1029/2009WR008319.
36. Liu, G., Borden, R. C. and Butler, J. J., 2018. Simulation Assessment of Direct Push Injection Logging for High-Resolution Aquifer Characterization. *Groundwater*. . doi:10.1111/gwat.12826. .
37. McCall, W. and T.M. Christy, 2010. Development of a hydraulic conductivity estimate for the Hydraulic Profiling Tool (HPT), The 2010 North American Environmental Field Conference & Exposition: Conference Program with Abstracts: Session VII.
38. Butler, J.J., Jr., P. Dietrich, V. Wittig, and T. Christy, 2008. Characterizing hydraulic conductivity with the direct-push permeameter. *Ground Water* 45(4), 409-419.
39. Liu, G., G.C. Bohling, and J.J. Butler, Jr., 2008. Simulation assessment of the direct-push permeameter for characterizing vertical variations in hydraulic conductivity. *Water Resources Research* 44, W02432. doi:10.1029/2007WR006078.
40. Klute, A., and C. Dirksen, 1986. Hydraulic conductivity and diffusivity: Laboratory methods, In: *Methods of Soil Analysis, Part 1., Physical and Mineralogical Methods*, ed. by A. Klute, *Agronomy Monograph 9*, American Soc. of Agronomy, 687-734.
41. American Society for Testing and Materials International, 2016. D5084. Standard test methods for measurement of hydraulic conductivity of saturated porous materials using a flexible wall permeameter. West Conshohocken, PA, USA. Doi:10.1520/D5084-16A.

42. Purvance, D.T., and R. Andricevic, 2000. On the electrical-hydraulic conductivity correlation in aquifers. *Water Resources Research* 36, 2905-2913.
43. Slater, L., and D.P. Lesmes, 2002. Electrical-hydraulic relationships observed for unconsolidated sediments. *Water Resources Research* 38(10). doi:10.1029/2001WR001075.
44. Christy, C.D., T.M. Christy, and V. Witting, 1994. A percussion probing tool for the direct sensing of soil conductivity. In *Proceedings of the 8th National Outdoor Action Conference*, 381-394. Westerville, Ohio: National Ground Water Association.
45. Schulmeister, M.K., J.J. Butler, Jr., J.M. Healey, L. Zheng, D.A. Wysocki, and W. McCall, 2003. Direct-push electrical conductivity logging for high-resolution hydrostratigraphic characterization. *Ground Water Monit. Remediat.* 23(3), 52-62.
46. Keys, W.S., 1990. Borehole geophysics applied to ground-water investigations, USGS *Techniques of Water-Resources Investigations*, Book 2, Chapter E2, 150 pp.
47. Walsh, D., P. Turner, E. Grunewald, H. Zhang, J.J. Butler, Jr., E. Reboulet, S. Knobbe, T. Christy, J.W. Lane, Jr., C.D. Johnson, T. Munday, and A. Fitzpatrick, 2013. A small-diameter NMR logging tool for groundwater investigations. *Groundwater*, 51(6): 914-926.
48. Grunewald, E., D. Walsh, P. Turner, J.J. Butler, Jr., R. Knight, E. Reboulet, S. Knobbe, and T. Christy, 2011. Field demonstration of nuclear magnetic resonance (NMR) logging tools for groundwater and environmental investigations (abstract). In: *Symposium on the Application of Geophysics to Engineering and Environmental Problems (SAGEEP)*.
49. Knight, R., D.O. Walsh, J.J. Butler, Jr., E. Grunewald, G. Liu, A.D. Parsekian, E.C. Reboulet, S. Knobbe, and M. Barrows, 2016. NMR logging to estimate hydraulic conductivity in unconsolidated aquifers. *Groundwater*, 54(1): 104-114. doi:10.1111/gwat.12324.
50. Lunne, T., P.K. Robertson, and J.J.M. Powell, 1997. *Cone penetration testing. Geotechnical Practice*. CRC Press, 352 pgs. ISBN 978-0419237501.
51. Robertson, P.K., 2009. Interpretation of cone penetration tests – a unified approach. *Canadian Geotechnical Journal* 46(11): 1337-1355.
52. Freeze, R.A., and J.A. Cherry, 1979. *Groundwater*, Prentice Hall, 604 pp.
53. Bear, J., 1972. *Dynamics of Fluids in Porous Media*, Dover, 764 pp.
54. Carrier, W.D., 2003. Goodbye, Hazen; Hello, Kozeny–Carman, *J. Geotech. Geoenviron.*, 129, 1054-1056.

B.7 See Also

- [Kansas Geological Survey Direct Push Methods Research](#)
- [Kansas Geological Survey Well Tests Research](#)
- [Geoprobe Direct Image Systems](#)
- [EPA Characterization and Monitoring Technologies for Environmental Sites](#)

APPENDIX C

Publications and Presentations

C.1 Journal Articles

1. Falta, R.W. and Wang, W., 2017. A Semi-analytical Method for Simulating Matrix Diffusion in Numerical Transport Models. *Journal of Contaminant Hydrology*, 197:39-49.
2. Muskus, N. and Falta, R.W., 2018. Semi-analytical Method for Matrix Diffusion in Heterogeneous and Fractured Systems with Parent-Daughter Reactions. *Journal of Contaminant Hydrology*, 218: 94-109.
3. Liu, G., R. Borden, and J.J. Butler, Jr., 2019, Simulation assessment of direct push injection logging for high resolution aquifer characterization. *Groundwater*, doi: 10.1111/gwat.12826.
4. Borden, R.C., Cha, K.Y. and Liu, G., 2020, A Physically Based Approach for Estimating Hydraulic Conductivity from HPT Pressure and Flowrate, *Groundwater*, <https://doi.org/10.1111/gwat.13039>.
5. Borden, R.C. and Cha, K.Y., In Preparation, Estimating Impact of Matrix Diffusion on Groundwater Cleanup Time, *Journal of Contaminant Hydrology*.
6. Liu, G., S. Knobbe, J.J. Butler, Jr., and R. Borden, In Preparation, Direct Push Injection Logging for High Resolution Characterization of Low Permeability Zones. *Groundwater*.

C.2 Enviro.wiki Articles

1. Liu G. and Butler, Jr. J.J. 2018. Characterization Methods – Hydraulic Conductivity, www.ENVIRO.wiki.
2. Falta, R.W., and K. Pham. 2019. REMChlor-MD, www.ENVIRO.wiki.
3. Borden, R.C., 2020. Matrix Diffusion, www.ENVIRO.wiki.

C.3 Presentations and Posters

1. Falta, R.W., Newell, C.J. and Farhat, S.K., Development of a Practical Approach for Modeling Matrix Diffusion Effects in Groundwater Models, presented at the 10th International Conference on Remediation of Chlorinated and Recalcitrant Compounds, Palm Springs, CA, May 2016.
2. Falta, R.W., A Semi-Analytical Method for Modeling Matrix Diffusion in Fractured and Heterogeneous Systems, REMTEC Remediation Technology Summit, Denver, CO, March 2017.
3. Liu, G., S. Knobbe, J. J. Butler, Jr, E. C. Reboulet, R. Borden, G. Bohling, Direct push injection logging for high resolution characterization of low permeability zones, NovCare (Novel Methods for Subsurface Characterization and Monitoring) 2017 Conference, Dresden, Germany, June 2017.
4. Liu, G., Knobbe, S., Butler, Jr, J.J., Borden, R.C. and Bohling, G., Hydraulic profiling tool (HPT) for high resolution characterization of low permeability zones, SERDP & ESTCP Symposium 2017. Washington DC, Nov. 2017.
5. Cha, K.Y., Borden, R.C. and Yuncu B. Using Direct Push Logs (HPT & CPT) for Groundwater Modeling, SERDP & ESTCP Symposium 2017. Washington, DC, Nov. 2017.
6. Liu, G., Knobbe, S., Butler, Jr, J.J., Reboulet, E.C., Borden, R.C. and Bohling, G., Direct push injection logging for high resolution characterization of low permeability zones. Abstract (H32A-08), AGU Fall Meeting, New Orleans, LA, Dec. 2017.

7. Liu, G., S. Knobbe, R. Borden, and J. J. Butler, Jr (2018), A low permeability extension of Hydraulic Profiling Tool: challenges and solutions. Abstract (H51A-08) presented at 2018 AGU Fall Meeting, Washington D.C., 10-14 Dec.
- 8.
9. Falta, R.W., Muskus, N., Newell, C. and Farhat, S., REMChlor-MD: A Screening Level Remediation Simulation Model that Considers Matrix Diffusion, 11th International Conference on Remediation Chlorinated and Recalcitrant Compounds, Palm Springs, CA, April 2018.
10. Cha, K.Y., Borden, R.C. and Yuncu, B., Slower than Expected Aquifer Cleanup –Back Diffusion or Something Else?, 11th International Conference on Remediation of Chlorinated and Recalcitrant Compounds, Palm Springs, CA, April 2018.
11. Cha, K.Y., Borden, R.C. and Yuncu, B., Using Hydraulic Profiling Tool (HPT) for Site Characterization, SERDP & ESTCP Symposium 2018, Washington, DC, Nov. 2018.
12. Falta, R.W., Using the Vinsome and Westerveld Method for Modeling Matrix Diffusion in Numerical Transport Simulations, presented at the *2018 TOUGH Symposium* at the Lawrence Berkeley National Lab, Berkeley, CA, October 8-10, 2018.
13. Cha, K.Y., Borden, R.C., Yuncu, B. and Liu, G., Improved Methods for Estimating K with Hydraulic Profiling Tool (HPT), 2019 Bioremediation Symposium, Baltimore, MD, April 2019.